QUANTITATIVE MODELLING FOR OPTIMIZATION OF THE CZOCHRALSKI GROWTH OF SILICON

by

THOMAS ARTHUR KINNEY

B.A.Sc., University of Waterloo
(1986)
M.S.C.E.P., Massachusetts Institute of Technology
(1988)

Submitted to the Department of Chemical Engineering
in partial fulfillment of the requirements for the degree of

DOCTOR OF SCIENCE

at the

MASSACHUSETTS INSTITUTE OF TECHNOLOGY

June 1992

Signature of Author .....
Department of Chemical Engineering
February 10, 1992

Certified by .....
Robert A. Brown
Arthur D. Little Professor
Head of the Department of Chemical Engineering
Thesis Supervisor

Accepted by .....
William M. Deen
Professor, Department of Chemical Engineering
Chemical Engineering Graduate Officer

QUANTITATIVE MODELLING FOR OPTIMIZATION OF THE CZOCHRALSKI GROWTH OF SILICON

by

THOMAS ARTHUR KINNEY

Submitted to the Department of Chemical Engineering
on February 12, 1992, in partial fulfillment of the
requirements for the degree of
DOCTOR OF SCIENCE

Abstract

Silicon is vital to the microelectronics industry, and demands the highest quality from the silicon substrate, as measured by perfect crystalline structure, compositional correctness, and large surface area. Presently, industrial growth of $20\,cm$ or larger silicon boules in Czochralski (CZ) systems scaled-up linearly from smaller systems is plagued by the catastrophic propagation of dislocations. The concentration of oxygen and *in situ* annealing schedule are critical factors in this phenomenon (Lin and Benson, 1987). The failure of linear scale-up occurs because the physical phenomena governing the operating state of the CZ puller are nonlinear. The nonlinearities reflect the complex balance between heat transfer by radiation, conduction and convection, mass transfer, fluid flow, solidification kinetics, free boundary dynamics and solid-state physics in the CZ chamber. Numerical modelling is used to analyze this process because of its ability to approximate physical detail more cheaply and with greater flexibility than an experimental apparatus.

The failing of most large-scale numerical models has been their dependence on empirical boundary conditions, their lack of accounting for all heat transfer mechanisms, or their inability to accurately simulate melt flow. Hence, the objective of this thesis is to develop a general method for simulating heat transfer, melt flow and free boundaries in the CZ silicon growth which can be used for optimization, and to test its accuracy by simulating a specific system and comparing predictions with measurements.

The Integrated Hydrodynamic Thermal-Capillary Model, or IHTCM, comprises a comprehensive model of heat transfer and melt convection with an efficient finite-element/Newton method for solving the equations as a function of operating conditions and system design. It combines a description of heat transfer by conduction and diffuse, gray radiation between all components within the typical CZ enclosure with calculation of axisymmetric, steady-state, laminar convection in the melt. The IHTCM computes the meniscus shape, the shape of the melt/crystal interface and the radius of the crystal simultaneously with the temperature and flow fields. These outputs in turn determine the thermoelastic stress in the crystal which is an indicator of the likelihood of dislocation formation (Jordan et al., 1986), and the partitioning of dopants or impurities.

The experimental apparatus used for the comparison was a Siltec $254\,mm$ crystal

puller. The experiment measured the thermal field throughout the growth chamber. A specially designed thermowell was used to obtain a temperature profile spanning the voids in the chamber. Also the melt-solid interface shape was obtained by x-ray analysis, which provides a second, more local measure of the temperature field. The measurements were compared to an extension of the IHTCM to account for a passive thermowell tube in radiative equilibrium in the CZ chamber.

The good agreement between these measurements and predictions, provides some of the strongest practical conclusions from this thesis. A realistic estimate of the thermal stresses was computed and showed that the thermoelastic stress was undeniably greater than the critical resolved shear stress which is a benchmark value for the stress required to deform a material by glide and multiplication of dislocations. The fact that *single* crystal material was grown strongly suggests that the *generation* of dislocations in large-scale silicon growth is a determining factor. Also, the IHTCM was unable to calculate a steady-state flow field with the flow mechanisms combined due to increasingly convoluted flow patterns as the correct parameter values were approached; the actual flow is time-dependent and three-dimensional. This deficiency demonstrates the need to account for time-dependence in a model of CZ flows in large systems. The melt-solid interface shape, which is highly sensitive to the flow field, was deflected in the correct direction when natural convection was included, but was not accurately predicted when all flow mechanisms were combined. A modification to account for turbulent transport in the melt was the final extension of the IHTCM in this thesis.

The IHTCM was augmented to account for turbulent fluid flow and heat transfer with a $K-\epsilon$ prescription for these quantities. The $K-\epsilon$ /IHTCM yields a robust prediction of the mean transport rates at realistic growth conditions and accurately predicts the observed melt/solid interface shape. The transport of oxygen is also predicted with the $K-\epsilon$ /IHTCM and the effects of crystal and crucible rotation on oxygen transport agree qualitatively with those reported in the literature.

The accurate thermal predictions of the IHTCM, made possible by radiative heat-transfer modelling, indicate that the solution to the dislocation problem lies in suppressing the nucleation of dislocations. This issue has since received devoted attention from a colleague (Maroudas, 1992). Models of axisymmetric/steady-state melt flow produce a multiplicity of solutions close to the realistic viscosity, and therefore cannot predict the transport in large-diameter melts with rotation and natural convection. The $K-\epsilon$ /IHTCM for turbulent transport uniquely predicts realistic conditions, accurately predicts the heat-transfer near the melt/solid interface, and agrees qualitatively with the effects of crystal and crucible rotation rate on oxygen transport. The $K-\epsilon$ /IHTCM can explore wide ranges of operating parameter-space and hence has good potential for optimizing a large-scale CZ crystal-puller.

Thesis Supervisor: Robert A. Brown
Title: Arthur D. Little Professor
Head of the Department of Chemical Engineering

Acknowledgments

Above all, I would like to thank Dr. R.A. Brown who has made my stay at M.I.T. the rich educational experience I was seeking. I am grateful for his encouragement and advice, as well as that of my thesis committee (Profs. H.H. Sawin, George Stephanopoulos, J.W. Tester and Dr. M.J. Wargo), and my collaborators at I.B.M. (Dr. Tom Strudwick and especially Dr. K.M. Kim). All my future achievements will be due in large part to their positive influence. I am grateful to the I.B.M. corporation which provided financial support for part of this project and to the National Science Foundation for bountiful grants of computer time at the Cornell National Supercomputer Facility.

The most enjoyable part of my doctoral work was presenting my efforts to interested researchers in the semiconductor crystal growth community. The pearls of this experience are my friendships with Prof. Georg Müller, Dr. Dieter Hoffmann and Dr. Hiroyuki Uchida; I regret not being able to collaborate with them in the pursuit of my postgraduate goals.

I consider myself extremely lucky to have the support and companionship of Anna, which have endured these past years. With them I have never doubted the beauty of my life, even during my most trying personal moments here. Now we can finally pursue our common dreams! I credit my mother Johanna for unflinching love and confidence with respect to my abilities; thanks, Mom. My brothers Allan, Evert, George and Jan are too tall for my liking, but have compensated with appreciation for my *academic* stature, and the rock & roll megagroup **Three Uncles and a Deaf Baby** has kept me company on many all-nighters in Room 66-256. Aunt Mary, you'll finally get the graduation photograph I promised.

I could not have chosen a better group of colleagues. I have the utmost confidence that Agathaggelos, Bruce, Costas, David, Dimitrios, Do "jacuzzi" Kim, Howard, Jim, Lou, Mark, Nick, Paul, Phil, Ram, Reza, Sanjay and those boys from 66-246 will lead highly productive lives and make those around them very happy. They did that for me. And thank God for Arline.

I am also grateful for the expert and sympathetic services of the M.I.T. medical department as my pit crew during my stay at M.I.T.

I dedicate my efforts in this thesis to all my brothers: if this achievement of mine were somehow to inspire you to increased fruition of your talents that I have always admired, then I will have accomplished something truly worthwhile. As a matter-of-fact, I can't imagine a greater outcome.

Contents

List of Figures

List of Tables

Chapter 1

Modelling Czochralski Silicon Growth

Summary

The last forty-five years since the advent of the transistor has seen microelectronics blossom from being an industrial novelty to being one of the most compelling forces in today's world. Electronics is poised to supersede transportation as the world's largest industry and has been a compelling factor in the redistribution of population to suburban centers, the increased technological requirements in education and the replacement of the labor-oriented work force with a highly-skilled working class. Electronics has even proven itself to be a major political force: superior electronic systems were undeniably a decisive factor in the United Nations forces' recent Persian Gulf victory and inferior electronics has helped provoke the downfall of collectivist societies whose economies withered and popularity crumbled as they failed to keep pace with the so called "high-tech" advances of free-market countries. The driving force behind this electronics revolution has been the advancement in microelectronics technology, which has been due to remarkable achievements working with the electronic properties of the single-crystal state of elemental silicon.

Silicon has made the microelectronics revolution possible. Its unique ability to retain a single-crystalline structure in spite of severe processing conditions and to grow a native oxide have been responsible for its premier status in electronic devices. Spearheading this revolution have been advances in high speed integrated circuit manufacture, which demand the highest possible quality from the silicon substrate. Quality in this context can be defined as:

- perfect crystalline structure: synonymously, the absence of dislocations

- compositional correctness, and
- large surface area.

Achieving these requirements ensures the electrical and mechanical integrity of the substrate, and enables the maximum degree of integration per chip.

Silicon substrate is grown by the Czochralski method (CZ), a process whereby a solid crystal is *pulled* from a pool of its own melt. Theoretical analysis or modelling of silicon growth by CZ has been underway since the early 1950's, but these models had little impact on practical technique compared to experience gained through trial-and-error experimentation, at least until the mid-1980's. By that time chip manufacturers were demanding silicon boules of sufficiently large diameter that linear scale-up of successfully operating smaller-diameter systems was failing at appreciable rates. This failure was not surprising, however, since the physical phenomena governing the operating state of the CZ puller are not linear. The nonlinearities are manifestations of the complex balance between heat transfer by radiation, conduction and convection, mass transfer, fluid flow, solidification kinetics and free boundary dynamics that must be maintained for the successful growth of a silicon boule. Attempts to produce a tractable *experimental model*, i.e. an analogous physical system, with the same characteristics as large-scale CZ silicon growth are hindered due to the severe processing conditions. Conventional investigations have been limited to low temperature studies, which do not duplicate the radiative heat transfer in the true CZ process. In order to directly observe flows, clear fluids are used in conventional procedure, but they do not conduct heat as readily as silicon melt, which behaves as a liquid metal. It is feasible that in the near future state-of-the-art measurement techniques will obviate the need for model experiments because the required measurements will be performed *in situ* in silicon systems. On the other hand, *mathematical models* have been limited by the complexity of the equations describing the physics of CZ. The simplifications necessary to obtain closed-form expressions from the governing equations neglect important interactions, while precise models require huge numerical formulations for their solution.

High speed supercomputers have enabled researchers to solve the pertinent transport equations computationally. The computer enables numerical analysts to improve the gross approximations necessary to obtain closed-form expressions and also to build computational simulators that solve equations for which analytical results cannot be obtained whatsoever. Accurate modern numerical treatments for the resulting equations give results for parameter ranges which are much more realistic than analytical treatments or

experimental models, and numerical techniques are available to handle troublesome non-linear phenomena such as multiplicity of steady-state solutions and transitions to time dependence.

The approach *proposed* for this thesis is to build a computational model of CZ silicon growth, to compare it with data from a real CZ system for verification, and finally to devise optimal growth strategies with the model, using the actual system to test them. A steady-state Integrated Hydrodynamic Thermal-Capillary Model (IHTCM) was constructed to provide a comprehensive axisymmetric model of heat transfer, laminar melt convection and free boundaries with an efficient finite-element/Newton method for solving the model equations. Thermophysical properties were gleaned from available literature and the model was tested with measurements of the thermal field and interface shape from a commercial-scale CZ crystal puller[1]. The comparison with the temperature measurements was within the uncertainty of the measurement, but indicated that thermal stresses, used by our model to predict dislocation densities, could not be directly related to dislocation formation. Hence, further investigations into microscopic processes governing the formation of dislocations has been undertaken in a separate research project. The flow field in the melt could not be resolved for correct values of the thermophysical properties. These results and the premature termination of the experimental program dictated that an attempt at optimization using our model would be premature and ineffective, and that a more useful approach would be to further study the physical phenomena. The final work of this thesis was to extend the equations of fluid flow to encompass turbulent transport. Modelling turbulence introduced a greater level of complexity to the model but simplified the mean-flow structure as the correct thermophysical property values were approached. The measured melt/solid interface shape was accurately predicted by the $K-\epsilon$ /IHTCM, and the effects of crystal and crucible rotation on oxygen concentration in the crystal from different systems were qualitatively predicted as well. In light of this work, the $K-\epsilon$ /IHTCM accurately depicts the heat transfer and qualitatively predicts the transport of oxygen in a commercial-scale CZ puller. The $K-\epsilon$ /IHTCM can be used for optimization of process design and control when the dislocation density in grown crystals is successfully related to macroscopic quantities experienced during growth.

[1] A Siltec Corporation 254 *mm* hot-zone furnace.

1.1 Introduction

Since the advent of the transistor in 1947, the semiconductor industry has grown to enormous proportions. The 1991 worldwide sales volume was about 60 billion dollars and the industry is expected to grow by a further 10% through 1992 (Weber, 1992). The growth of the semiconductor industry has been due to processing innovations which have shrunk device dimensions by several orders-of-magnitude since 1960 (Keyes, 1981). Size reductions cut cost of production, reduce power consumption in the device and improve its speed. Smaller dimensions enable greater amounts of integration on a single chip, which further increases circuit speed, due to the shorter effective distances the electrons must travel. Although GaAs promises faster speed, lower power dissipation and higher resistance to radiation, silicon's more rugged mechanical properties and ability to grow a native oxide keep it the dominant substrate material. In fact, of all the integrated circuits (IC's) sold in the U.S. in 1990, 55% were metal oxide silicon (MOS) monolithic IC's and most of the remainder used silicon as the substrate material (1990 Electronic Market Data Book). The silicon substrate for most of these circuits is grown by the Czochralski (CZ) method, introduced originally for growing metal single crystals (Czochralski, 1917).

Although improvements to lithographic procedure drive the advances in circuit miniaturization, the maximum degree of integration depends critically on the quality of the substrate material. For a compositionally homogeneous and perfectly single-crystalline substrate the minimum size of a device is ultimately limited by induced electric fields, which cause breakdown of the p-n junction (Keyes, 1981). The first fundamental objective of silicon bulk growth research is to help approach this barrier of minimum device size by economically producing defect-free and compositionally uniform silicon single crystals. Composition in this context refers to the concentrations of both *dopants* which are intentionally added to the melt primarily for electrical properties, and *impurities* which unavoidably find their way into the crystal and also affect the crystal's properties. The second objective is to expedite further integration of devices by producing increasingly larger diameter substrates. The inherent complexity of the physical phenomena in CZ makes empirical study cumbersome and costly and also has hindered development of models that combine accuracy and tractability. Consequently, processing strategies formulated from simplified theory and limited empirical knowledge have met with considerable difficulty coping with demands for increasingly large-diameter and compositionally uniform single crystals.

This research has attempted to provide the foundation for an accurate and systematic

way of optimizing and redesigning CZ by developing a model and testing it with operating data from a real CZ apparatus. Outlined in Chapter 2, the Integrated Hydrodynamic Thermal-Capillary Model, or IHTCM, was devised to account for the relevant nonlinear physics in the CZ system to the maximum practical degree. The IHTCM comprises a comprehensive model of heat transfer and melt convection with an efficient finite-element/Newton method for solving the equations as a function of operating conditions and system design. It combines a detailed description of heat transfer by conduction and diffuse, gray radiation between all components within the typical CZ enclosure with calculation of axisymmetric, steady-state, laminar convection in the melt. The IHTCM is based on the concept of a thermal-capillary model for meniscus-defined crystal growth (Brown, 1988) which includes the computation of the meniscus shape, the shape of the melt/crystal interface and the radius of the crystal simultaneously with the temperature and flow fields. The finite-element/Newton methods have been developed especially for efficient solution of the this highly coupled equation set. By including this coupling and an accurate model of heat transfer, the IHTCM is designed to be capable of predicting the temperature field throughout a CZ system, the interface morphology and the fluid flow field. These outputs are in turn used to determine the thermoelastic stress in the crystal which is an indicator of the likelihood of dislocation formation (Jordan et al., 1986), and to determine the partitioning of dopants or impurities.

Chapter 3 details the experimental testing phase of the IHTCM. The experimental apparatus used for the comparison was a Siltec crystal puller at IBM's East Fishkill facility under the direction of K.M. Kim. The focus of the experiment was to provide as accurately as possible a measure of the thermal field throughout the entire growth chamber. This was accomplished by equipping the Siltec apparatus with thermowell entry ports and using a specially designed thermowell to obtain a temperature profile spanning the entire cavity of the growth chamber. Also the melt-solid interface shape during steady growth was obtained by post-growth determination using x-ray analysis. This provides a second, more local measure of the temperature field but it is limited to the vicinity of the melt-solid interface. Since the experimental system was not outfitted for thermowell insertion prior to the beginning of this work, the retrofitting of the Siltec CZ system for measurement at IBM and development of the detailed version of the IHTCM for comparison at MIT were performed as parallel activities, with periodic communication between the two groups. The results from the measurements were compared to an extension of the IHTCM to account for a passive thermowell tube in radiative equilibrium in the CZ chamber.

The good agreement between these measurements and predictions, irrespective of predicted flow strength, provides some of the strongest practical conclusions from this thesis. Given confidence in the computation of the thermal field, a realistic estimate of the thermal stresses was computed. The thermoelastic stress field in the growing silicon boule was undeniably greater than the estimated critical resolved shear stress which is a benchmark value characterizing the stress required to deform a material by glide and resulting multiplication of dislocations. The fact that *single* crystal material was grown strongly suggests that the *generation* of dislocations in large-scale silicon growth is the determining factor. Also, the IHTCM was unable to calculate a steady-state flow field with the flow mechanisms combined due to increasingly convoluted flow patterns which were difficult to differentiate numerically as the correct parameter values were approached; the actual flow is likely time-dependent and three-dimensional. This deficiency demonstrates the need to account for time-dependence in a model of CZ flows in large systems. The melt-solid interface shape, which is highly sensitive to the flow field, did not compare favorably with the calculations involving natural convection only, but was more accurately predicted when crucible rotation also was applied. These results indicate two important facts: that under CZ growth conditions, any dislocations in the silicon single crystal would propagate and multiply, and that the melt hydrodynamics for CZ growth cannot be adequately depicted by a steady-state laminar simulation. To pursue the kinetics of dislocation formation necessitates a consideration of microscopic phenomena, which could receive only shallow treatment in the context of this thesis, and thus has received devoted attention from a colleague (Maroudas, 1992). A modification to account for time-dependent transport in the melt was undertaken as the final extension of the IHTCM in this thesis.

Chapter 4 describes the approach taken to model the time-dependent fluid flow and heat transfer in the CZ apparatus. Instead of pursuing a direct time-integration approach, the IHTCM was augmented to accommodate turbulent fluid flow and heat transfer through the melt with a $K-\epsilon$ prescription for these quantities. The theory behind the turbulence approach is reviewed in Chapter 4 along with results from using different versions of the $K-\epsilon$ /IHTCM. The $K-\epsilon$ /IHTCM yields a reliable prediction of the mean transport rates at realistic growth conditions and accurately predicts the observed melt/solid interface shape. The transport of oxygen is also predicted with the $K-\epsilon$ /IHTCM and the effects of crystal and crucible rotation on oxygen transport agree qualitatively with those reported in the literature.

Although application of results on the Siltec apparatus was preempted, several conclu-

sions important to the model-based optimization necessary for improving silicon growth are drawn in Chapter 5. The accurate thermal predictions of the IHTCM, made possible by radiative heat-transfer modelling, strongly dismiss thermal stress minimization for the prevention of dislocations in large-diameter silicon boules. Rather, the solution to this problem lies in suppressing the nucleation of dislocations. Models of axisymmetric/steady melt flow produce a multiplicity of solutions close to the realistic viscosity, and therefore cannot predict the transport in large-diameter melts with rotation and undamped natural convection. The $K-\epsilon$ /IHTCM for turbulent transport uniquely predicts realistic conditions and accurately predicts the heat-transfer near the melt/solid interface. As well, the achievement of a robust $K-\epsilon$ -model formulation in the IHTCM has shown that augmented axisymmetric and steady-state finite-element/Newton models can account for the effects of turbulent heat transfer in large CZ systems. Also, in a purely illustrative context, growth parameters are varied to explore the potential of the $K-\epsilon$ /IHTCM for optimizing a large-scale CZ crystal-puller.

The remainder of this chapter provides background material to enable meaningful discussion of the field of crystal growth modelling. Section 1.2 describes the CZ growth procedure and then qualitatively describes the interacting physics of CZ growth. The description gives both a chronicle of important observations on melt growth and a conceptual picture of the physical mechanisms governing the process. Section 1.2 concludes by detailing major advances in the practice of silicon growth, as well as recent experiences which have motivated the great increase in modelling. Section 1.3 details previous modelling approaches which have appeared in the literature, including model experiments, analytical approaches and large-scale numerical models. It further illustrates the complexity of the physics in CZ and the difficulty in producing a credible model. This section provides the choices for a numerical modelling approach in this thesis and the asymptotic analyses presented serve as a check for the accuracy of the model. Section 1.4 addresses the importance of thermophysical properties for crystal growth modelling and Section 1.5 states the outlook of this thesis work, based on the information in Sections 1.2-1.4.

1.2 The Czochralski growth technique

1.2.1 Why Czochralski is used for growing silicon

Crystal growth involves the transition from an amorphous phase to a solid growing crystal. Single crystals are grown by a variety of techniques to take advantage of the desirable

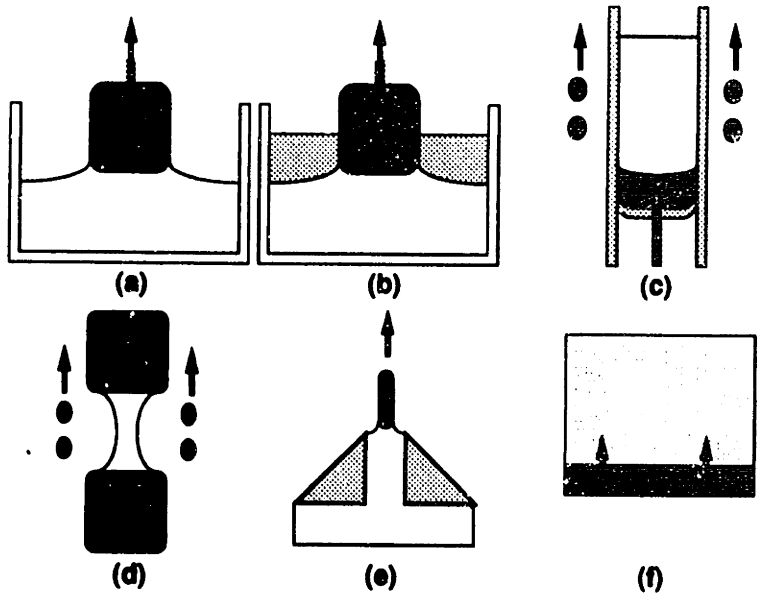

Figure 1-1: Semiconductor growth techniques: (a) Czochralski (b) liquid-encapsulated Czochralski (c) Bridgman (d) Zone-refining (e) Film-feeding (f) Epitaxial.

physical properties of the crystalline state, including mechanical, electrical, optical, thermal and magnetic properties. The choice of growth method may depend on a combination of economic and physical concerns, including: minimum required rate of production, tolerances on dislocations and impurities, the morphology of the (moving) solidification front, density change upon solidification, latent heat of fusion, heat transfer, stoichiometry, species transfer and in-situ thermal stresses on the crystal. Several of the principal methods for semiconductor growth are listed in Table 1.1 and the form of the solidification front for each case is depicted schematically in Figure 1-1; of those listed in the table, all but the last two would be considered bulk growth methods. The production of device-quality semiconductors places the most stringent demands on bulk growth methods because the crystal must possess perfect chemistry and structure and nearly perfect shape while it is grown.

The choice of CZ for growth of silicon substrates continues to be justified in spite of active development of alternative methods for growing single crystals. Firstly, bulk growth is much faster for producing single crystal material than epitaxial growth, typically on the order of $10\mu m\, s^{-1}$, compared to about $10^{-2}\mu m\, s^{-1}$. The absence of a constricting ampoule is an advantage over the Bridgman or gradient-type techniques, since silicon expands upon freezing. This expansion endangers both the ampoule and the crystal,

Table 1.1: Semiconductor Growth Techniques

Method	Types of Crystal Product
Czochralski (CZ)	bulk low vapor pressure melts which expand upon freezing, e.g. Si,Ge
liquid-encapsulated Czochralski (LEC)	bulk high vapor pressure melts which expand upon freezing, e.g. GaAs,InAs,InP
Bridgman, gradient freeze techniques	bulk growth of high vapor pressure melts and low yield-point crystals
float zone, zone refining	high purity material, e.g. Si,Ge
ribbon, dendritic growth, film-fed	polycrystalline Si for solar cells
vapor-phase epitaxial processes	thin epitaxial layers of GaAs, Si, SiO_2
liquid-phase epitaxy, (LPE)	thin epitaxial layers for optical devices

(Ghandhi, 1983)

due to the possibility of fracturing the ampoule or destroying the crystal structure of the grown material. In addition, the contact between the melt and the quartz crucible in the CZ growth of silicon yields an oxygen presence which, typically in concentrations up to approximately $25 ppma$, has the beneficial effects of increasing crystal hardness, and forming inert complexes with (gettering) heavy metal impurities. However, harmful effects such as swirl defects and oxidation-enhanced diffusion have also been attributed to oxygen incorporation (Ghandhi, 1983). Resistivity, the primary electrical characteristic, is a function of the dopant concentration in the crystal, but also the level of contaminants. The variation of resistivity across the chip surface is important since variations of $5-10\%$ (Ghandhi, 1983) are typically the maximum tolerable. CZ meets comparable specifications to other bulk growth methods, although problems with fluctuation due to flow instability are less prevalent with methods that maintain smaller molten zones, such as zone refining. Dislocation-free devices are desirable, because defects tend to accumulate impurities which cause undesired current paths, and resultant device failure. CZ consistently produces single-crystal silicon at diameters less than approximately $20\,cm$. CZ growth, synonymously *crystal pulling*, is thus the logical choice of method for growth of silicon substrate.

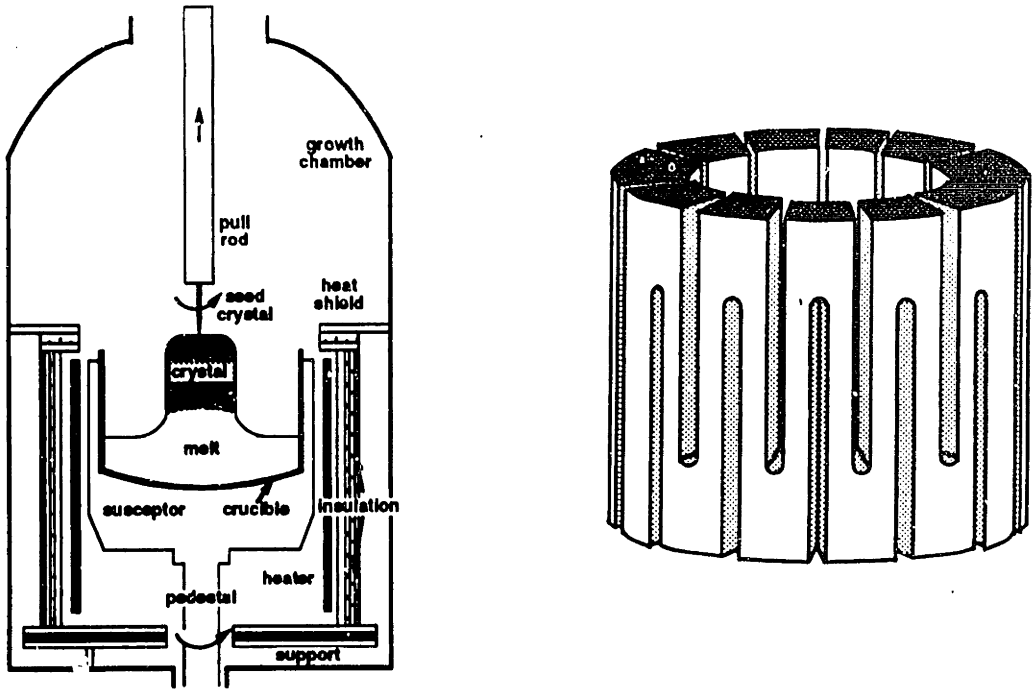

Figure 1-2: (a) The CZ apparatus. (b) Perspective view of the heater.

1.2.2 The CZ apparatus and growth procedure

The apparatus in this study is a very common design for growth of up to 15 cm diameter crystals. The Siltec crystal puller (see Figure 1-2), holds its molten silicon charge in a quartz crucible. This crucible is housed in a graphite susceptor and mounted on a graphite pedestal which is attached to a geared shaft, enabling the system to be rotated and raised or lowered. The heater is a graphite resistance heater with a picket-fence construction, as shown in Figure 1-2b. Surrounding the heater is a heat shield assembly, consisting of graphite plates and graphite felt, resting on a quartz support. The chamber walls are made of stainless steel, and a water-cooled jacket surrounds the chamber. The pull rod is a vertical shaft, with a small single-crystal seed attached to its chuck. The pull rod may also be rotated. The crystal is withdrawn by vertical motion of the pull rod. Measurement points for the process typically include a view port for manual control, thermocouples and pyrometers for temperature control, image sensing and load cell for crystal shape control. Manipulated variables for the process are the heater power, the pull rate and crucible lift rate. These are changed to achieve desired set point for crystal radius and temperature ,which may be measured at one or more points in the system. A low-pressure inert gas stream is used to continuously purge the system and remove contaminants evolving from the system, .

The apparatus must be scrupulously clean to start, to avoid contamination. The charge is polycrystalline silicon and usually a dopant, which is melted in the crucible. A single crystal seed of diameter less than $1\,cm$ is properly oriented for the desired growth plane in the pulling chuck and is lowered to the surface of the melt, where a stable solid-liquid interface is established. The seed also must be perfectly centered or the growing crystal will lose axisymmetry. Crystal pulling begins with a seeding procedure (Dash, 1959) whereby the crystal is pulled quickly down [2] at a rate of typically $60\,cm \cdot hr^{-1}$ to small radius so that dislocations, which are inevitably created by the seeding process, are frozen into the cold material and do not propagate. The dislocations move slower than the accelerated pull rate and thus become trapped away from the growth interface. The pull rate is next slowed, effecting a dramatic increase in the radius to almost a square profile in the shouldering phase. (At the largest diameters the substantial weight of the crystal may be supported by mechanical calipers to relieve the stress on the crystal neck.) CZ growth is a batch process. The crystal grows and melt is depleted throughout the growth run. As a result, the process is inherently transient, with a characteristic time scale of greater than five hours. The depleting melt level and growing crystal mean that the thermal environment, and consequently the transport of momentum and mass, is in a continual state of change. During the growth period, the heater power is gradually varied and the crucible is lifted to maintain constant heating of the melt, since the melt level drops while the crystal grows. This is achieved by maintaining set point temperatures at convenient locations in the apparatus, for example, on the relatively cool surface of the insulation. The pull rate is varied to maintain the crystal set point radius. The crystal and crucible are rotated to influence the fluid flow in the melt to enhance uniformity of temperature and dopant concentration. Growth proceeds as the melt level drops until the crucible is nearly empty, when the crystal is grown inward [3] again to minimize thermal shock upon withdrawal. Total batch time for a $30\,cm$-long crystal is greater than five hours. A crystal boule is shown in Figure 1-3, alongside its calculated shape, as predicted by a scalar model. Typically the operating procedures for growing quality crystals have been arrived at through intuition and experience and the variants on this basic method used industrially are thus often a closely-guarded secret. Because the practice of experimental trial-and-error is expensive (the raw material cost alone is approximately $\$1000\,kg^{-1}$) and time-consuming (a typical growth run may consume several days), there is considerable incentive for physical simulation and mathematical

[2] "necking"
[3] "coning"

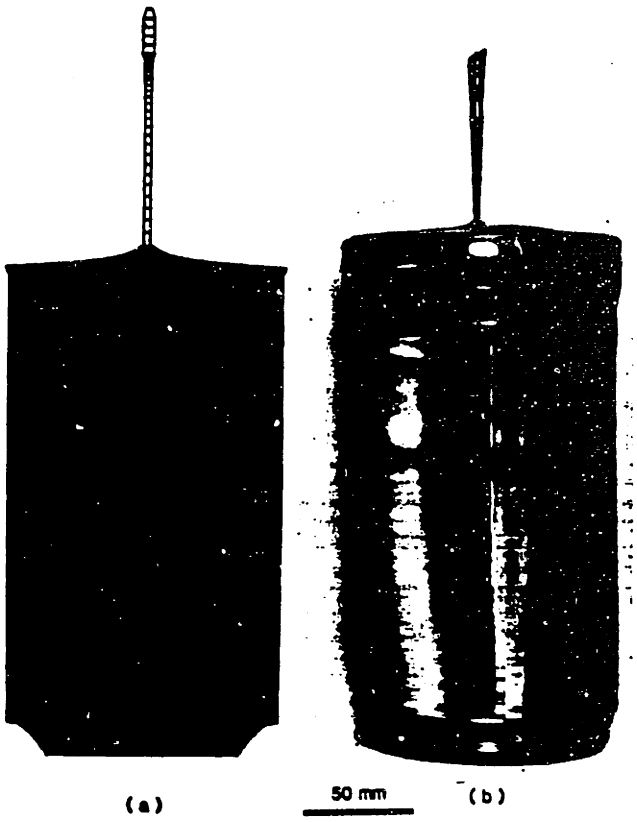

Figure 1-3: (a) Scalar prediction of crystal shape and (b) the actual silicon boule. After Kim et al., 1983.

modelling.

1.2.3 Observations on the interacting physics of CZ

In this Section an attempt is made to explain the physics of CZ growth. The task is difficult since the individual transport processes are related and any two may be interdependent. The purpose of this discussion is to explain how the phenomena arise, and to chronicle physical observations of them. The notions presented in this section will be used repeatedly throughout the Thesis, and are intended to provide the essential background for making conclusions from the results of this project. The description in this section is presented in physical terms, mathematical description is deferred to a later section. That section, Section 1.3, is intended to provide the background for justification of the modelling approach taken in this work.

The order of the subsections here is somewhat arbitrary; a discussion of free boundary effects is presented first primarily to emphasize the balance of processes necessary for crystal growth in a CZ puller. A discussion of heat transfer follows, since heat transfer is the prevalent consideration in any melt growth configuration. Next fluid flow is described, since it is very strongly dependent on the thermal field. Similarly, a discussion of dopant transport follows the discussion of flow, since dopant transport is highly dependent on flow. Finally, a discussion of dislocation phenomena in silicon is presented, drawing on material from all of the four previous subsections. Describing the interdependences between the individual physical phenomena is an important goal of this section. Given these five phenomenological classifications (i.e. free boundaries, heat transfer, fluid flow, dopant transport and dislocation phenomena) there are twenty possible dependences between them. Figure 1-4 depicts the individual phenomena with blocks and qualitatively denotes the importance of dependences by the thickness of the arrows joining them. In discussing one physical process, its physical basis and range of observed states will be detailed first and its function as an independent process (the tail of an arrow in Figure 1-4) will be mentioned second. Of the five aspects mentioned above, only dislocation transport is considered to be a purely dependent process. Due to the similarity in physical properties between silicon and certain other materials, experiments with molten metals or other semiconductors will often be used to infer behavior about silicon. Especially where flow is concerned, fluids with the same Prandtl number are expected to perform similarly.

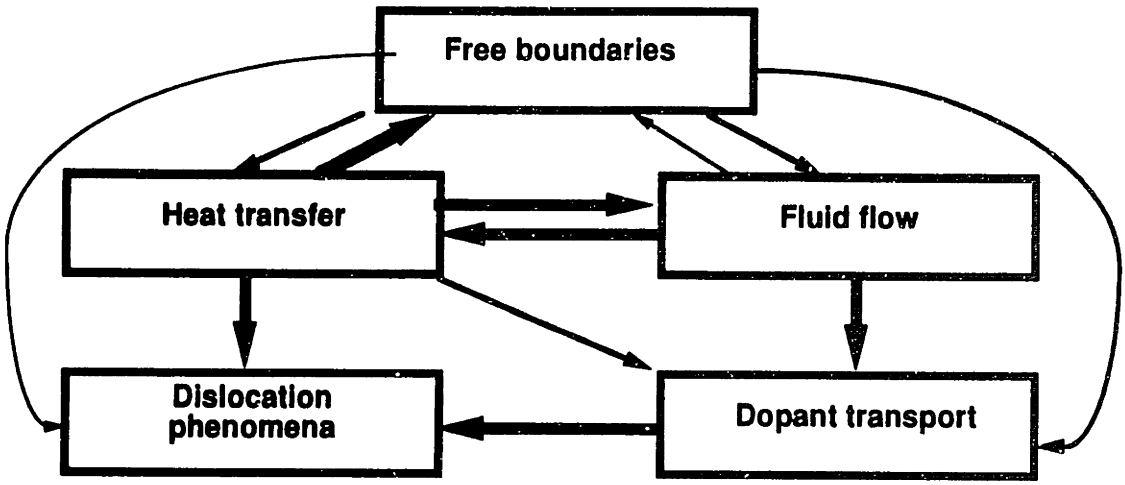

Figure 1-4: Interactions between individual physical phenomena in CZ. The arrow thickness denotes the relative importance of the interaction.

Free boundaries

The CZ system comprises a beautiful combination of interacting physics and its successful operation hinges upon a delicate balance between heat transfer, fluid flow and free boundary dynamics on the scale of the system dimensions, as opposed to microscopic processes which cannot be directly measured. There are three moving boundaries in the system, the crystal radius, the melt-solid interface and the melt-gas meniscus. These boundaries move in the sense that they are fixed by the processing conditions, rather than a physical boundary such as the crucible wall.

In stable growth the crystal radius achieves equilibrium with the thermal environment, since the heat liberated at the growth interface must be accommodated by thermal flux into the crystal. This coupling can be illustrated by considering the melt-solid interface as a simplified heat transfer system; see Figure 1-5a. The heat conducted *into* the crystal $-Q_s$ is equal to the heat conducted from the melt Q_m and the heat source due to the latent heat of fusion: $-Q_s + Q_m + \Delta H\dot{m} = 0$. A simple relation for the crystal radius is obtained by assuming that Q_s is due to to heat transferred from the crystal radial surface and that the transfer rate is constant over the surface. This gives the relation $Q_s = \pi R_s L_s h_s$, where h_s is a heat transfer coefficient. Similarly heat conducted from the melt is considered to be constant over the area of the melt-solid interface, yielding

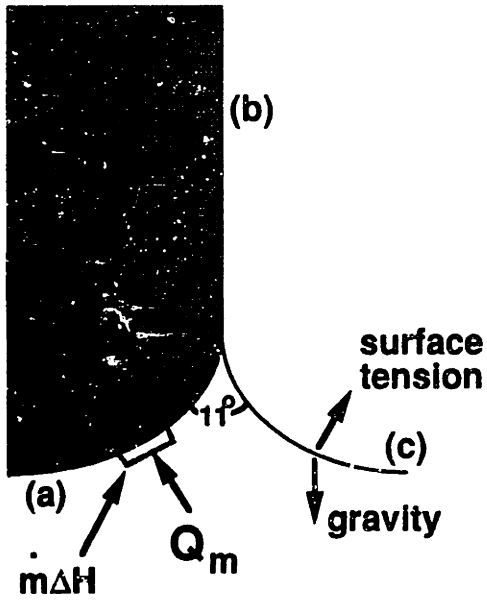

Figure 1-5: Free boundaries in CZ: (a) melt/solid interface, (b) crystal radius, and (c) melt/gas meniscus.

$Q_m = \pi R_s^2 h_m$. Since the mass growth rate can be also expressed in terms of radius: $\dot{m} = V_p \pi R_s^2 \rho$, the crystal radius is given by:

$$R = \frac{L_s q_s}{\Delta H V_p \rho + q_m} \tag{1.1}$$

Under these assumptions the crystal radius decreases with pull rate and heat transfer coefficient h_m from the melt, but increases with heat transfer coefficient h_s from the crystal to the surroundings. Although this analysis is oversimplified the inverse relation between radius and pull rate has been long recognized (Billig, 1956) and persists as a basis for feed-forward control schemes in CZ today (Kim et al., 1983). During CZ growth the heat transfer from the crystal and melt change steadily due to the batch nature of CZ, and the heat transfer from the melt may change suddenly due to transient convection in the melt. The pull rate is used as the primary control variable to keep the radius constant.

During the stable growth which occurs at the low growth rates of CZ the melt-solid interface traces out the locus of the melting point. Under typical bulk-growth conditions the melting point does not vary due to surface curvature or alloy formation. By far the determining factor is the thermal environment of the crystal puller and particularly

the flux of heat due to convection in the melt. This was clearly demonstrated for a similar experimental system (Carruthers and Winegard, 1967) by the dramatic influence of heating configurations on the melt-solid interface in solidification of lead alloys.

Observation of the melt-solid interface is not possible *in situ* by conventional means, but can be obtained by post-growth analysis of the crystal. This analysis entails longitudinally slicing the boule, and chemically etching the longitudinal face which axially differentiates regions of varying chemical composition, evident as vertical striations. Visual inspection or x-ray topography of this surface can then be used to trace out the interface shape; see Figure 1-6. Applying an electrical pulse through the crystal also has been used to locate the interface by instantaneously disturbing the solute incorporation rate, thereby producing a sharp line in the etched crystal (Lichtensteiger et al., 1978).

Interface deflection has been correlated with dislocation density (Billig, 1956), motivating crystal growers to desire flat interfaces. However, higher melt-solid interface deflections and dislocation densities are both products of a highly curved thermal field which results in higher stress due to differential thermal expansion in the crystal. It is this stress that enhances the propagation of dislocations. The melt-solid interface fluctuates (solidifies and remelts) very rapidly in time due if the thermal environment is unsteady; see Figure1-6b. This remelting has been linked to increased quantities of swirls (deKock et al.,1974) which have been related to dislocation formation by self-multiplication of larger A-microdefects (deKock et al.,1975).

CZ growth works only for materials that wet their own crystal, so that when the crystal is pulled from the melt, the melt clings to the crystal, forming a meniscus. The steady meniscus shape results from a balance of forces including gravity, surface tension and normal stresses due to the flowing medium. The attachment point between the melt and solid is characterized by a growth angle which for silicon has been experimentally verified as a constant 11 $\pm 1°$ (Surek and Chalmers, 1975) from the tangent to the crystal radial surface; see Figure 1-5c. This may seem incomplete, considering that this growth angle results from a balance of the three surface energies at the trijunction (melt-solid, solid-gas and melt-gas) and therefore also should require consideration of the angle relative to the melt-solid interface. It is conjectured that the melt extends for a small distance up the vertical crystal surface, which would explain the observation. At any rate, the form assumed by all three free boundaries dictates the shape of the domains for transport of heat and material. Therefore, all of the transport processes are inherently dependent upon the free boundaries.

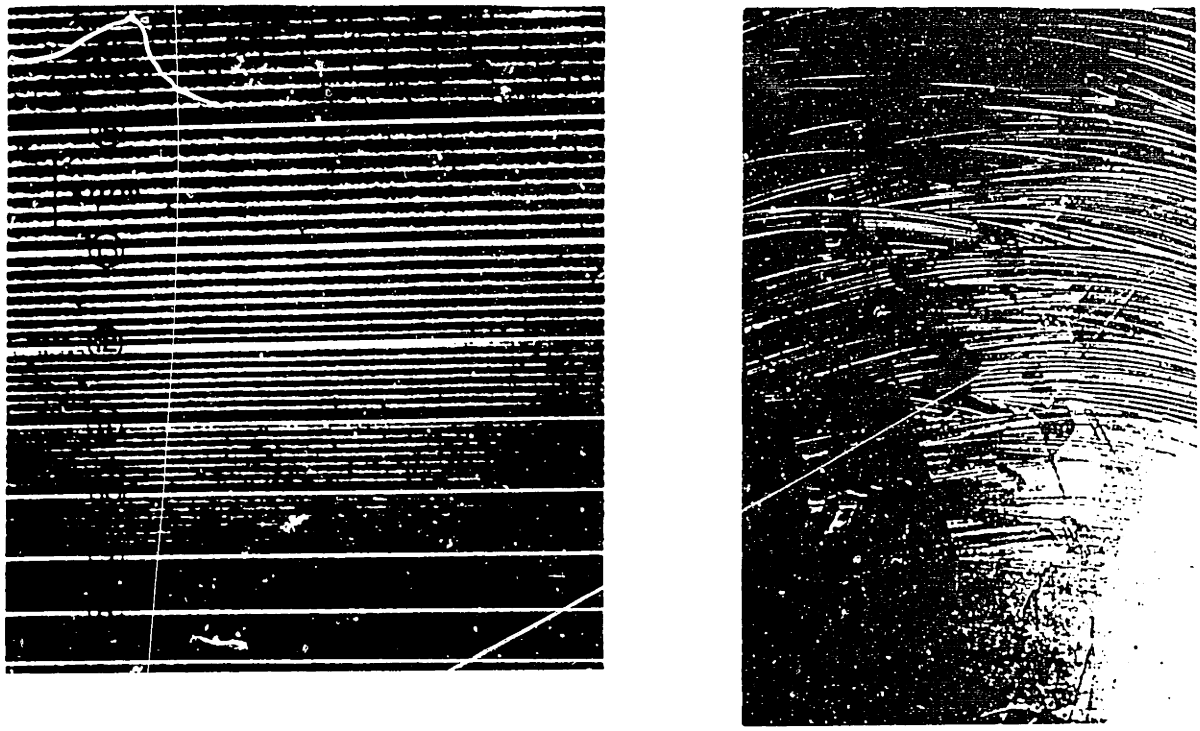

Figure 1-6: X-ray topography measurement of melt-solid interface by striations for (a) steady interface shape and (b) unsteady interface shape. After Kim et al., 1978.

Heat transfer

Heat transfer is a major concern for any process involving molten metals or semiconductors, even without the demands of achieving semiconductor-grade material. There are two sources of heat in the system, the heater and the latent heat release at the melt solid interface. All heat is eventually transferred to the cooling jacket surrounding the chamber walls.

In the present study heat is supplied by a graphite resistance heater, as is typical for silicon growth. Heat is transferred almost entirely by radiation between exposed surfaces of the system components, which frustrates conventional engineering because radiation is a nonlinear phenomenon. The gas pressure in silicon growth systems is typically low, with the result that a negligible amount of heat is transferred to the gas phase. The experimental apparatus at IBM for example, operates at $10\,Torr$ with a flow-rate of $4.7 \times 10^{-3}\,m^3 s^{-1}$. Radiative transmission *through* system components, or internal radiative transfer, occurs to a small extent. In intrinsic, i.e. undoped, silicon under about $1000°C$, the material is effectively transparent to infrared radiation (Wolfe and Zissis, 1978), but this temperature range is experienced only near the top of the growing crystal. Although quartz is visibly more transparent than silicon, the fused silica crucibles transmit much less radiation at high temperatures (Wolfe and Zissis, 1978), and less than optically trans-

parent quartz (Strudwick and Kim, 1988). Therefore internal radiative transmission is not expected to be significant in the crucible either. Tracing the flow of radiative energy between the system components is complicated, and spectral and angular material properties will be overlooked here. However, it is worthwhile to consider that all of the surfaces reflect incident energy to some degree, and some of the surfaces in the CZ apparatus such as the chamber top, melt surface and crystal are specular, reflecting radiation according to Snell's law, while others are diffuse. Many commercial growers employ radiation shields at critical locations in their pullers to control the radiative heat flow. Uniformity of the radiation also is essential to crystal growth; since the CZ apparatus possesses many asymmetries, the crucible is rotated to maintain even azimuthal heating of the melt, and the crystal is rotated to ensure even azimuthal heat flux into the crystal. In the absence of rotation, a CZ-grown crystal will deviate from the center of the crucible and travel towards cold spots in the chamber.

Within the solid components heat is transferred by conduction, usually the simplest mode of heat transfer to analyze. The variety of different materials in the growth chamber and the peculiar geometry complicates heat conduction. The thermal diffusivity of the materials is difficult to anticipate, since it may strongly vary depending on the processing conditions in the case of the silicon crystal, or on the method of preparation, in the case of graphite components. The thermal diffusivity of the chamber materials varies gradually with use, since the structure of certain components such as graphite felt changes due to contamination with use. The silicon crystal is a striking example of dependence on processing conditions, since, as a semiconductor, its thermal conductivity changes drastically with temperature and doping, depending on whether there are sufficient free electrons for the material to behave as an electrical insulator or conductor.

Transport by thermal convection is a dominant effect in the melt, as opposed to the tiny extent of convection in the solid crystal. In spite of having a Prandtl number of about 10^{-2}, the very high driving forces for convection result in much more heat transport than conduction alone. Observations of thermal convection in crystal growth are inferred from the melt-solid interface shape of the grown crystal, or by insertion of thermocouples directly into the melt. Experiments in simpler crystal growth systems (Carruthers and Winegard, 1967) have demonstrated the effects of thermal convection. By quenching the system and relying on preferential etching along the melt-solid interface, the effect of thermal conditions on the melt-solid interface shape, even for very small rectangular systems of width $\sim 1\,cm$, was verified. Fluctuating temperature measurements with molten tin indicated time dependence under the conditions of crystal

growth (Cole and Winegard, 1962). These fluctuations can be reflected in an oscillating melt-solid interface shape. The investigation of the growth of gallium-doped germanium by Kim et al., 1978 revealed that thermal convection was oscillatory depending on the melt aspect ratio. The melt-solid interface passed through chaotic, oscillatory and finally steady-state regimes as the melt was depleted in a vertical Bridgman system.

Fluid flow

Buoyant and surface tension-driven flows arise from thermal gradients in the melt, due to the thermal expansion and thermocapillary effects. Since heating is applied primarily to the crucible wall, the basic buoyancy-driven flow is comparable to an analogous simplified system where fluid is confined in a cylinder with heated wall and cooled top. Fluid is expected to rise at the heated wall, and fall toward the center of the container (see Figure 1-7a). Evidence for the effect of buoyancy on flow was provided by the previously discussed effects on melt-solid interface shape (Carruthers and Winegard, 1967). Thermocapillary convection arises from the surface tension increasing at lower temperatures, so the basic thermocapillary driving force is expected to be along the melt surface from the crucible towards the crystal. It drives fluid along the melt surface toward the crystal and the fluid subsequently recirculates through the bulk of the melt back to the surface. Experiments under low-gravity conditions minimized the effect of buoyancy (Lamprecht et al., 1983) and showed that the undamped effect of the thermocapillary driving force can be as profound as buoyancy; a low Pr number fluid in a heated container was found to exhibit intense flows under microgravity conditions. The buoyant effect of solute gradients are important for alloy growth and may be neglected for silicon, since the dopants are present only in very dilute amounts.

The presence of natural convective flows is evidenced indirectly by temperature fluctuations, interface shape transitions and solute deposition behavior, but direct observation of the flows is not yet standard practice, due to the high temperatures, need for isolation and opaqueness of the melt. Direct observation of suspended particles in CZ silicon flows has recently been accomplished on a $75\,mm$ CZ puller at NEC (Kakimoto et al., 1988). Their flow visualization was performed using x-ray radiography with a tracer particle. They found that natural convective flows could be of either an axisymmetric or non-axisymmetric pattern, depending on the symmetry of the thermal field. Unavoidable asymmetries occur, due to a number of factors including viewports or nonideal current paths in the heater, the effect of cooling on the heater mounts, etc. By minimizing the thermal asymmetry, they achieved what appear to be axisymmetric natural convective

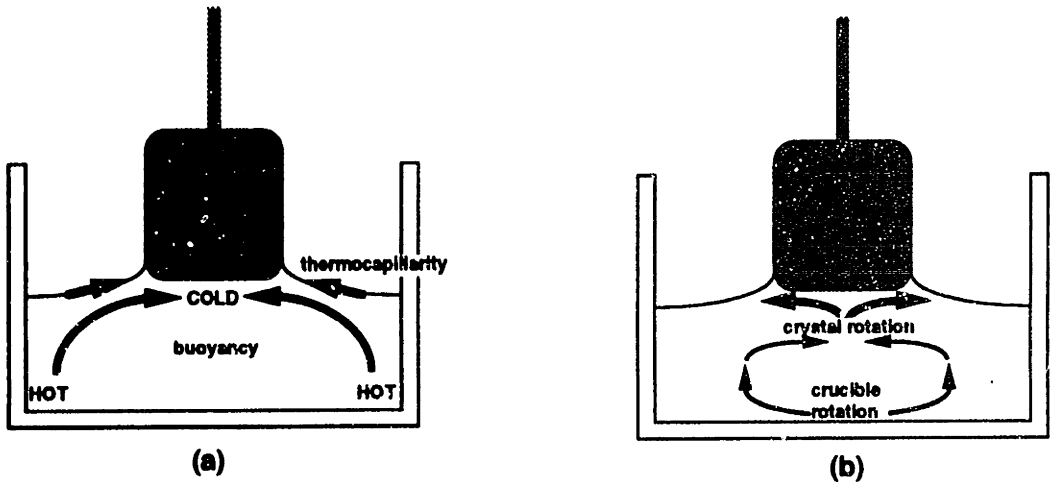

Figure 1-7: Schematic depiction of (a) natural convection and (b) forced convection driving forces.

flow. The complexity of the observed flows in such a small system

The rotations of the crystal seed and crucible are used primarily to force flows which establish uniformity. Crystal rotation enhances uniformity of the near-field flow near the solidification front. It primarily imparts angular momentum to the fluid in the immediate vicinity of the melt-solid interface. In addition, this rotation induces a strong centrifugal acceleration which tends to force fluid away from the crystal radially; see Figure 1-7b. These actions favor a stable flow, performing the critical functions of establishing a controlled thermal and solutal boundary-layer in front of the crystal, and calming natural convective forces near the melt-solid interface. Indirect evidence of the action of crystal rotation flows by the deposition rate of solutes was first shown by Burton et al., 1953a in a system small enough that thermal effects were negligible. The rate of rotation was found to have a strong influence on the deposition rate of solutes, which was assumed to occur due to the influence of rotation rate on the diffusion boundary-layer thickness. Meridional flow induced by crystal rotation alone is expected to be drawn vertically upward from the crucible bottom to replace the displaced fluid along the crystal surface, as shown in Figure 1-7b.

Crucible rotation ensures uniformity of the heating of the melt, which is essential for smoothing out thermal asymmetries endemic in the heating (Kakimoto et al., 1989). It

gives a strong solid body rotation to most of the melt, but also produces a meridional force unless there is a stress-free boundary on the melt surface, which would occur in the absence of a crystal or with the crystal rotating at the same rate as the crucible. This force acts radially outward along the crucible bottom and radially inward along the melt-crystal surface due to centrifugal action. Observation of the flow associated with crucible rotation can be inferred by the effect of crucible rotation on increasing oxygen deposition rate (Hirata and Hoshikawa, 1980). Flow visualization of the isolated forced convection flows in CZ silicon growth is both difficult and of dubious utility, since natural convective flows are always present in systems of industrial proportions.

While convection has the potentially beneficial effect of enhancing transport through the melt phase, the driving forces for convection are large enough in industrial systems that the flow becomes unsteady, and the combination of forced and natural convection only exacerbates the instability. These unstable flows destabilize the heat and dopant flux in the melt through movement with the bulk flow. Visualization studies (Kakimoto et al., 1989) suggest that rotating the crucible destroys axisymmetry of the natural convective flow and that the purely natural convective flow and combined flow are unsteady. Ideally, crystal rotation should be sufficiently high in order to protect the solidifying crystal from the effects of this unsteady or nonaxisymmetric flow. In addition to inherent time dependence of the unsteady melt flow with frequencies on the order of seconds (Cole and Winegard, 1962), melt convection is affected greatly by the depletion of the melt, which represents a gradual change in the aspect ratio of the melt with a time scale on the order of hours. Thus, the behavior of flow at one stage in the growth cannot be generalized to the entire process. Evidence of the batch time scale effects on the flow were first inferred by changes in the doping striations and melt-solid interface shape over the length of the experiment in directional solidification of *InSb* (Kim et al., 1972) and later *Ga*-doped *Ge* (Kim et al., 1978). As the melt became shallow, fluctuations in doping and interface shape diminished dramatically, from chaotic patterns to steady oscillations and finally uniform behavior.

A vivid demonstration of the batch dynamics and rotation rates on flow was the visualization experiment at NEC (Kakimoto et al., 1990a) which demonstrated, with 3.5 *cm* crystal and 75 *mm* diameter melt, that deep melts produced nonaxisymmetric time-dependent flow, irrespective of crystal or crucible rotation rate, while for shallower melts the symmetry is highly dependent on rotation rate; these transitions are portrayed in Figure 1-8. The nonrotating flow was axisymmetric and steady, as was the flow when crystal rotation alone up to 10 *rpm* was applied. The flow was axisymmetric but time-

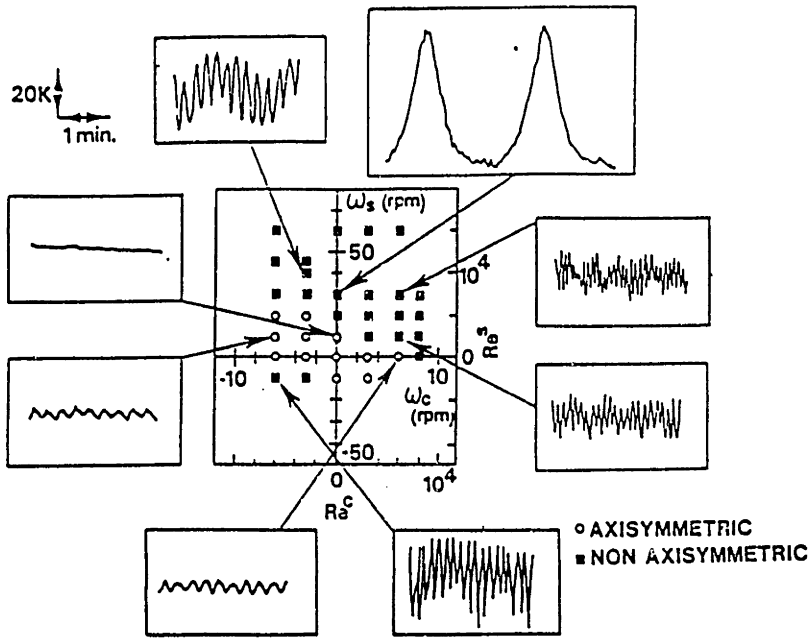

Figure 1-8: Map of flow regimes for silicon melt flow in a 75 mm crucible from Kakimoto et al., 1990c.

dependent for flow with crucible rotation only up to 6 rpm. At higher crystal and crucible rotation rates the flow was nonaxisymmetric and time-dependent. The axisymmetric particle trajectories differed somewhat between natural convection alone and in combination with crucible rotation, showing more circulation underneath the crystal when crucible rotation was applied. The effect of crystal rotation above 10 rpm was to destroy the axisymmetry and steadiness; the critical value was higher when the crucible was counterrotated rather than corotated. Although the relationship between rotation and stability was convincingly established, the authors provided little insight into the mechanism of the instability, other than connecting it to the magnitude of the rotation rate, and in particular to the choice of relative direction of rotation. Either crystal rotation or crucible rotation combined with natural convection can destroy the steadiness and symmetry of the flow; additionally, a marginally nonaxisymmetric flow due to crystal rotation can be made stable under certain conditions by counterrotating the crucible.

Flows in CZ can be damped with the application of a magnetic field since silicon melt is electrically conducting. Dopant striations disappeared from the center of the boule and temperature fluctuations ceased (Kim and Smetana, 1985; Kim and Smetana, 1986) showing that flows are considerably arrested in axial magnetic field growth (AMCZ). However, the radial segregation of solute was degraded and for this reason magnetic fields

are not universally used to control unsteady flows. Horizontal magnetic fields have been preferred by some researchers, in spite of their asymmetric effect (Lin and Benson, 1987).

Dopant transport

The transport of solutes, including dopants and contaminants, is a critical aspect of CZ crystal growth, but can be considered a dependent phenomenon in that mass transfer does not affect the other transport processes, except for the appearance of dislocations, for which the dependence is still not completely clear. These solutes enter the melt in several ways. Dopants are normally added into the charge in concentrations of $10^{16} - 10^{19}\, cm^{-3}$ to achieve the desired electrical effect in the crystal. Contaminants that are not added to the charge find their way into the melt from various sources: dissolution of the quartz crucible is the source of oxygen in CZ-grown silicon, and erosion of the system components is the primary source of carbon. Solutes leave the melt either via incorporation into the growing crystal or through evaporation from the melt surface, in the case of oxygen.

The incorporation of atoms into the growing crystal can be considered to occur at equilibrium, since the growth rate is only on the order of $10\,\mu m \cdot s^{-1}$ while the kinetics of solidification usually occurs on a much faster time scale. Since impurities are strictly in the dilute limit their incorporation can be characterized by a Henry's Law relation for the equilibrium segregation coefficient constant $K_{eq} \equiv c_s/c_m$, the ratio of equilibrium solute concentration of impurity in the solid to that in the melt directly adjacent (see Figure 1-9 and Table 1.2 which correlates K_{eq} with atomic dimensions). The fact that many important dopants have coefficients much different than unity is a problem, since the melt may tend to become either enriched or depleted with respect to the solute during growth. The ideal situation is to maintain conditions such that the effective segregation coefficient, $K_{eff} = \frac{c_s}{\overline{c_m}}$, based on the average melt concentration $\overline{c_m}$, is close to one. This means that the solute concentration stays constant in the melt and that the crystal thus a perfectly homogeneous dopant distribution. Since solute transport through the melt is intimately connected with details of the melt flow, adjustment of parameters to enhance or impede convection during growth can be used as a control parameter (Burton et al., 1953b). The quartz crucible on the other hand is dissolving during CZ growth, as there is a driving force to saturate the melt with oxygen. The SiO_2 of the crucible dissolves into the molten silicon, dissociating into liquid Si and monomeric oxygen 0 and possibly other Si_xO_y complexes (Yen and Tiller, 1991). The saturation level of oxygen in silicon melt has been accurately measured (Hirata and Hoshikawa, 1980). The solubility of oxygen at the melting point of silicon is $2.8 \times 10^{18}\, cm^{-3}$ or $57 ppma$, which

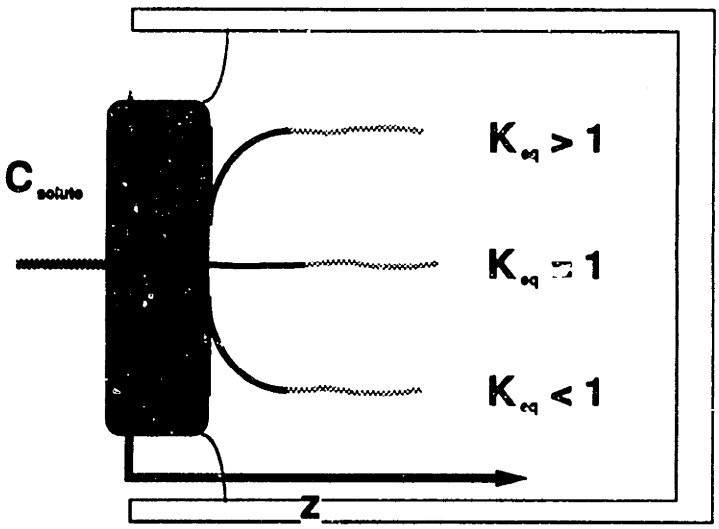

Figure 1-9: Schematic depiction of solute segregation at the melt-solid interface.

means that there must be an oxygen sink in order to achieve the $\sim 20 ppma$ observed in practice (Kim and Langlois, 1990). The loss of oxygen at the melt-gas surface due to evaporation of highly volatile SiO ensures that the saturation level of oxygen in the melt never reaches equilibrium with the solidifying silicon.

The transport of solutes through the melt phase is highly dependent on the flow in the melt, due to both the strength of the flows in CZ and the small diffusivity of solutes in liquid metals. The dependence on forced flow was first illustrated (Burton et al., 1953a) through the dependence of solute deposition on crystal rotation rate. Oscillations in the flow have a more acute effect on the rate of solute flux into the crystal than the rate of heat flux. A crystal grown with a steady melt-solid interface shape may exhibit short time-scale fluctuations in the impurity composition over time, due to unsteady convection. These fluctuations, known as dopant *striations*, have been used extensively to gauge the steadiness of flow; see Kim and Smetana, 1985, for example. In addition, rejection of dopants at the melt-solid interface enriches the melt so that more solute is incorporated toward the end of a growth run. The most striking demonstration of the interaction between the flow and solute fields is the x-ray visualization experiment (Kakimoto et al., 1990b) which shows the solute boundary-layer due to the solute's higher absorption of x-rays. The solute boundary layer in front of the melt-solid interface was not radially constant, nor was it even axisymmetric. The boundary-layer thickness, δ,

Table 1.2: Equilibrium segregation coefficients in silicon

Dopant	Coefficient K_{eq}	Tetrahedral Covalent Radius Å
Fe	8×10^{-6}	.
Au	2.25×10^{-5}	1.50
In	3.6×10^{-4}	1.44
Cu	4×10^{-4}	1.35
Al	1.8×10^{-3}	1.26
Ga	7.2×10^{-3}	1.26
Sb	0.02	1.36
C	0.07	.
As	0.27	1.18
P	0.32	1.10
B	0.72	0.88
O	1.6	.

was approximately $0.5\,mm$, which was significantly less than the asymptotic prediction of $2\,mm$ which considers only crystal rotation. The lack of a symmetric boundary-layer in fact accounts for the so-called *rotational striation*, which corresponds with the period of crystal rotation.

The behavior of solutes in the crystal receives scant treatment in this work, but is also important to the success of CZ silicon growth. Although processes in the solid phase occur much more slowly than in the melt, the silicon and impurities diffuse and react appreciably in the solid phase, and these behaviors are intimately coupled to the structural, mechanical and electrical properties of the as-grown substrate. The most controversial contaminant is oxygen, and its exact function is the subject of ongoing debate. Oxygen is incorporated into the growing crystal as an interstitial impurity, i.e. it resides *between* lattice points. These interstitials condense as the crystal cools, possibly forming stacking faults and microscopic dislocation loops, known as A swirl microdefects (deKock et al.,1974). At lower temperatures the nucleation of oxide precipitates (heavy metal oxide complexes) occurs on these defects, followed by growth of these precipitates. The remaining interstitial oxygen forms a donor complex in the silicon substrate. The effect of *in situ* annealing is critical on the formation of these structures, and thus, accurate determination of the cooling rate in the crystal is important from a kinetic standpoint as well, since the amount of time the crystal spends at a certain temperature will determine the degree to which chemical phenomena are allowed to proceed. Besides, the thermal stress field in the crystal may play a significant role in causing microdefects to spawn macroscopic dislocation loops, and further causing these dislocations to propagate

through the crystal.

Dislocation phenomena

The genesis of dislocation defects is the subject of ongoing research. On one hand it may be considered that the issue is one of preventing the small number of existing dislocations from becoming mobile by maintaining stress levels below the critical resolved shear stress (CRSS). An alternative line of thinking is that the crystal can be grown completely dislocation-free, and that conditions can be maintained to avoid generating even a single dislocation, thereby precluding concern for exceeding the CRSS in the crystal.

The most common method for determining the dislocation density is the etch-pit density (EPD) measurement, which entails etching of the crystal surface by an oxidant, followed by dissolution of the oxide. Preferential etching of the dislocated region occurs, revealing pits which can be detected by optical microscope. This method can only reveal the number of dislocations reaching the surface, and not the chemical constituents, crystallography or nature of the defects below the surface. Various x-ray techniques, transmission electron microscopy and scanning electron microscopy techniques have been used to study the crystallography, impurities and electrical characteristics of dislocations and microdefects which are not readily analyzed by conventional EPD. Microdefects are *noncrystallographic* defects, bearing no orientational relationship to each other or to the crystal and they show up as empty etch pits, smaller than dislocation etch pits and with no geometrical structure as shown in Figure 1-10. Two types of these have been observed in swirl patterns in *Si* crystals grown by the float zone technique. "A" microdefects are larger detectable clusters detectable by transmission electron microscopy (TEM) and formed by nucleation of excess self-interstitials on oxygen-precipitate clusters. These complexes occur at lower temperatures, while "B" microdefects are smaller clusters forming at higher temperatures, and are only TEM-detectable when decorated with copper. They form dislocation loops of size up to $\sim 40\mu m$, under very slow growth rates which permit their maximum size. These defects are thought to be correlated with complexes of impurity atoms, primarily the concentrations of oxygen and carbon, and the cooling rate of the crystal (Chikawa, 1987). Other microdefects in *Si* include "D" defects which are vacancy clusters and form at higher growth rates (Chikawa, 1987) and "I" defects which are microprecipitates of oxygen (Abe et al., 1983). Dislocations may be generated when A-defects grow beyond critical dimensions and self-multiply due to thermal stresses (deKock et al.,1975).

The primary source of dislocations in small-diameter CZ-grown silicon is thermal

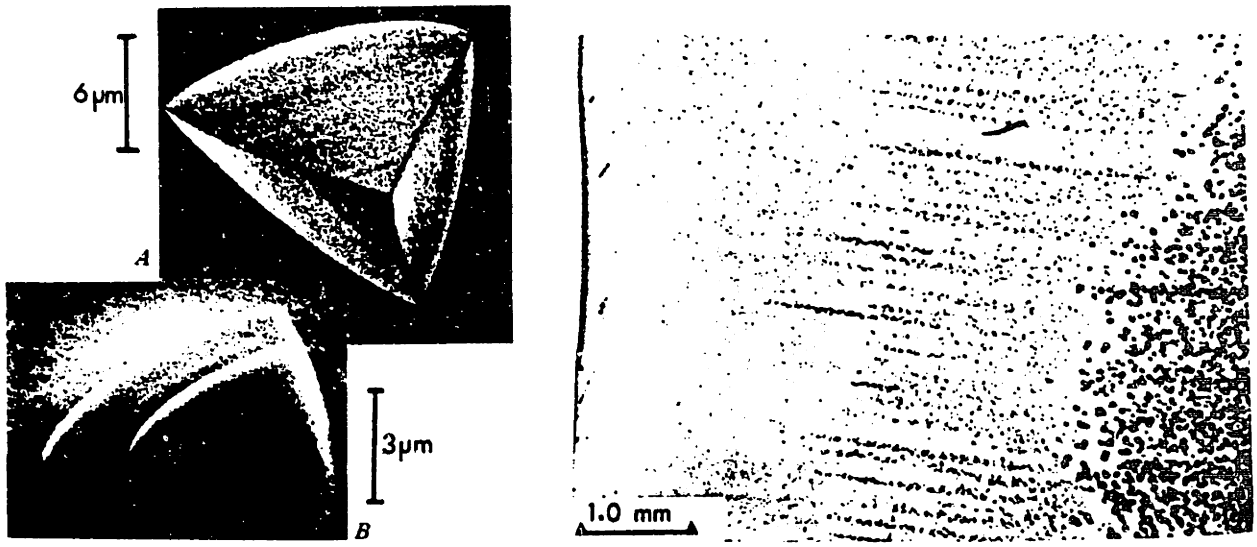

Figure 1-10: Defects and microdefects in silicon: (a) dislocation etch pit (b) microdefect (c) A and B-type swirls. From Ravi, 1981.

shock induced by dipping the necessarily cold seed crystal into the molten silicon. This was demonstrated by the achievement of dislocation-free crystals (Dash, 1959) by carefully adjusting the growth parameters immediately after seeding, to inhibit the propagation and multiplication of these dislocations. The propagation of dislocations once they are in the crystal has been correlated with thermal stress in the crystal, beginning with the observations of Billig, who noticed that dislocation densities were especially high in crystals with high interface curvatures, which correspond to highly curved temperature fields, and thus high thermal stresses. Conclusions regarding the relative importance of these three phenomena, microdefect generation, transition to macrodefects and macrodefect propagation will be drawn in Chapter 3 of this thesis.

Due to the expansion and contraction caused by temperature variation the solid crystal undergoes considerable stress upon emerging from the melt. The cooler crystal at the surface tends to contract less than the center, resulting in a hoop stress whereby there is tensile stress in the core and compressive stress near the periphery of the crystal. The stress experienced by the crystal is intimately connected with the final dislocation density in the grown material, when dislocations are present. Traditional analysis characterizes a material as possessing a regime of elastic deformation where the stress and strain are related linearly until its upper yield point, when dislocations become mobile and plastic

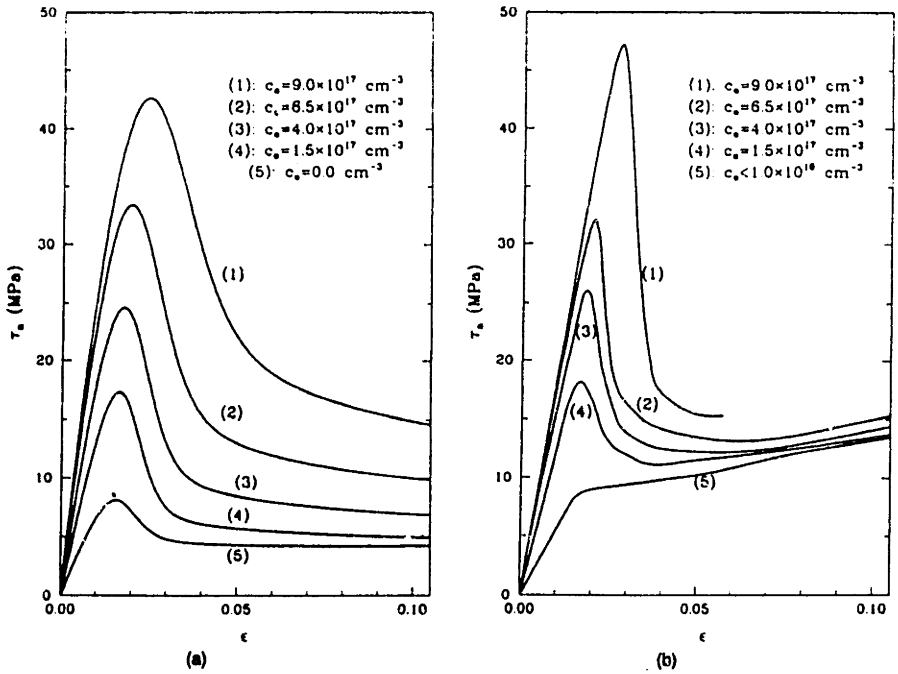

Figure 1-11: Predicted and experimental stress-strain curves for silicon, Maroudas and Brown, 1991b.

deformation occurs; see Figure 1-11. This upper yield point is commonly referred to as the critical resolved shear stress (CRSS), and specifically refers to the critical value of the stress component in a particular crystallographic direction. The regime of plastic deformation is complex, as the stress is first relieved past the upper yield point, but passes subsequently through a minimum, the lower yield point, then either remaining constant or increasing due to a phenomenon known as work-hardening. Following this notion, plastic deformation can be eliminated in silicon by maintaining the thermoelastic stress below the CRSS value. For silicon it is also known that the CRSS changes dramatically due to impurities, especially oxygen concentration (Maroudas and Brown, 1991b), which provides added incentive for the control of oxygen in the system, since high values of CRSS are preferred. The CRSS also changes dramatically with temperature, since at lower temperatures materials are much more resistant to plastic deformation.

1.2.4 Evolution of the State-of-the-Art

The intent of this subsection is to outline the development of practical techniques for CZ growth and to motivate the present research from the limitations that have recently been encountered. The emphasis here is on illustrating the early successes of trial-and-error

practice, followed by the inability of trial-and-error to unravel the complex phenomena encountered for large-diameter growth.

Achieving Zero Dislocation Density

Silicon boules that are used for device manufacture today are perfectly single-crystal material. Grown-in defects are eliminated with the Dash technique outlined in Section 1.2.2. Before this technique became standard practice dislocations were found to be generated mostly near the surface of the ingot, and could be correlated with curved melt-solid interfaces (Billig, 1956). This correlation can be explained since curved interfaces result from a high ratio of radial to axial temperature gradients, which produces thermal stress. Recognizing that curved interfaces were correlated with dislocation generation, growers had taken measures to maintain planar growth interfaces by, for example, using pull rates over an order-of-magnitude lower than Billig's brave $360 - 3600\,\mu m\,s^{-1}$. The low growth rates result in lower but still measurable dislocation densities, and these were reduced to zero by Dash seeding. In qualitative terms, the rapid pulling of the crystal in Dash seeding results in a very small diameter (less than $1\,cm$) for over $1\,cm$ length, causing any dislocations resulting from the shock of seeding to effectively terminate at the crystal surface, forming closed dislocation loops which are frozen into the material and can not propagate to the melt-solid interface. This procedure was the key procedural development that enabled crystal growers to successfully increase diameters up to the $20\,cm$ range, while maintaining a perfect crystalline structure with no measurable dislocation density. In the growth of $20\,cm$ diameter silicon boules however, the catastrophic propagation of dislocations has been observed, which provides added motivation for this thesis work. A prohibitive percentage of the $20\,cm$ crystals grown industrially at IBM [4] with otherwise perfect control were being classified as *polysilicon*, while the remainder were *completely* dislocation-free (Strudwick and Kim, 1988).

While the removal of grown-in dislocations is absolutely necessary to attain single crystal silicon boules, dislocations propagate catastrophically in large diameter growth in spite of the Dash method. Thinking along the lines of lowering stress in the crystal to levels below the CRSS has led several researchers to attempt designing novel heat transfer systems, including cooling jets directed at the crystal, so-called after-heaters or coolers around the crystal and radiation shields. However, attempts at arresting the propagation by design modifications with the purpose of controlling the cool-down

[4] Exact figures are unavailable, but lack of success may have motivated IBM's withdrawal from the silicon growth business.

phase of crystal growth have yet to become standard practice for the elimination of dislocations. Reductions in pull rate by an order-of-magnitude may help to lower thermal gradients, but are of limited utility because of the huge penalty to productivity. There has accordingly been a large increase in establishing the behavior of microdefects in the hope of discovering their role in the generation of dislocations. However, there have not yet been any proven industrial methods for minimizing the production of microdefects which in turn yield dislocation-free crystals in $\sim 20\,cm$ silicon growth. It is apparent that a successful growth strategy must combine controlled deposition of oxygen, carbon and other impurities with an *in situ* annealing schedule for control of the dislocation generation.

Achieving desired and uniform dopant concentrations

To achieve uniformly doped and chemically pure crystals, it is necessary to eliminate contamination, mechanical vibration, thermal fluctuation, unevenness in boundary-layers, and control the oxygen level in the crystal. Semiconductor growth facilities run at reduced pressures in a continuously-purged inert gas environment for the purposes of sweeping away contaminants evolving from the system, which include SiO gas evaporating form the melt, carbon from the graphite components which erode in the presence of oxygen and trace metallic and organic contaminants from the mechanical parts and the inert gas itself. Variation in the intended dopants occurs vertically along the crystal's length due to the equilibrium segregation coefficient not being unity, and latitudinally across the crystal radius due to the action of the flow field and the action of the free surface as a sink for some impurities. Axial uniformity is judged both by the concentration difference between the head and tail of the boule and microscopic vertical striations. Striations have deleterious effects on device performance, which increase with miniaturization (Shockley, 1961), whereas the head-to-tail concentration difference must be minimized in order to keep as much of the crystal length as possible within processing specifications. The long length-scale uniformity depends on the gradual enrichment or depletion of the melt nutrient. Experimental evidence (Utech and Flemings, 1966; Kim et al., 1978) and theoretical study (Hurle et al., 1968) have showed that striae were due to fluctuations resulting from unstable convection in melt growth systems.

Attempts to control solute segregation by influencing the flow patterns have met with mixed results. Universally growers use relatively high crystal rotation rates, which promote azimuthal uniformity. Attempts to steady time-dependent convection are at the forefront of ongoing research. It was found experimentally by Kim and Smetana, 1985

that attempts to eliminate dopant striations by application of a vertical magnetic field worked for the centerline of the crystal, but worsened the radial segregation. Transverse magnetic fields (Witt et al., 1970) produced adverse effects on the solute distribution, probably due to the remaining Marangoni force in the transverse direction. On the other hand, oxygen becomes depleted in the melt as the surface area of the crucible-melt contact is reduced, so that gradually increasing the crucible rotation rate has been used to increase the dissolution rate. Gradually increasing crucible rotation rate and periodically starting and stopping or reversing the crucible rotation rate (Murgai, 1985) have been explored as methods to enhance transport through the melt. A second purpose for these investigations is to lessen the fluctuations in solute deposition which occur when nonmixing eddies with drastically different solute loadings exhibit time-dependent motion. In such cases, the crystal is bombarded by waves of varying solute concentration.

Achieving large-diameter boules

One of the ways device integration has been achieved is through larger chip sizes, which necessitated crystal boules larger than the $1\,cm$ diameter boules Billig was growing in 1955. Although the crystal need not be strictly uniform in diameter, fluctuations in diameter enhance the likelihood of nonuniformities within the the crystal structure and composition. Hence, shape control has received much attention in addition to pushing to larger diameters. Larger chips have been realized only with the refinement of the CZ process to a delicate technique from its beginnings as an offshoot of the metalcasting industry. Crystals grown by Billig, 1955 had noticeable corrugations due to thermal asymmetry and mechanical vibration. A seed crystal not precisely oriented in the center of the crucible, for example, will result in such asymmetry. Improvements of CZ equipment in precision and isolation from random disturbances have reduced these problems. Production rooms are shockproofed and any essential vibrating equipment is insulated. Contamination is minimized by ultrapure ingredients and the process is carried out with a minimum of operator intervention in a clean-room environment. Larger-diameter crystals are lifted with the aid of mechanical calipers, to ease the stress on the crystal seed. Procedural and mechanical innovations have also been key advances which enabled the industry to scale up its equipment essentially linearly to the point where $20\,cm$ diameter crystals are the present state of the art.

The melt meniscus in CZ growth is dynamically unstable (Surek, 1976), since a perturbation in the contact angle tends to grow in time, resulting in either uncontrolled

inward growth [5] of the crystal, or uncontrolled outward growth [6]. The elimination of operator error in diameter control improved the yields in CZ. Measurements commonly used in automatic feedback control systems for automatic diameter control (ADC) include optical pyrometry, laser sensing, TV imaging, x-ray imaging and weight gain methods (Bardsley et al., 1977a; Bardsley et al., 1977b). The pyrometry is used to keep the heating on the desired trajectory, since the heater behavior is subject to long time-scale changes due to contamination and degradation. The imaging and weight gain methods are different ways to keep track of the diameter of the growing crystal. Pull rate has the most immediate effect on crystal radius as a manipulated variable, and is preferred as a control variable over heater power. Control of crystal diameter is no longer a concern, due to the effectiveness of these feedback control schemes. The major focus of silicon crystal growers is to achieve low dislocation density and compositional uniformity at large diameter.

1.2.5 An optimization approach

The goals for the crystal grower today are to manipulate the apparatus to maintain the shape of the crystal and safe impurity levels without the appearance of dislocations. Longer-term concerns are to maximize the radius of the growing crystal and the pull rate. These aspects of crystal growth are intimately coupled to each other, through the transport processes in the melt and other system components which are nonlinear in nature and have not yet been adequately addressed by changes to operating procedure. The goals of the crystal grower can be presented in an optimization context. Posed as a minimization problem, it is desired primarily to minimize the dislocation density, the deviation from set point impurity concentration and the concentration gradients. As well, the pull rate and crystal radius should be maximized. The optimization problem is stated as

$$\begin{array}{ll} \textit{minimize} & \gamma_1 N + \gamma_2 |c - c_{set}| + \gamma_3 |\nabla c| \\ & -(\gamma_4 V_p + \gamma_5 R) \\ \textit{subject to} & \textit{system constraints} \\ & \textit{process physics} \end{array} \tag{1.2}$$

where N is the number of dislocations, c is the concentration of impurities or dopants, ∇c signifies the gradient of the concentration field and measures uniformity, and $\{\gamma_i\}$ are

[5] "pinching off"
[6] "flaring"

weighting coefficients which reflect the material specifications. Note that in the above formulation the value of γ_1 would be very large so that no dislocations would be tolerated. Also note that the optimization is stated without referring to whether an optimal control or design is being sought. The constraints imposed on the optimization are the physics involved in the process and practical bounds on the parameters of operation. Since it is too time-consuming to adequately explore the space of parameters with an actual experiment, it is essential that an accurate model be developed to relate the system's inputs and outputs for use in studies aimed at achieving optimal design and/or control. It is appropriate that these goals be stated as a simultaneous optimization, rather than a sequence of unrelated objectives in the same process, since experimental evidence points to intense coupling of the transport phenomena.

1.3 CZ growth modelling

Mathematical models for CZ growth have progressed from simple linear scalar heat balances, such as the one described in Section 1.2.3, to huge computer formulations with spatial discretizations on the order of tens of microns, while experimental models have developed from stirred tanks of water solutions to actual silicon samples. Simple models of process dynamics have been applied on-line, interpreting measurements of the process status and correcting controllable parameters to steer the system along the correct trajectory. Combined with feedback control these models have achieved success in controlling crystal diameter (Bardsley et al., 1977a). Experimental models have revealed complex flow behavior, which only now with the advent of x-ray observation techniques is possible *in situ*. The push to larger length-scales necessitates online control of more variables than just diameter, however, and to complicate the situation the variables usually can be neither measured nor *inferred*, so feedback is not the immediate solution to CZ's woes. Therefore larger mathematical models which accurately predict the salient physics of the CZ process are required for the development of *feed-forward* schemes. This Section will trace the development of CZ modelling including experimental models and mathematical models from those which can be employed with the simplest programmable controller to the most sophisticated large-scale simulations. The purpose of this Section is to provide a survey of modelling approaches for justification of the modelling approaches described in subsequent chapters. Experimental models will be described first, indicating the benefits they have given to crystal growth, and explaining their limitations for addressing the complexity of industrial scale CZ. Mathematical modelling will also be described, out-

lining simple models whose applications have been direct and widespread, and building in complexity to the most sophisticated formulations, illustrating the difficulty that such models have in generating practical results.

1.3.1 Experimental Models

The notion of an experimental model has been mentioned several times as the type of model which is a physical analog of the actual system. The motivation for use of analogs is clear since the actual CZ system is very costly, intricate, operates at high temperatures, cannot be visually observed, has opaque materials and is not amenable to switching on and off to collect data over brief periods of time. Experimental models have been used mostly to aid in explaining the flow phenomena in CZ growth, and with the advent of modern measurement techniques for opaque fluids, experimental models may soon be producing detail to rival numerical simulations. For many years the most valuable insights into the physics of CZ were gained by these methods. Data were obtained by direct visual monitoring of the flow patterns of a transparent fluid, although this excluded liquid metals, which made it impossible to directly simulate the thermal convection since the Prandtl number was usually incorrect. By operating these experiments in conventional laboratory equipment researchers were able to forego the complications of establishing a growth facility, although such studies do not mimic the radiative heat transfer. The most promising model experiments being performed today use flow visualization with x-ray scanning of tracer particles in the optically opaque silicon melt. Similar techniques may soon enable *in situ* measurements in large-scale systems.

Effects of crystal and crucible rotation were investigated for a 1 : 1 glycerine-water solution which has a viscosity of $5.0cP$ (Carruthers and Nassau, 1968). The flow patterns shown in Figure 1-12 are those observed in the experiment. The Taylor-Proudman analysis predicts flows characterized by regions of constant angular velocity which are separated by detached stagnation or *free shear* layers. This terminology refers to the boundary-layer formed in the interior of the domain, rather than on a fixed boundary. In the free shear layers viscous effects are important while flow is inviscid in the rotating regions. The meridional circulation in the lower Taylor-Proudman cell is radially converging at the top and diverging at the bottom of the crucible, while the opposite applies for the upper cell. The experimentally visualized flows show the dominance of crucible rotation effects. Except when the crucible rotation rate is small or zero, the cell associated with crystal rotation is either unnoticeable or restricted to the neighborhood of the

crystal surface. This is certainly anticipated since the crucible wall also rotates, which, in the absence of slip, applies much more torque to the fluid than the smaller-radius crystal. Although the flow situation in actual growth also involves natural convection, crystal growth practice is to use a counterrotation ratio very similar to that in the highlighted diagram in Figure 1-12. In the model system this choice ensures that the bulk of the fluid is rotating with the crucible, which in a CZ system would smooth out thermal asymmetries in the heating; the flow has a stagnation region and a vigorously mixed upper cell near the crystal surface which would smooth the effects of natural convective flow on the heat and mass flux rates into the solid.

A simulation of CZ flow induced by crystal rotation and buoyancy (Shiroki, 1977) demonstrated the nonlinear interaction between forced and buoyant convection. The experiment used $0 - 66 wt.\%$ sugar-water solutions to vary the solution viscosity between $0.5 < \mu < 20 cP$, with SiC particles added for flow visualization. The observed main flow consisted of a single rotation-driven vortex near the crystal, irrespective of solution viscosity. For the solution with viscosity closest to silicon, crystal rotation had little effect on the temperature, which was measured by thermocouples inside the solid plug representing the crystal. The thermal conductivity was $\sim$ 100 times less than that of silicon. Both forced and natural convection cells were observed simultaneously. Although increasing rotation rate from $15\,rpm$ to $100\,rpm$ asserted the forced convection cell the temperature measured at the "crystal" remained constant. The buoyancy-driven effects were limited due to the low Grashof number for the apparatus, which was only $\sim (10^4)$, compared to $\sim (10^9)$ for the Siltec system modelled here, so it is likely that the system heat transfer was conduction-dominated.

A more vivacious attempt at simulating CZ flows driven by a combination of buoyancy, thermocapillarity and crystal rotation was performed by Lamprecht et al. (1983), who used a melt of $NaNO3$ ($T_{mp} = 307°C, Pr = 9.25$). This study was one of the first model experiments to combine all of the major driving forces. The flow visualization was accomplished by adding tracer particles which were hollow spheres of quartz glass. The melt was contained in a $17.5\,mm$ radius crucible with a $5\,mm$ radius "crystal", yielding a Grashof number of $\sim 10^6$. Although no crystal was grown, sufficient heat was supplied to duplicate the temperature required to grow a real crystal. It was found that a crystal rotation rate of $120\,rpm$ was required in order to establish a flow stagnation point at the edge of the crystal. At lower rotation rates the radial flow at the crystal edge was inward due to thermocapillary forces. The major importance of this work was to illuminate the importance of Marangoni flows, which dominated the surface meridional circulation.

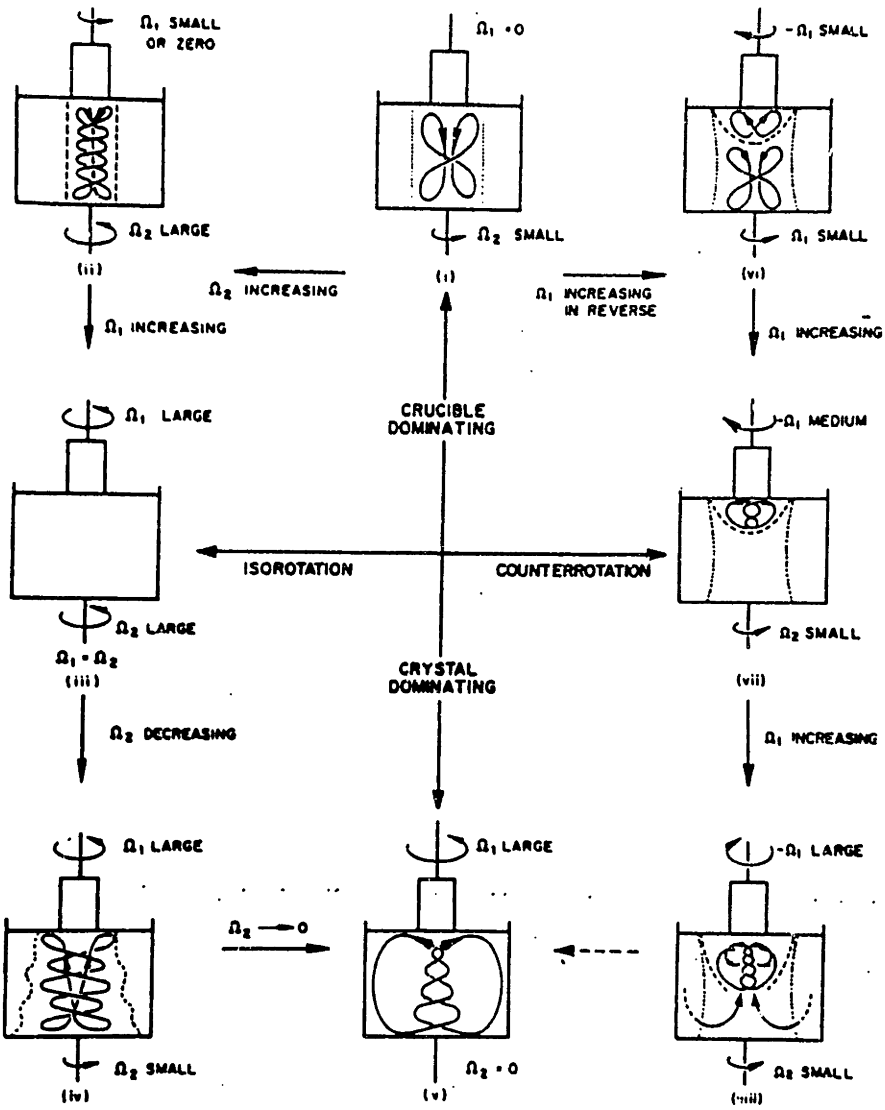

Figure 1-12: Flow visualization results of Carruthers and Nassau, 1968.

It also was shown that surface contamination could create a drastic change since the thermocapillary effect was arrested in a number of trials with a layer of silicone oil. It was found that a rotational Reynolds number of at least 800 was required to establish dominance of crystal rotation over the thermally-driven flow.

Experimental models have most accurately imitated the behavior of oxide or fluoride melts, because the restrictions of having a clear working fluid. The experimental apparatus of Jones, 1983a was designed to accommodate both rotational forces and natural convection simultaneously using a working fluid of glycerol/water ($Pr \sim 10$), with both nigrosine dye and ground fish scales to visualize the flow. With an isothermal melt, crystal rotation yields a nonaxisymmetric flow pattern, and with rotation greater than $7\,rpm$, the flow became time-dependent with waves moving toward the wall along the melt surface. With only crystal and crucible rotation his system also yielded a nonaxisymmetric flow pattern, with a large oval pattern rotating in the direction of crystal rotation on the melt surface, and two smaller cells circulating in the opposite sense; see Figure 1-13a. The flow field with natural convection and no rotation was axisymmetric, but showed fluctuations in the descending column of fluid underneath the stationary disk, and also in the horizontal boundary-layer along the fluid surface. This horizontal layer exhibited a "spoke" pattern, due to a three-dimensional buoyancy-driven instability, resulting in latitudinal rolls (Jones, 1983b). When crystal rotation was combined with buoyancy-driven convection up to $Gr \sim 10^9$, the rotation rate could be adjusted so that crystal rotation or buoyancy dominates, yielding limiting flow patterns. At crystal rotation rates of $5\,rpm$ and $10\,rpm$ the buoyancy force results in a downward spiralling flow under the crystal. However at $15\,rpm$ the rotation is strong enough to force this downward spiral beyond its periphery and the flow assumes a nonaxisymmetric swirling pattern, similar to an eight-pointed spur shape (see Figure 1-13b). Large temperature fluctuations accompany the unsteady flow. With counterrotation and heating the flow exhibited the swirling pattern and the rapidly rotating spiral under the crystal. Large irregular temperature fluctuations were observed throughout the melt. Further studies made by Jones clarified the exact balance between buoyancy and crystal rotation forces. The details of the exact balance have mixed importance for the flow in CZ; crucible rotation, thermocapillarity and the low Pr are highly important factors for CZ, but $3D$ behavior in CZ is a key to understanding the experimental results.

The combined effects of rotation, buoyancy and thermocapillarity have been investigated using high Pr silicone oil (Munakata and Tanasawa, 1990). Cholesteric liquid crystal pellets were used to indicate temperature in the melt. This study featured a

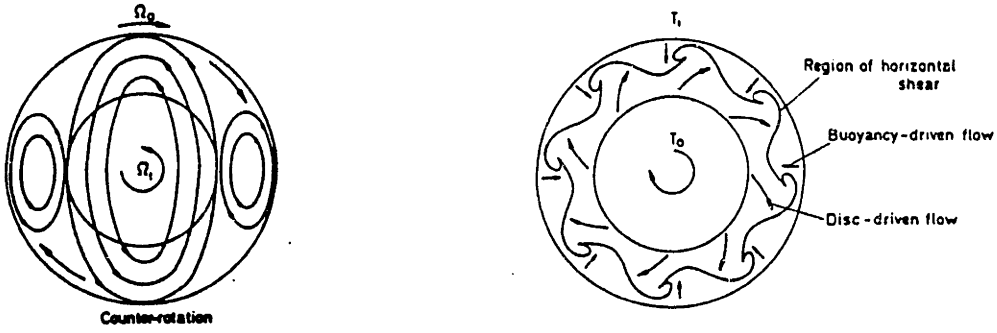

Figure 1-13: Flow visualization results of Jones, 1983a, for (a) crystal and crucible counterrotation (b) crystal rotation with natural convection.

range of high Pr oils, to demonstrate the effect of changing the Prandtl number from $1 < Pr < 1000$ on the flow and thermal profile. They found that the onset of unstable convection was influenced by Pr, Gr and crucible rotation rate, and they characterized this onset by a critical crystal rotation Reynolds number $Re_{s,c}$. This value decreased with Prandtl number $Re_{s,c} \sim Pr^{-2/3}$ and with Rayleigh number approximately linearly for the range $10^5 < Ra < 10^6$. The critical Reynolds number exhibited a minimum when the crucible was not rotated, and increased with co- or counterrotation. The critical Reynolds number also varied from a low of about $5\,rpm$ to a high of $\sim 1000\,rpm$ in this study. It is difficult to generalize these results to CZ growth of silicon, other than to estimate that the flow is likely to be unstable for rotational Reynolds numbers greater than $\sim 10^4$ if $Ra \sim 10^5$ and the crucible is not rotated. Similar experiments with silicone oil of $Pr \sim 5000$ and liquid crystal markers by Ozoe et al., 1990 showed that for $Gr \sim 370$ and $1 < Re_s < 3.5$, an oscillatory flow appeared, and that the period of oscillations passed through a maximum as the flow experienced a transition from natural convection to rotation dominance. Again, however, translation of results for silicone oils to silicon melt is difficult due to the lack of a good match in the Prandtl number of the fluid.

A most promising area for experimental simulation of heat transfer and flow in Czochralski melts is to adapt the use of various measurement techniques to a low-melting

metal, such as mercury, since the Pr of mercury is 0.026, very close to that of silicon melt. Non-visible spectra visualization techniques have been used (Kakimoto et al., 1988), but lack precision since the tracer particles are inertial. Measurements would be easier to perform and control at the lower temperatures permitted by mercury, so that the comparison between mathematical models and realistic conditions could be made more sound. Initial efforts with low Pr fluids have focussed on thermal convection in closed cavities, and have measured temperature and velocity fluctuations to gauge convection levels. The development of unsteady natural convection in the horizontal Bridgman configuration has been studied using temperature measurements (Pratte and Hart, 1990). In a rectangular channel of varying width they found that primary instabilities occurred due to *longitudinal* rolls, i.e. cells with an axis *perpendicular* to the heated end walls, as opposed to the steady convective cells oriented latitudinally. The primary instabilities were thus an inherently three-dimensional effect. The critical Grashof number for the onset of instability was strongly correlated with the width of the system, since only an integer number of cells can fit into a confined container. The critical Grashof number varied from $Gr_c \sim 22 \times 10^3$ for a three-cell mode in a 6.31 cm wide container, to $Gr_c \sim 39 \times 10^3$ for a one-cell mode in a 1.98 cm wide container and $Gr_c \sim 200 \times 10^3$ for a one-cell mode in a 0.99 cm wide container. A recent review by Roux, 1990 of similar experimental studies (Hart and Pratte, 1990; Hung and Andereck, 1990; Wang et al., 1990) concluded that the primary instability goes through period doubling and/or generates subharmonic instabilities, before becoming quasi-periodic and eventually chaotic. The onset of oscillating behavior was found to be significantly different than analytical predictions. This type of result illustrates the importance of experimental models compared to mathematical ones.

Advanced experimental techniques can push experimental models to the point where they are very accurate analogs and are highly measurable. The insights into flow mechanisms are potentially extensive. In addition, it is feasible to trace solutes through the melt by the controlled injection of known concentrations of solute and controlled withdrawal at the "crystal" surface, measuring the solute content of the removed material. Although flow simulation has been the emphasis of this section, it should be mentioned that experimental models of *in situ* annealing are effected by subjecting crystal samples to controlled annealing environments. These yield data on the growth of microdefects and dislocations. This will not be dealt with in detail here; rather, the results of this thesis will be used to indicate the importance of these phenomena.

Experimental models hold the potential of yielding large amounts of data for the

verification of scientific theory and mathematical models. However, the flexibility of computational analysis is decidedly in favor of using mathematical models for design and control of the CZ process. The greatest ultimate use of the experimental models will therefore be to provide accuracy for mathematical models.

1.3.2 Analytical approaches to heat transfer analysis

This section describes closed-form expressions for the analysis of heat transfer. There are two objectives of such analyses, the prediction of free boundary shapes and the prediction of the thermal field to be used to estimate the thermal stress in the crystal. The simplest type of mathematical analysis derives from the heat transfer equations an online model which attempts to relate an important manipulated variable such as pull rate V_p, to the steady value of a controlled free boundary variable such as crystal radius. These models can either be obtained from an oversimplification of the physical processes or from purely empirical correlation. Billig considered maximum pull rate to occur when the entire melt region is at the melting point. Latent heat release at the melt-solid interface is then the only source of heat, and is dissipated by radiation from the crystal to a much cooler ambient, yielding (Billig, 1955)

$$V_p = \frac{1}{\rho \Delta H} \sqrt{\frac{2}{3} \frac{\epsilon_s k_s T_s^5}{R_s}}. \tag{1.3}$$

The relation was supported by his results and, with minor variations and feedback, similar models persist in control schemes today. A slightly more complicated model used an empirical scalar relation based on the notion that the heat flux from the melt depends directly on the temperature effected by the heater, T_h, while heat flux into the crystal depends on its radius R_s. It considered the time-dependence to be governed by a fin-cooling relation and gave a feed-forward trajectory for heater temperature,

$$R = \left[\frac{1}{V_p + 0.417} + \frac{40.1}{T} \right] \exp(\gamma t) \tag{1.4}$$

obtaining good experimental agreement on 12.5 cm crystals (see figure 1-3) without any feedback control (Kim et al., 1983). An extended scalar model (Srivastava et al., 1985) replacing time with an explicit dependence on the height of the crucible h_c and the height of the melt h_m was developed and empirically fitted to conduction-dominant simulation results by Derby and Brown, 1987a. Similarly they related the melt-solid interface de-

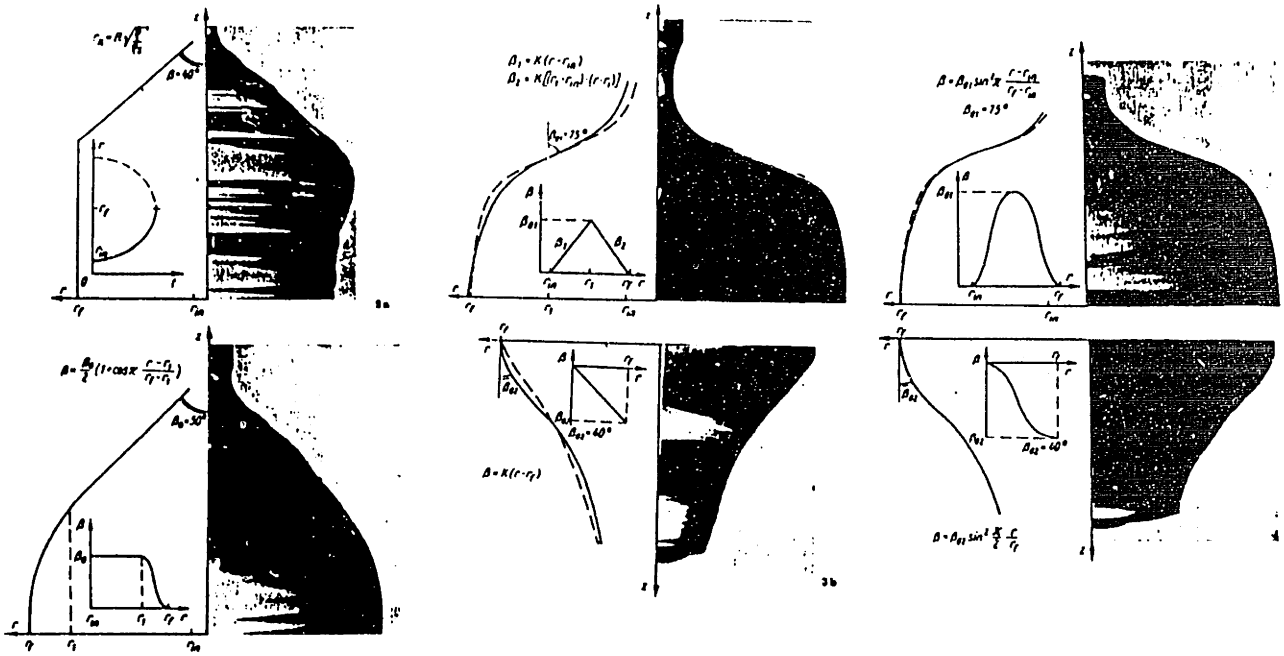

Figure 1-14: Implementation of transfer-function model-based feedback control, after Satunkin and Rossolenko, 1986.

flection to terms involving the wetted crystal area $\sim R^2$, the crystal periphery $\sim R$ and the temperature supplied by the heater. Citing a very good fit to the model predictions, presumably the following equations could be empirically adjusted to produce accurate control of a CZ puller (Srivastava et al., 1985).

$$V_p = \frac{\gamma_1}{R} - \frac{\gamma_2 h_c \Delta T}{R} - \gamma_3 \frac{\Delta T}{h_m} \tag{1.5}$$

$$\Delta h_0 = \Delta h_0|_{t=0} - (\gamma_4 R - \gamma_5 R^2)\Delta T \tag{1.6}$$

The development of transfer function models is motivated by their use in (linear) control theory where they attempt to anticipate the linearized process dynamics, given that a steady state exists. These models are used to improve the dynamic response of feedback controllers. A transfer function relating crystal diameter to heater input has been empirically calculated to be subsequently used as a basis for control algorithms by Hurle et al., 1986. A transfer function based on linearized equations governing the meniscus shape was developed to design a weight-gain diameter controller, and successfully grew crystals with good agreement in the shouldering and coning in phases as shown in Figure 1-14 (Satunkin and Rossolenko, 1986).

An even more sophisticated MIMO control scheme was developed based on linearized

theory (Gevelber, 1988). In that approach, a low-order model was used to analyze the performance of an improved multivariable control scheme to control crystal diameter, melt temperature gradient, crystal temperature gradient and interface shape. Unfortunately the work lacks experimental verification. It also fails to relate to the variables of dislocation density and solute distribution. Nor do these approaches provide any insight into the difficulties encountered for larger crystal diameters, which is not addressable with their control variables. With the development of advanced measurement techniques even the melt-solid interface is potentially measurable, and on-line models of transfer function type are ultimately of the utmost utility for anticipating dynamic response. Transfer function models are intended to improve feedback control loops by providing them with some knowledge of the process physics; however, these models are intended to work in connection with PI controllers so that inadequacy to cope with nonlinearities will be corrected. The purpose of this work is to devise a model which can be used to produce better feed-forward growth strategy or design a better puller. Therefore, the interest in obtaining a model capable of calculating steady-state operation from purely physical grounds is essential, as opposed to models which must be empirically tuned or which are purely for dynamic response.

The prediction of the thermal field in the crystal is of paramount concern in order to quantify the effect of annealing time and thermal stress. The equations for heat transfer can be solved analytically given an amenable form of the thermal boundary conditions on the crystal. One way this was accomplished was described by Tsui and Tsou, 1963 who employed the solution of the steady-state heat conduction equation for a cylinder with fixed temperatures at either end, and on the circumference a linear heat flux term representing the radiative heat loss. There is an analytical solution to this problem, if the radiative ambient temperature is taken to be equal to one of the end temperatures, most logically the cold one. Analytical expression in terms of a series of Bessel function solutions yields

$$\frac{T-T_c}{T_h-T_c}=\sum_{n=1}^{\infty}\frac{2cJ_0(\alpha_n\eta)\sinh\alpha_n\left(\frac{l}{a}-\xi\right)}{(c^2+\alpha_n^2+H^2)J_0(\alpha_n)\sinh\alpha_n\frac{l}{a}} \tag{1.7}$$

where α_n are roots of the equation

$$cJ_o(\alpha_n)=\alpha_nJ_1(\alpha_n) \tag{1.8}$$

and J_0 and J_1 are the Bessel functions of the first kind of zeroth and first order, respectively (Carslaw and Jaeger, 1947).

Adjusting this analysis to calculate the interface deflection necessitates adjusting the boundary condition on the hot end of the crystal. This has been done by considering uniform heat input q to an infinitely long cylinder which radiates to a uniform temperature environment, as described by Wilcox and Duty, 1966. This simple model, truncated after the first term in an infinite expansion, gives the interface shape with nonlinear dependence on radius.

$$\frac{z}{R} = -\left(\frac{k}{qR\,a_1}\right)\log\left[\frac{a_1(a_1^2+H^2)J_0(a_1)\sum_{a_i>0}\frac{1}{a_i(a_i^2+H^2)}}{J_0(a_1\frac{r}{R})}\right] \tag{1.9}$$

The approaches outlined above neglected heat transfer in the melt and are probably sufficient for situations where convective heat transfer is small due to very small diameter crucibles. However, heat transfer in the melt is extremely important which accounts for the lack of successful application of Bessel-function solutions to control of melt-solid deflection for large-diameter crystals. Potential applications of such expressions could include on-line estimation of melt-solid deflection for small crystals or in magnetic CZ growth and on-line estimation of the thermal field in the annealing crystal under a uniform radiative environment. The thermal field estimation is probably accurate for the portion of the crystal which is greater than a crystal radius away from the melt-solid interface, to eliminate the effects of heat flux from the melt.

1.3.3 Asymptotic analyses of fluid flow

Complicated nonlinear interactions occur in the melt phase, where the Navier-Stokes equations are considered to adequately describe the fluid's behavior. Asymptotic study of the melt flow involves isolating regions of parameter space where physical behavior is dominated by some prevalent mechanism. For example it can be determined under what conditions heat transfer in the melt is governed by conduction only, hence justifying the use of analytical models to predict heat transfer in the crystal, as described in the previous section. Study of these asymptotics is essential, since they provide the framework for understanding the process and also provide the means, through dimensionless groups, to characterize experimental results and compare with larger-scale computational efforts. This discussion proceeds by describing the asymptotic behavior of the individual flow mechanisms, as a parallel to the descriptions in Section 1.2.3. This section is intended to provide rigorous explanations for the observations in Section 1.2.3., and to provide

means for checking the predictions of the flow model developed in this thesis. Laminar flow is assumed throughout. The consequences of this assumption will be discussed in Chapter 4.

Crystal rotation

An important yet controversial boundary-layer flow is associated with crystal rotation, which interacts with the other flow mechanisms, and the thermal and solutal fields to determine the local solidification rate and segregation behavior. The near-field flow in front of the melt-solid interface can be described by the similarity solution for an infinite disk rotating upon a semi-infinite liquid. According to the similarity form, the velocity components v_r and v_θ are linear functions of r, while v_z is independent of r. For small distance from the rotating disk $|z - z_0|$, the axial flow component is given in consistent notation by

$$v_z = 0.51\omega_s^{3/2}\nu^{-1/2}(z - z_0)^2, |z - z_0| < \sqrt{\frac{\nu}{\omega_s}}. \tag{1.10}$$

The momentum boundary-layer in front of the crystal scales with $Re_s^{-1/2}$, $\delta \simeq 0.8\sqrt{\frac{\nu}{\omega_s}}$. The crucible and crystal Reynolds numbers are measures of the rotational driving forces to the viscous forces in the melt. It has been shown (Sackinger, 1989) that, even with a curved melt-solid interface, the similarity analysis yields excellent predictions for the near-field flow in the absence of other driving forces up to $r = 0.75R$. This boundary-layer analysis, known commonly as the *von Kármán* or *Cochran* flow solution, has been a cornerstone in the thinking surrounding CZ flow and especially solute deposition. However it may be a flawed approach since the boundary-layer analysis may be subject to indirect effects from the other flow mechanisms. One of the tasks of fluid mechanical study of the CZ system is to test the validity of such commonly held axioms.

Crucible rotation

The flow induced by the crucible rotation is of a different nature altogether. Since the walls of the container are also moving, the basic flow is one of a solid body rotation of the entire fluid, rather than the von Kármán depiction. The presence of the crystal makes the picture more complex unless the crystal rotation rate is identical to that of the crucible in which case the whole system rotates with equal azimuthal velocity; the situation of counterrotation is more commonly encountered. When rotating at different speeds the solution structure basically splits into two major regions, one of solid body

rotation at the crucible rotation rate for $r > R_s$, and the other of solid body rotation at a rate slightly less than the crucible rotation rate for $r < R_s$. The boundary-layers due to the crystal and crucible rotation are known as Ekman layers, and the region separating the two major cells is known as a free-shear layer (Hide and Titman, 1967). For the vertical *Taylor-Proudman* column inhabiting the region under the crystal $r < R_s$, the rotation rate depends only weakly on the crystal rotation rate. The boundary-layer structure depends on whether there is corotation or counterrotation. For corotation, the boundary-layer flows are of von Kármán type with a superimposed vertical drift along the axis of symmetry toward the faster spinning "disk" (Batchelor, 1951); for this flow the Taylor-Proudman column under the crystal behaves like a confined fluid between two spinning disks. The boundary-layer in front of the crystal scales with $Re_s^{-1/2}$ and depends on the ratio of crucible to crystal rotation

$$\delta = R_s Re_s^{-1/2} \left(1 - \frac{\omega_c}{\omega_s}\right)^{-1/4}. \tag{1.11}$$

For counterrotation which is more common in silicon growth, there exist two distinct Taylor-Proudman circulations and a layer between them where the vertical velocity changes sign, as shown in Figure 1-15. The upper cell has a half-length of

$$\delta_1 = 1.07 R_s Re_s^{-1/2}[1 - 0.15\eta + O(\eta^2)], \tag{1.12}$$

where η is a small parameter for crystal growth (Jones, 1988). This parameter measures the deviation from the crucible rotation rate which yields zero azimuthal velocity for the transition layer; i.e. $\eta = 0$ implies that the separation layer between the two Taylor-Proudman cells has zero azimuthal velocity

$$|\omega_c| \simeq \omega_s(\frac{3^{1/6}}{2} - \eta). \tag{1.13}$$

The upper boundary-layer of the lower cell has boundary-layer length

$$\delta_2 = 1.29 R_s Re_s^{-1/2}[1 + 0.83\eta + O(\eta^2)]. \tag{1.14}$$

These boundary-layer lengths δ_1 and δ_2 depend on crystal rotation mainly when η is small, which applies for normal conditions for CZ silicon growth. The boundary-layer at the crucible bottom has thickness $\delta_c \simeq \sqrt{\frac{\nu}{\omega_c}}$, similar to that for the crystal.

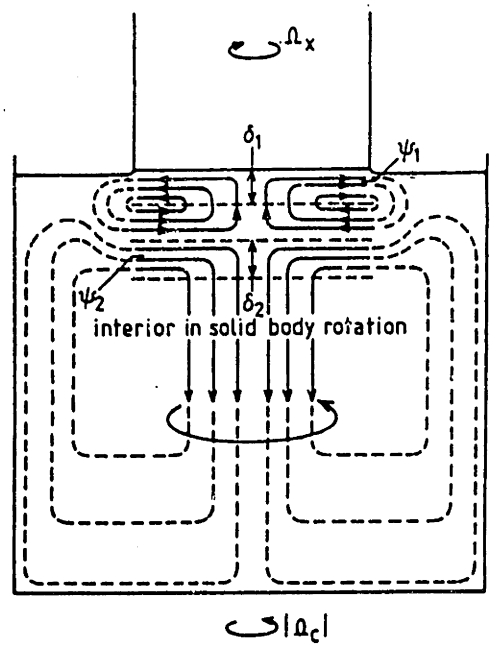

Figure 1-15: Flow streamlines in CZ geometry with counterrotation of crystal and crucible, from Jones, 1988.

Buoyancy

The action of buoyancy-driven flow, isolated from other driving forces, was analyzed for the horizontal Bridgman configuration (Camel and Favier, 1986). This geometry is a rectangular box of fluid with insulated top and bottom and a temperature difference between the two ends. At high levels of the thermal Grashof number, the flow changes from the Stokes flow to a boundary-layer flow, where the core of the melt behaves as an "inertial flywheel", inviscid and rotating with the scaling $Re \sim Gr_T^{1/2}$. The thermal Grashof number is a ratio of the buoyancy driving force to the viscous forces in the melt. The resulting boundary-layer on the walls scales with $Gr_T^{-1/4}(Re^{1/2})$ and the tangential and normal velocity components obtain the following scalings:

$$v_t \sim Gr^{3/4}x \tag{1.15}$$

$$v_n \sim Gr^{3/4}x^2. \tag{1.16}$$

These boundary-layers separate from the walls near the corners. The situation in CZ growth can be approximated similarly as a cylinder heated from the side, with insulated bottom and top. The flow has boundary-layers along the crucible wall and bottom, and the melt surface and which scale with $Gr_T^{-1/4}$ as confirmed by Sackinger, 1989, similar to

the result for flow in a box.

Thermocapillarity

A thorough analysis of isolated thermocapillary flow (Zebib et al., 1978) is based on the assumption that the temperature gradient remains $O(1)$ over most of the free surface. This results in a constant vorticity over the free surface; the alternative assumption, that the temperature gradient is confined to boundary-layers adjacent to the stagnation points leads to scaling that is inconsistent with their calculations (Zebib et al., 1978). The first premise results in a boundary-layer flow over the free surface with thickness that scales with $Ma^{-1/3}$. The surface tangential and normal velocities are scaled accordingly:

$$v_t \sim Ma^{-1/3} \tag{1.17}$$

$$v_n \sim Ma^{-2/3}. \tag{1.18}$$

The analysis predicts surface velocity to be a *decreasing* function of Marangoni number, which was borne out by their calculations. The magnitude of the core circulation is also found to scale with $Ma^{-1/3}$. The cold corner regions become very complicated due to the constant shear surface meeting a solid surface at right angles. Here the flow turns over a horizontal scaling of $O(Ma^{-2/3})$ and a vertical scaling of $O(Ma^{-1/3})$. The detail of the flow is determined over smaller and smaller subscales, but is unimportant to the overall transport. The boundary-layer scalings along the rigid walls are of $O(Ma^{-1/2})$.

Scaling analysis for combined flows

None of the above analyses strictly apply in the CZ growth of silicon, because all of the driving forces interact to some extent. The most complete asymptotic analysis of combined flow mechanisms in the absence of a magnetic field is due to Jones. He developed asymptotic scalings for the four flow mechanisms described above and developed expressions for the relative influence of each effect on convective heat transfer in the limit of strong convection (Jones, 1984 and 1988). These scalings involve the Grashof number $Gr \equiv Ra/Pr$ which scales buoyancy to viscous forces, the Ekman number $Ek_s \equiv \nu/|\omega_s|R_s^2$ which scales viscous to Coriolis forces and the Reynolds number for surface tension driven flows $Re_\sigma \equiv Ma/Pr$ which scales thermocapillary to viscous forces, where Marangoni Ma, Rayleigh Ra and Prandtl Pr numbers are defined in Table 2.1. The constant a is the aspect ratio of the melt, ϵ is the fraction of the melt temperature drop through the interior, s is the ratio of crystal radius to crucible radius and η has been introduced in

Eq. (1.13).

These scalings are obtained from the equations of motion for the streamfunction ψ, and the azimuthal velocity v and the equation of energy, which are stated in Jones' notation as

$$\begin{aligned} \underset{[A]}{\frac{\nu}{r}L^4\psi} - \underset{[B]}{\alpha g T_r} + \underset{[C]}{2v_z\frac{v}{r}} + \underset{[D]}{\frac{1}{r^2}J(\psi, L^2\psi)} &= 0, \\ \underset{[E]}{\kappa\nabla^2 T} + \underset{[F]}{\frac{1}{r}J(\psi, T)} &= 0, \\ \nu(\underset{[G]}{\nabla^2 v - \frac{v}{r^2}}) + \underset{[I]}{\frac{1}{r^2}J(\psi, rv)} &= 0, \end{aligned} \tag{1.19}$$

where the operators J, L^2 and ∇^2 are defined by

$$\begin{aligned} J(a,b) &= a_r b_z - a_z b_r, \\ L^2 a &= r(\frac{1}{r}a_r)_r + a_{zz}, \\ \nabla^2 a &= \frac{1}{r}(ra_r)_r + a_{zz}. \end{aligned} \tag{1.20}$$

The letters below the equations (1.19) will be used to refer to the magnitude of the various terms required to perform the scalings in this section. It has already been determined that, of the two rotations forcing convection, that crucible rotation has the dominant effect except for the immediate neighborhood in front of the melt-solid interface. On the other hand, the effects of thermally-driven convection tend are complementary rather than competing. Both buoyancy and thermocapillarity force flows in the direction of lower temperature, although one is a bulk and the other a surface phenomenon. It is important therefore to decide which of these two is the dominant effect. In the surface tension boundary layer the ratio of buoyancy to thermocapillary forces is given by the ratio of terms $\frac{[B]}{[A]}$, which yields:

$$\left[\frac{buoyancy}{thermocapillarity}\right]_{melt\ surface} \sim a^3 Gr Re_\sigma^{-\frac{5}{3}} \approx 10^{-2}, \tag{1.21}$$

and thus thermocapillarity dominates the flow in this region. However, in the interior of the melt the ratio of the magnitudes of the buoyancy-driven stream function $\psi_b = 0.25\nu R_c \epsilon^{1/2} Gr^{1/2}$ to the thermocapillary stream function $\psi_s = \nu R_c Re^{1/3}$ is given by the

ratio $\frac{\psi_b}{\psi_c}$, which yields:

$$\left[\frac{buoyancy}{thermocapillarity}\right]_{interior} \sim 0.25\epsilon^{\frac{1}{2}} Gr^{\frac{1}{2}} Re_\sigma^{-\frac{1}{3}} \approx 30 \tag{1.22}$$

which indicates that buoyancy tends to be the dominant driving force for flow in the interior. The presence of this buoyancy-driven interior flow gives rise to a stream function of $2\psi_b\delta_s/H$ in the Marangoni layer, where H is the melt depth. The relative importance of buoyancy to Marangoni convection in the Marangoni layer due to the indirect effect of buoyancy in the bulk is given by the ratio $2\psi_b\delta_s/H\psi_s$, which yields

$$\left[\frac{buoyancy}{thermocapillarity}\right]_{melt\ surface} \sim 0.5\epsilon^{\frac{1}{2}} aGr^{\frac{1}{2}} Re_\sigma^{-\frac{2}{3}} \approx 1. \tag{1.23}$$

Thus, the flow in the surface-tension boundary-layer is expected to be driven partly by buoyancy. At any rate, the dominant effect of thermocapillarity is expected to be limited to a thin layer along the melt surface.

The combination of natural and forced convection is an even more intricate matter. The condition for buoyancy driving force to overwhelm the crystal rotation force, i.e. term $[C] << [D]$ is that the following expression be greater than one:

$$\left[\frac{buoyancy}{crystal\ rotation}\right]_{crystal\ surface} \sim 0.25\epsilon a^4 s^2 GrE_s^2 \approx 1. \tag{1.24}$$

Therefore, the buoyancy-driven flow should be affected somewhat by the effect of crystal rotation. On the other hand, the condition for which the combined effects of rotation (with counterrotation assumed) dominate buoyancy in the boundary-layers $[B] << [D]$ is that the magnitude of the following expression be less than one:

$$\left[\frac{buoyancy}{crystal\ rotation}\right]_{\delta_1} \sim 1.4a^3 s^4 GrE_s^{5/2}(1 + 0.73\eta) \approx 10^{-2} \tag{1.25}$$

$$\left[\frac{buoyancy}{crystal\ rotation}\right]_{\delta_2} \sim 3.6a^3 s^4 GrE_s^{5/2}(1 + 4.2\eta) \approx 10^{-2}. \tag{1.26}$$

For rotation to be dominating buoyancy in the interior the condition is that the following expression be less than one:

$$\left[\frac{buoyancy}{crystal\ rotation}\right]_{\delta_1} \sim 0.3\epsilon^{1/2} s^{-1} Gr^{1/2} E_s^{1/2}(1 + 0.83\eta) \approx 200. \tag{1.27}$$

Table 1.3: Asymptotic scalings for forced and natural flows in CZ.

Relative magnitude		In the domain	Scaling
of	to		
buoyant force	thermocapillary force	Marangoni layer	10^{-2}
buoyant flow	thermocapillary flow	interior	30
buoyant flow	thermocapillary flow	Marangoni layer	1
buoyant force	crystal rotation	crystal surface	1
buoyant flow	crucible and crystal rotation	δ_1	10^{-2}
buoyant flow	crucible rotation	δ_2	10^{-2}
buoyant flow	crucible rotation	interior	200
convection	conduction	interior	75

The scalings are summarized in Table 1.3. For the conditions of the silicon growth experiment in this Thesis. One would therefore expect the free surface flow to show marked thermocapillary effects, the flow along the crucible sidewall to be dominated by buoyancy, the flow along the crucible bottom to be dominated by crucible rotation and along the crystal surface to be dominated by crystal rotation as indicated schematically in Figure 1-16. The interior flow is expected to be determined mostly by buoyancy.

1.3.4 Analytical considerations for heat and mass transfer in the melt

Using the result from Cochran flow for crystal rotation alone, the boundary-layer distance δ of the solute field is determined such that $C_\delta = C_L$, and it scales with $\frac{\mathcal{D}}{\nu}^{1/3} Re_s^{-1/2}$ (Burton et al., 1953b):

$$\delta = 1.6 \mathcal{D}^{1/3} \nu^{1/6} \omega_s^{-1/2}. \tag{1.28}$$

This result has been adopted as an approximate means for monitoring solute deposition via flow induced by crystal rotation rate, since, with the boundary-layer model, K_{eff} is related to δ by:

$$K_{eff} = \frac{K_{eq}}{K_{eq} + (1 - K_{eq}) \exp(-V_p \delta D)}. \tag{1.29}$$

The ideal situation would be to maintain conditions such that $K_{eff} \rightarrow 1$, which according to the Cochran flow model can be achieved by adjusting the crystal rotation rate to control δ.

The solute boundary-layers for oxygen adjacent to the crucible wall and melt surface can be estimated by assuming that the solute boundary layers scale with the velocity

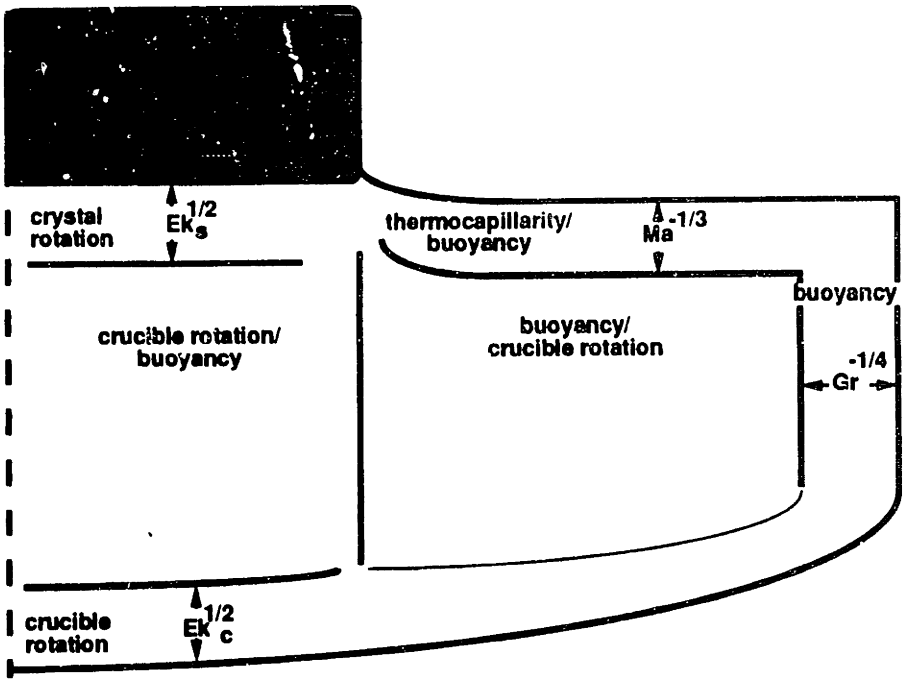

Figure 1-16: Schematic of boundary-layer structure, showing boundary-layer scalings and dominant flow mechanisms in the different regions of the melt.

boundary-layers, by a proportionality constant Δ:

$$\delta_s = \delta_v \Delta, \Delta < 1.0. \tag{1.30}$$

For molten semiconductors the Schmidt number is greater than one, meaning that diffusion resistance dominates viscous resistance, so it is reasonable to assume that these boundary-layers for scale with $\Delta = Sc^{-1/3}$ (Bird et al., 1956). Since the $Sc > 1.0$ and $Re >> 1.0$ for these systems, it is a good assumption to consider the solute to be well-mixed outside of the boundary-layers.

Consideration of heat transfer is more involved since CZ experiences the offsetting conditions where flows are vigorous $Re >> 1.0$, while conductive heat transfer is relatively fast compared to viscous time scales $Pr << 1.0$. Thus, it is important to determine the conditions under which the Péclét number $Pe = RePr$ assumes limiting values. The convection of heat due to buoyancy is negligible in the interior of the melt when the ratio $\frac{[F]}{[E]} << 1$, which is given by the following expression for the case where buoyancy dominates in the interior:

$$\left[\frac{convection}{conduction}\right]_{interior} \sim 0.5\epsilon^{1/2} Pra^{-1} Gr^{1/2} \approx 75. \tag{1.31}$$

On the other hand the convection of heat due to rotational effects in the interior is negligible if the following expression is less than one:

$$\left[\frac{convection}{conduction}\right]_{interior} \sim 1.5a^{-1}sPrEk_s^{-1/2}(1-0.83\eta) \approx 0.3\,. \qquad (1.32)$$

Conduction dominates in the boundary-layers when $Pr << 1$, which is true for silicon, so it may be noted that when convection is highly prevalent in the interior, the melt may be considered isothermal except for the boundary-layers, and further, that the thermal boundary layers coincide with the momentum boundary-layers due to the low Prandtl number.

1.3.5 Analytical approaches to dislocation modelling

Here two approaches to the analytical prediction of dislocation density in the growth of semiconductors are considered. The first of these is the notion that dislocations are produced by crystallographic glide, induced by excessive thermal stresses during growth. The dislocation density corresponding to one of the twelve $111, < 1\bar{1}0 >$ slip systems is proportional to the amount of slip, dictated by the resolved shear strain component (Jordan et al., 1986). This assumption dictates that only thermoelastic stresses need to be calculated in order to predict the pattern of the ultimate dislocation density. Their analysis first calculated the temperature distribution in an idealized cylindrical crystal with the Bessel function solution described in Section 1.3.2. With this temperature distribution, the components of linear thermoelastic stress can be determined analytically in terms of Bessel function expressions, using the assumption of plane strain, which implies no displacements in the z direction (Boley and Weiner, 1960):

$$\sigma_r = 2h_1 e^{p_1\psi/2}\frac{aE}{1-\nu}(T_f - T_a)\sum_{n=1}^{\infty}\frac{h_p\sinh\beta_n(\psi_t-\psi)+\beta_n\cosh\beta_n(\psi_t-\psi)}{(h_1^2+\alpha_n^2)J_0(\alpha_n)(h_p\sinh\beta_n\psi_t+\beta_n\sinh\beta_n\psi_t)}\left[\frac{J_1(\alpha_n)}{\alpha_n}-\frac{J_1(\alpha_n\rho)}{\alpha_n\rho}\right], \qquad (1.33)$$

where ψ_t is the ratio of the length of the crystal to its radius at time t and ψ is the dimensionless axial coordinate, while ρ is the radial coordinate. Analogous expressions hold for the θ, z components of the stress tensor. The components of the stress tensor can be resolved using trigonometric relations into their components resolved onto the $111, < 1\bar{1}0 >$ system. With the assumption that stresses are mostly elastic and are not completely relieved by plastic flow, the relation $d \sim \sum_{i=1}^{12}\sigma_{111,<1\bar{1}0>}$ is realized. Agree-

ment with this analysis for $GaAs$ crystals was very good, providing a foundation for the widespread popularity of this approach. However, the computed stresses using this approach are regularly in excess of the CRSS significantly, and it is doubtful that the assumptions of this approach are valid if the stresses are greater than the CRSS by a factor of two or more (Maroudas and Brown, 1991a).

The alternative approach is the Haasen model for plastic deformation dynamics (Alexander and Haasen, 1968), which is based on the notion of almost complete plastic relief of stress by dislocation formation and multiplication. The total stress is assumed equal to a fictitious elastic stress minus a plastic relief, related to the plastic component of strain. The rate of plastic strain is related to the dislocation density by the Orowan equation (Orowan, 1940). Following the notation of Maroudas and Brown, 1991a the rate of change of plastic strain is measured by ϵ^p, the square root of the second invariant of $\mathbf{e}^p$ (i.e. $\sqrt{\mathbf{e}^p : \mathbf{e}^p}$), to the number density of dislocations:

$$\frac{D\epsilon^p}{Dt} = \phi b u N(\mathbf{x}). \tag{1.34}$$

This correlation involves the dislocation velocity u, which in turn must be related to the physical state of the material and the material properties. Assuming that the dislocation velocity u can be modelled by a thermally activated mechanism and further is proportional to the effective stress τ_{eff} yields:

$$u = B_0 \tau_{eff}^m \exp(-Q/kT). \tag{1.35}$$

The effective stress τ_{eff} in turn can be considered proportional to the square root of the number density of dislocations, which exert a back stress due to dislocation-dislocation interactions:

$$\tau_{eff} = \begin{cases} \tau - A\sqrt{N}, \tau > a\sqrt{N} \\ 0, \tau \leq a\sqrt{N} \end{cases}. \tag{1.36}$$

Having related the plastic strain to the dislocation density, the population dynamics of dislocations must also be modelled. Assuming that dislocations are generated by the motion of other dislocation yields the following rate law

$$\frac{DN}{Dt} = \beta u N, \tag{1.37}$$

where the rate constant β is proportional to the effective stress. These equations are combined to form a complete model. Asymptotic scaling in the limit of negligible

back stress, $\delta = \sqrt{A^2 K/Gb} << 1$, and large dislocation Damköhler number $D = \frac{KB_0R}{V_p}\sigma_0^{m+1}\exp(-\frac{Q}{kT})$, which measures the relative magnitude of dislocation velocity to the growth rate of the crystal, yields the solution

$$y(\zeta) = \frac{y_0 e^{D\zeta}}{1 + 2y_0(e^{D\zeta} - 1)} \tag{1.38}$$

where the ultimate dislocation density is given by

$$N_\infty = K\sigma_0^2/2Gb. \tag{1.39}$$

The Haasen model in the limit $N_0 = 0$ will yield a uniform zero dislocation density, irrespective of the stress field or thermal conditions. This possibility is somewhat more insightful than the CRSS-based approach which provides only the slip mechanism for dislocation propagation since the value of N_0 can be taken as zero or nonzero depending on other factors; however, for the growth of $GaAs$ for example, the CRSS-based approach appears to match the data well, since single-crystal material is never grown. Thus, the Haasen model leaves open the possibility of correlating the interface or initial dislocation density N_0 to micromechanical phenomena, such as the nucleation of dislocation loops from microdefects.

The analytical models in general provide a convenient framework for expediently relating process parameters given a fixed operating state. Changes in control trajectory or design can be overcome by empirically fitting constants or adding new terms or in practice by feedback control. However analytical approaches are also limited in that they assume dominant behavior and neglect important couplings such as radiation and free boundaries. It is the purpose of this thesis to develop with a general model that will be able to span many modes of behavior with the accuracy of capturing important couplings which defy a closed form; therefore the present work requires an exact treatment of the modelled physics which is only possible with a numerical model.

1.3.6 Numerical modelling

There have been many numerical models proposed to solve the transport equations in CZ silicon growth. The motivation for these efforts is similar in spirit: to eliminate simplifying assumptions and thus improve the accuracy of the prediction. Categorizing these is quite difficult because so many of the studies have overlapping work; each effort has a primary objective and includes a number of indirect couplings so that, for example,

every study on solute segregation considers fluid flow, but only some of these consider radiative boundary conditions and only some others consider free boundaries. So the next section will review the important works in the field and attempt to emphasize the major contributions of each.

Numerical simulation of the CZ process will be categorized into three areas: thermal analyses to address the likelihood of dislocation generation using the temperature distribution in the crystal and to calculate the melt-solid interface shape, flow analyses to address the transport of impurities through the melt phase, and analyses of the combined heat transfer and fluid flow to determine the interdependence. Initial calculations of heat transfer in the silicon boule used a boundary condition whereby radiation occurred to a uniform-temperature ambient (Akiyama and Yamaguchi, 1968). They also employed a complex relationship of the thermal conductivity with temperature, including both lattice and electronic effects. With such realistic boundary conditions and nonconstant conductivity, the Bessel function solution does not apply. It is very important to include these nonlinear effects because heat flow and especially the radial heat flow due to radiation from the crystal periphery are important in determining the temperature gradients and thermal stresses.

The calculation of macroscopic solid-liquid interface shape is a necessity for accurate determination of the thermal stress in the neighborhood of the melt-solid interface and was first addressed computationally in the framework af a heat transfer calculation for the crystal phase only (Wilcox and Duty, 1966). The analysis assumes a linearized radiative heat transfer loss from the crystal and a boundary condition on the melt-solid interface that included both heat transfer from a constant-temperature melt and latent heat release; the results differ only slightly from the analytical expression in Equation (1.9), which locates the melt-solid interface at the melting point isotherm in a cylindrical fin with uniform heat input at one end. It was found that the Biot number for heat transfer from the crystal was the primary determinant of the melt-solid interface shape which indicates that the shape is highly sensitive to the exact details of the radiative environment which are approximated by the heat transfer coefficient. The approximation of constant heat flux from the melt is itself a crude approximation which neglects convective heat flux.

Crowley was the first to address the problem of determining the free interface shapes by coupling the calculation of heat transfer in the crystal to the heat transfer through the melt phase (Crowley, 1983). Her approach cast the heat transfer in the region of the melt-solid interface as a moving-boundary problem, solving for the first time in

the CZ geometry the position of the meniscus, melt-solid interface and heat transfer via conduction in the melt and solid phases simultaneously. The incorporation of the melt-gas meniscus into the calculation requires solution of the Laplace-Young equation of capillary statics. This was accomplished with an approximate solution using least-squares fitted parameters from exact solutions of the Laplace-Young equation (Hurle (1986)). With a prescribed-temperature boundary condition at a vertical level in the melt corresponding to the base of the meniscus Crowley was able to predict the dynamic response of the thermal field and crystal shape to step changes in heat input. However, the temperature prescription by an exponential of r^2 is at best a guess at the correct thermal profile and pays no attention to the details of the geometry of the system or the convective nature of the melt.

From the level of modelling which relates heat input to the crystal shape, quantitative connections can be drawn between independently adjustable parameters. The couplings become progressively more accurate as features are added to remove approximations. The first step in a series of models of increasing detail leading up to the present work (Derby et al., 1985) was a quasi-steady-state thermal-capillary model (QSSM) calculation that produced heater temperature trajectories for growth which represented the first use of a large-scale model for the development of a system-oriented processing strategy. The notion of a thermal-capillary model (TCM) refers to a model which calculates both the thermal field and interface shapes (and should not be confused with *thermocapillary* convection). The modelling approach was a steady-state generalization of Crowley's thinking which replaced the analytical approximation of the melt-solid interface with an exact numerical solution of the Laplace-Young equation, and was extended to include the principal components in the interior of the CZ apparatus, that is, the crystal, the melt, the crucible, the susceptor and the heater. The heat transfer was assumed to occur solely by conduction through the components, except for a small convective component in the crystal, and by radiation and convection through the intercomponent gaps. The heater was assumed to be at constant temperature. All surfaces exchanged heat via radiation and conduction with a constant temperature ambient, except the crucible sidewall, which exchanged heat with the constant temperature heater. This model is analogous to a situation where a cooling pipe surrounds all components except for the crucible sidewall. The strength of the approach was demonstrated by the ability to test the effects of arbitrary changes, such as heater power, ambient temperature, etc., to the thermal field, interface shape and crystal radius with a sequence of calculations at decreasing melt volumes. It was found that certain combinations of parameters produced flatter interfaces and lower

temperature gradients and others indicated deleterious possibilities by predicting melt undercooling and nonexistence of the steady-state solution (see Figure 1-17). However, the assertion of Derby that the model is accurate enough to direct design modifications but not accurate enough for on-line control of diameter and melt-solid interface shape requires clarification: radius can be measured on-line and controlled through feedback while model-based *feed-forward* control can be used to both improve the response of the ADC and provide some control over melt-solid interface shape, depending on the model's accuracy. For design the accuracy requirement is more stringent since feasibility of the design is absolutely essential.

The correct boundary condition to be applied to all exposed surfaces in a modelled CZ apparatus is one of radiative heat flux where radiation may be exchanged directly or via reflections between any two surfaces in the chamber. Whereas earlier models featured radiation to a uniform-temperature ambient, detailed radiative heat transfer analysis has been incorporated into many recent models, the first one of which was limited to a finite element grid imposed on the crystal (Williams and Reusser, 1983). Their approach was partly experimental as they used infrared thermal imaging to measure the surface temperatures of a boule growing in a Siltec puller, and then used the measurements as fixed boundary conditions for their conduction model. With a complex iterative procedure they were able to predict convex melt-solid interfaces[7].

The Gebhart method was employed by Ramachandran, 1985 to show that radiative heat transport between exposed surfaces was an important factor at the elevated temperatures of CZ silicon growth. This method will be discussed in Chapter 2 in detail. Their analysis was limited to heat transfer in the crystal and they calculated concave interface shapes using the best estimate of applicable thermophysical property data, achieving reasonable agreement with the measurements of Williams and Reusser. They also demonstrated that the amount of heat flux from the melt through the melt-solid interface makes the interface more convex as it is increased. That model was extended to include a melt phase and in an attempt to perform design calculations also included correlations about the forced convection from the gas phase on the cooling crystal to investigate influencing interface shape through jet cooling by Srivastava et al., 1986. It showed a tendency to more concave interface shape at higher cooling rates, with heat input held constant. This may seem counterintuitive but occurred since heat input was constant and the pull rate was necessarily increased. Their effort was prophetic for large-

[7]In this thesis the terms convex and concave will be referenced to the crystal. Hence, an crystal that is shaped like a converging lens is termed convex, and like a diverging lens, concave.

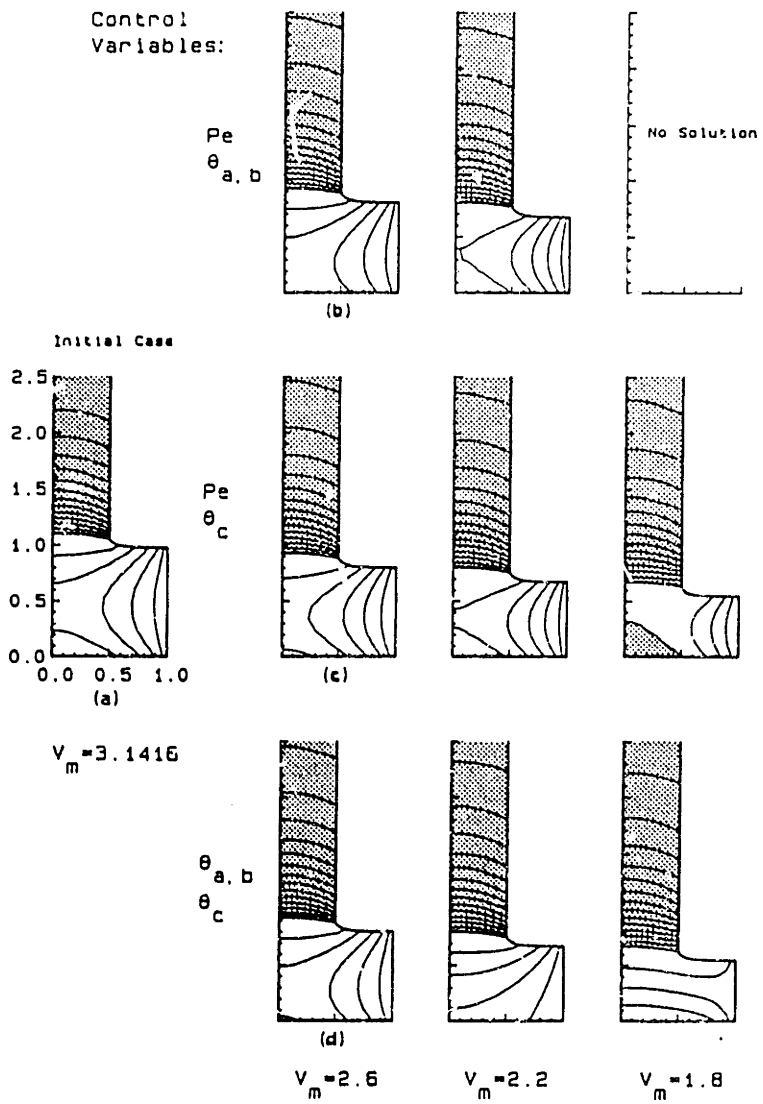

Figure 1-17: Solutions from the QSSM of Derby et al., 1987b. Beginning with an initial simulation shown in (a), simulations at decreasing melt level show the evolution of the thermal field during growth with constant heater temperature, crystal radius and interface deflection, using (b) pull rate and bottom ambient temperature as control variables, (c) pull rate and crystal ambient temperature as control variables, and (d) bottom and crystal ambient temperatures as control variables.

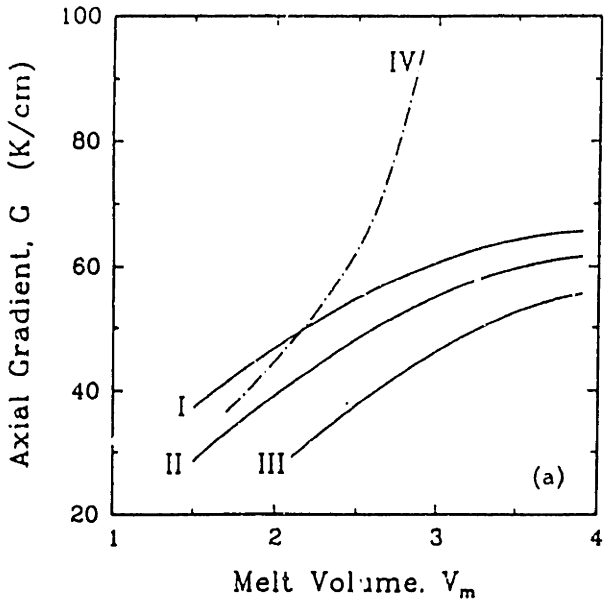

Figure 1-18: Comparison between radiative heat transfer calculations from Atherton et al., 1987. Curves labelled I–III denote calculations with interacting radiative heat transfer between surfaces while curve IV denotes a calculation with radiation to uniform fixed ambient temperatures.

scale modelling of CZ, illustrating the ability to control more than one parameter using more than one manipulated variable, such as cooling rate and pull rate. Diffuse-gray radiation was also included in the MIT CZ simulator (Atherton et al., 1987). The differences between the fully radiative simulation and idealized case are evidenced by direct heat transmission between the crucible wall and the crystal at low melt volumes as shown in Figure 1-18. Atherton et al., 1987 also showed the effects of changing the so-called "ambient temperature" input parameter and the level of insulating or cooling effect on the crucible bottom to the model solution. These changes could be effected by design modifications such as changing the cooling to the chamber wall or increasing the pedestal thickness in order to achieve controlled thermal gradients or melt-solid interface shapes.

With small CZ melts or very mild temperature gradients the heat transfer in the melt may be conduction-dominated. Dynamic models can study the long-term dynamics associated with the dropping melt level or the shorter-term dynamics associated with the fluctuating fluid motion. For conduction-dominated models the longer-term dynamics is the object of study. The original QSSM was recast by Derby and Brown, 1987a into

a dynamic conduction-dominated thermal-capillary model, in order to incorporate the batch-time dynamics of the system with a more detailed depiction of the apparatus than Crowley afforded. They were able to demonstrate perfect control of crystal diameter with an idealized PI controller, operating with perfect measurement and no time delays. In addition, they demonstrated the need to change the effective growth rate in the QSSM, in order to account for the dropping melt level. With this change, the QSSM performed very well in predicting the same states during the growth run predicted by the transient model. Eventually a fully time-dependent and radiatively-coupled finite element code was employed to investigate the use of various PID control settings on the quality of diameter control (Derby et al., 1987). Since diameter control is a solved problem industrially, such time-dependent conduction-dominated simulations are probably most useful for analysis of the seeding process, where the growth velocity is important to the thermal profile in the crystal. A similar model was used by Thomas, 1988 to perform dynamic calculations of both silicon growth and the LEC growth of GaAs. It achieved reasonable agreement between predicted and actual diameters. The model was extended to predict the dislocation density from these thermal profiles (Thomas, 1988).

The ultimate utility of thermal analysis without melt convection is to relate controllable parameters to the dislocation density. Thermoelastic stress calculations have been used extensively to indicate where dislocations are most likely to form. The calculated stresses are likely to result in dislocations where they exceed the resolved shear stress. Thermoelastic stresses computed using a finite element model showed that the largest stresses in the CZ system occur near the melt-solid interface and that elastic anisotropy, whereby three constants are used to characterize the stress-strain relation for a material, can play a major effect on the stress field (Lambropoulos, 1987). Thomas coupled results from his dynamic calculations of growing silicon crystals with thermoelastic stress calculations to show how heater design can be used to lower the stress patterns in the growing crystal, potentially reducing dislocation density (Thomas, 1988). This type of parameter investigation has motivated exhaustive attempts at optimal design, especially for the LEC growth of *GaAs*, where the model reproduces data with more accuracy than in silicon. The accepted alternative model for plastic deformation is the Haasen model. Thomas employed both the thermoelastic stress calculation and the asymptotic limit (Equation (1.39)) of the Haasen model for a quantitative prediction of the likelihood of defect formation. His thermoelastic stress computation exceeded the nominal CRSS by a factor of four and the maximum value of dislocation density was 2×10^4 for silicon. He demonstrated that lowering both axial and radial thermal gradient in

LEC $GaAs$ growth was clearly beneficial in reducing defect density. By adjusting operating parameters he was able to reduce the predicted dislocation density by almost an order-of-magnitude, with the maximum defect densities occurring near the melt-solid interface. One of the difficulties of generalizing Thomas' results is uncertainty in the thermal modelling, since it could be that the temperature field is inaccurately predicted compared to an operating CZ puller. The arbitrary choice of ambient temperature could have been fortuitous in producing agreement with the experimental crystal shape. Also, his numerical solutions are subject to the same initialization condition as mentioned by Maroudas and Brown, 1991a, i.e. zero dislocation density is identically predicted for a zero initial dislocation density, and he provides no insight as to when the single crystal state occurs.

The analysis of melt flow by computational modelling permits the study of nonlinear phenomena not limited to asymptotic expressions. In addition, it permits the evaluation of melt-solid interface shapes and realistic thermal boundary conditions for the system. The transport of dopants and oxygen is highly dependent on flow and since the behavior of microdefects is highly dependent in impurities, the appearance of dislocations is also potentially linked to flow. Flow analysis, therefore, may hold crucial results for CZ silicon growth.

Initial numerical analyses extended the scope of earlier models to include both steady-state heat transfer and steady, laminar fluid flow arising from rotation and buoyancy, for a melt of $Pr \simeq 0.3$, which was supposed to be germanium (Kobayashi and Arizumi, 1970; Kobayashi and Arizumi, 1975). Forced and buoyant flow were computed with the Navier-Stokes equations as part of the determination of melt-solid interface shape. They showed that increasing the rotation rate of the $1\,cm$ crystal from 0 to $40\,rpm$ increased the concave interface shape from $-0.35\,mm$ to $-0.75\,mm$ deflection, while increasing crucible rotation rate caused concavity to decrease. Their ability to draw quantitative conclusions regarding the effect of rotation rates on the melt-solid interface shape even for such a small system demonstrated the need of accounting for melt phase convection in order to accurately determine this shape. Later they abandoned the integrated model, eliminating the free boundary and heat transfer calculation in the crystal, in order to concentrate specifically on aspects of the melt flow. Their computations of the details of rotationally driven flows achieved good agreement with observed flow patterns (Carruthers and Nassau, 1968). However the calculation was done still with $\nu \approx 10\nu_{Si}$.

Another group opted to cover both steady-state and dynamic simulations of fluid flow in the CZ system (Crochet et al., 1983). Their steady-state simulations for Ge as

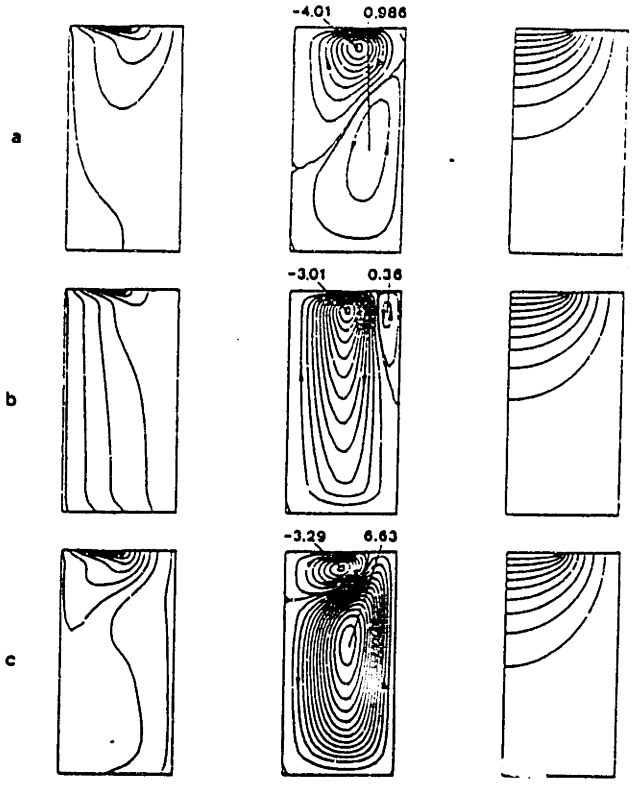

Figure 1-19: Results of Crochet et al., 1983, for flow with crystal rotation, crucible rotation and natural convection combined. Figures a, b and c show the solution with fixed $Gr = 2 \times 10^4$ and $Re_s = 500$ at three different crucible rotation rates, (a) $Re_c = 10$, (b) $Re_c = 100$ and (c) $Re_c = -100$.

the model fluid, $Pr = 0.015$ included buoyancy and rotation in their isolated and combined motions. The predictions involving only rotation rate agreed with Kobayashi and Arizumi's latter publication. When forced rotation was combined with natural convection it was found that crystal rotation could be increased to dominate buoyancy. However, at a fixed crystal rotation rate, the effect of changing the crucible rotation rate was profound. With corotation, the crystal rotation cell was predominant through a large portion of the melt, almost eliminating the buoyancy driven cell. However, this could be due to the low buoyancy effect since the Grashof number was only $\sim 10^6$. When counter-rotation was attempted the flow regime changed drastically so that the buoyancy-driven cell was greatly reinforced and the crystal rotation cell was compressed to a small zone underneath the crystal (see Figure 1-19).

The hydrodynamic thermal-capillary model of Sackinger, 1989 was unique in its time in that it coupled solution of the melt flow with heat transfer in the other system components and with the interface shape calculation. Steady-state heat transfer in the crystal

and crucible, the meniscus shape, fluid flow and the solid-liquid interface location are determined simultaneously, enabling an exhaustive study of the flow mechanisms and their relationship to the heat transfer and melt-solid interface shape. His calculations were performed by solving for the heater temperature required to sustain a given crystal radius. He definitively established the form of steady buoyant convection, illustrated the formation of thermal boundary-layers in spite of the low Pr and predicted the change of melt-solid interface shape from concave to convex with increasing buoyant convection. He showed the transition to a multi-celled buoyant convection regime at low melt volumes and demonstrated the application of a vertical magnetic field to arrest flows.

The predictions were found to obey asymptotic scaling rules derived for boundary-layer flows under high magnetic field strengths by Hjellming and Walker, 1987a. A strong dependence on radiative properties of the melt surface was demonstrated by the effect of changing emissivity from $\epsilon_m = 0.30$ to $\epsilon_m = 0.05$, which caused a $40K$ difference in heater temperature and an increase in interface deflection due to increased natural convection. Sackinger, 1989 determined that the boundary-layer flow from crystal rotation compares well to the Cochran analysis for radii less than $0.75R_s$, and that crucible rotation produces effects expected due to the work of Carruthers, Kobayashi, etc. His calculations of thermocapillary convection and were found to produce effects at least equal in magnitude to those of buoyant convection. A comparison with the scalings of Zebib et al., 1978 was provided but erroneously scaled the tangential velocity with $Ma^{2/3}$, which should be $Ma^{-2/3}$, and so incorrectly made the comparison. In an attempt to achieve a realistic simulation with all effects combined, Sackinger used a magnetic field of $500Gauss$ and avoided crucible rotation entirely. The motivation for including the magnetic field and neglecting the crucible rotation is not explicitly stated. In his range of parameter space, it was noticed that changes in the crystal rotation rate increased concavity of the melt-solid interface, as it did when only crystal rotation rate was applied. With a $2000Gauss$ magnetic field, crystal rotation of $20rpm$ and buoyancy and thermocapillarity at their appropriate literature values he found that the tangential, normal and azimuthal velocity components local to the melt-solid interface had self-similar profiles up to $\sim 75\%$ of the crystal radius.

The major strength of Sackinger's effort was its thoroughness in examining individual effects. Its weaknesses were a failure to address realistic operation, either by comparison with experiment or at least adequately accounting for the combined flow mechanisms, and a failure to relate the results to issues of interest for CZ, i.e. solute segregation or dislocation density. Parallel but independent from the work of Sackinger is the work of

Tsukada et al., 1988, who devised a simulation similar both in spirit and method to that of Sackinger. The major differences are the inclusion of Gebhart's method for radiation and that crystal radius was solved for as an unknown, rather than solving for heater power to compute the desired crystal radius. They also did not combine the flow mechanisms in a single simulation, since no results with combined mechanisms have been presented by this group, even though they employed a low value of the thermal expansion coefficient $\beta \approx 10^{-5} K^{-1}$.

Fluid flow in CZ is time-dependent, and so there is considerable incentive to model unsteady flow. Langlois has generated a large body of work based on a finite-difference code (Langlois, 1977) dedicated to evaluating the bulk flow in CZ geometry with sufficient resolution to handle realistic physical parameters for silicon. His first study is restricted to the melt phase so that the rest of the system heat transfer is ignored for practicality: the high resolution required and time integration preclude further complication of the model. His earliest results concentrated on the effects of crucible and crystal rotation, and limited natural convection to a thermal expansion coefficient of $\beta = 10^{-5} K^{-1}$, for which the thermal field is only just becoming affected by natural convection, with $Pe \sim O(1)$. Later simulations (Langlois and Lee, 1983) show fine details of the transient $2D$ flow not predicted–at least to the knowledge of the author–by any other group. In their figure (see Figure 1-20) of the meridional flow streamlines there are no less than five rotational cells arranged horizontally through the melt, each one stretching almost from the bottom of the melt to the top– definitely not the boundary-layer structure with the inviscid core predicted by Sackinger for purely buoyant flows. No indication is given in their article if the solution is at a steady state. The calculation was performed for a crucible of $7\,cm$ radius and crystal $3.5\,cm$ radius, with crucible rotation of $15\,rpm$ and crystal rotation of $22\,rpm$, with $\beta = 10^{-5} \rightarrow 10^{-4} K^{-1}$. Although they do not show thermal or solutal fields in this simulation, it is likely that there is a high degree of convective flux in the interior with no coherent boundary-layer structure, due to the multiple cellular structure of the flow.

Later, species transport equations were included in addition to the magnetic field by Kim and Langlois, 1989; their nonmagnetic results again showed a complex multicellular pattern, which did not achieve steady-state. The basic characteristics of this flow were the vertically oriented cell adjacent to the crucible wall, a transition layer of ill-defined layers in the interior and a strong circulation underneath the periphery of the crystal, with poorly defined circulation underneath the center of the crystal. This effort included simulation of boron dopant transport through the melt. Kim and Langlois, 1989 reported

no evidence of a solute boundary-layer; the dopant was being swept away due to strong radial circulation in the negative-r direction due to a combination of natural convection and crucible rotation. In further efforts (Kim and Langlois, 1989) to explain the experimental results for the segregation of gallium in silicon, they simulated a larger crucible of $15.24\,cm$ radius, and obtained a meridional circulation with approximately *twelve* cells. The flow was not steady although this may have been due to the contribution of buoyant convection due to solutal gradients. Again, no solutal boundary-layer was observed, and the solute was well-mixed i.e. $C \approx k_0 C_\infty$ was borne out by the experimental result as well as the calculation. Kim and Langlois, 1990 produced studies of oxygen segregation, with the larger crucible without an applied magnetic field; the flow was not steady, but yielded much less confusing circulations, where individual effects are easily discernable. In fact, the solution oscillated "slowly" (no period of oscillation was reported) around a main solution, which had approximately five vertical cells for a crystal rotation rate of $30\,rpm$, and six with a rate of $15\,rpm$ or $10\,rpm$, the main difference being that at $30\,rpm$ the solution had a predominant cell similar to a Taylor-Proudman circulation. Although the analyses of Kim and Langlois, 1990 neglect curved interfaces and detailed heat transfer for the entire system, the results are the most detailed analyses for axisymmetric time-dependent flow and solute segregation. They have shown that CZ flows are definitely time-dependent and likely defy simple boundary-layer models.

The actual flows in CZ are also three-dimensional, and there exist models which attempt to capture this behavior. The most detailed depictions of the melt flow are fully three-dimensional simulations of Mihelčić, 1985, which neglect details external to the melt. As a precursor to their three-dimensional model, a time-dependent marker-and-cell (MAC) technique was used to simulate both liquid copper and silicon in constant crucible rotation, as well as the Czochralski accelerated crucible rotation technique (CACRT) (Mihelčić et al., 1982). This technique, whereby the rotation of crystal and/or crucible is modulated between two values with a fixed period, is intended to enhance mixing in the melt by breaking up nonmixing flow patterns. Mihelčić et al., 1982 found the axisymmetric formulation to be steady for combinations of rotation rates without free convection. They found that natural convection was dominated by crucible rotation, but that it was comparable in strength to crystal rotation. With natural convection and both rotations the flow pattern was almost steady, with several vortices appearing, dominated by circulations similar to Taylor-Proudman cells. They observed, for combined free and forced convection from the crucible, the periodic breakup and reformation fo the Taylor-Proudman column with a period of about $3.4s$. Without crucible rotation,

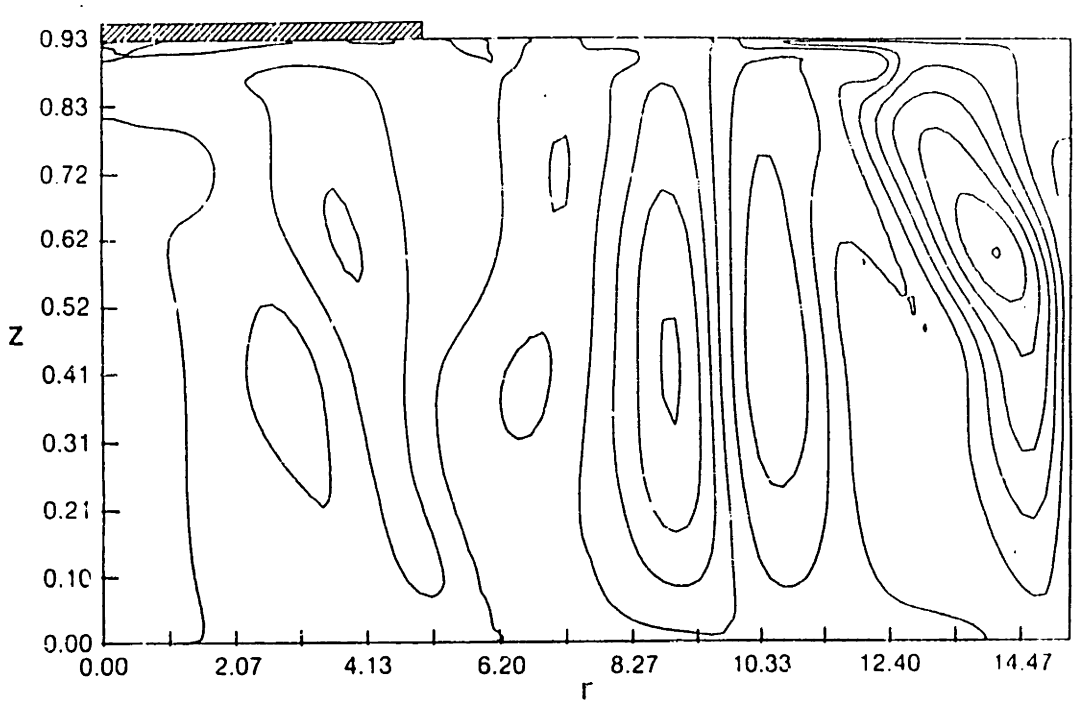

Figure 1-20: Multicellular flow streamlines of nonmagnetic CZ flows from Langlois and Lee, 1983.

only small oscillations outside of the Taylor-Proudman column appeared. They recommend isorotational arrangement to enhance total stirring of the melt, and the CACRT for periodic breakup of the nonmixing Taylor-Proudman cells. Their value of the thermal expansion coefficient for silicon was only $\beta = 10^{-5}K^{-1}$. In later work they produced a fully three-dimensional situation (Mihelčić and Wingerath, 1987), and to force the system into $3D$ they impose an asymmetric thermal boundary with maximum $\Delta T = 4K$ along the crucible wall, which is actually a conservative number. The flow with only buoyancy ($\beta = 10^{-5}K^{-1}$) and crystal rotation gave asymmetric flows, which were first corrected with an axial magnetic field and then promoted by a stationary transverse field. The meridional flows in the nonmagnetic case are highly irregular for an axisymmetric heating situation.

The MAC program of the Jülich group was adapted to use boundary-fitted coordinates to solve the problem of interface shape (Kopetsch, 1988). The MAC technique has been adapted by Sawada et al., 1990 into a "new simplified marker-and-cell" technique (NSMAC) to compute flows which are transient, highly asymmetric with $\beta = 10^{-5}K^{-1}$ which agreed well with temperature measurements.

Kakimoto et al., 1989

used a commercial code "FLUENT", based on the finite volume method, to simulate

steady-state three-dimensional flow in the crucible. The imposed thermal boundary condition was based on measurements made in their puller and had temperature differences of $160K$ and $16K$ at diametrically opposed positions. Both scenarios with only natural convection showed unidirectional flow, which agreed qualitatively with the observations. Extension to time-dependent or rotating flows was not feasible, since the simulations took an average of $10\,hours$ on the NEC SX-II supercomputer.

Time-dependent three-dimensional flows have been computed by Chan et al., 1987 using the linearized block implicit (LBI) method with a finite-difference discretization. Unfortunately they only reported results up to $Gr = 6 \times 10^6$, which achieved steady state. They were able to show miniscule asymmetric effects due to a continuous liquid feed (CLF) design modification. Their lack of further illustrations of realistic conditions seems to stem from a difficulty of obtaining solutions at more demanding convection levels due to problems in obtaining convergence or the requirements of increased computer time.

Researchers at Sumitomo Metal Industries (Miyahara et al., 1990) have recently developed an approach which accounts for detailed radiative heat transfer interactions throughout the interior of the CZ apparatus; see Figure 1-21a. This approach had been shown to yield important detail in the thermal field by Dupret et al., 1990. To accurately model a crystal puller necessitates the use of such detail when modelling radiative exchange. The thermal profile in the crystal both during growth and after withdrawal from the melt was computed to study different annealing schedules for the crystal.

The Sumitomo group has circumvented the prediction of time-dependence with a description of statistically steady turbulence in the melt through the use of a $K - \epsilon$ model (Kobayashi et al., 1991). They demonstrated that convection was dominant for a crucible radius of $20\,cm$, but that conduction was dominant for $7.5\,cm$ radius. In a subsequent paper they demonstrated that the turbulence model, stripped of the global heat transfer, predicted quantitatively correctly the enhancement of heat transfer with *increasing* crucible rotation rate (see Figure 1.3.6) and qualitatively predicted the trend in temperature fluctuations with crucible rotation rate. These results are shown in Figure 1.3.6. He found that there was a $10 - 20°C$ decrease in melt temperature with crucible rotation increasing from $2 - 10\,rpm$, and that the increase in rotation increased the fluctuations in the temperature. Both predictions agreed with the experimental results and cannot be predicted with a $2D$ laminar flow code, since increasing the crucible rotation rate would impede meridional circulation through Coriolis force.

At the present time, the description of the flow in CZ is still very much in question. Models have yet to produce predictions which are unequivocally in agreement with ther-

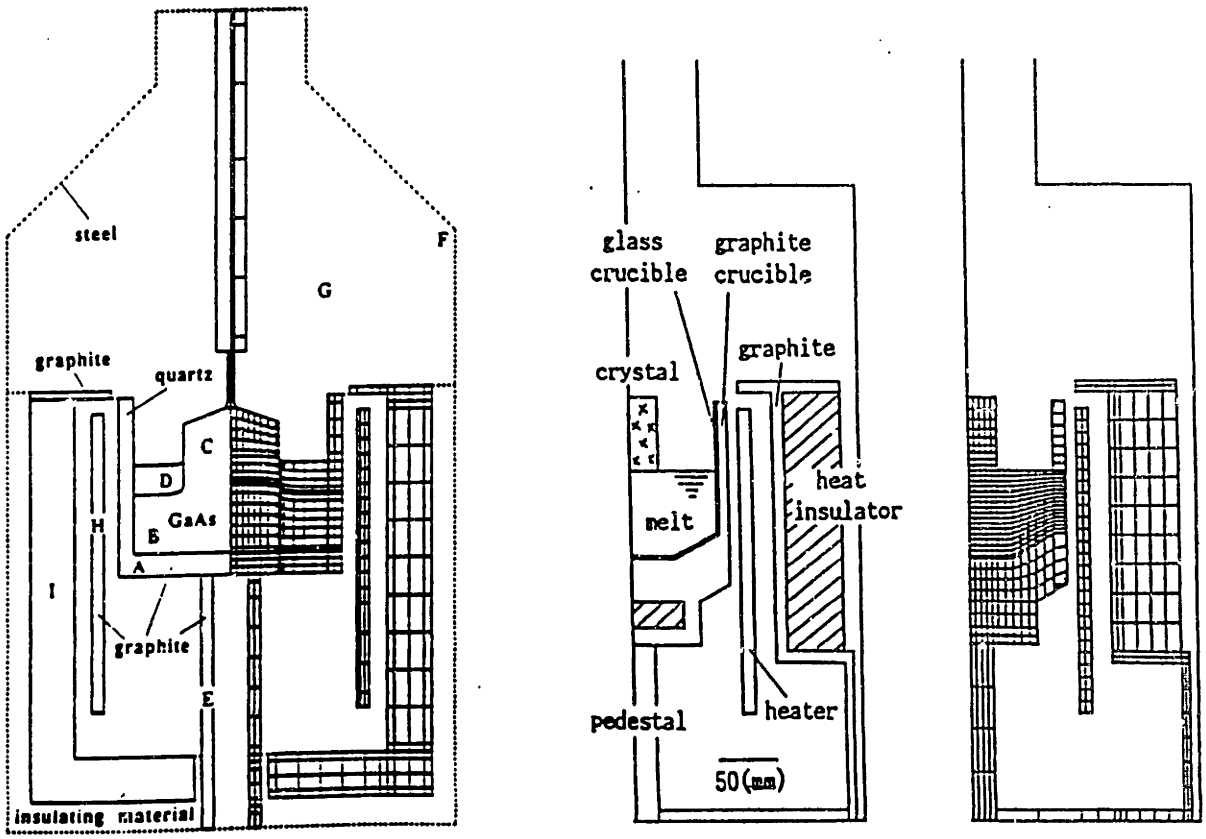

Figure 1-21: Depictions of detailed radiation in the CZ chamber (a) from Dupret et al., 1990 and (b) from Miyahara et al., 1990.

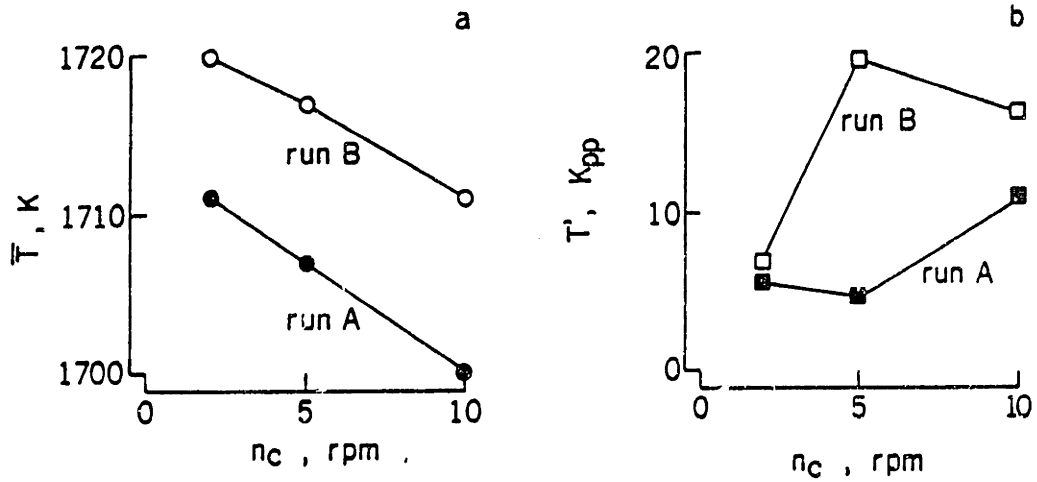

Figure 1-22: (a) Increased heat transfer with *increasing* crucible rotation rate, and (b) increased temperature fluctuations with increasing crucible rotation rate, from Kobayashi et al., 1991.

mal or concentration measurements. Flow visualization, although still in its infancy for fluids like silicon, is indicating that most of the models in use for predicting flows in silicon, are probably lacking in accounting for the essential features of nonaxisymmetry and time-dependence. In fact, proof of similar numerical methods' accuracy in determining unsteady flow in low Pr fluids at high Gr in very simple nonrotating geometries is still incomplete (Roux, 1990).

1.4 Physical Property Data

The previous sections have been concerned with the depiction of physical mechanisms in CZ. Any mathematical model's accuracy is limited by the accuracy of the physical property data, in addition to the simplifying assumptions which make it tractable. In the case of CZ silicon growth the situation is extreme, due to the paucity of available data owing to the high temperatures involved.

The physical properties necessary for input into the mathematical models for CZ growth suffer from uncertainty due to lack of thermophysical property data and variability in the properties from run to run. Since model results are only as accurate as the

thermophysical database accurate values must be used for quantitative information to be obtained. The conflict between physical detail and the accuracy of properties is an important consideration when developing a model. Building a more physically detailed simulation potentially offers more accurate results. However, including more detail also increases the number of physical constants required. Each new structural component included in the analysis requires at least thermal conductivity and radiative emissivity for the material. In the case of silicon, constants governing flow and solidification also are required. The inaccuracy of additional constants may nullify the potential gain of the increased model detail.

Thermal conductivity is an essential property. There are extensive tabulations of thermal conductivity for the materials of interest (Touloukian, 1970; Goldsmith et al., 1961) . The difficulty with using conductivity values from the literature is that the reported values were usually measured at much lower temperatures. Extrapolation of low temperature data is subject to inherent unquantifiable uncertainty whereas the temperatures of CZ silicon growth necessitate special measurement techniques for conductivity. Also, the measurements performed at high temperature are less certain than those at low temperature due to the effect of radiation of the sample to the surroundings of the container, usually a calorimeter. To thoroughly discuss conductivity is a formidable task. It is worthwhile to examine a handful of salient notions which illustrate the difficulty of choosing a particular constant set of properties to describe the system.

Heat conduction can be thought of to occur by the vibration and motion of electrons and atoms situated in a lattice; this picture is strictly true only for solids. The vibration and motion of free electrons is a most effective means of transporting thermal energy and thus materials with a higher free electron density usually conduct heat more readily. The carrier concentration in semiconductors depends on both the doping level and temperature since electrons can be thermally excited into conduction bands. Although the electron mobility suffers at higher temperatures, these temperatures usually far exceed the melting point. For electrical insulators the thermal conductivity is due to lattice vibration, and is usually expressed as varying with an inverse power of temperature, i.e. $k \sim (1/T^x), x \sim 1$. The thermal conductivity of metals is conventionally related to both the electrical conductivity and temperature, $k \sim \sigma T$ and generally decreases with temperature, approaching a constant at temperatures much greater than the Debye temperature, which is $625K$ for silicon (Ashcroft and Mermin, 1976).

The measurements of conductivity are typically performed under vacuum conditions in a silvered container, with the sample between two plates, one at a slightly higher

temperature and one at a lower temperature, but with a calorimeter attached so that the integrated heat flux is measured (Tye, 1969). Unfortunately it is inevitable that the container does exchange some radiation with the sample, unless it is at the same temperature. There is also the issue of internal radiative transmission of the material, i.e. radiation passing through the solid material. This is unavoidable, for example, in silicon or graphite fiber felt. In silicon there is partial transparency, which becomes more prevalent at lower temperatures, so energy can be transmitted by radiation internally. In the case of graphite, individual graphite fibers or nodules can radiate through the porous structure of the graphite. This is a partial explanation for the drastic variation in conductivities of graphite materials. The measured conductivities will account for this mode of transfer, as it is impossible to distinguish spectral dependence of the energy transfer.

The parameters for thermal radiation have a very strong effect on simulation results and also incorporate many complex physical phenomena. Again, a few details are sufficient to establish the connection between radiation and the properties used to model it. Optical properties can be considered also to be determined by electronic characteristics of a material. Both core and free electrons interact with electromagnetic radiation. The free electrons are associated with typical optical behavior of metals which is lacking in insulators. For example, insulators are transparent to infrared radiation whereas metals are in general opaque in this spectral range. This is due to absorption by free electrons, and therefore semiconductors tend to metallic behavior in the melt, at high temperatures or under doped conditions.

The most common method of radiative characterization in models is by the Gebhart method (Hottel and Sarofim, 1967). This assumes that all interactions takes place at the material surface and that a single parameter, the *emissivity* ϵ (related to the reflectivity by $\rho = 1 - \epsilon$) characterizes the surface behavior. This emissivity denotes the fraction of emitted radiation as compared to an ideal *black body* which emits the maximum amount of energy at each wavelength in the electromagnetic spectrum. The *emittance* of a material, used to relate the radiative flux to the temperature, varies, in general, with wavelength, orientation and temperature. To assume that the emissivity is the fraction of blackbody radiation, independent of wavelength, is not generally true, since emittance has a spectral dependence, and to assume that radiation is emitted diffusely, i.e. equal emittance in all directions over the hemisphere from a point on a plane, is also not generally true, since emittance has an orientational dependence. Metals in particular usually have large tangential emittance. The relation of emissivity to reflectivity is justified for most mate-

rials. although for those that transmit interally, i.e. silicon, quartz, graphite felt, it is not strictly valid, since radiation may pass through entirely or may be extinguished over some distance into the solid. The assumption of diffuse reflectivity also is flagrantly violated for *smooth* metals, i.e. the reflection occurs via Snell's law for specular surfaces including the silicon melt, solid and stainless steel. These effects are especially prevalent in CZ only in the immediate neighborhood of the melt surface. Away from this surface nonideal radiation behavior is offset by the size and geometrical symmetry of the apparatus.

The material properties of semiconductors, including viscosity, thermal expansion coefficient and thermocapillary coefficient, have been extensively reviewed, but not convincingly established. The research on thermophysical properties has been carried out mainly by Russian scientists. Recent measurements (Kakimoto et al., 1990c) on the viscosity of $GaAs$, for example, found values a factor of two lower than the accepted literature (Glazov et al., 1969), and similar discrepancies for silicon are likely. For the thermal conductivity of silicon melt, there is particularly little data due to the high melting point, corrosivity, convection, and electrical conductivity which make the experiment difficult. The thermal conductivity measurements, hampered traditionally by convection, promise to be improved with new hot wire measurement techniques (Nakamura et al., 1988), which, when applied in microgravity environments, yield accurate measurements. There is much evidence to support some of the values, for example, the thermal expansion coefficient appears to have been measured accurately, since it is a correlation with density and temperature, and the growth angle for silicon has been measured experimentally (Surek and Chalmers, 1975) for a variety of growth conditions and is thought to be constant. However, during an actual experiment these values may change due to contamination. The thermocapillary coefficient (and obviously then the surface tension and growth angle), for example, is known to decrease dramatically with contamination (Lamprecht et al., 1983). In summary, a survey of the relevant physical properties to modelling silicon growth is presented here, showing the range of literature values for the most uncertain physical properties.

The densities of the various substances (Touloukian, 1970) have been taken as constant values, considering that thermal expansion effects have a negligible effect on density. The density of molten silicon has been taken to be a constant $2.51\,g \cdot cm^{-3}$ which was measured at $40°C$ above the melting point. The range of values for this appear to be up to $\pm 0.1\,g \cdot cm^{-3}$. The density of solid silicon is considered to be $2.33\,g \cdot cm^{-3}$, with an expected uncertainty of $\pm 0.01\,g \cdot cm^{-3}$. The heat capacities of melt and solid silicon have been taken to be $1.04J \cdot g^{-1}K^{-1}$. The thermal conductivity of all substances is

important since conductive heat transfer occurs in all components. The conductivity of molten silicon is considered to be $0.64\,W \cdot cm^{-1}K^{-1}$, while the conductivity of the crystal is considered to be an inverse function of temperature, $0.22\,(1683/T)\ W \cdot cm^{-1}K^{-1}$ (Touloukian, 1970). Graphite is also considered to be an inverse function of temperature, but there is a considerable variation in reported values. A mean value is considered to be $0.4\,W \cdot cm^{-1}K^{-1}$. The conductivity of the graphite felt insulation is actually an increasing function of temperature. This occurs since the material is porous and there is actually radiation exchanged between the fiber filaments. However it is again subject to wide scatter, so a mean value of $0.004\,W \cdot cm^{-1}K^{-1}$ will be used. The quartz crucible conductivity is an increasing function of temperature also, an the value at the melting point will be used as the constant conductivity, $0.06\,W \cdot cm^{-1}K^{-1}$. The values of emissivity of the surfaces are also critical and are susceptible to inherent uncertainty. The melt is assumed to have an emissivity of 0.05, while the crystal is assumed to have a constant emissivity of 0.55, intended to approximate the average over the expected temperature range. The emissivity of the graphite material is assumed to be 0.65. This is lower than the average value for graphite emissivity, but it is felt that a lower value would better correspond to the condition of the surfaces in the experimental apparatus at IBM, having been subjected to repeated runs and hence been contaminated with deposited silicon, etc. The chamber top is assumed to have an emissivity of 0.07, since it is a highly polished surface while the emissivity of the chamber walls is assumed to be 0.5, which is more representative of typical stainless steel. The emissivity of the quartz is estimated from the data to be about 0.25, again being an approximate average for the temperature range of interest.

The possibility has been considered that, due to the uncertainty inherent in many of the physical property constants, that highly detailed radiation modelling should be foregone for the present and that time would be better spent on measuring thermophysical properties. However, it is precisely the development of refined models and demonstration of their potential that will motivate work on thermophysical property measurements, since modelling provides the most important use for these detailed measurements.

1.5 Outlook

The first step in pursuit of the goals of this thesis is to attempt to accurately predict the temperature and flow fields which can in turn be used to predict the likelihood of dislocation formation and the segregation of solutes. The approach employed in Chapter

Table 1.4: Physical properties used in the IHTCM simulation.

Property	Symbol	Value Used for Simulation
Thermal Conductivity [7]	k	$Wm^{-1}K^{-1}$
graphite	k_c	40.0
crystal	k_s	$22.0\,(T/T_{m.p.})$
melt	k_m	64.0
quartz	k_q	6.00
felt	k_f	0.4
Emissivity [7,8,9]	ϵ	**no units**
graphite	ϵ_c	0.65
crystal	ϵ_s	0.55
melt	ϵ_m	0.05
quartz	ϵ_q	0.25
felt	ϵ_f	1.0
stainless steel	ϵ_p	0.5
Density [10]	ρ	$kg\,m^{-3}$
crystal	ρ_s	2330
melt	ρ_m	2510
Electrical Conductivity [7]	σ	$S\,m^{-1}$
graphite	σ_c	1250
Silicon Melt [10,11,12]		
thermal expansion	β_m	$1.45 \times 10^{-4}\,(K^{-1})$
surface tension	γ	$742.6 \times 10^{-3}\,(Nm^{-1})$
thermocapillarity	γ_T	$4 \times 10^{-6}\,(Nm^{-1}K^{-1})$
melting point	T_m	$1683\,(K)$
viscosity	μ	$7 \times 10^{-4}\,(kg\,m^{-1}s^{-1})$
heat of fusion	ΔH	$1800.0\,(J\,kg^{-1})$
growth angle	ϕ_0	11.0°
Silicon Crystal [13,14,10]		
CRSS ($T_{m.p.}$)	τ^{CRSS}	$1.8 \times 10^6\,(Nm^{-2})$
Burgers vector	b	$3.8 \times 10^{-10}\,(m)$
Shear Modulus ($T_{m.p.}$)	G	$3.51 \times 10^{10}\,(Nm^{-2})$
Thermal Expansion	β_s	$5.2 \times 10^{-6}\,(K^{-1})$
Poisson ratio	ν_s	0.25
Oxygen in silicon [15,16]		
Solubility	c_{sat}	$4 \times 10^{23} \exp\left[\frac{-2\times10^4}{T}\right]\ (cm^{-3})$
Segregation	K_{eq}	1.6
Diffusivity	$\mathcal{D}$	$3 \times 10^{-4}\ (cm^2s^{-1})$

[7]Touloukian, 1970; [8]Goldsmith et al., 1961; [9]Kureha Felt Co., 1989

[10]Lucas, 1964; [11]Glazov et al., 1969; [12]Surek and Chalmers, 1975

[13]Suezawa, 1979; [14]Sumino, 1980

[15]Hirata and Hoshikawa, 1990; [16]Yen and Tiller, 1991

2 is to predict these two important fields simultaneously, including depiction of the free boundaries in the system. The justification for this approach is twofold: first, important couplings have been established between heat transfer, fluid flow and free boundaries and second, that the thermal-capillary model of Sackinger serves as an excellent basis from which to begin such a task. The major limitations of the model are its axisymmetric and steady-state qualities. However, the models which include three-dimensionality and time-dependence cannot include a complete system depiction and therefore are of little potential use in optimization; they tend to take many man-years to develop and tax computer resources very heavily. The thermal-capillary modelling approach can be generalized to a complete system model with quite good resolution in a simulation that runs on the order of one hour on an IBM-3090, and so it has a very strong potential for useful design calculations.

Chapter 2

Development of the Integrated Hydrodynamic Thermal-Capillary Model (IHTCM)

Summary

Models of CZ silicon growth have been developed to various levels of sophistication; however, increases in model complexity have failed to solve the most acute problems of silicon growth, as described in Chapter 1. This deficiency has arisen partly due to unknown physical phenomena and partly because models produce volumes of information with pointwise precision in space and time, while measurements necessary for verification are sparsely available, and betray influence from factors not included in the mathematical description. Specifically, previous investigators have failed to quantitatively demonstrate their models' ability to accurately predict, rather than correlate, measurable quantities from the thermal and flow fields in large-scale CZ configurations. Most models do not include the complexity of heat transfer in a CZ system and depend on fixed boundary conditions from temperature measurements (for example Williams and Reusser, 1983; Langlois, 1977) or estimations (for example Tsukada et al., 1988); with those temperatures eliminated as calculation variables these models could neither be compared to thermal data nor employed as a general design and optimization tool, which is the long-term objective of numerical modelling. Two models have been developed without dependence on such input. One of these was applied to germanium and gallium arsenide (Dupret et al., 1990) and the other was applied to silicon (Miyahara et al., 1990); both neglected convection. In order to address the objectives of low dislocation density, compositional uniformity and large diameter it is important to simultaneously model the

thermal field, flow field and free-boundary shapes.

The temperature distribution is most critical because it establishes the solidification front, thermal convection in the melt and thermal stresses in the crystal all of which are determining factors in the quality of the grown crystal; therefore accurate heat transfer modelling is the unifying theme of this chapter. In order to predict the thermal field without imposing measured temperatures that only apply to the experimental situation, artificial fixed boundary conditions on the interior of the CZ apparatus are ousted for boundary conditions which are always realized in practice: for this the temperature at the chamber walls is the logical choice. The model must therefore account for radiative transmission of energy, since the chamber walls exchange heat with the system only by radiative interaction. It must also include convective transport, since purely conductive analysis of heat transfer neglects convective heat flux in the melt, and precludes similar detail about the solute field. Therefore, the model will combine a heat transfer package encompassing conduction, convection and radiation along with the computation of free boundaries which determine the shape of the domains. In this chapter the existing TCM's are extended to encompass radiation throughout the CZ chamber and the changes and impacts on model performance are reviewed. Computational feasibility limits the complexity of physics that can be included practically in an integrated model. The potential for important answers to the issues of crystal growth established in subsequent chapters will determine whether more detailed effects still need to be incorporated.

This chapter details the development of the Integrated Hydrodynamic Thermal-Capillary Model. The IHTCM approach is justified in Section 2.1. Various modelling approaches are considered and a strategy is deduced. Then the equations to be modelled are outlined in Section 2.2, starting from a general formulation and noting simplifications which yield more tractable forms. The numerical method in Section 2.3 builds on previous work (Sackinger, 1989) and contains similar information. Detail is focussed on novel developments and an attempt to give credit to the creators of the previous versions of the model is made, without swamping the description with distracting numbers of references. The impact of the model changes to performance is also addressed in Section 2.3. The tests of the model follow in Section 2.4, illustrating the predictions of the IHTCM in physically distinct scenarios.

2.1 Introduction

The objective of this thesis is to provide a systematic and quantitatively accurate model for use in optimizing a CZ crystal puller. It is envisioned that processing strategies will be devised off-line to meet the specifications of crystal shape, low defect density and uniform dopant profile, and subsequently fed forward to provide an optimal growth trajectory; alternatively the model could be used to evaluate alternative design configurations for the deduction of an optimal design. The model must be constructed according to the physical laws and empirical observations explained in Chapter 1. Heat transfer, and to an even greater extent mass transfer, depend very strongly on subtle details of the melt flow due to the melt velocities which enhance heat and mass transfer. In order to achieve quantitative accuracy, detailed flow calculation must be included in order to estimate actual transfer rates. Free-boundary modelling is necessary to provide quantitative information on the transport phenomena, especially since the deformation of the media is greatest near the critical melt-solid interface. Radiative boundary conditions are the key to obtaining a heat balance which can be generalized to any geometry.

The model must provide an accurate yet practical depiction of the observed phenomena outlined in Chapter 1. Modelling approaches that neglect convection, free boundaries or radiative transfer cannot achieve the objectives. The analytical models in Section 1.3 and simpler numerical models in Section 1.4 can therefore only provide the means to verify more complicated approaches. Many numerical formulations calculate flow fields in CZ. There are axisymmetric and three-dimensional models, as well as steady-state and time-dependent models. Few of these flow models attempt to simultaneously calculate the interface shape and fewer still attempt to calculate the radiative heat transfer in a depiction of the full system geometry. The reason is that increased detail requires more complexity in the solution algorithm, computations, computer memory and real time. Table 2.1 summarizes the computer usage and level of model detail from CZ numerical models presented in the literature. Presented also in the table is an estimated operation count since actual *CPU* times are only sparsely reported. (The estimation is based on the product of the number of equations with the square of the bandwidth for LU decomposition for a rectangular domain with elemental dimensions $n \times 2n$.) Between the estimated operation-counts and the reported run-times it is evident that modelling either time-dependence or three-dimensionality of the fluid flow under realistic conditions increases the computational requirement by orders-of-magnitude due to the need for discretization in time or the third dimension. Including free boundaries and radiation heightens the

computational burden, but only by a factor of about two.

Three-dimensionality and time-dependence will be neglected in the IHTCM. The time scale for the crystal growth apparatus to change growth parameters is on the order of minutes or longer; the resolution of fluctuations in the flow field which occur over fractions of a second would wastefully consume resources in order to produce suitable average quantities which are useful to the crystal grower. Similarly, CZ growth strategies nearly always are axisymmetric and so the azimuthally-averaged growth condition is of prime interest to the crystal grower. Hence, resolution of these items is of secondary importance in the development of control and design strategies. Omitting time-dependence and three-dimensional from the model also minimizes the required model development and computer usage. Run times of approximately one hour are possible with a two-dimensional steady description and enable expedient simulation for a wide range of input parameters. Unfortunately, measurements of the average and time-varying fluxes are not available in the literature on CZ, and so the effect of time-dependence in actual systems is difficult to judge. Neither has the contribution to the azimuthally-averaged flux from azimuthal variations been established. Consequently, it cannot be stated precisely how appropriate is the two-dimensional , steady-state laminar flow model for the CZ system in this Thesis. Chapter 4 attempts to relax these restrictions, and predicts the average transport rates in the limit of fully-developed turbulence.

This effort begins with a steady-state description of flow, free boundaries and radiation to quantitatively predict the salient aspects of CZ silicon growth. Representation of the thermal boundary conditions is critical. The chamber wall in the test system is cooled and is imposed as an essential boundary condition. The heat transfer in the various components is linked by a radiative natural boundary condition. Convection in the melt is calculated through a steady-state depiction of the flow and simultaneous heat transfer. Computational feasibility is insured by providing a sufficient discretization for the phenomena mentioned.

The family of thermal-capillary models developed at MIT is the basis for the present model (Derby, 1986; Atherton et al., 1987; Thomas, 1988; Sackinger, 1989). The approach has been shown to successfully model the free-surface coupling with heat transfer, with radiation heat transfer and with fluid mechanics separately in its various incarnations. In the description of the model formulation and numerical method, repeated references to these authors could be made. As a practical alternative this paragraph describes the incremental contributions broadly and Section 2.2 describes the present method in detail without indicating its historical development. The first thermal-capillary model

Table 2.1: CZ models: summary of physical detail and computational requirements.

	Authors	Physical Depiction				
		space	time	mesh	radiation	field variables
1	Kim et al., 1986	2D	unsteady	fixed	idealized	T, ψ, S, Ω
2	Kim et al., 1990	2D	unsteady	fixed	idealized	T, ψ, S, Ω
3	Kim et al., 1989	2D	unsteady	fixed	idealized	$T, \psi, S, \Omega, c_{Ga}$
4	Mihelčić et al., 1982	2D	unsteady	fixed	idealized	$T, \mathbf{v}$
5	Mihelcić et al., 1987	3D	unsteady	fixed	idealized	$T, \mathbf{v}$
6	Sackinger, 1989	2D	steady	moving	idealized	$T, \mathbf{v}, P$
7	Sackinger et al., 1988	2D	steady	moving	idealized	$T, \mathbf{v}, P$
8	Tsukada et al., 1988	2D	steady	moving	idealized	$T, \mathbf{v}$
9	Kobayashi et al., 1991	2D	steady	fixed	idealized	$\overline{T}, \overline{\psi}, \overline{S}, \epsilon, K$
10	Kakimoto et al., 1989	3D	steady	fixed	idealized	$T, \mathbf{v}$
11	Miyahara et al., 1990	2D	steady	moving	detailed	T
12	Bornside et al., 1990	2D	steady	moving	detailed	T
13	Srivastava et al., 1985	2D	steady	moving	detailed	T

	Method	CPU time	Estimated[1] Relative Op. count	Computer	Rating[2]
1	finite-difference	$27min/(model)sec$	$f(\Delta t)$	IBM3081	7.4
2	finite-difference	$2000(model)sec$	$f(\Delta t)$	IBM3090	1.0
3	finite-difference	$45sec/(model)sec$	$f(\Delta t)$	IBM3090	1.0
4	marker-and-cell	N.A.	$f(\Delta t)$	IBM 3033	7.0
5	marker-and-cell	N.A.	$f(\Delta t \times \Delta\theta)$	Cray X-MP	0.32
6	finite-element	$\leq 170sec/iteration$	1.0	Cray X-MP	0.32
7	finite-element	$\leq 360sec/iteration$	1.0	Cray X-MP	0.32
8	finite-element	N.A.	1.4	NEC SX-I	0.34
9	finite-element	N.A.	2.0	N.A.	N.A.
10	finite-volume	$10h$	$f(\Delta\theta)$	NEC SX-II	0.28
11	finite-element	N.A.	0.15	N.A.	N.A.
12	finite-element	$\leq 210sec/iteration$	0.15	IBM3090	1.0
13	finite-element	N.A.	0.06	N.A.	N.A.

"N.A. " signifies that no data was published.

[1] A relative value of 1 is assigned to the HTCM. Only steady, two-dimensional models are estimated. The dependence of time-stepping models on discretization in time is denoted by $f(\Delta t)$ and three-dimensional models on discretization in the azimuthal direction by $f(\Delta\theta)$.

[2] Computer speed is rated as the time required to solve dense systems of equations using the LINPACK routines, relative to the speed of a Cray-1S, as reported by Dongarra, 1987.

for CZ or LEC crystal growth (Derby, 1986) followed a proven approach for locating the melt-solid interface in a crystal growth system (Ettouney and Brown, 1983). It simulated conductive heat transfer only in the melt, and radiation and convective heat loss to a uniform temperature ambient. The melt-gas meniscus was located by the Laplace-Young equation and the melt-solid interface at the melting point isotherm. The heater was modelled as a constant temperature block which supplied a constant temperature ambient exclusively to the crucible sidewall. A time-dependent version of the model was developed to capture batch-dynamics in a conduction-dominated model (Derby and Brown, 1987a). A radiative heat transfer package was added to the original code (Atherton et al., 1987) and was shown to yield considerable changes to the computed thermal profiles, subject to the property values used for the surfaces in question. A further accessory code was developed (Thomas, 1988) which used the thermal field of the crystal as input to produce both a profile for the thermal stress and a leading-order asymptotic prediction of the ultimate dislocation density in the crystal, based on the Haasen model of dislocation dynamics. Further work on TCM's (Sackinger, 1989) foresook radiative analysis for a steady-state axisymmetric depiction of fluid flow, illustrating the coupling between the thermal field, flow and interface shape for a variety of operating parameters. Most of the components for the present analysis had existed previously in some form, and hence the work has had a custodial flavor. Since it brings various models together the name *Integrated* Hydrodynamic Thermal-Capillary Model (IHTCM) was chosen.

2.2 Mathematical formulation

The basic thermal-capillary model used in the IHTCM is a synthesis of earlier TCM's. All transport and surface shapes are taken to be axisymmetric around the axis of a cylindrical coordinate system positioned along the growth axis of the crystal. Accordingly asymmetries in the heat transfer caused by features of the SILTEC system, such as view ports and the picket-fence-shaped heater are not included in the model. The geometry for the CZ model, based on the Siltec furnace in operation at K.M. Kim's laboratory in East Fishkill, is shown schematically in Figure 2.2a and to scale in Figure 2.2b. The notation introduced in this figure is carried on throughout the remainder of this thesis. The regions are denoted by m for the melt phase, s for the solid crystal, c for the crucible, h for the heater, su for the susceptor, sh for the graphite shields and f for the graphite felt insulation. To refer to arbitrary components either the subscript i will be used or no subscript will be used at all. The system is laid out in cylindrical (r, θ, z) coordinates, and

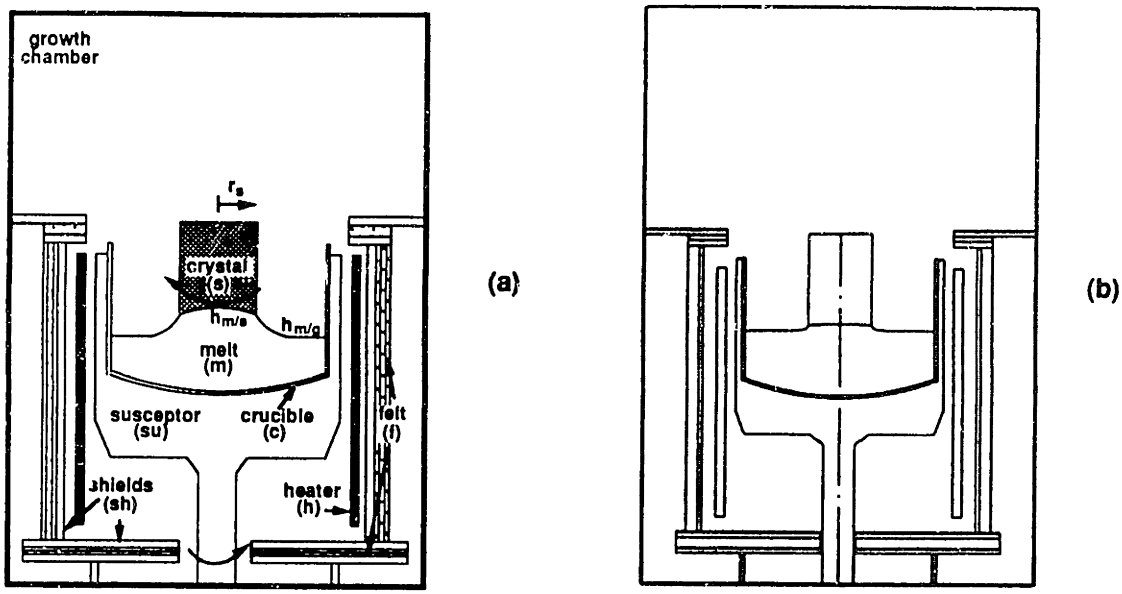

Figure 2-1: Model representation of Kim's apparatus (a) drawing with domain labels (b) model scale 1:10.

all variables are constant functions of θ, due to cylindrical symmetry. The free boundaries are the crystal radius, the melt-solid interface height and the melt-gas meniscus height, denoted by R_s, $h_{m/s}(r)$ and $h_{m/g}(r)$, respectively. The height variables $h_{m/s}(r)$ and $h_{m/g}(r)$ are single-valued functions of the radial coordinate r.

2.2.1 Field Equations

Equation of energy

The transport equations to be solved in the CZ apparatus are the equations of thermal energy transfer and fluid momentum transfer. The first simplification is that the void space in the apparatus, which is filled with low pressure argon is neglected as taking part in the transport processes. The gas is considered to have no thermal or solutal gradients, to be perfectly transparent to radiative energy and provide an infinite sink for convected energy. Therefore the domains which constitute the model are solid, melt and effective solids such as the porous graphite felt and the picket-fence-shaped heater[3].

A description of the transport equations follows. The equations are stated in a di-

[3]Although the graphite of the heater has negligible porosity, the heater's "picket-fence" construction translates into an azimuthally-averaged void fraction of ~ 0.22.

Table 2.2: Details of SILTEC puller construction and operating parameters for the experiment.

Materials of Construction		*Operating Parameters*	
Component	*Material*	*Parameter*	*Value*
crucible	fused silica, $254mm$	boule diameter	$8.25\ cm$
susceptor	graphite	pull rate	$6.35\ cm \cdot hr^{-1}$
heater	graphite	crucible rotation	$-8\ rpm$
heat shield	graphite	crystal rotation	$+20\ rpm$
insulation	graphite felt	shell temperature	$200\ ^{\circ}C$
chamber wall	stainless steel	heater power rating	$40\ kW$
chamber top	polished stainless steel	chamber pressure	$10\ Torr$
chamber gas	argon		

mensional form, breaking the tradition of previous TCM authors. There are important motivations for this. The choice of scales based on physical properties and system dimensions may be entirely inappropriate. For example, a viscous scaling for velocity in a highly convected flow will not yield $O(1)$ quantities for velocity. More importantly, the values of the poorly-scaled dimensionless numbers would only be misleading. The dimensionless numbers calculated based on simulation results to obtain $O(1)$ quantities will be the only ones mentioned.

In the IHTCM the thermal field is computed throughout all components of the CZ system. Heat transfer in all phases is assumed to be by isotropic conduction, in the melt and crystal also by convection and in the graphite resistance heater alone by an electrical source as shown in the energy equation

$$\boxed{\rho C_p \frac{\partial T}{\partial t} +}\ \rho_i C_{p,i} \mathbf{v} \cdot \boldsymbol{\nabla} T = \boldsymbol{\nabla} \cdot (k \boldsymbol{\nabla} T) + j_h^2 \sigma_h. \tag{2.1}$$

The time-derivative in the box is assumed zero for steady state but appears as nonzero in Chapter 4; ρ is the density of any material, C_p is its heat capacity and k is its thermal conductivity. The subscript i refers to the mobile phases, the melt ($i = m$) and crystal ($i = s$). The convection of heat due to bulk motion appears as the second term in Equation (2.1) and applies to both melt and crystal. In the melt $\mathbf{v}$ is an unknown vector and in the crystal $\mathbf{v} = V_p \mathbf{e}_z$, where V_p is the pull-rate of the crystal. In the heater only, heat is generated by passing a current density j_h through the material with electrical

resistivity σ_h. The voids in the picket-fence-shaped heater are accommodated for in the treatment of radiative heat transfer described below.

The boundary conditions for energy transport provide the coupling between the heat transfer components. Surfaces in contact are assumed to be in thermal equilibrium and the heat fluxes between the elements are balanced, except for the heat flux owing to the latent heat contribution at the melt-solid interface. A statement of the local heat balance across the melt solid interface is

$$k_m(\mathbf{n}\cdot\nabla T)_m - k_s(\mathbf{n}\cdot\nabla T)_s = -V_{eff}\Delta H_{fus}\rho_s(\mathbf{n}\cdot\mathbf{e}_z) \tag{2.2}$$

where $\mathbf{n}$ is the outward-pointing normal to the interface. The effective growth rate is

$$V_{eff} = \frac{V_p}{1 - R_s^2\rho_s/R_c^2\rho_m} \tag{2.3}$$

and is used to calculate the latent heat release includes the rate of growth due to the melt level's dropping, and is the key to achieving an accurate quasi-steady approximation of the transient thermal profile (Derby et al., 1987b). All exposed surfaces in the CZ enclosure are assumed to exchange heat by diffuse, gray radiation and by convection to the surrounding gas. The local heat flux from an element of exposed surface with temperature T is written as

$$k\mathbf{n}\cdot\boldsymbol{\nabla}T = h_c(T - T_{ac}) + \sigma_{SB}\epsilon(T^4 - T_{ar}^4), \tag{2.4}$$

where ϵ is the surface emissivity, σ_{SB} is the Stefan-Boltzmann constant, h_c is a convective heat transfer coefficient based on the gas flow-rate, T_{ac} is the effective temperature of the gas for convective transport and T_{ar} is the effective temperature for radiation. The Biot number Bi scales the importance of convection into the gas relative to conduction to the surface from the particular solid phase or melt and the radiation number Rd scales the importance of radiative loss to conduction to the surface; both dimensionless groups are defined in Table 2.3. The estimates for these parameters show that radiation is the prevalent mechanism at higher temperatures.

The effective ambient temperature T_{ar} of Equation (2.4) is an artificial variable that contains information about radiative exchange between all elements of the enclosure. This variable is computed using Gebhart's method (Gebhart, 1971) based on the assumptions that all surfaces are optically thick, and emit and reflect radiation in a diffuse pattern. A brief development is given here to pinpoint the nature of these approximations. A

Table 2.3: Important dimensionless parameters and expected values for the conditions of growth. Physical properties precede other constants and arbitrary scales are set in parentheses. Estimates are given for the experimental apparatus.

Symbol	Definition	Dimensionless Group and Physical Significance	Range of Values
Bo	$\frac{\rho}{\gamma} g (R_c^2)$	Bond Number = Ratio of gravity to surface tension force.	500
Bi	$\frac{1}{k} h_c (R_c)$	Biot Number = Ratio of convective heat transfer into gas to internal conduction.	$10^{-2} \rightarrow 1$
Ca	$\frac{\mu}{\gamma} v_{max}$	Capillary Number =Ratio of inertial forces to surface tension.	10^{-4}
Ek_s	$\frac{\mu}{\rho} \frac{1}{\lvert\omega_s\rvert R_s^2}$	Ekman Number =Ratio of viscous force to Coriolis force.	10^{-4}
Ek_c	$\frac{\mu}{\rho} \frac{1}{\lvert\omega_c\rvert R_c^2}$	Ekman Number for crucible rotation =Ratio of viscous force to Coriolis force.	10^{-5}
Gr	$\frac{\beta\rho^2}{\mu^2} g\Delta T_m (R_c^3)$	Grashof Number =Ratio of buoyant to viscous forces.	10^{10}
Ma	$\frac{\gamma_T \rho C_p}{k\mu} \Delta T_m (R_c)$	Marangoni Number =Ratio of thermocapillary force to viscosity.	10^5
Pe	$\frac{\rho C_p}{k} v_{max} (R_c)$	Péclét Number =Ratio of heat convection to conduction.	$> 10^2$
Pr	$\frac{\mu C_p}{k}$	Prandtl Number =Ratio of conductive to viscous time scales.	10^{-2}
Ra	$\frac{\beta\rho^2 C_p}{\mu k} g\Delta T_m (R_c^3)$	Rayleigh Number =Ratio of buoyant convection to conduction.	10^7
Rd	$\frac{e}{k} \sigma_{SB} (T_{m.p.}^3 R_c)$	Radiation Number =Ratio of surface radiation to internal conduction.	$10^{-2} \rightarrow 1$
Re	$\frac{\rho}{\mu} v_{max} (R_c)$	Reynolds Number =Ratio of convective to viscous forces	$> 10^4$
Ro	$2\frac{\lvert\omega_s - \omega_c\rvert}{\lvert\omega_s + \omega_c\rvert}$	Rossby Number =Ratio of inertial to Coriolis force.	5
S	$\frac{\Delta H_{fus}}{C_p} (T_{m.p.})^{-1}$	Stefan Number =Ratio of latent heat to temperature scale.	1
We	$\frac{\rho}{\gamma} v_{max}^2 (R_c)$	Weber Number =Ratio of inertial forces to surface tension.	$< 10^2$

radiative heat balance for any surface point j in the enclosure is given by the difference between emitted and absorbed radiation, where absorbed energy originates from all surface points i

$$[k\mathbf{n}\cdot\nabla T - h_c(T-T_{a^c})]_j = \sigma_{SB}\epsilon_j T_j^4 - \sigma_{SB}\int^S G_{ij}\epsilon_i T_i^4 dS_i. \tag{2.5}$$

G_{ij} is the fraction of energy leaving point i which is absorbed at j (after any combination of direct and reflected trajectories). The first two approximations, that surfaces are diffusely emitting and optically thick, are introduced in an expression for G_{ij}

$$G_{ij} = F_{ij}\epsilon_j + \int^S F_{ik}\rho_k G_{kj(i)} dS_i. \tag{2.6}$$

The first term represents direct radiative exchange from i to j, while the second term is the reflected radiation, integrated over all reflecting surfaces. Here F_{ij} is a view factor, a purely geometrical term representing the fraction of the solid angle emanating from point i which intercepts point j; ϵ_j is the emissivity of point j, which by the assumption of optical thickness is taken equal to its absorptivity. Therefore the emissivity is related also to the reflectivity $\rho_k = 1 - \epsilon_k$.

The exchange factor $G_{kj(i)}$ is the fraction of energy reflecting from point k to be absorbed at j which originated at point i. A further expansion for $G_{kj(i)}$ can be stated involving the four-point exchange factor $G_{lj(ik)}$ and the view factor $F_{kj(i)}$, which is the view factor from point k to j, assuming that the energy originated at point i. Such view factors are important only for *spectral* surfaces, which reflect energy according to Snell's law for mirror-like surfaces; see Figure 2-2a. In the CZ system the melt, crystal and chamber top surfaces may behave in this way. For the CZ system it is expected that $G_{kj(i)}$ would differ significantly from G_{kj} only for the handful of elements on the crystal and crucible that border the melt surface, and that higher-order exchange factors would be negligible. This is due to the fact that the specular reflections will only produce an important change near to a geometrically detailed area with spectral surfaces, which occurs only near the juncture of the melt and solid surfaces in CZ. Further, a negligible fraction of radiation will undergo more than one specular reflection; see Figures 2-2c and 2-2d. Thus the assumption of diffuse reflection, i.e. $F_{kj(i)} = F_{kj}$ for all i, which relates G_{ij} to itself with ϵ as the only physical property required should provide an accurate

measure of the heat transfer in the system:

$$G_{ij} = F_{ij}\epsilon_j + \int^S F_{ik}\,(1-\epsilon_k)\,G_{kj}dS. \tag{2.7}$$

The accurate depiction of spectral reflections would entail evaluating the successive view factors $F_{kj(i)}$, $F_{lj(ik)}$, etc., and Gebhart factors $G_{kj(i)}$, $G_{lj(ik)}$, etc., until G_{ij} converges.

For a system of discrete surfaces the Gebhart factors are obtained from the following relation

$$[F_{ij}(1-\epsilon_j) - \delta_{ij}]\,G_{ik} = -F_{ik}\epsilon_k, \tag{2.8}$$

where $[F_{ij}(1-\epsilon_j)-\delta_{ij}]$, G_{ij} and $F_{ik}\epsilon_k$ are matrices. The vector of radiative ambient temperatures of surfaces i of the enclosure is written as a sum over all other elements with varying elemental areas

$$[T_{ar}]_i \equiv \left[\frac{A_j\epsilon_j G_{ji}T_j^4}{\epsilon_i A_i}\right]^{1/4} = \left[G_{ij}T_j^4\right]^{\frac{1}{4}}. \tag{2.9}$$

The radiative ambient temperature is the surface temperature which would exchange zero net radiation with its surroundings. The Gebhart factors require the view factors between all surface elements of the enclosure; this computation is discussed in Section 2.3. The enclosure is composed of all component surfaces in the CZ system and the surrounding chamber, which is modelled as an isothermal boundary with temperature $473\,K$.

The picket-fence heater is difficult to model because it lacks axisymmetry. To consider the heater as a solid body neglects a significant amount of direct radiative coupling between the susceptor and the heat shield, and underestimates the heater temperature required to sustain a given thermal field within the susceptor. The approximation of axisymmetric heat transfer considers the heater as a continuous medium, but permits a fraction Ξ of the incident radiative energy to pass unimpeded through the heater. This continuous medium approximation is justifiable given typical crucible rotation rates, because rotating the crucible smooths out any significant azimuthal variation in heat flux through the susceptor. The fraction of radiative energy which passes through, Ξ, is taken to be equal to the ratio of empty space between the heater's pickets to the total volume of a solid object and equals 0.22 for the heater in the Siltec apparatus in this Thesis. This is implemented by evaluating the geometric view factors for radiation twice, once with and once without a solid body present, and forming a composite view factor with

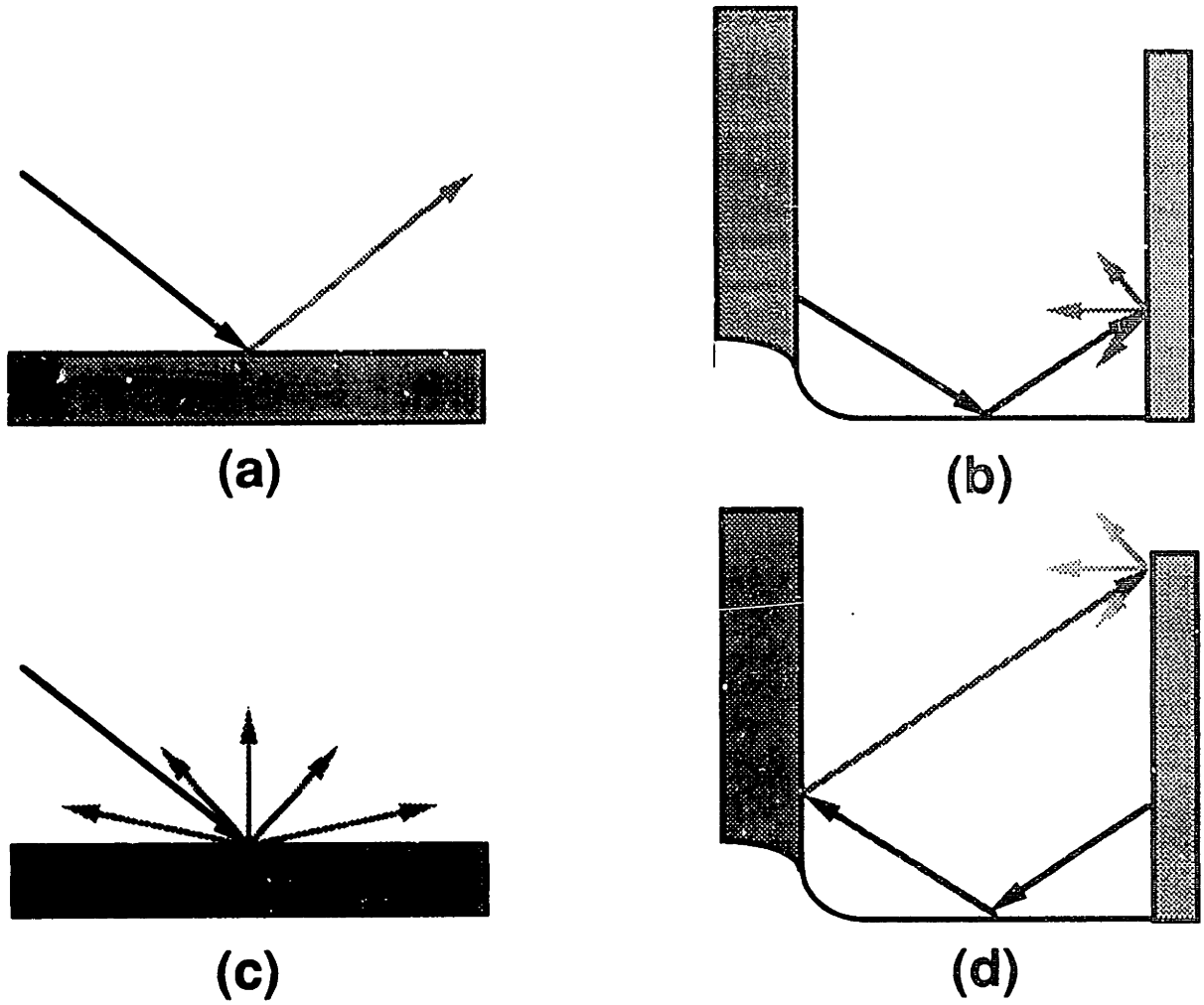

Figure 2-2: (a) Spectral reflection (b) diffuse reflection (c) trajectory with one spectral reflection (d) trajectory with more than one spectral reflection.

the two values weighted appropriately:

$$F_{ij} = (1 - \Xi)F_{ij}^{I} + \Xi F_{ij}^{II} \tag{2.10}$$

where F_{ij}^{I} is the view factor matrix evaluated with a solid-bodied heater included and F_{ij}^{II} with it excluded. The energy equation ((2.1)) for the heater is multiplied by $(1 - \Xi)$ to obtain the overall heat balance, but this does not affect the computed temperatures.

Equation of motion

Convective heat transfer is calculated by computing the velocity field $\mathbf{v}(r, z)$ in the melt. The forces of crystal rotation, crucible rotation, temperature-driven buoyancy and thermocapillarity are considered. The field equations for steady-state, laminar, transport of the momentum of an incompressible, Newtonian fluid are given, with the Boussinesq approximation as

$$\boxed{\rho\frac{\partial \mathbf{v}}{\partial t}+}\ \rho\mathbf{v}\cdot\boldsymbol{\nabla}\mathbf{v} = -\boldsymbol{\nabla}P + \boldsymbol{\nabla}\cdot\left[\mu\left(\boldsymbol{\nabla}\mathbf{v} + \boldsymbol{\nabla}\mathbf{v}^{\dagger}\right)\right] + \rho\beta\mathbf{g}(T - T_{m.p.}) \tag{2.11}$$

$$\boldsymbol{\nabla}\cdot\mathbf{v} = 0, \tag{2.12}$$

where μ is the fluid viscosity and β is the thermal expansion coefficient. Again the time-dependent term in the box is assumed zero for the steady-state calculation. The linear term $\rho\beta\mathbf{g}(T - T_{m.p.})$ provides the mathematical description of thermal buoyancy.

The boundary conditions for velocity along the crucible wall and the melt/crystal interface provide no slip and no penetration and hence ignore the very small component $(17.5\mu m \cdot s^{-1})$ of velocity in the $z-$direction through the melt-solid interface caused by crystal growth. It will be shown later that this velocity can be included with negligible effect on the bulk fields. In the meridional (r, z) plane these conditions on the crystal and crucible walls are

$$\mathbf{t}\cdot\mathbf{v} = 0 \qquad \mathbf{n}\cdot\mathbf{v} = 0. \tag{2.13}$$

Rotation of the crucible at the rate $\Omega = \omega_c$ and rotation of the crystal at rate $\Omega = \omega_s$ are included in the no-slip boundary conditions along either the crystal or crucible as

$$v_\theta = \Omega\, r. \tag{2.14}$$

The boundary conditions for velocity along the centerline are similar; no fluid is allowed

to penetrate the centerline $r = 0$ in the meridional plane

$$\mathbf{n} \cdot \mathbf{v} = v_r = 0, \tag{2.15}$$

and the azimuthal velocity there is also zero

$$v_\theta = 0. \tag{2.16}$$

However, velocity tangential to the centerline (in the z-direction) is permitted by a stress-free boundary condition:

$$\mathbf{e}_z\mathbf{n} : \boldsymbol{\nabla}\boldsymbol{\sigma} = \mu\frac{\partial v_z}{\partial r} = 0 \tag{2.17}$$

where the total stress tensor is $\boldsymbol{\sigma} \equiv P\mathbf{I} - \left[\mu\left(\boldsymbol{\nabla}\mathbf{v} + \boldsymbol{\nabla}\mathbf{v}^\dagger\right)\right]$. The velocity boundary conditions along the meniscus are more complicated to implement, because the meniscus shape is not known *a priori*. However, the no-penetration condition applies

$$\mathbf{n} \cdot \mathbf{v} = 0 \tag{2.18}$$

and a stress-free condition applies in the azimuthal direction

$$\mathbf{e}_\theta\mathbf{n} \cdot \boldsymbol{\nabla}\boldsymbol{\sigma} = \mu\frac{\partial v_\theta}{\partial n} = 0. \tag{2.19}$$

The thermocapillary driving force along the meniscus arises in a tangential stress balance as

$$\mathbf{tn} : \boldsymbol{\sigma} = -\gamma_T \boldsymbol{\nabla}_t T = -\gamma_T \frac{\frac{\partial T}{\partial r}}{\sqrt{1 + (h'_{m/g})^2}} \tag{2.20}$$

where $\mathbf{t}$ is the unit tangent vector to the meniscus in the (r,z) plane, $\boldsymbol{\nabla}_t$ is the surface gradient operator in the tangential direction and $h'_{m/g}$ is the slope of the meniscus.

2.2.2 Free Boundaries

Specification of the free-boundary physics completes the IHTCM by defining the shape of the domains. The melt/crystal interface is determined as the melting point isotherm

$$T(r, h_{m/s}) = T_{m.p.}. \tag{2.21}$$

The shape of the meniscus between melt and gas is determined from the balance of

normal stresses at this boundary, expressed in terms of a balance between hydrostatic pressure due to gravity, surface tension acting through the mean curvature $\mathcal{H}$ of the interface and normal viscous and dynamic pressure forces caused by motion in the melt. This normal force balance is written as a modified Young-Laplace equation as

$$2\gamma\mathcal{H} = \rho g(h_{m/g}(r) - \lambda) - \mathbf{nn}:\boldsymbol{\sigma} \tag{2.22}$$

where $(\mathbf{nn}:\boldsymbol{\sigma})$ is the dynamic component of the normal force and $\mathbf{n}$ is the unit normal to the meniscus. The curvature is calculated as

$$2\mathcal{H} = \frac{h''_{m/g}(r)}{(1+(h'_{m/g}(r))^2)^{3/2}} + \frac{h'_{m/g}(r)}{r(1+(h'_{m/g}(r))^2)^{1/2}}. \tag{2.23}$$

The height of the melt in the crucible at any radial location from the axis of symmetry is $h_{m/g}(r)$ and λ is a reference pressure difference between the melt and the ambient above. The Bond Number $Bo \sim 500$ scales the importance of hydrostatic pressure to surface tension in shaping the meniscus, indicating that surface tension is only important in a thin layer where the curvature is large. The Weber number $We \sim 100$ scales the dynamic normal force to surface tension. This force is small over most of the melt surface, and so there is typically little effect of flow on the meniscus shape. The growth angle formed by the tangent vectors to the crystal/ambient and melt/gas surfaces, $\phi_0 = 11°$ is known from measurements for growth on the {111} crystal surface (Surek and Chalmers, 1975) and determines the height of the meniscus at the trijunction.

$$\left.\frac{\partial h_{m/g}}{\partial r}\right|_{r=R_s} = -\cot 11° \tag{2.24}$$

The melt forms an angle of 90° with the solid crucible in the present model. In all the calculations of this thesis the crystal radius is specified as a constraint $R_s(P_h) = R_{set}$ and the power to the heater is calculated in order that the radius constraint be satisfied. This need not be the case, and other TCM's have employed different sets of constraints, such as fixing the heater temperature and calculating the crystal radius, or fixing both the crystal radius and interface deflection and calculating *two* ambient temperatures in order to satisfy the two constraints (Derby et al., 1987). The specification of the thermal-capillary model is completed by using the volume of the melt as the constraint that sets the reference pressure difference λ. Usually there is little effect of the fluid force on the meniscus shape and λ approaches the value $h_{m/g}(r)$ at the crucible wall. The interface

shapes also satisfy the constraint of fixed total volume, given by the integral

$$\int_0^{R_s} \left[h_{m/s}(r) - h_c(r)\right] r dr + \int_{R_s}^1 \left[h_{m/g}(r) - h_c(r)\right] r dr = \frac{V_m}{2\pi}. \tag{2.25}$$

2.2.3 Thermoelastic stress

For the computation of thermoelastic stresses, the approach will be adopted unchanged from previous work (Thomas, 1988). Enough development is given here to expose the thermal driving force for the stress. The formulation solves the equation of equilibrium in terms of the displacement vector $\mathbf{u} = (u, 0, w)^\dagger$

$$(1 - 2\nu_s)\,\nabla^2\mathbf{u} + \boldsymbol{\nabla}\left(\boldsymbol{\nabla}\cdot\mathbf{u}\right) - 2\left(1 + \nu_s\right)\beta_s\boldsymbol{\nabla}T = 0, \tag{2.26}$$

where ν_s is the material Poisson ratio, and β_s is its thermal expansion coefficient. Since it is formulated in terms of $\mathbf{u}$ Equation (2.26) automatically satisfies compatibility. A temperature gradient yields a nonzero displacement but not necessarily a strain $\epsilon = \frac{1}{2}(\boldsymbol{\nabla}\mathbf{u} + \boldsymbol{\nabla}\mathbf{u}^\dagger)$ since a gradient in the displacement function is also required. An alternative yet equivalent formulation in terms of the thermoelastic stress tensor σ_s involves simultaneously satisfying the equations of equilibrium, or the Cauchy equation

$$\boldsymbol{\nabla}\cdot\boldsymbol{\sigma}_s = 0 \tag{2.27}$$

and compatibility (the requirement for existence of a displacement function $\mathbf{u}$)

$$(1 + \nu_s)\nabla^2\boldsymbol{\sigma}_s + \boldsymbol{\nabla}\boldsymbol{\nabla}tr(\boldsymbol{\sigma}_s) + \beta_s E\left(\frac{1 + \nu_s}{1 - \nu_s}\right)\nabla^2 T\boldsymbol{\delta}_{ij} + \beta_s E\boldsymbol{\nabla}\boldsymbol{\nabla}T = 0 \tag{2.28}$$

where E is Young's modulus and $tr()$ is the trace operator. Of the equivalent representations the displacement representation is preferred over the stress formulation because it involves solving for only the vector components, rather than the entire stress tensor, and so has fewer unknowns in the finite-element formulation. Once the displacement vector is known, the strain tensor ϵ and stress tensor σ_s are calculated directly. The stress formulation here is only meant to clarify that *curvature* of the temperature field due to the operators $\nabla^2 T\boldsymbol{\delta}_{ij}$ and $\boldsymbol{\nabla}\boldsymbol{\nabla}T$ provides a driving force for the thermoelastic stress.

The stress-strain behavior is assumed to be completely linear and elastic, which is valid for small strains which induce stresses below the upper yield stress. The thermoelastic stress provides only a relative measure of the driving force for dislocation generation,

due to the plastic contribution to the stress relief. Asymptotic analysis of a constitutive model describing plastic deformation (Maroudas, 1992) has shown that the thermoelastic stress provides the scaling,

$$N_\infty = \frac{K\sigma_0^2}{2Gb}, \tag{2.29}$$

for the number of dislocations in dislocated silicon under common operating conditions. σ_0, the *von Mises* stress, is the square root of the second invariant of the stress tensor. Therefore, thermoelastic stress alone is sufficient for predicting dislocation density in CZ-grown silicon containing more than zero dislocations.

2.2.4 Mass transport

Solutal convection usually can be neglected for CZ silicon growth. It has been treated for gallium in silicon where the solute gradient was found to contribute hydrodynamically (Kim and Langlois, 1989). This was attributed to the steep concentration boundary layer in front of the melt-solid interface resulting from a distribution coefficient (8×10^{-3}) much lower than unity. Oxygen, the solute of interest in this study, has a segregation coefficient close to one, and should thus not be expected to form a boundary layer at the melt-solid interface. In addition, the melt-gas interface provides a ready sink for oxygen, so the concentration remains dilute. Since the concentration is small the coupling of the equation of motion with the equation of oxygen transport can be neglected and it is formulated as a steady-state convection-diffusion equation

$$\mathbf{v} \cdot \boldsymbol{\nabla} c = \boldsymbol{\nabla} \cdot (\mathcal{D} \boldsymbol{\nabla} T). \tag{2.30}$$

The boundary conditions are more intriguing; see Figure 2-3. Equilibrium relationships apply at the crystal-melt interface, the crucible-melt interface, and the melt-gas surface. The segregation coefficient of elemental oxygen dissolved in silicon is taken to be constant at 1.6 (Yen and Tiller, 1991). The melt surface condition will be an essential boundary condition, with the surface concentration of oxygen equal to zero (Carlberg et al., 1982). The boundary condition on oxygen concentration on the crucible sidewall is given by a temperature-dependent correlation (Hirata and Hoshikawa, 1990) for the solubility of oxygen in silicon

$$c_{O,sat.} = 4 \times 10^{23} \exp\left[\frac{-2 \times 10^4}{T}\right] \tag{2.31}$$

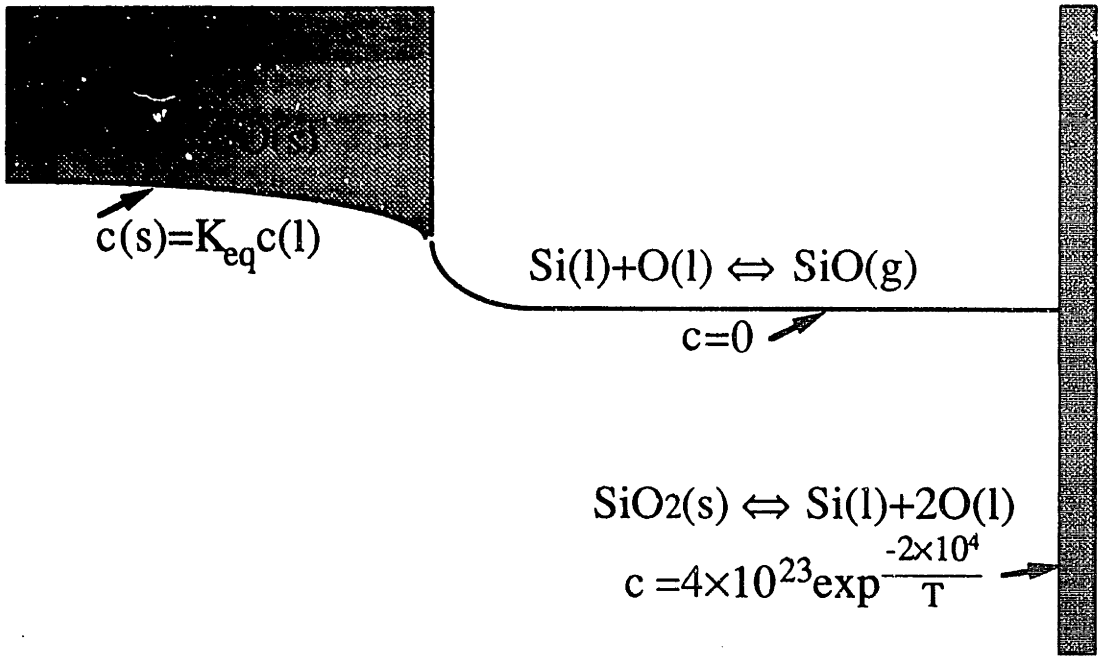

Figure 2-3: Boundary conditions for oxygen segregation model.

assuming that the dissolution reaction is given by:

$$SiO_2(solid) \rightleftharpoons Si(melt) + 2O(dissolved\ in\ melt). \tag{2.32}$$

The IHTCM can also compute the transport of oxygen from the flow field of the hydrodynamic model.

2.3 Numerical Method

The set of differential and algebraic equations described by Equations (2.1)-(2.31) is converted to a system of nonlinear algebraic equations using the finite element discretization, Galerkin weighted residuals and numerical quadrature. The Newton-Raphson method is used to solve the resulting system of equations. This procedure has been skilfully described elsewhere (Sackinger, 1989). It is reviewed here because radiation modelling has substantially changed the numerical structure. In addition, the radiation-related program changes are described.

2.3.1 Discretization

The finite-element method is chosen as the method of discretization since it is well-suited for handling moving boundaries. The boundaries are defined explicitly as element edges in the finite-element grid, and the finite-element mesh deforms to locate these element boundaries in order to satisfy the *distinguished* free-boundary equations. The locations of the remaining mesh nodes are related algebraically to the free-boundary shapes by constant ratios. These are specified to ensure sufficient resolution near regions of high deformation, such as the curved part of the meniscus, and regions of expected boundary-layer formation. Boundary-layers are expected to form along all the melt boundaries during the flow calculations, as described in Section 1.3.3 and depicted schematically in Figure 1-16. The deformable elements are those which are algebraically related to the crystal radius, melt-solid interface or melt-gas interface shapes. Elements in the melt, crystal and crucible deform in the r- and z-directions. The shapes of the melt-solid interface and melt-gas meniscus are represented by one-dimensional Lagrangian quadratic polynomials $\{\Gamma^j(r)\}$ (Finlayson, 1980), and hence the approximation for interface shape is given by

$$h(r) = \sum_{j=1}^{N_i} h^j \Gamma^j(r), \tag{2.33}$$

where the coefficients $\{h^j\}$ of the approximation are the nodal approximations to the function. The values of the interface shape coefficients are determined by satisfying the equations for the free boundaries which also depend on the field variables T and $\mathbf{v}$. Since the finite elements conform to these interface shapes, the shape of the mesh is coupled through the equations for the free boundaries to the transport equations.

The transport equations are evaluated on each element, and the finite-element method performs identical elemental calculations as a function of elemental shape. To effect this a set of local elemental coordinates (ρ, ζ) are mapped to the global (r, z) coordinates by a biquadratic Lagrangian basis function:

$$r = \sum_{i=1}^{9} r_i \phi^i(\rho, \zeta) \qquad z = \sum_{i=1}^{9} z_i \phi^i(\rho, \zeta), \tag{2.34}$$

where the coordinates of each node are (r_i, z_i) and the biquadratic Lagrangian basis functions defined in terms of (ρ, ζ) are $\{\phi^i(\rho, \zeta)\}$.

In the finite-element framework, the field variables are approximated by expansions in the global basis functions $\Phi^i(r, z)$. Pressure is the one field variable that requires a lower-

order representation (Carey and Oden, 1983), due to its function as a Lagrange multiplier in the continuity equation. It is expanded in piecewise linear functions $\{\Psi^i(r,z)\}$.

$$
\begin{aligned}
T(r,z) &= \sum_{i=1}^{N} T^{(i)}\Phi^i(r,z) \\
\mathbf{v}(r,z) &= \sum_{i=1}^{N_m} \begin{Bmatrix} v_r^{(i)} \\ v_z^{(i)} \\ v_\theta^{(i)} \end{Bmatrix} \Phi^i(r,z) \\
P(r,z) &= \sum_{i=1}^{N_p} P^{(i)}\Psi^i(r,z)
\end{aligned}
$$

N is the total number of nodes, N_m is the number of nodes in the melt and N_p is the number of bilinear nodes in the melt. The coefficients are the finite-element approximations of the nodal values of the field variables.

2.3.2 Formulation of algebraic equations

The field equations are transformed into a weak form by Galerkin's method of weighted residuals. This involves taking the inner product of the equation with the basis functions $\{\Phi^i\}$. The integration is evaluated over all the domains. In the case of the energy equation this treatment yields the following equation:

$$
\begin{aligned}
&\int_m \Phi^i \rho C_p \mathbf{v}\cdot\nabla T dV + \int_s \Phi^i \rho C_p V_p \mathbf{e}_z\cdot\nabla T dV + \int \nabla\Phi^i\cdot(k\nabla T)dV - \int_h \Phi^i j^2\sigma dV \quad (2.35)\\
&\quad - \oint_{h_{m/s}(r)} V_{eff}\Delta H_{fus}\Phi^i(\mathbf{n}\cdot\mathbf{e}_z)dS + \oint_{\delta D}\Phi^i[h_c(T-T_{a^c}) + \sigma_{SB}\epsilon(T^4 - T_{a^r}^4)]dS = 0,
\end{aligned}
$$

where $i = 1,...,N$ denotes the residual equation for each node, m, s and h represent the melt, solid and heater respectively and δD represents the exposed boundary on any domain. The boundary condition for radiation finds its way into the formulation as the natural boundary condition on δD which arises in the weak form due to the integration by parts of the elliptic operator as

$$
\int \Phi^i\nabla\cdot(k\nabla T)dV = \oint \Phi^i(k\mathbf{n}\cdot\nabla T)dS - \int(\nabla\Phi^i)\cdot(k\nabla T)dV. \qquad (2.36)
$$

It injects the coupling between surface nodal temperatures and surface shapes through the artificial variable T_{a^r}. Nine-point Gaussian quadrature is used to evaluate all volume integrals and three-point all surface integrals. With the numerical integration the PDE's

are converted into nonlinear algebraic equations.

The momentum transport equation is handled similarly

$$\int_m \boldsymbol{\Phi}^i \rho \mathbf{v} \cdot \boldsymbol{\nabla} \mathbf{v} dV - \int_m \boldsymbol{\nabla} \boldsymbol{\Phi}^i P dV + \int_m \boldsymbol{\nabla} \boldsymbol{\Phi}^i \cdot \left[\mu \left(\boldsymbol{\nabla} \mathbf{v} + \boldsymbol{\nabla} \mathbf{v}^\dagger \right) \right] dV \tag{2.37}$$

$$- \int_m \boldsymbol{\Phi}^i \cdot \mathbf{e}_z g \beta \rho (T - T_{m.p.}) dV \tag{2.38}$$

$$- \oint_{h_{m/g}(r)} \boldsymbol{\Phi}^i \mathbf{n} : \left[-P\mathbf{I} + \left[\mu \left(\boldsymbol{\nabla} \mathbf{v} + \boldsymbol{\nabla} \mathbf{v}^\dagger \right) \right] \right] dS = 0,$$

where $\{\boldsymbol{\Phi}^i\}$ represents the basis function $\{\Phi^i\}$ multiplied by the three unit vectors $\{\mathbf{e}_r, \mathbf{e}_\theta, \mathbf{e}_z\}$ for each component of the velocity in the melt. The natural boundary condition involving stress is a practical concern only on the melt-gas interface, owing to the thermocapillary boundary condition. The boundary conditions for the momentum equation are a mixture of essential (velocity) and natural (stress) conditions. The no-slip and no-penetration conditions are enforced on the solid boundaries in a strong sense by setting v_r and v_z to zero and v_θ to $r\Omega$. Along the boundary at the centerline both v_r and v_θ are set to zero and the tangential stress is set as

$$\mathbf{e}_z \mathbf{n} : \boldsymbol{\sigma} = \mu \frac{\partial v_z}{\partial r} = 0. \tag{2.39}$$

The boundary conditions on the melt-gas meniscus are more involved. The condition of no penetration is satisfied in the integral sense

$$\oint^{m/g} \Phi^i \mathbf{v} \cdot \mathbf{n} dS = 0 \tag{2.40}$$

and is used to replace the z-component of the momentum equation. The stressed condition of the meniscus is accounted for by the integral of the r-component of the interfacial stress

$$\begin{aligned} \oint_{m/g} \boldsymbol{\Phi}^i \mathbf{e}_r \mathbf{n} : \boldsymbol{\sigma} dS &= \oint_{m/g} \Phi^i h_{m/g}(r)' P \\ &+ \oint_{m/g} \Phi^i 2\mu \frac{h'_{m/g}(r)}{1 + (h'_{m/g}(r))^2} \left[-(h'_{m/g}(r))^2 \frac{\partial v_r}{\partial r} \right. \\ &\left. + h'_{m/g}(r) \left(\frac{\partial v_z}{\partial r} + \frac{\partial v_r}{\partial z} \right) - \frac{\partial v_z}{\partial z} \right] dS \\ &+ \oint_{m/g} \Phi^i \gamma_T \frac{\frac{\partial T}{\partial r}}{\left[1 + (h'_{m/g}(r))^2 \right]^{3/2}} dS \end{aligned} \tag{2.41}$$

wherein the third term on the right-hand-side of the equation provides the thermocapillary force.

For the incompressibility condition, the Galerkin weighted residual method is applied with the linear basis function

$$\int_m \Psi^j \nabla \cdot \mathbf{v} dV = 0, \tag{2.42}$$

where $\{\Psi^i\}$ represents the basis function $\{\Psi^i\}$ multiplied by the unit vectors $\{\mathbf{e}_r, 0, \mathbf{e}_z\}$ for each velocity component in the continuity equation. This equation is consistent with the kinematic condition on velocity. Pressure functions as a Lagrange multiplier for the continuity equation. However, since only gradients of pressure appear in any equation, an arbitrary reference pressure $P(0,0) = 0$ is imposed to remove the indeterminacy.

The free-boundary equations are treated with both integral and pointwise formulations. The melt-solid interface equation provides the coupling between the temperature field and the interface shape. It is formulated as a residual equation

$$\oint_{r=0}^{r=R_s} \Gamma^i [T(r, h_{m/s}(r)) - T_{m.p.}] dS = 0 \tag{2.43}$$

The modified Laplace-Young equation provides the shape of the meniscus. It is coupled weakly with the flow field through the term for the fluid normal force and is solved as an integral condition

$$\oint_{r=R_s}^{r=R_c} \left\{ \gamma \frac{(\Gamma^i)' h'_{m/g}(r)}{\sqrt{1 + (h'_{m/g})^2}} + \Gamma^i [\rho g (h_{m/g}(r) + \lambda) - \mathbf{nn} : \sigma] \right\} dS + \gamma \Gamma^{i=1} (\cos 11^\circ) = 0. \tag{2.44}$$

The wetting angles at the crystal and crucible are included as natural boundary conditions for the modified Laplace-Young equation, as first done by Derby and Brown, 1986. Only the growth angle of 11° is included in Equation (2.44), because the crucible wetting angle of 90° yields a zero contribution since $(\cos 90^\circ) = 0$. The volume constraint and wetting angle conditions are also included as residual equations. The volume constraint is formulated as a weighted integral condition.

2.3.3 Solution procedure

The residual equations (2.35)-(2.44) form a vector of nonlinear algebraic equations,

$$\mathbf{R}(\mathbf{x}; p) = \mathbf{0}, \tag{2.45}$$

where $\mathbf{x}$ is the solution vector and p is a parameter which may be varied to compute different solutions. The nonlinearities arise from the temperature-dependent conductivity and radiative boundary conditions in the energy equation, the convective transport term in both the momentum and energy equations, the curvature term in the normal force balance on the meniscus and the dependence of all the transport equations on the free boundary shapes. To accommodate these nonlinearities an iterative solution method is required. The Newton/Raphson method has been the method of choice for most of the TCM manifestations, due to its potential for quadratic convergence for even highly nonlinear equations, and it is adopted here. The potential advantages of other methods are barely mentioned in this section since this study focusses on the accuracy of the physical depiction.

Newton's method takes an initial guess of the solution vector $(\mathbf{x};p)$, and updates it according to the following relation, until the residual vector $\mathbf{R}(\mathbf{x};p)$, is approximately zero:

$$(\mathbf{x};p)^{i+1} = (\mathbf{x};p)^{i} - [\mathbf{J}(\mathbf{x};p)^{i}]^{-1}\mathbf{R}(\mathbf{x};p)^{i}. \tag{2.46}$$

By using the complete Jacobian matrix $\mathbf{J}(\mathbf{x};p)^{i} = \nabla\mathbf{R}(\mathbf{x};p)^{i}$. all interactions between the temperature field and interface shapes are accounted for in the iterative procedure and quadratic convergence results, given a close enough initial guess. Quadratic convergence describes an iterative procedure where the dimensionless solution error is the square of the error at the previous iteration, i.e. $error^{i+1} = C(error^{i})^{2}$, where C is a constant. An example of quadratic convergence as compared to linear convergence is shown in Figure 2-4, and demonstrates that quadratic convergence typically requires only several iterations to reach an effective error criterion of 10^{-6} or less. This rapid quadratic convergence is the primary attraction of Newton's method..

The disadvantage of Newton's method is that the Jacobian matrix has to be computed and factorized each iteration. Therefore the sparsity of the Jacobian matrix determines the computational burden. On a fixed mesh with no radiative boundary conditions the Jacobian has a banded structure, due to the coupling of unknown coefficients to the other nodal values in the same element (Thomas et al., 1987). For the quadrilateral elements used here, a particular nodal value is coupled to values in a maximum of four elements, resulting in the Jacobian structure shown schematically in Figure 2-5a. The size and shape of the dense part of the matrix is important because numerical operations need be performed only on these entries. The frontal solution procedure used in this work avoids storage of the complete Jacobian matrix by writing the vectors of the factorized "U" part of the Jacobian matrix to out-of-core storage as soon as they have been formed by LU

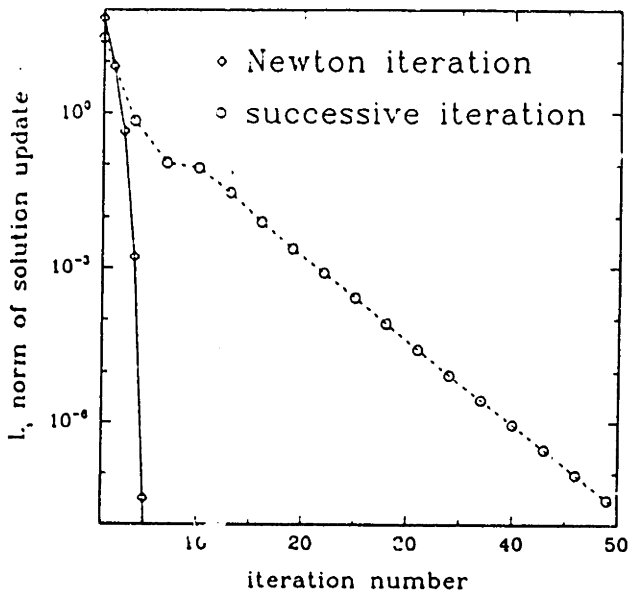

Figure 2-4: Plot showing iterative procedures with both quadratic and linear convergence rates, from Bornside et al., 1990.

decomposition, and thus freeing core storage space.

In the frontal solution method used in this work matrix elimination is performed within an *active matrix*, which is formed during the march through the finite-element grid (see Figure 2-5a). It receives contributions from those equations which are not fully formed. The number of operations for LU decomposition of $\mathbf{J}(\mathbf{x};p)^i$ depends on the total number of equations and the dimensions of this active front (Hood, 1976). The *frontwidth*, i.e. the maximum length of a vector in the active matrix, was lowered by marching in the direction of thinnest mesh cross-section. Because CZ melts are typically shallow, the mesh is assembled and eliminated by marching in the vertical z-direction, in contrast to previous TCM's.

The addition of free-boundary dependence defies this banded structure, introducing additional structure within and outside of the previous band. The shape unknowns are coupled to all equations within the band, not just the adjacent elements, so the interface shapes appear as vertical lines stretching the entire bandwidth; see Figure 2-5b. In addition, the melt volume constraint is coupled to all the interface shape values, and so a *single* equation appears as an extra row to the previous banded structure, forming the so-called arrow matrix structure. This extra equation carried can be carried in the active matrix through the entire factorization or included at the bottom of the matrix;

in either case the frontwidth increases during the march through the elements by the growing number of surface unknowns encountered until they are all are accounted for; at that time the volume constraint can be solved.

Another change in the Jacobian matrix structure is caused byto the radiation modelling, which most perturbs the banded structure. Surface nodal values of temperature and position become coupled to the determining equations of one another. In the present formulation every central surface temperature node is coupled to every other and to every noncentral shape variable on moving element boundaries (see Figures 2-6 and 2-5c). This violates the sparsity of the Jacobian matrix introducing an additional sparse pattern particular to the surface geometry. The size of the active matrix becomes larger by a dimension equal to the number of surface elements in the radiation enclosure (temperature dependence) plus the number of moving surface elements (moving-boundary dependence). This is unavoidable with the full Newton method; the following paragraph describes developmental phases of the IHTCM which avoided this large frontwidth increase.

The first implementation of the IHTCM had a much smaller bandwidth with the radiative enclosure split by an imaginary wall extending upward from the crucible to the chamber top. That approach was eliminated because the imaginary wall was an artifice which could be justified only when the crucible blocks almost all radiation from the heater moving inward. It restricted the flexibility of the model, preventing alternative arrangements, which could be used for lowering thermal stress in the crystal; see Bornside et al., 1991 for examples. Nonetheless, an approach with segregated radiation enclosures could be used with considerable cost savings if there were to be a long-term dedicated effort on one particular geometry. In the present model, only the cavity between the heat shield and the chamber wall is fully segregated from the main radiative enclosure.

That first stage in the model's development considered all components within the susceptor as a module and the heater and heat shield as a distinct module. Separate iterations were carried out for the two units in sequence, with the effective ambient temperatures being updated each iteration (Bornside et al., 1990). This multiple-iteration scheme converged linearly with the number of iterations, and was more costly than the full Newton method. Other quasi-Newton methods have not been extensively tested, but could provide a cost-effective alternative to the full-Newton formulation, especially for flow calculations where temperatures external to the melt change little. Srivastava et al., 1985 describe such a method, for example.

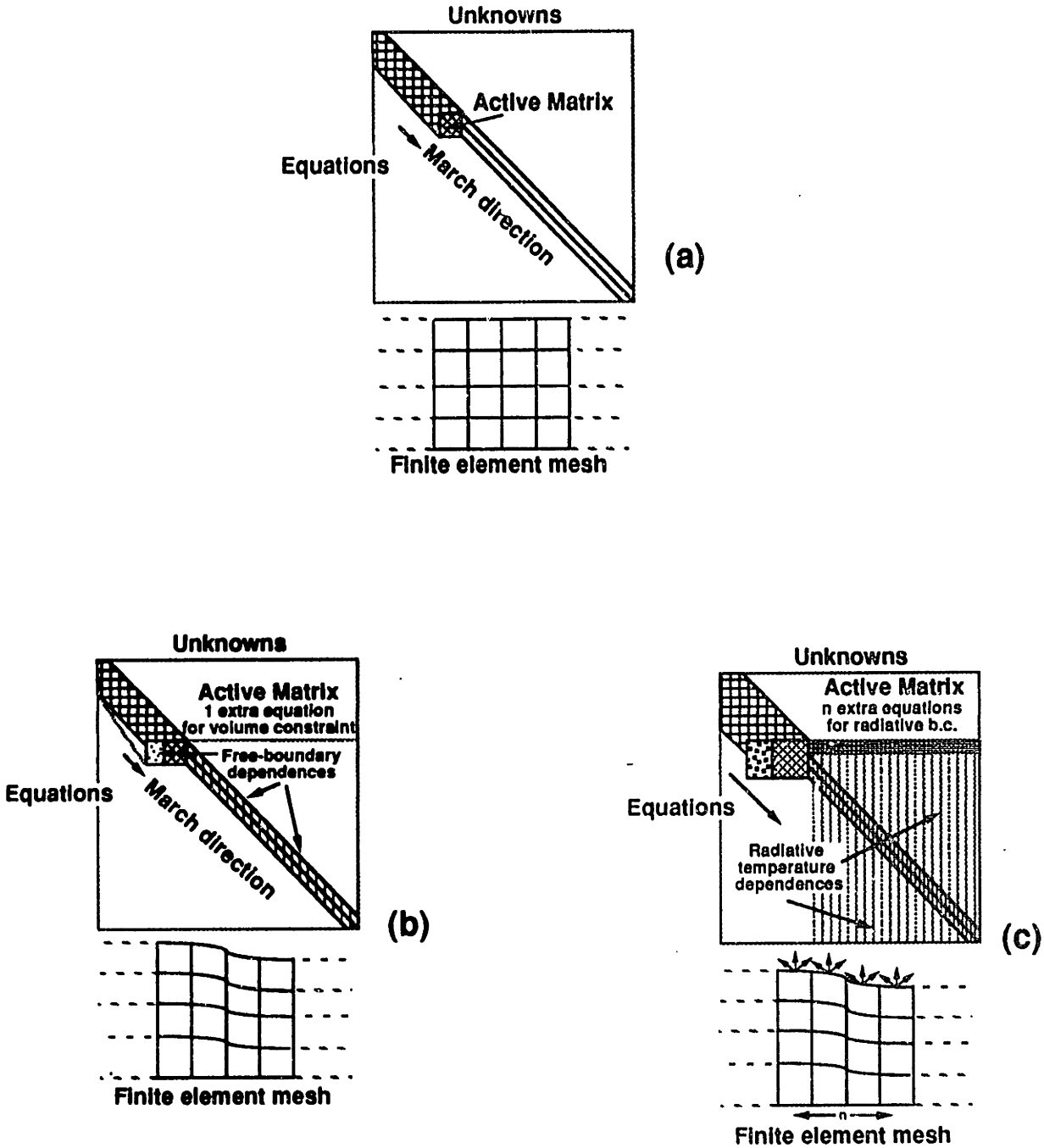

Figure 2-5: Structure of the Jacobian matrix: (a) with a fixed mesh, (b) with a deformable mesh, and (c) with a moving mesh and radiation.

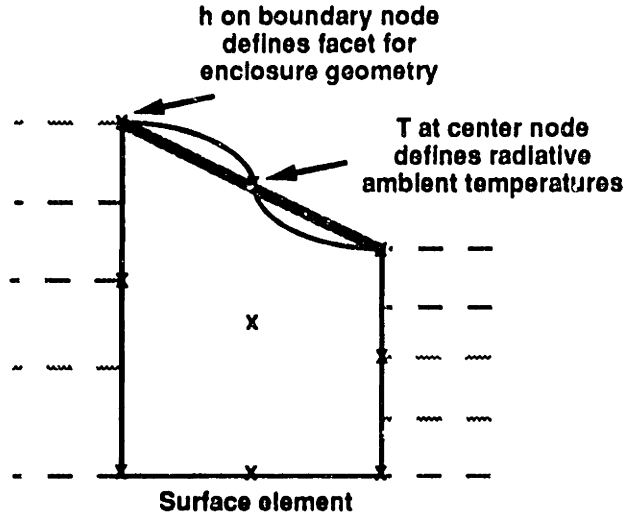

Figure 2-6: Surface element for radiation treatment in the IHTCM.

2.3.4 View factor calculation

Radiation modelling was first added to the TCM by Atherton et al., 1987 using the FACET routines (Shapiro, 1983) which compute view factors using discretization in all three spatial coordinates. The implementation coupled conductive heat transfer and interface shapes to radiative transfer using Gebhart's method. Derivatives of the ambient temperatures with respect to the interface shape variables were not implemented, although the nonlinearity due to these derivatives does not require more iterations for error criterion of more than about 10^{-6}. Calculation of the view factors alone took as much time as a single Newton iteration for the purely thermal model. The FACET routines since have been partially supplanted with analytical expressions for simple axisymmetric shapes, which avoid azimuthal discretization (Bornside et al., 1990). For a given view factor, the analytical calculation is faster by the order of the azimuthal discretization. Unfortunately the analytical scheme is restricted to monotonically varying shapes. All elements outside the crucible are calculated using an updated version of FACET. Also, the meniscus shape deforms slightly due to fluid normal stresses and this shape cannot be computed with the analytical expressions, so a complex hybrid procedure is now in place. The present model has eliminated moving mesh on the susceptor's outer boundaries so that the view factors outside of the crucible need to be calculated only once per converged

solution. The derivatives of the Gebhart factors with respect to the interface positions for the Jacobian matrix are approximated using a finite-difference approximation with the analytical view factors. The fixed view factors are calculated with FACET, and need to be calculated only once because these surface shapes do not change between successive iterations.

2.4 Test Simulations

A number of computer simulations were performed to understand the heat transfer and convection in the Siltec system, to test the sensitivity of the results to variations of the parameters, and to test the importance of convection in the melt for predicting global heat transfer and melt/crystal interface morphology. Simulations to test the model were performed by omitting convection altogether and by decoupling the four mechanisms for convection in the melt: buoyancy-driven convection, thermocapillary motion, and crystal and crucible rotation. Results of this kind demonstrate the correctness of the IHTCM's depiction of the system physics. This section serves both to gauge the ability of the IHTCM to model the heat transfer, convection and free boundaries of the CZ system, and to judge the relative magnitude of the individual driving forces for heat transport the flow field and the free-boundary shapes.

2.4.1 Conduction-Dominated Case

As a starting point, the result of a simulation for the SILTEC system without convection in the melt is shown in Figure 2-7 along with the mesh which contains 11007 nodes over 2656 elements. A fine discretization is used in the melt (see Figure 2-8) in anticipation of the resolution required for the boundary layers in the fluid flow. The power to the heater needed for balancing heat transfer in the simulation is listed in Table 2.5 along with other important benchmarks of the calculation. The power to the heater $\mathcal{P} = 45kW$ is an upper bound on the requirement for the real system, because convective heat transfer in the melt lowers the required heater temperature and the needed energy. The case of conduction-dominated heat transfer also gives the maximum temperature gradients; the maximum heater temperature is $1955K$ and the temperature difference between the lower outer corner of the melt and the melt/solid interface is $124.4K$. The melt/crystal interface is predicted to be concave with a deflection of $-2.0mm$.

Including radiation in the model provides heat transfer between all surfaces and ac-

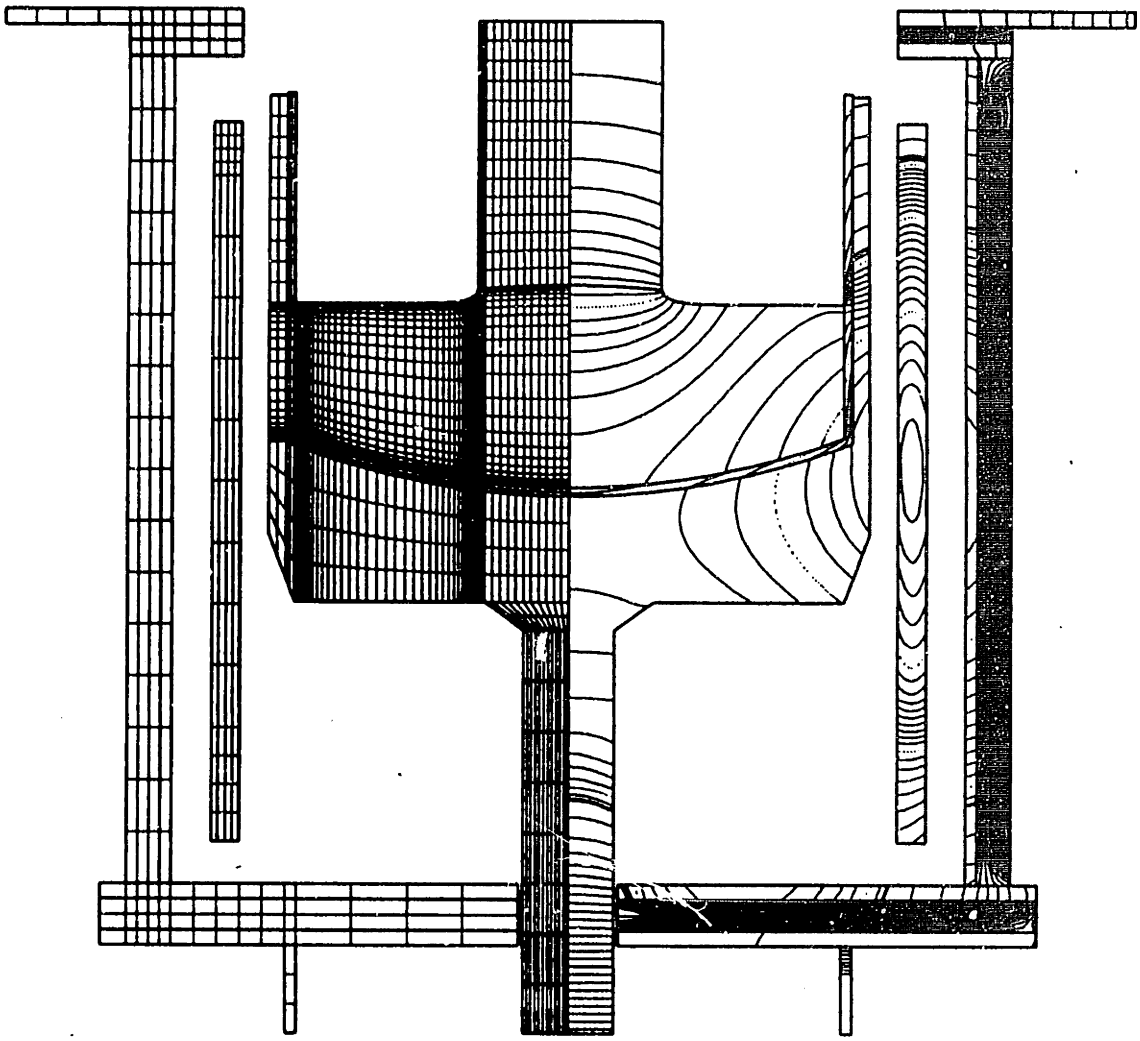

Figure 2-7: Simulation with no melt flow showing the entire thermal field and the finite-element mesh. The melting-point isotherm at $1683K$ is indicated by a thicker line. Isotherm spacing is every $10K$ starting at $1690K$ and every $50K$ below $1650K$. Dotted lines are every $100K$ starting at $1700K$.

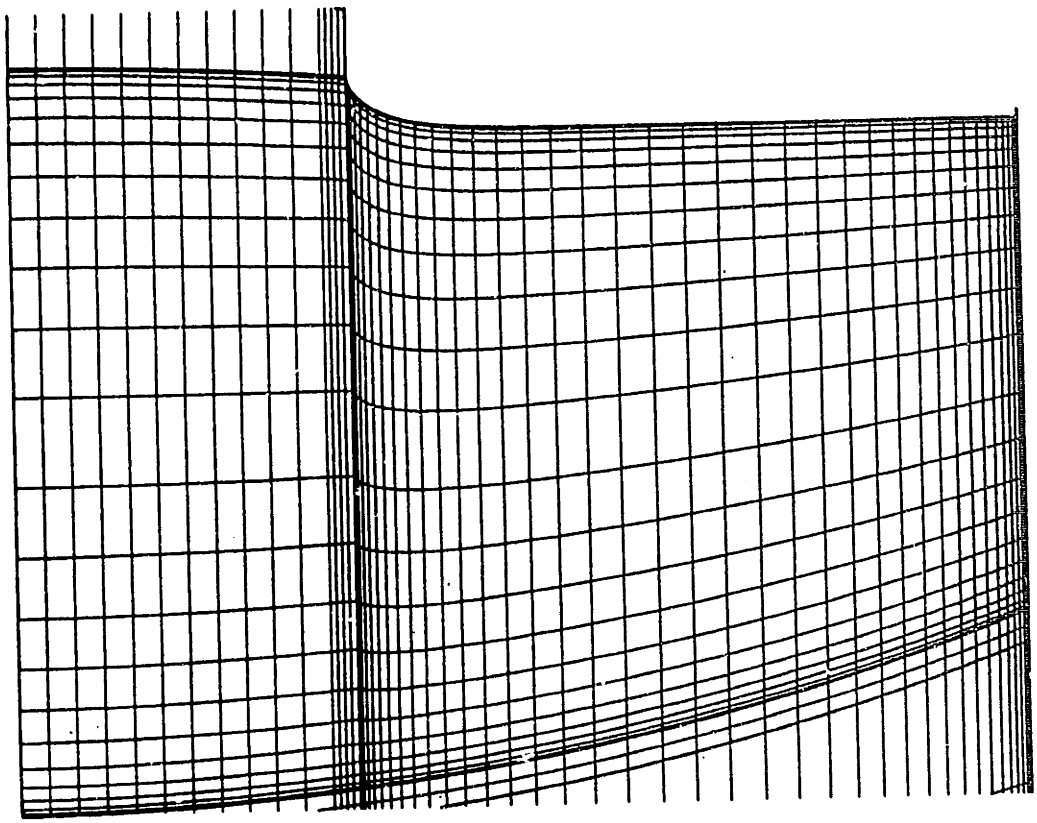

Figure 2-8: Mesh in melt region only. Smaller elements are included along the surfaces to resolve the boundary-layers that are expected to form there. There are 25 elements in the vertical direction and 55 elements in the horizontal direction.

cordingly each exposed surface element has a unique radiative ambient temperature. The radiative ambient temperatures for elements contained within the susceptor are compared with the surface temperatures in Figures 2-9a-f. These ambient temperatures vary considerably. The relative position of the ambient and surface temperatures reveal the direction of radiative heat flow in the system. Radiative loss only occurs from the crucible, melt, crystal top and susceptor bottom surfaces. The crystal peripheral surface is seen to lose heat by radiation for an axial distance of approximately one crystal radius from the trijunction, but up higher gains heat by radiation. This high lateral heat flow close to the trijunction is expected to yield high thermal stresses there. Although radiative ambient temperature profiles could be fixed in order to lower the computation time, selecting a single radiative ambient temperature for any surface would neglect important variations that change the thermal gradients which drive convection in the melt and stress in the crystal.

The importance of the thermal field is in the gradients which give rise to natural convection in the melt and thermal stress in the crystal. The von Mises invariant of the thermoelastic stress tensor in the crystal for the conduction-dominated simulation is shown in Figure 2-10 in units of the critical resolved shear stress at the melting point. It is seen that the maximum along the melt/solid interface of $4.1 \times CRSS$ is also a local maximum, where the $CRSS = 1.87MPa$. The maximum thermal stress in the cases evaluated for sensitivity show similar patterns and extremal values. It has been shown (Bornside et al., 1991) that extensive design and pull rate changes must be made in order to achieve order-of-magnitude reductions in the thermal stress.

The thermal field in Figure 2-7 depends on many thermal conductivities and emissivities of which the emissivities have the most experimental variation, as described in Section 1.4. The sensitivity of the simulation results with respect to variations in these parameters is explored here in point form and summarized in Table 2.4.

- The emissivity of solid graphite used for these simulations is lower than the reported average (Touloukian, 1970), as justified in Section 1.4. The effect of changing the graphite emissivity from 0.65 to 1.0 is to drop the heater temperature substantially; the maximum temperature in the heater T_{max} drops from $1955K$ to $1911K$, but important measures of the thermal field inside the crucible, ΔT_m, Δh and τ_{max} change little.

- Lowering the conductivity of the insulation by an order-of-magnitude reduces the required heater power to $34.3kW$ as less heat is lost through the shields to the

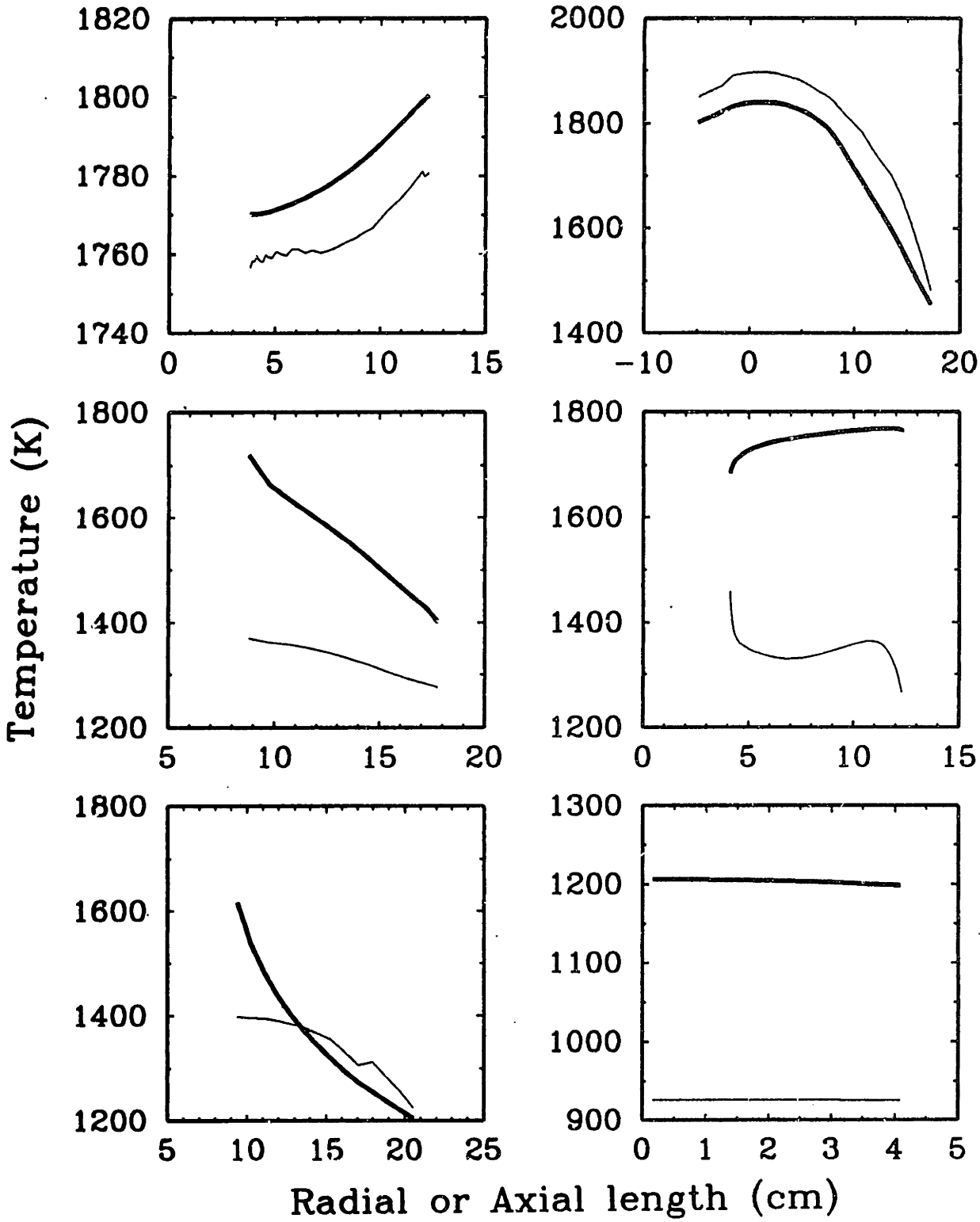

Figure 2-9: Profiles of radiative ambient temperature and surface temperature along (a) susceptor bottom, (b) susceptor wall, (c) crucible wall, (d) melt surface, (e) crystal radial surface, and (f) crystal top surfaces: bold curves signify surface temperatures and thin curves are the radiative ambient temperatures.

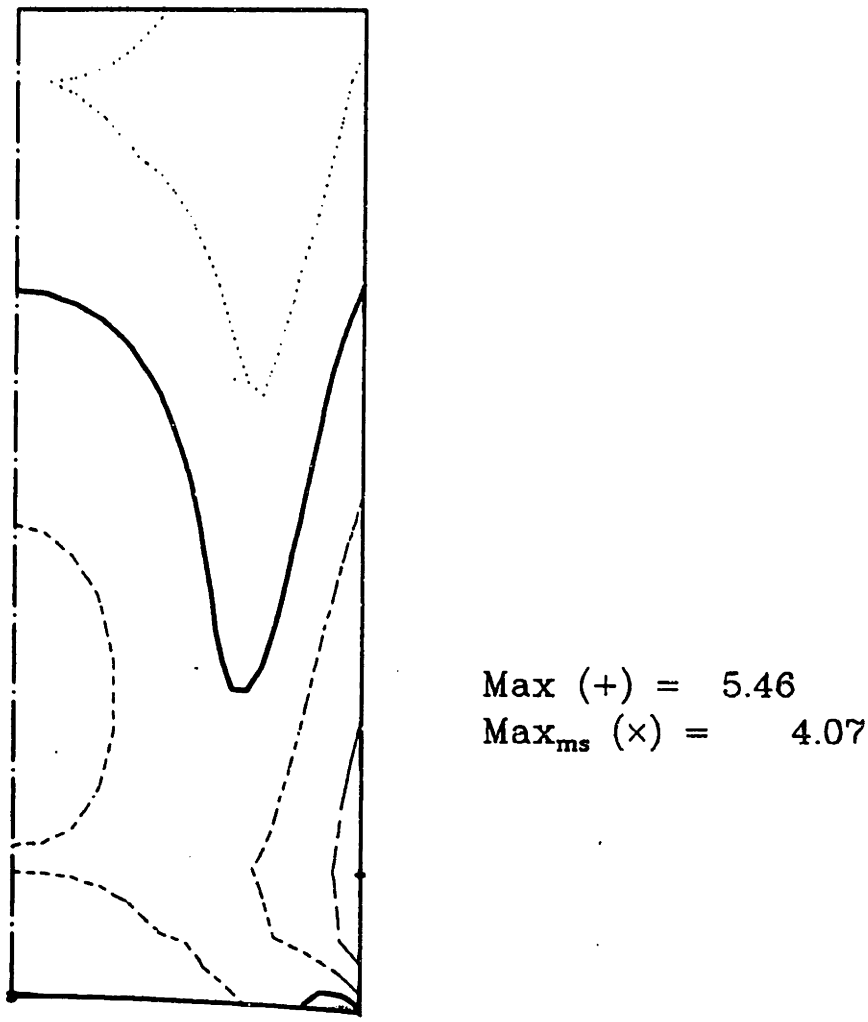

Figure 2-10: Prediction of the von Mises stress in the crystal for conduction-dominated case. Stress contours are 0.5, 1, 2, 4 and 8 times the value of the CRSS; CRSS=1.8 × $10^7 dyn \cdot cm^{-2}$. The maximum stress is 5.5 times the CRSS and is located on the crystal radial surface; the maximum stress at the melt/solid interface is 4.1 times the CRSS and is located at the centerline.

surroundings, but again the critical measures of thermal gradient inside the crucible change little. The temperature gradient in the melt ΔT_m decreases very slightly to $121.9K$ from 124.4.

- The treatment of the heater as explained in Section 2.2 is unique to this work, and increasing the cutout factor to 0.33 primarily increases the heater temperature to $1971K$, the thermal field within the susceptor changing little, as ΔT_m decreases only $0.9K$..

- The thermal field throughout the chamber is only marginally affected by a change in the chamber wall emissivity from 0.5 to 0.3, because the chamber is already well-insulated. A better-insulated chamber loses less heat, and T^{max} and ΔT_m are reduced to $1944K$ and $117.6K$, respectively. The melt is affected because the chamber wall exchanges radiation directly with the surfaces contained by the susceptor.

- When the emissivity of the top surface changes from 0.07 to 0.3 very little increase is observed in the thermal gradient. This change was made in addition to decreasing the conductivity of the felt insulation.

These changes could be realized by selecting different materials, or by surface contamination during growth. They point to the utility of the model for design alterations. However, it appears that there is little to gain by changing the properties of the outer components besides reducing the power requirement, since the critical measures of the thermal field within the crucible are hardly sensitive to these changes.

A more subtle effect is the sensitivity to the emissivity of the crucible wall, which produces some change to the thermal field under conduction-dominated conditions, but prevents model solution at high driving forces for natural convection. It is seen from Figure 2.4.1a that the temperature field in the crucible changes with increased crucible emissivity. At the higher emissivity the crucible acts as a more effective heat transfer fin, giving locally lower temperatures. The effect of this in the melt is largest near the trijunction between melt, crucible wall and ambient, where the temperature is noticeably depressed. Along the melt surface the temperature approaches a constant value toward the crucible wall in the base-simulation in Figure 2-7. The temperature along the melt surface in Figure 2.4.1a passes through a maximum and then decreases toward the crucible wall. This reversal in the surface temperature gradient produces strong driving forces for secondary natural convective motion opposite to the primary flows. With increasing

Table 2.4: Summary of sensitivity results.

Change	Amount	T_{max}	$\mathcal{P}$	ΔT_m	Δh	τ_{max}	$(\tau_{m/s})^{max}$
None	$\bowtie$	1955	45.0	124.4	-2.0	5.5	4.1
Graphite ϵ	$0.65 \rightarrow 1.00$	1911	45.9	125.7	-1.9	5.4	4.0
felt k	$4 \times 10^{-3} \rightarrow 4 \times 10^{-4}$	1935	34.3	121.9	-2.1	5.5	4.1
top ϵ	$0.07 \rightarrow 0.30$	1939	34.6	124.6	-2.0	5.6	4.2
cutout factor Ξ	$0.22 \rightarrow 0.33$	1971	44.6	123.5	-2.0	5.5	4.1
wall ϵ	$0.50 \rightarrow 0.30$	1944	43.2	117.6	-2.3	5.3	4.0
crucible ϵ	$0.25 \rightarrow 0.59$	1947	45.4	112.0	-2.4	4.9	3.7
melt k[4]	$0.64 \rightarrow 32.0$	1854	39.9	2.9	-1.4	5.9	4.3
view factors[5]		1922	43.1	99.1	-1.9	4.8	3.3

[4] This simulation was done to estimate the effect of high convection.

[5] This simulation was done to estimate the effect of specular radiation.

convection the melt becomes more isothermal and the melting-point isotherm enters the melt at this corner; see Figure 2.4.1b. No solution was found above certain values of the buoyancy and thermocapillary coefficient. This is attributed to the melting point isotherm tending to stretch across the entire melt surface, rendering the radius set-point unobtainable. Whether the observation of flaring which occurs in practice is due to this same phenomenon is unknown; however, reports of difficulties associated with transparent quartz crucibles which transmit more heat than fused silica were made by the experimental collaborators in this project (Strudwick and Kim, 1988).

The effect of specular radiation cannot be explored rigorously with the present model. However, qualitative effects can be predicted in an *ad hoc* way by assuming that all radiation from the crystal that reaches the melt surface is reflected directly across to the crucible wall. This eliminates the radiation lost by diffuse reflection off the melt surface to the ambient above, and approximates the specular view factor $F_{kj(i)}$, as explained in Section 2.2. This change was implemented as a test case by increasing the view factors between the elements on the crystal wall and opposing elements on the crucible by the summation of all view factors to the melt surface. In addition, the melt reflectivity was set to 1.0 and the crucible emissivity was increased to 0.59. This change increased the heat transfer in the horizontal direction across the annular gap, and lowered the maximum thermal stress at the interface by 10% to $3.3 \times CRSS$, as shown in Figure 2-12. Accounting for detailed specular interactions would likely change the stress by a similar amount.

The melt-solid interface shape has been solved analytically by Wilcox and Duty, 1966

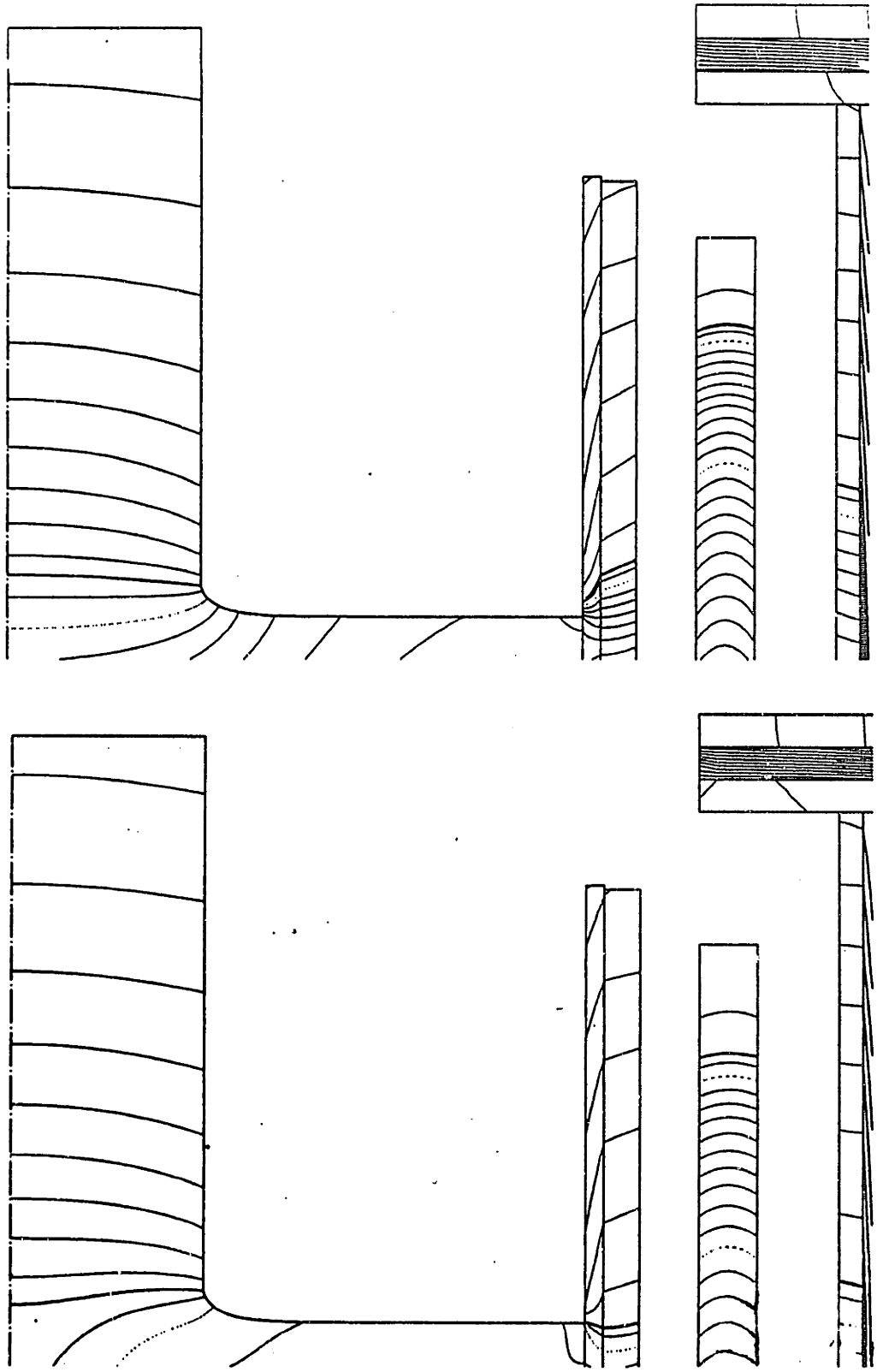

Figure 2-11: Sensitivity of computed temperature field to crucible emissivity; (a) $\epsilon_c = 0.59$ with no convection and (b) $\epsilon_c = 0.59$ with natural convection as the only driving force for flow. The melting-point isotherm at $1683K$ is indicated by a thicker line and begins to enter the melt at the crucible/melt/ambient trijunction in (b). Isotherm spacing is every $10K$ starting at $1690K$ and every $50K$ below $1650K$. Dotted lines are every $100K$ starting at $1700K$.

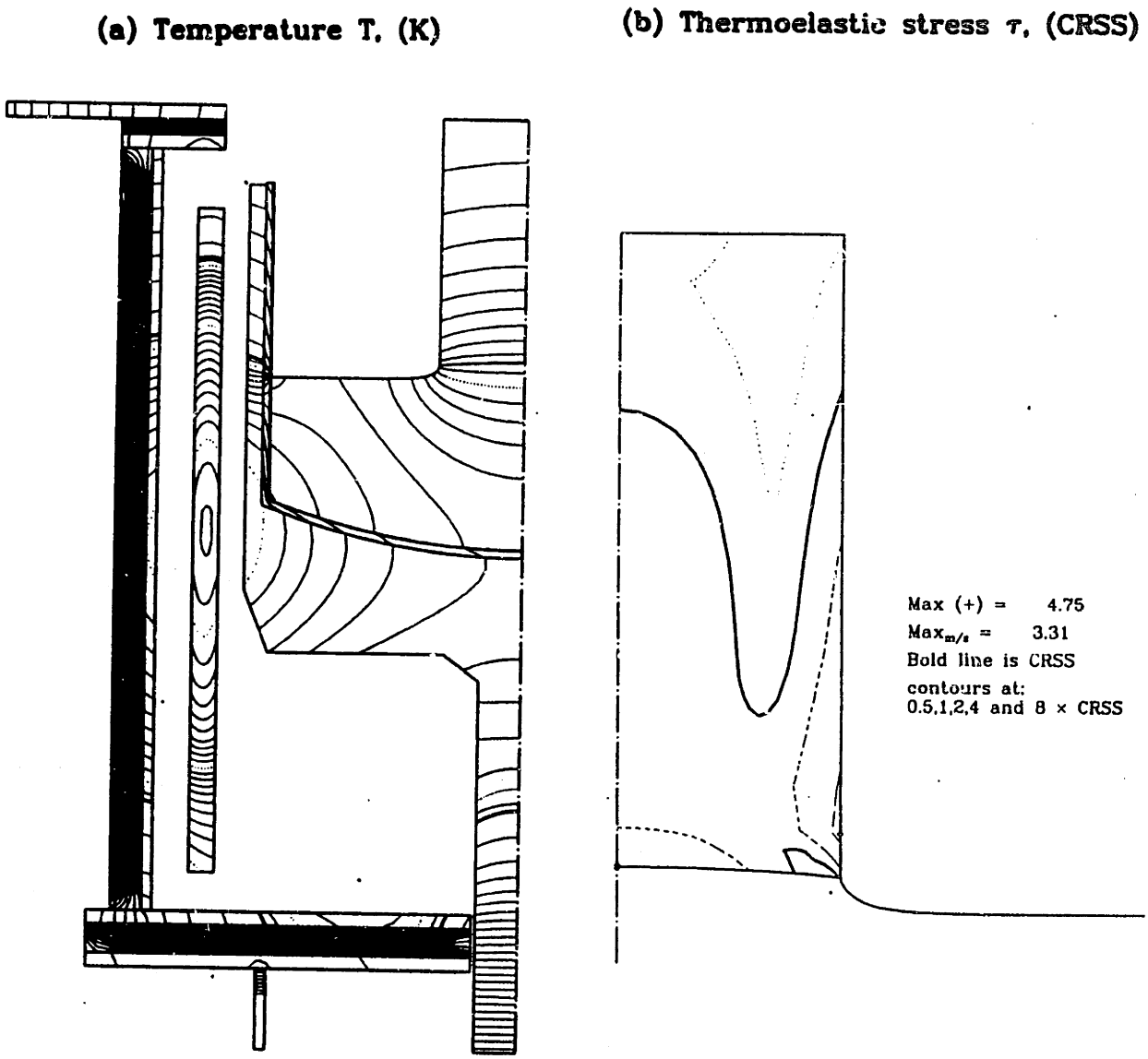

Figure 2-12: Simulation with no melt flow to estimate the effect of specular reflections. Prediction of (a) temperature field, and (b) von Mises stress in the crystal, are shown. The melting-point isotherm at $1683K$ is indicated by a thicker line in (a). Isotherm spacing is every $10K$ starting at $1690K$ and every $50K$ below $1650K$. Dotted lines are every $100K$ starting at $1700K$. In (b), stress contours are 0.5, 1, 2, 4 and 8 times the value of the CRSS; CRSS=$1.8 \times 10^7 dyn \cdot cm^{-2}$.

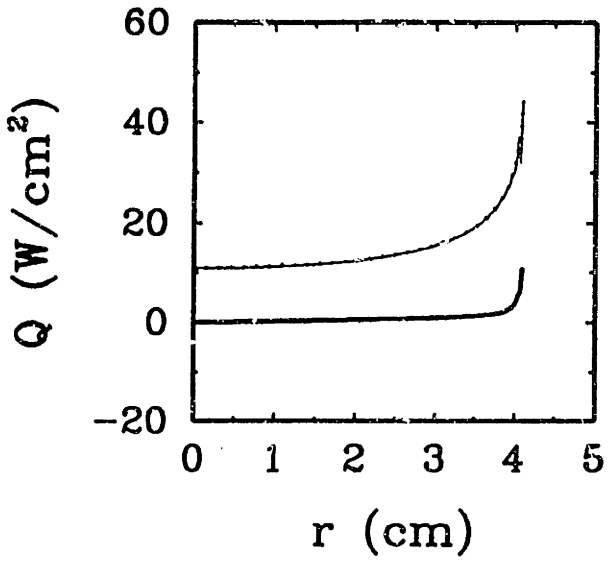

Figure 2-13: Heat flux across the melt/solid interface taken from the conduction dominated simulation in Figure 2-7. Shown are the vertical heat flux at trijunction height (···), vertical heat flux at interface (——) and lateral heat flux at interface (——).

using a Bessel-function solution as described Section 1.3.1. This solution can be compared with the melt-solid interface shape from the conduction-dominated simulation. First the validity of the assumption of constant vertical heat flux at the level of the trijunction is checked. The horizontal plane at a height equal to the trijunction height is taken as the basis for this determination. The plot of heat flux versus radial coordinate in Figure 2-13 shows that the heat flux is fairly constant between $0 \leq r \leq 0.75R_s$, and then increases rapidly toward the trijunction. The analytical approximation is made by calculating an effective linear heat transfer coefficient $H \sim 0.04$ based on the chamber wall temperature. The analytical result for this parameter value is $\Delta h = 2.5mm$ (Wilcox and Duty, 1966), which is in reasonable agreement with the calculated $2.0mm$. Perhaps the most important conclusion from this positive comparison is that an analytical expression can be used under conduction-dominated conditions that are realized under microgravity, under high magnetic field or in extremely small systems, to infer the melt-solid interface deflection online. Results that follow show the high sensitivity of interface shape to convection, which defies analytical approximation.

The basic temperature gradients that drive buoyant and thermocapillary motions are clearly seen in Figure 2-7. A negative vertical and positive horizontal temperature

gradient exist to drive the established patterns of buoyant and thermocapillary convection. The temperature gradient in the melt is far from uniform though, and near the trijunction between melt, crystal and ambient the isotherms are nearly horizontal . As convection lowers temperatures throughout the melt, a cell rotating in the opposite sense to the main flow will develop in this corner, driven by a small negative radial temperature gradient. The Grashof number $Gr = \frac{\beta\rho^2}{\mu^2} g\Delta T_m \ (R_c^3)$, scaled with the temperature difference from the conduction-dominated simulation is 3.5×10^{10} and the Marangoni number is 2.3×10^6; so convection is expected to be intense, although these scalings will change as temperatures decrease in the melt due to convection. The effect of convection on the melt is qualitatively predicted in a gross sense by increasing the melt conductivity. Setting the melt conductivity to 50 times the actual value yields a much reduced melt thermal gradient, but the thermal stress in the crystal is almost unaffected. This simulation cannot account properly for the melt/solid interface shape, since the details of convective transport are not accounted for by isotropic conduction.

2.4.2 Melt Convection Cases

The flows driven by the different mechanisms for convection are isolated in the calculations displayed in Figures 2-14–2-31, where results are given for crystal rotation (Figure 2-14), crucible rotation (Figure 2-17), combined rotations (Figure 2-21), thermocapillary motion (Figure 2-26) and buoyancy-driven motion (Figure 2-31). In each case, the calculations are for the conditions of operation of the SILTEC system listed in Table 2.2, but with the other flow mechanisms suppressed. Contours are shown of the temperature field throughout the system, the streamlines in the (r, z) plane and the azimuthal velocity v_θ. Pertinent parameters and results for each of the simulations are listed in Table 2.5. Results listed there include the power $\mathcal{P}$ to the heater, the temperature difference across the melt surface ΔT, the circulation rate ψ_{max} of the most intense meridional flows in the melt and the maximum stress at the melt/solid interface $(\tau_{m/s})^{max}$.

Crystal Rotation

The simplest flow in the CZ geometry is driven by crystal rotation in the absence of crucible rotation or buoyancy. Crystal rotation, as demonstrated in Figure 2-14, drives a meridional flow depicted in the clockwise direction; fluid is thrown outward by centrifugal force and recirculates because of mass conservation to rise under the crystal. The impact of hot melt flowing toward and outward along the melt/crystal interface increases vertical

Table 2.5: Summary of results from simulations with no convection, and individual flow mechanisms.

Driving Force	T_{max} (K)	$\mathcal{P}$ (kW)	ΔT_m (K)	Δh (mm)
No Flow	1955	45.0	124.4	-2.0
Crucible Rotation	1952	44.8	122	0.0
Crystal Rotation	1930	43.8	93.2	-6.0
Both Rotations	1952	44.8	122	-0.2
Thermocapillarity	1878	41.7	34.3	9.0
Buoyancy	1882	41.2	40.6	4.2

Driving Force	ψ_{max} $(cm^3 \cdot s^{-1})$	ψ_{min} $(cm^3 \cdot s^{-1})$	$(v_\theta)_{max}$ $(cm \cdot s^{-1})$	$(v_\theta)_{min}$ $(cm \cdot s^{-1})$	$(\tau_{m/s})^{max}$ $(CRSS)$
No Flow	0	0	0	0	4.1
Crucible Rotation	0	-0.18	0.0	-10.3	3.2
Crystal Rotation	12.1	-0.16	8.6	0.0	6.2
Both Rotations	0.60	-0.42	8.6	-10.3	2.9
Thermocapillarity	11.7	-24.4	0.0	0.0	4.1
Buoyancy	9.0	-41.1	0.0	0.0	2.8

lateral heat transfer at the melt/solid interface, as shown in Figure 2-15. This causes the interface to become increasingly concave, which contrasts the results which follow for other convection mechanisms. The flow field near a rotating disk in a semi-infinite fluid is described by the von Kármán similarity form, and the analytical form for v_z has been given in Equation (1.10). Sackinger, 1989 demonstrated that the HTCM satisfies this limit at small radii. That analysis is duplicated here, and the comparison in Figures 2-16a-c shows that the similarity form applies almost exactly to radii as large as $r = 0.8R_s$.

Crucible Rotation

Crucible rotation predominantly introduces azimuthal motion in the melt which does not assist in heat transfer; hence, the isotherms are almost unchanged from the conduction-dominated state. The centrifugal pumping caused by the crucible motion creates a meridional flow underneath the crystal, because of the interference of the no-slip surface of the crystal with what would otherwise be a solid-body rotation; this motion is clearly shown in Figure 2-17 and has the form of a Taylor-Proudman cell (Greenspan, 1968) that rotates counterclockwise and thus marginally increases the heat transfer to the periphery of the melt/crystal interface (see Figure 2-18). The melt/crystal interface becomes nearly flat as a result.

The boundary layers on the crucible and crystal surfaces have qualitative similarities to the boundary-layer flows for crystal rotation alone. At the centerline the flow is similar to that for parallel rotating disks; the boundary layer at each disk is similar to the von Kármán form, with normal flow toward the crucible and the rotation rate of the bulk is less than that of the crucible. For $r > R_s$ the melt is approximately in solid-body rotation at the crucible rotation rate with no meridional flow. In the transition between these two regions the normal flow reverses direction completing the circulation.

The azimuthal, tangential and normal velocity components near the crystal surface are shown in Figures 2-19a-c. The von Kármán boundary-layer calculations (Cochran, 1934) rescaled with Re_c are added for qualitative comparison. The azimuthal velocity approaches the crucible velocity in the bulk near the crystal radius while near the centerline the azimuthal velocity reaches a peak of about $0.5r\omega_c$ before steadying at $0.4r\omega_c$. The boundary-layer becomes thicker toward the centerline, due to the slower rotation speed. All three velocity components overshoot their bulk values. The normal velocity reverses in the transition layer near the crystal periphery at $r \sim 0.85R_s$.

The boundary-layer profiles on the crucible bottom are not simple reflections of those

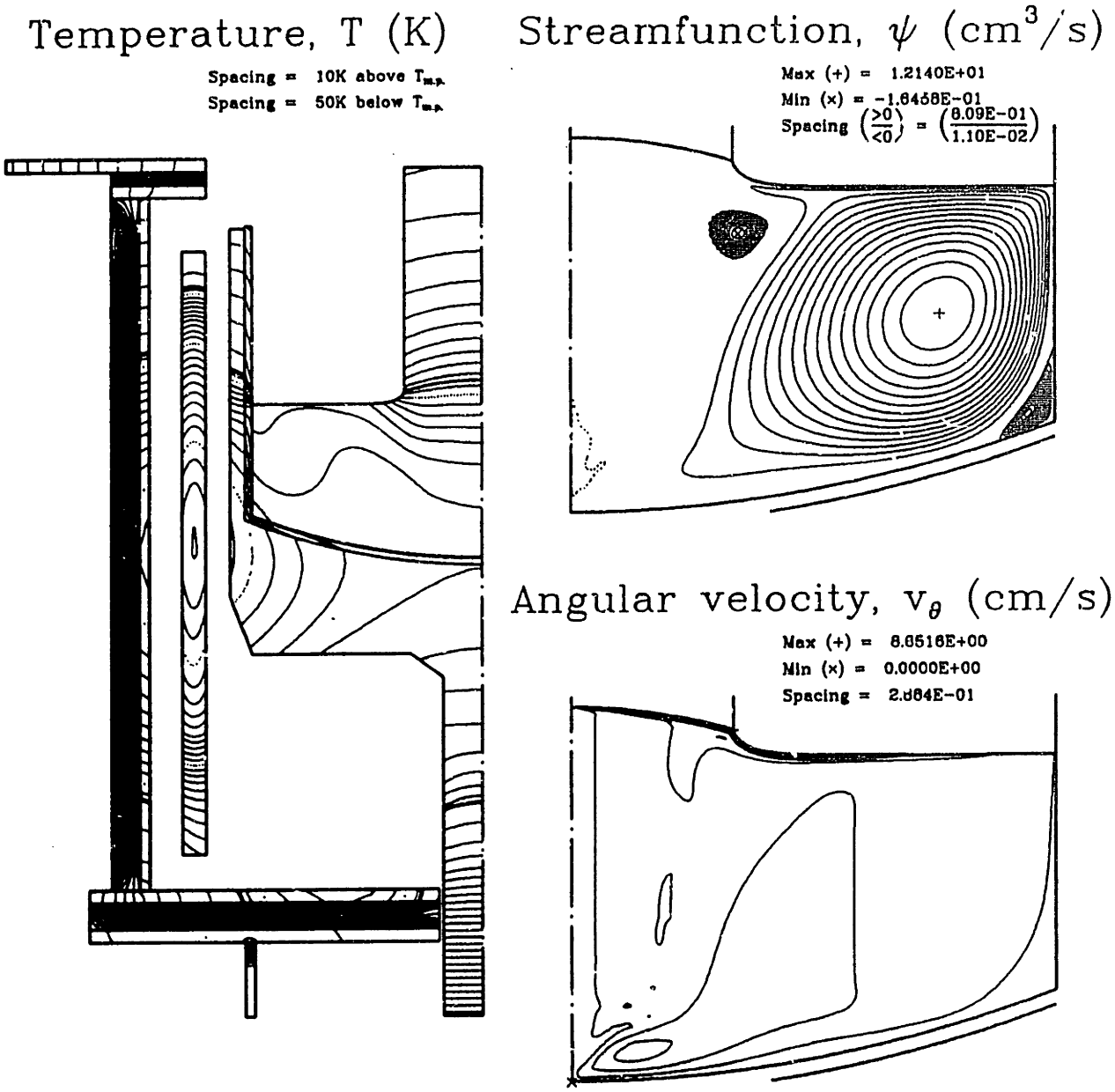

Figure 2-14: Thermal and flow fields with crystal rotation. Isotherms for temperature field are spaced $10K$ apart from $1690K$ and $50K$ apart below $1650K$. The melting-point isotherm appears as the thickest contour. Dotted contours are every $100K$ starting at $1700K$. Positive streamfunction contours are divided evenly between zero and the maximum; negative contours between zero and the minimum. Angular velocity contours are distributed likewise between zero and the maximum/minimum values.

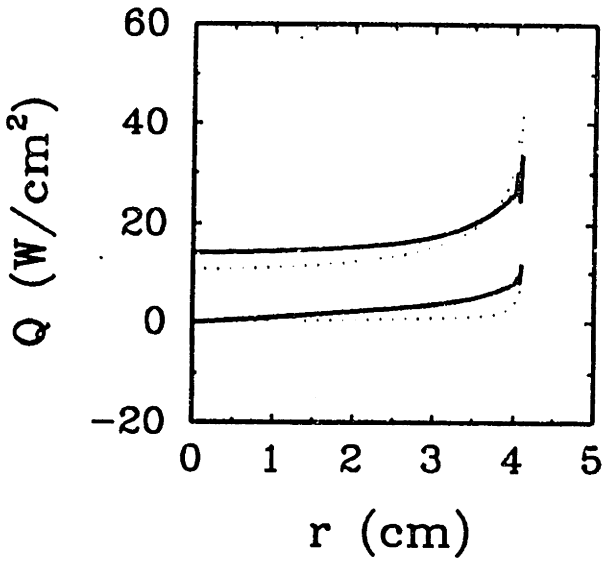

Figure 2-15: Heat flux at the melt/solid interface for the case of crystal rotation only; results for (——) crystal rotation, and (···) conduction-dominated simulations are shown. The upper curve is vertical heat flux and the lower curve is the horizontal component.

at the crystal surface; the overshoots in velocity components are much less. Also, the boundary layer is approximately constant from $0 \leq r \leq R_s$ and equal to the boundary-layer distance predicted by the von Kármám solution.

Combined crucible and crystal rotation

A solution for the IHTCM with combined crucible and crystal rotation is shown in Figure 2-21. The combined flows of crucible and crystal rotation yield two Taylor-Proudman cells, one attaching to the crystal surface and the other to the crucible surface. The cell rotating with the crystal is much smaller, due to the smaller amount of transmitted momentum from the crystal's small surface area. The heat transfer is governed mostly by the flow due to crucible rotation, and so the interface deflection is similar to that in Figure 2-17. The heat flux at the base of the crystal is shown in Figure 2-22. The cell rotating with the crucible is is more dilated than the Taylor-Proudman cell driven by crucible rotation alone, stretching from the centerline to approximately $r = 1.25R_s$, and has a higher maximum circulation. A scaling analysis for the smaller cell was reviewed in Section 1.3.1, and predicted a length of $2\delta_1 = 2.14R_sRe_s^{-1/2}$; the simulation predicts a distance of about 5 rather than 2.14 of these dimensionless units. Within the boundary

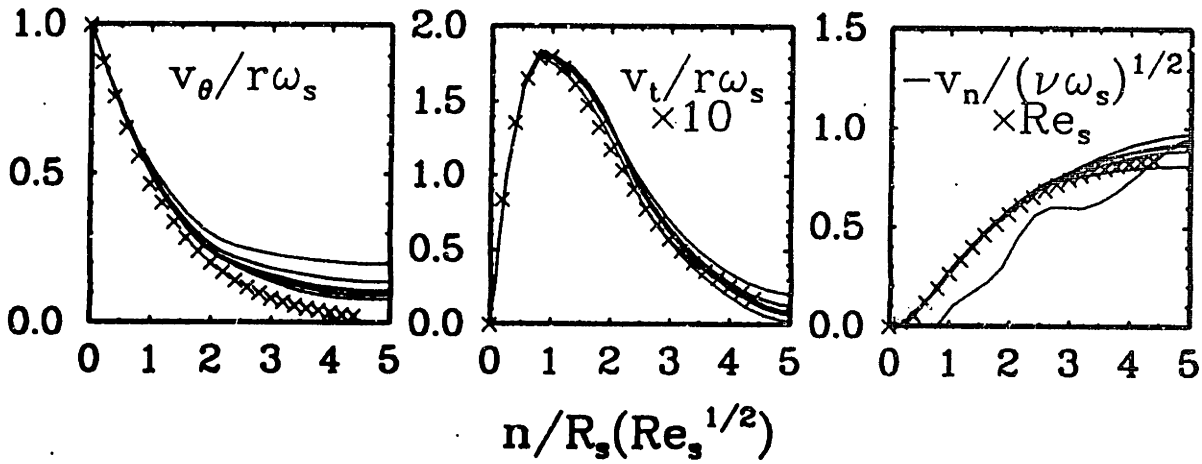

Figure 2-16: Boundary-layer structure of flows near the melt/crystal interface for calculations with crystal rotation. Shown are the (a) azimuthal velocity, (b) tangential velocity, and (c) normal velocity for (× × ×) the von Kármán similarity solution and (— —) simulation results plotted as a function of the normal distance from the melt/solid interface. The simulation results are plotted as five curves starting from the melt/solid interface at $r = 0.2, 0.4, 0.6, 0.8$ and $0.95 \times R_s$.

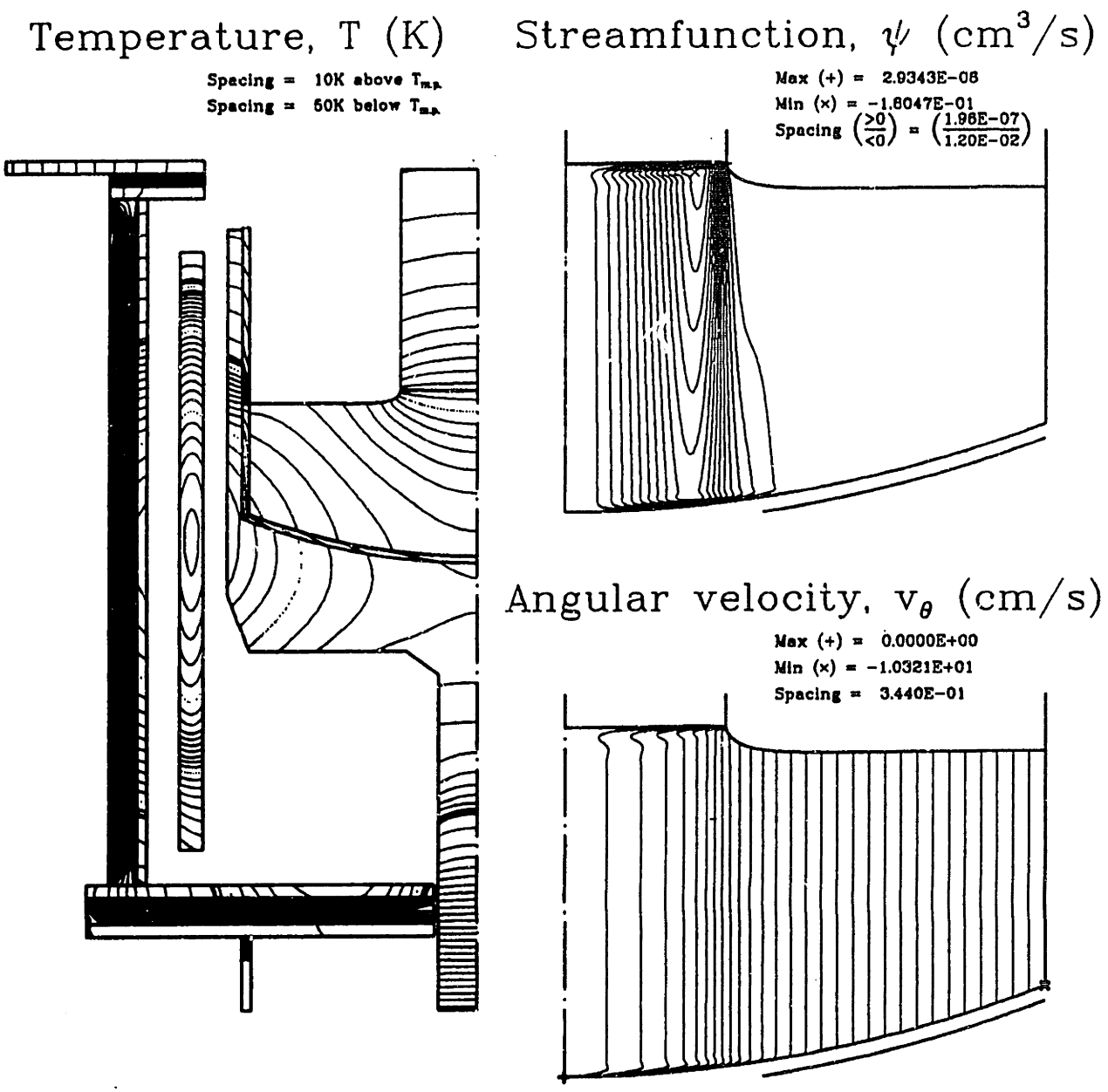

Figure 2-17: Thermal and flow fields with crucible rotation. Isotherms for temperature field are spaced $10K$ apart from $1690K$ and $50K$ apart below $1650K$. The melting-point isotherm appears as the thickest contour. Dotted contours are every $100K$ starting at $1700K$. Positive streamfunction contours are divided evenly between zero and the maximum; negative contours between zero and the minimum. Angular velocity contours are distributed likewise between zero and the maximum/minimum values.

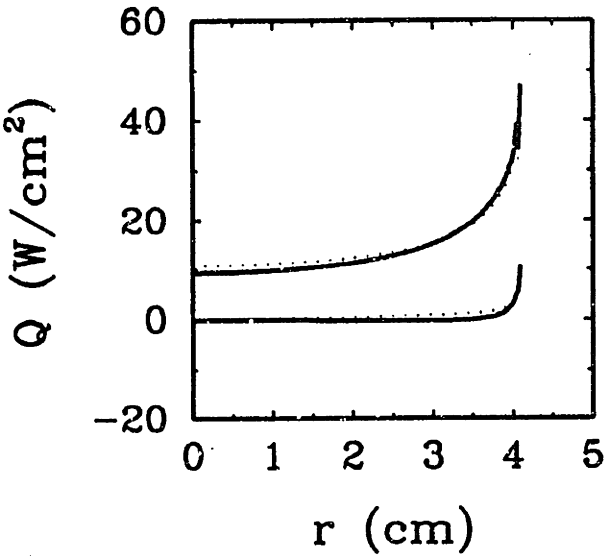

Figure 2-18: Heat flux at the melt/solid interface for the case of crucible rotation only; results for (——) crucible rotation, and (···) conduction-dominated simulations are shown. The upper curve is vertical heat flux and the lower curve is the horizontal component.

layer adjacent to the crystal the variation of velocity components is similar to the von Kármán analysis. The discrepancy between the upper-cell lengths is due to the assumption (Jones, 1988) that the larger cell rotates at about the same speed as the crucible; in the simulation, the rotation rate of the larger cell is in fact $\omega \simeq 0.3\omega_c$, which permits a thicker boundary layer near the crystal. The scaling for the boundary layer flow at the crucible bottom from $0 \leq r \leq R_s$ is consistent with the profiles from crucible rotation alone.

Thermocapillary motion

The coupling of the temperature gradients along the surface of the melt with the variation in the surface tension with temperature drives an intense convective flow toward the colder crystal over most of the melt surface. The inflection in the temperature field near the crucible wall leads to an intense flow in the upper corner of the melt. The radial velocity on the meniscus are higher than elsewhere; the maximum inward radial velocity in Figure 2-26 is $10.4\,cm \cdot s^{-1}$, compared to $5.7\,cm \cdot s^{-1}$ for the buoyancy-driven motion discussed below. As a result, the isotherms in the melt are extremely convected and the temperature difference across the melt decreases to $34.3K$, compared to the value

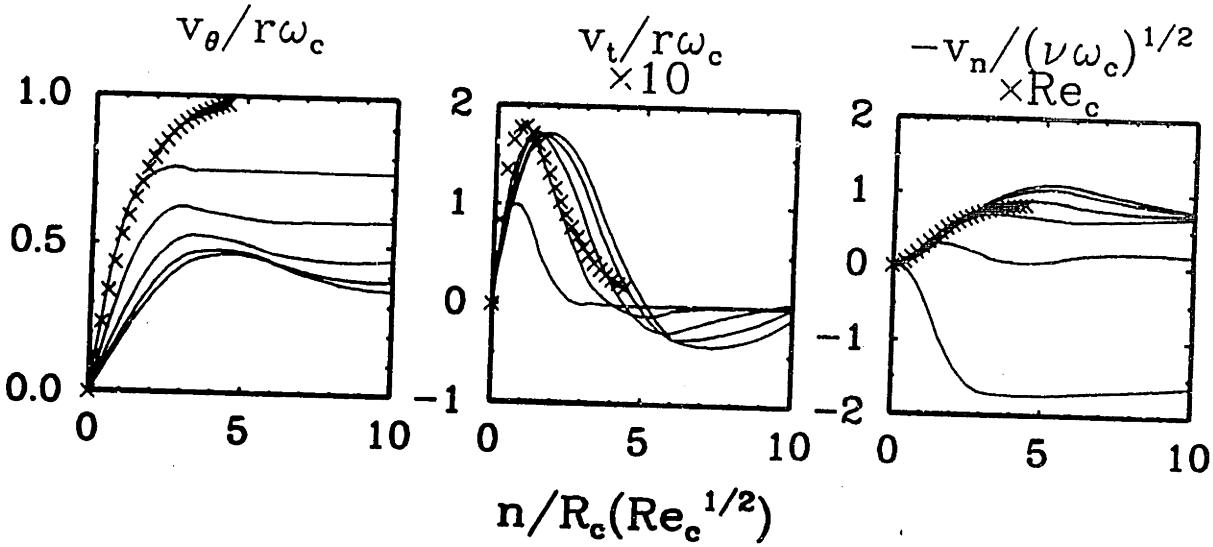

Figure 2-19: Boundary-layer structure of flows near the melt/crystal interface for calculations with crucible rotation. Shown are the (a) azimuthal velocity, (b) tangential velocity, and (c) normal velocity for ($\times\times\times$) the von Kármán similarity solution and (——) simulation results plotted as a function of the normal distance from the melt/solid interface. The simulation results are plotted as five curves starting from the melt/solid interface at $r = 0.2, 0.4, 0.6, 0.8$ and $0.95 \times R_s$.

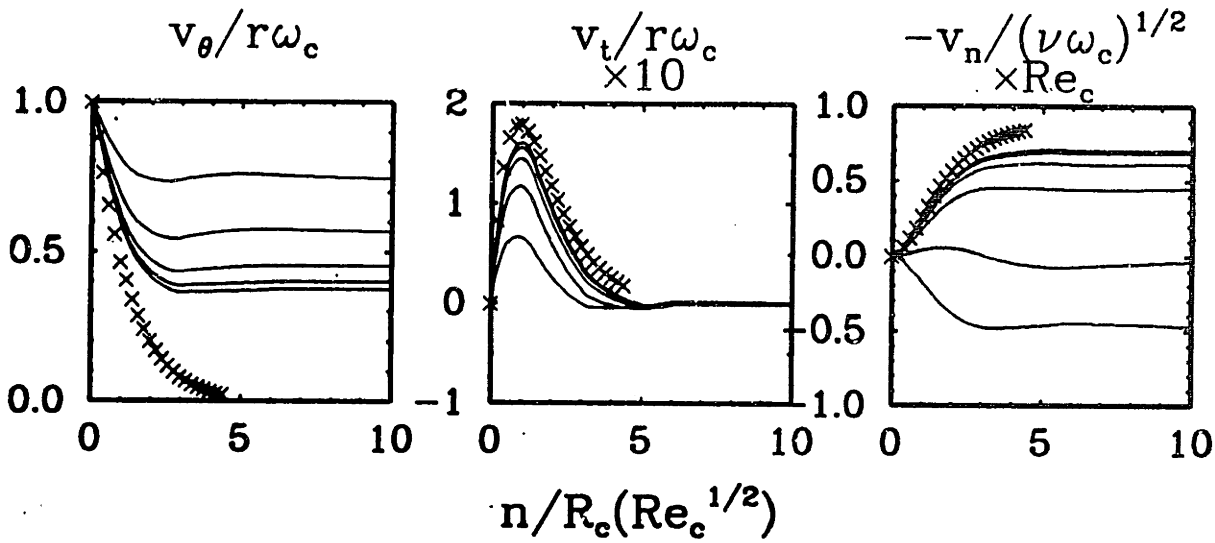

Figure 2-20: Boundary-layer structure of flows near the crucible bottom for calculations with crucible rotation. Shown are the (a) azimuthal velocity, (b) tangential velocity, and (c) normal velocity for (× × ×) the von Kármán similarity solution and (——) simulation results plotted as a function of the normal distance from the crucible bottom. The simulation results are plotted as five curves starting from the crucible bottom at $r = 0.2, 0.4, 0.6, 0.8$ and $0.95 \times R_s$.

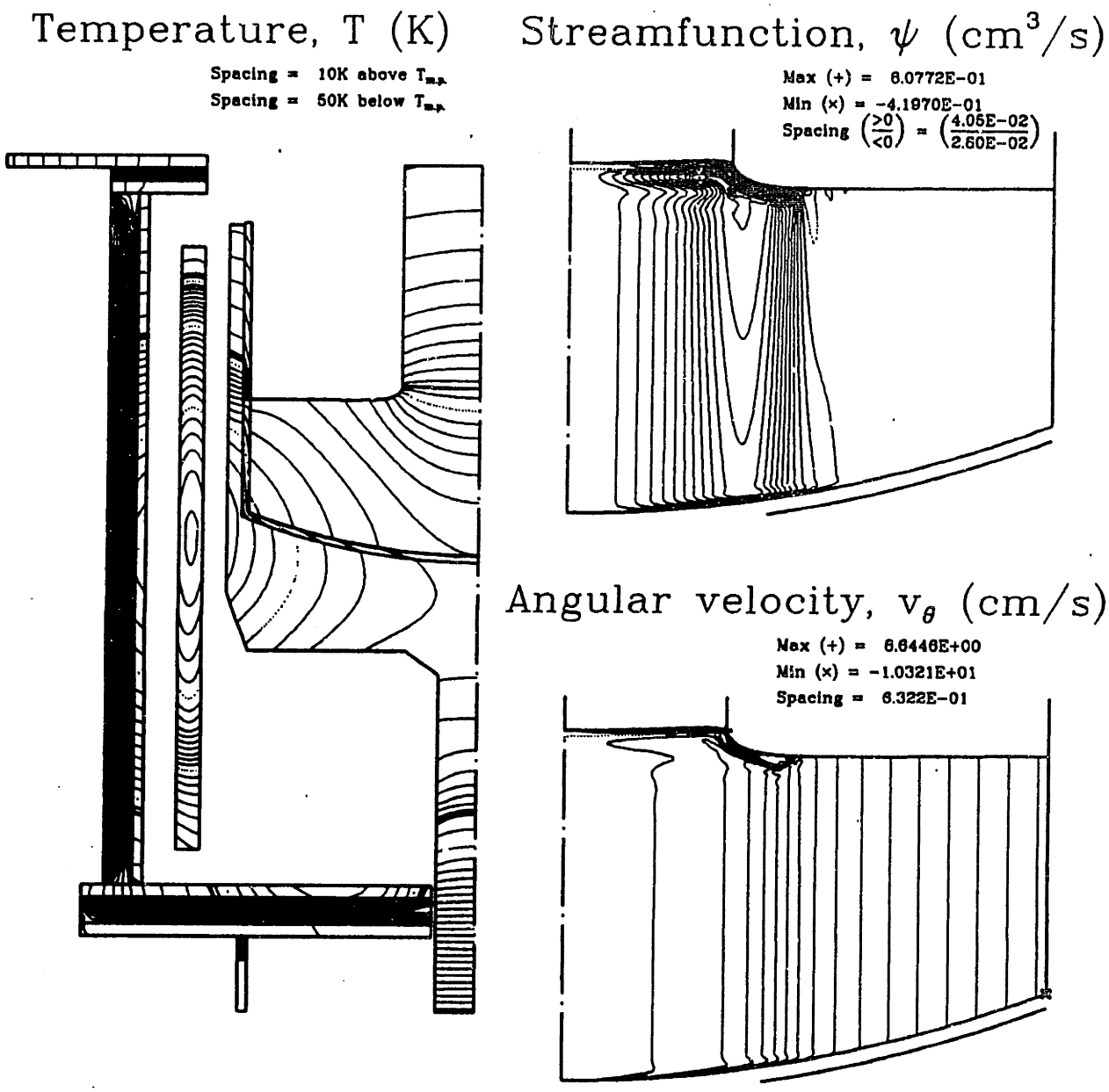

Figure 2-21: Thermal and flow fields with crucible and crystal rotation. Isotherms for temperature field are spaced $10K$ apart from $1690K$ and $50K$ apart below $1650K$. The melting- point isotherm appears as the thickest contour. Dotted contours are every $100K$ starting at $1700K$. Positive streamfunction contours are divided evenly between zero and the maximum; negative contours between zero and the minimum. Angular velocity contours are distributed likewise between zero and the maximum/minimum values.

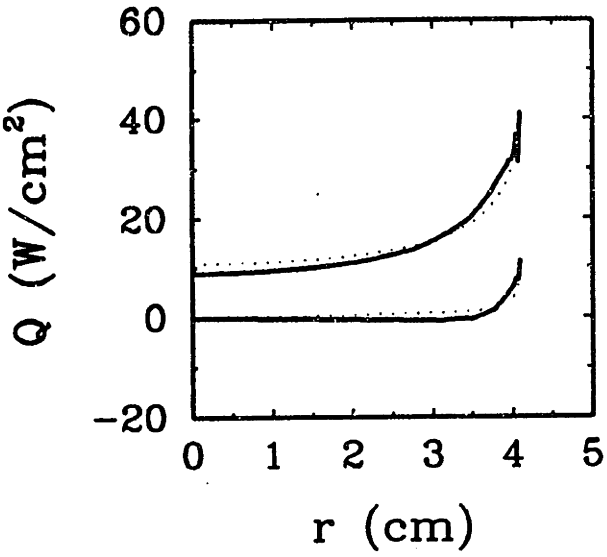

Figure 2-22: Heat flux at the melt/solid interface for the case of combined crucible and crystal rotation; results for (——) combined crucible and crystal rotation, and (···) conduction-dominated simulations are shown. The upper curve is vertical heat flux and the lower curve is the horizontal component.

of $124.4K$ for the conduction-dominated case. Most of this temperature difference is confined to thermal boundary layers adjacent to the crystal and the crucible. Thermocapillary motion accordingly has a large impact on the interface shape. The interface is deflected downward by almost $0.91\,cm$. The plot of heat flux at the base of the crystal clearly shows the effect of convection ; a large *negative* horizontal heat flux due to convection directs energy into the interface for $r > 2cm$ and the axial temperature gradient at the centerline is diminished considerably; see Figure 2-27.

Thermocapillarity yields a strong flow near the melt/solid interface at radii approaching R_s. The magnitudes of the tangential and normal velocity exceed those due to crystal rotation as $r \rightarrow R_s$ and so thermocapillarity is expected to dominate the transport there. Along the melt surface boundary layer of about $(Ma/Pr)^{-1/3}$ is calculated in the tangential velocity as expected (Zebib et al., 1978). The reversal in the tangential velocity due to the small counterrotating cell is evident. The radial and axial velocities are plotted for five different rays extending into the melt from the melt/crucible/gas trijunction. The velocities are seen to become very large over distances on the order of $\delta \sim (Ma/Pr)^{-2/3}$, which is expected (Zebib et al., 1978).

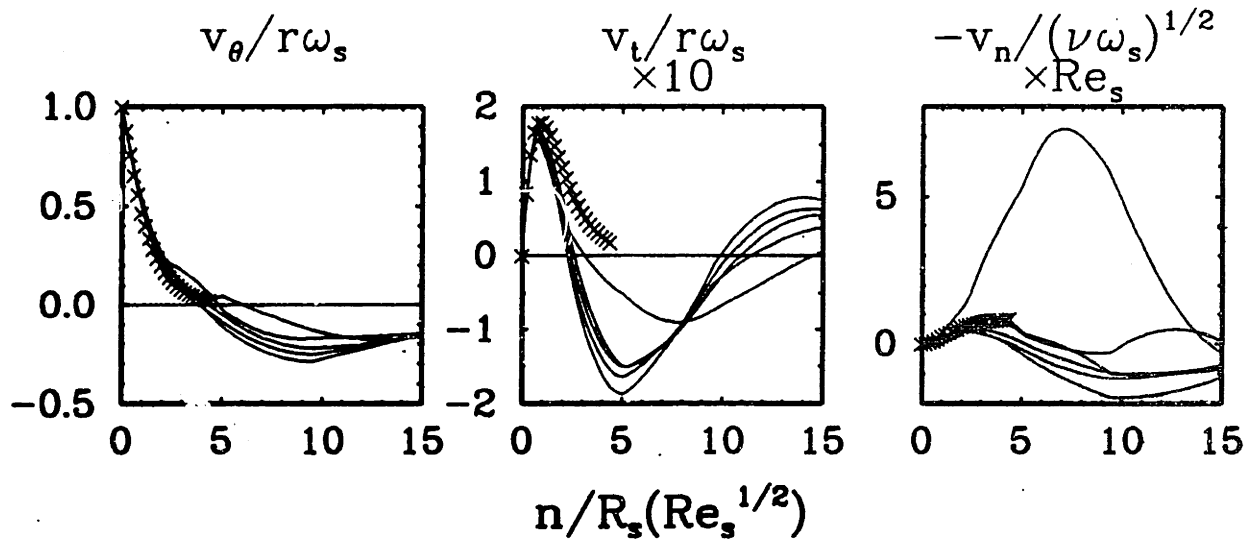

Figure 2-23: Boundary-layer structure of flows near the melt/crystal interface for calculations with combined crucible and crystal rotation. Shown are the (a) azimuthal velocity, (b) tangential velocity, and (c) normal velocity for (× × ×) the von Kármán similarity solution and (——) simulation results plotted as a function of the normal distance from the melt/solid interface. The simulation results are plotted as five curves starting from the melt/solid interface at $r = 0.2, 0.4, 0.6, 0.8$ and $0.95 \times R_s$.

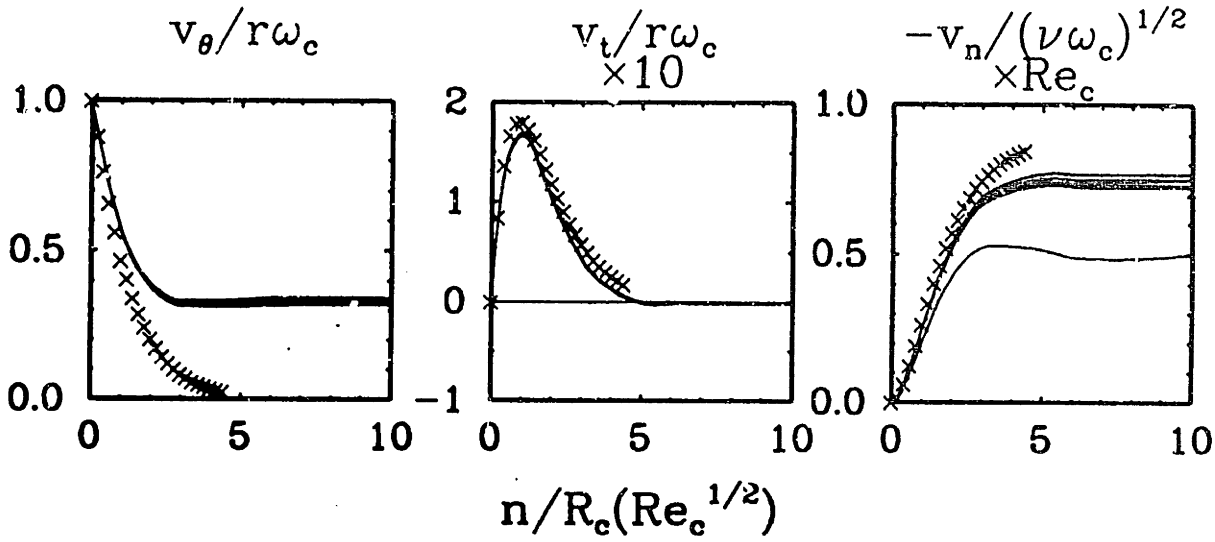

Figure 2-24: Boundary-layer structure of flows near the crucible bottom for calculations with crucible and crystal rotation combined. Shown are the (a) azimuthal velocity, (b) tangential velocity, and (c) normal velocity for ($\times$ $\times$ $\times$) the von Kármán similarity solution and (——) simulation results plotted as a function of the normal distance from the crucible bottom. The simulation results are plotted as five curves starting from the crucible bottom at $r = 0.2, 0.4, 0.6, 0.8$ and $0.95 \times R_s$.

The thermocapillary flow near both trijunctions is characterized by very high gradients in velocity and singularities in the pressure field. The melt surface, with nonzero thermocapillary shear-stress, meets the crucible wall or crystal surface, with a no-slip condition. Following the analysis of Moffatt, 1964, the streamfunction can be expressed in terms of polar coordinates at a trijunction, $\psi(r,\theta)$, which satisfy the Stokes equation with the form

$$\psi = r^{\lambda} f_{\lambda}(\theta), \tag{2.47}$$

where λ is the eigenvalue with smallest real part determined by substituting Equation (2.47) into the Stokes equation and solving with appropriate boundary conditions. The function $f_{\lambda}(\theta)$ in general is given by

$$f_{\lambda}(\theta) = A\cos\lambda\theta + B\sin\lambda\theta + C\theta\cos(\lambda-2)\theta + D\sin(\lambda-2)\theta. \tag{2.48}$$

For the trijunction-singularities $\lambda = 2$ solves the Stokes equation and the form of the streamfunction is

$$\psi = \frac{\tau}{\mu} r^2 f_2(\theta), \tag{2.49}$$

where τ is the shear stress along the melt surface at the wall. The pressure locally has a $\log r$ distribution and and the function $f_2(\theta)$ is given by (Moffatt, 1964)

$$f_2(\theta) = \frac{1}{8}(\cos 2\alpha - 1)^{-1}\left\{\cos 2\theta + \sin 2\alpha \sin 2\theta - 2\theta \sin 2\alpha + 1\right\}, \tag{2.50}$$

where α is defined as the angle spanned by an arc passing from the solid surface to the free surface, as shown in Figure 2-25. Hence, the form of the streamfunction at the crucible/melt/ambient trijunction is given with $\alpha = 90°$ as the simple expression

$$f_2(\theta) = \frac{1}{16}\left\{2\cos 2\theta - 1\right\}, \tag{2.51}$$

while the form of the streamfunction at the crystal/melt/ambient trijunction retains all the terms from Equation (2.50). The heat-flux at the crucible/melt/ambient trijunction is larger than at the crystal/melt/ambient trijunction because of the large radiative heat flux there as shown in Figure 2-9c and the large difference in conductivities between the melt and crucible, which preferentially draw heat from the melt located close to the crucible/melt/ambient trijunction. The singularity at the crystal/melt/ambient trijunction is not as extreme due to the lower temperature gradient and hence lower free-surface stresses there.

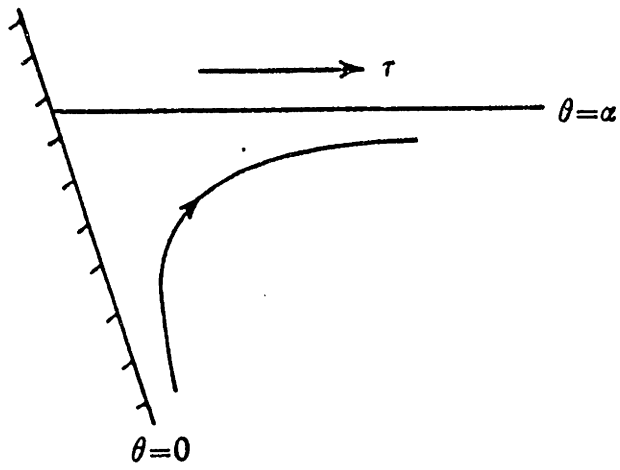

Figure 2-25: Schematic depiction of thermocapillary flow near trijunction, after Moffatt, 1964.

Buoyancy-driven flow

The flow field driven solely by buoyancy is shown in Figure 2-31 and also causes substantial convection. Again, two flow cells form: a large one that circulates up the crucible wall and out across the melt toward the crucible, and a weaker one driven by the inversion of the temperature field near the crucible/melt/gas intersection. The most striking difference between Figures 2-26 and 2-31 is the boundary layer structure in the buoyant streamfunction since the streamlines are more tightly bunched near the boundary of the flow and its core moves more slowly, i.e. has fewer streamlines. This boundary layer structure indicates that the flow is strong enough to overcome the low Prandtl number of the melt and that the temperature field is approximately well-mixed in the core with substantial gradients only along the crucible and crystal boundaries. The transition in flow structure from the conduction-dominated heat transfer for a low Prandtl number melt with moderate convection to a boundary-layer structure such as that shown Figure 2-31 was reported during calculations with the HTCM (Sackinger et al., 1988) and is not duplicated here. The convective motion in Figure 2-31 is strong and the temperature difference across the melt has been reduced to only $40.6K$. However, because the convection is less intense near the melt/solid interface. The melt/crystal interface in Figure 2-32 is less deformed than in the case of thermocapillary motion alone.

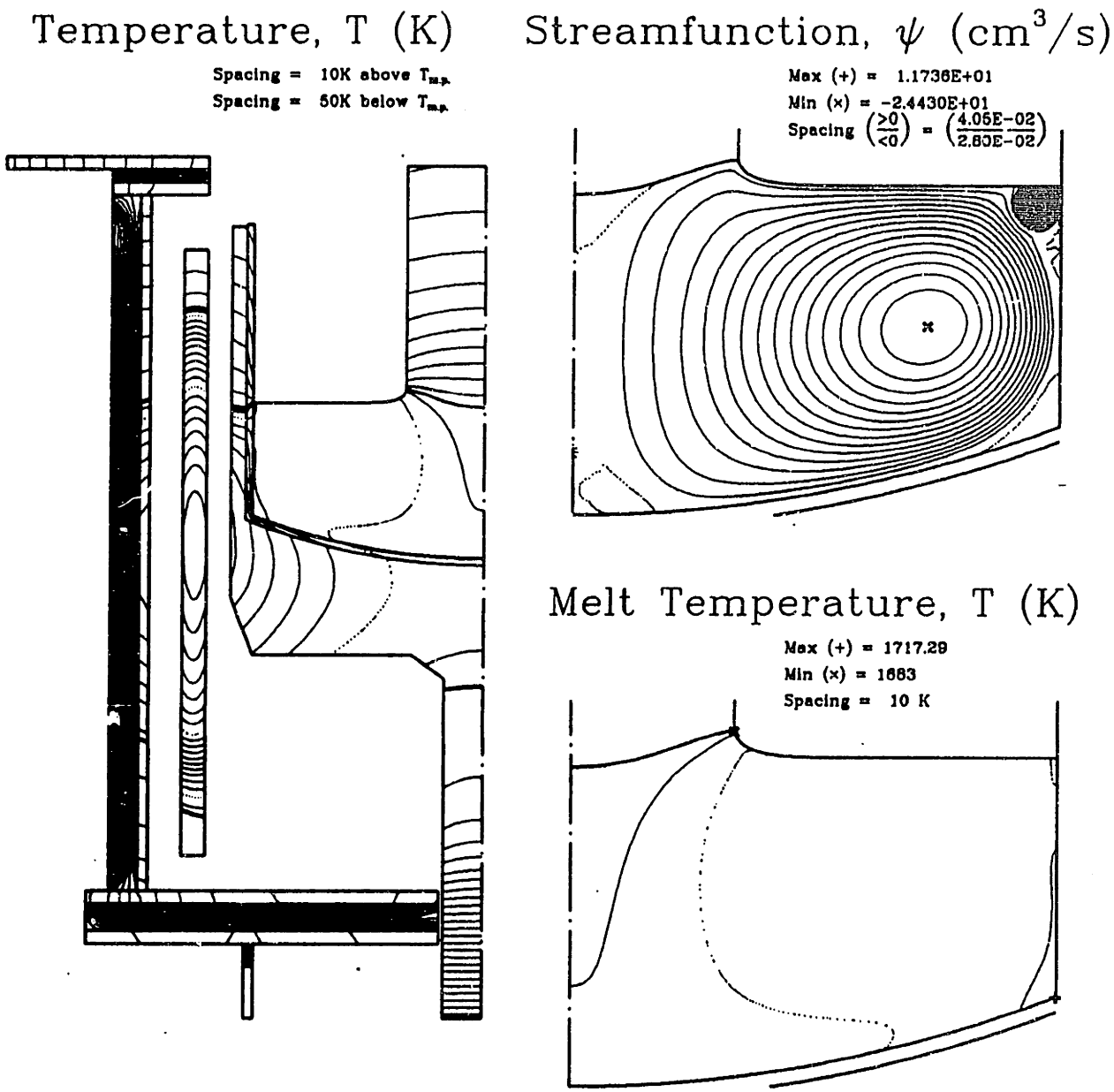

Figure 2-26: Thermal and flow fields with thermocapillary convection. Isotherms for temperature field are spaced $10K$ apart from $1690K$ and $50K$ apart below $1650K$. The melting-point isotherm appears as the thickest contour. Dotted contours are every $100K$ starting at $1700K$. Positive streamfunction contours are divided evenly between zero and the maximum; negative contours between zero and the minimum. Temperature field in the melt is highlighted to illustrate the effect of natural convection.

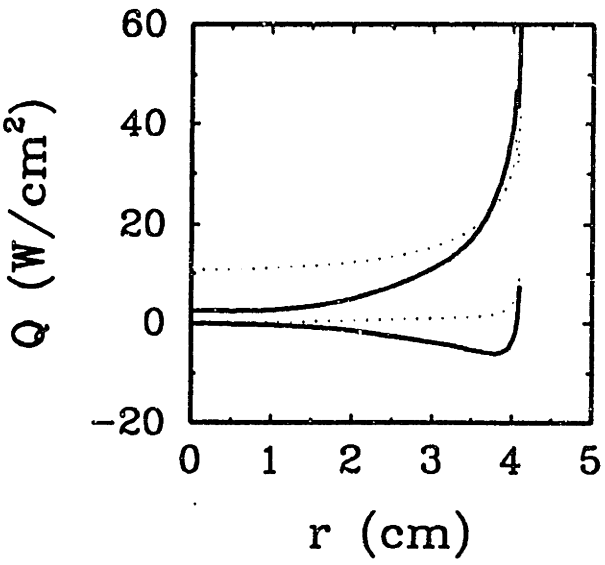

Figure 2-27: Heat flux at the melt/solid interface for the case of thermocapillary flow only; results for (——) thermocapillary flow, and (···) conduction-dominated simulations are shown. The upper curve is vertical heat flux and the lower curve is the horizontal component.

The tangential and normal velocities near the melt/solid interface are comparable with those of thermocapillary convection; see Figure 2-33. The tangential and normal velocities along the crucible wall are shown in Figure 2-34, scaled with $Gr^{-1/4}$. It is seen that a boundary-layer flow only exists at the wall for a distance of $1.5\,cm$ or so. The flow is detached from the wall near the lower corner, and in the upper corner exists a counterrotating cell driven by opposing temperature gradients.

Effect of convection on transport phenomena.

The melt/solid interface shape is a sensitive measure of the heat flux in that area. The direction of heat flow is normal to the interface by definition. The magnitude of the slope of the interface is given by the ratio of the radial temperature gradient to the axial temperature gradient. There is always a positive axial heat flux in these calculations, since the melt/solid interface shape is a single-valued function of the radial coordinate r. The heat flows inward for deflections toward the melt and outward for deflections toward the crystal. The heat flux profiles at the melt/solid interface in Figures 2-15,2-18,2-22,2-27 and 2-32 have shown the marked effect of convection on the radial heat flow.

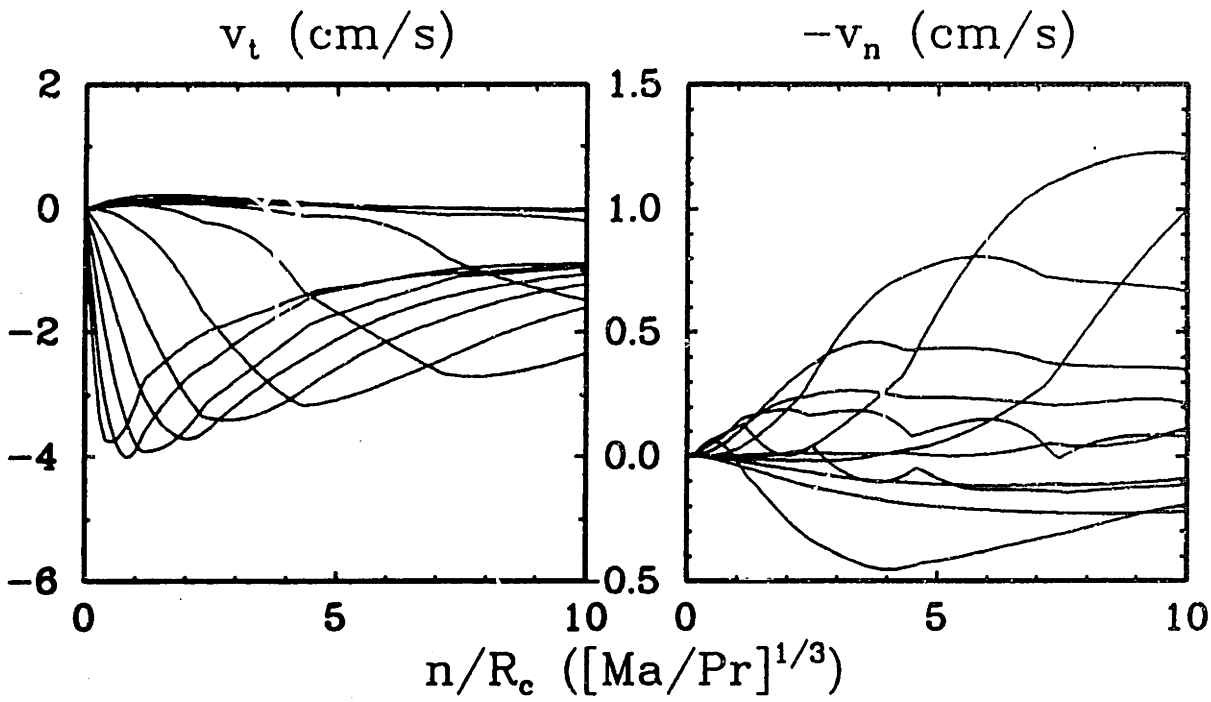

Figure 2-28: Flows near the melt/solid interface due to thermocapillary convection as a function of the distance normal to the melt/solid interface: (a) tangential velocity, and (b) normal velocity components. The simulation results are plotted as ten curves starting from the melt/solid interface at $r = 0.0, 0.1, 0.2, 0.3, 0.4, 0.5, 0.6, 0.7, 0.8, 0.9$ and $0.95 \times R_s$.

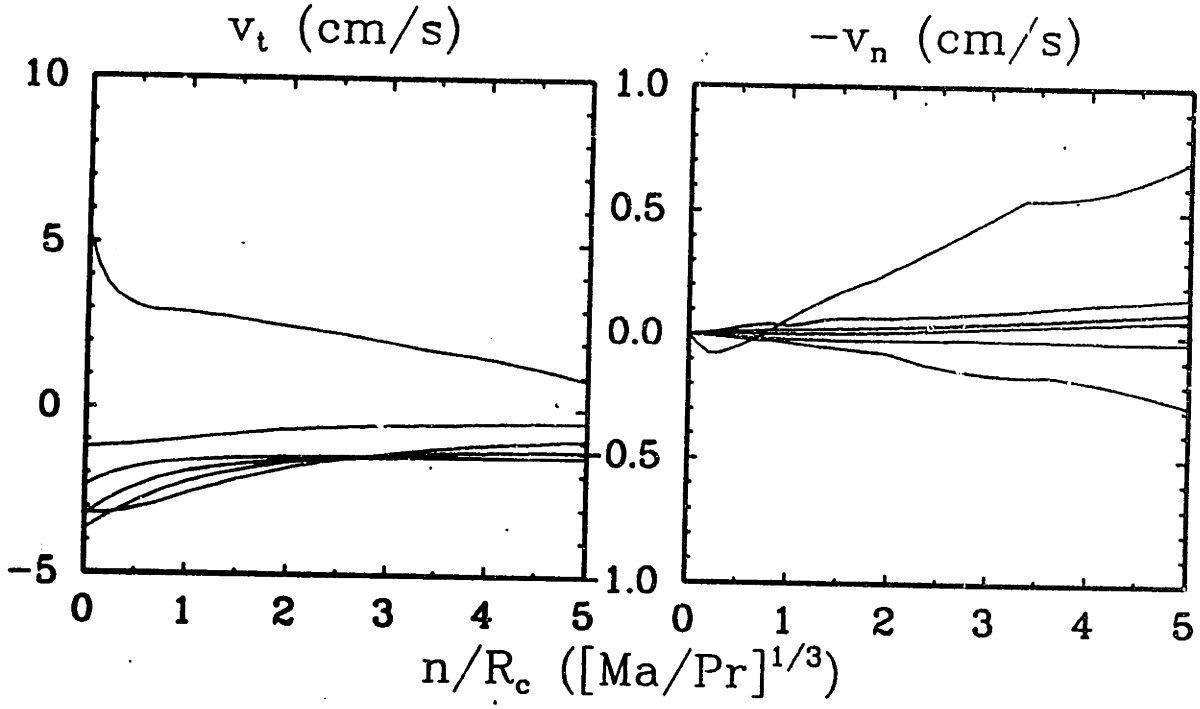

Figure 2-29: Flows near the melt/gas meniscus due to thermocapillary convection as a function of the distance normal to the melt/ambient meniscus: (a) tangential velocity, and (b) normal velocity components. The simulation results are plotted as six curves starting from the melt/ambient meniscus at $r = R_s + 0.0, 0.2, 0.4, 0.6, 0.8$, and $0.95 \times (R_c - R_s)$.

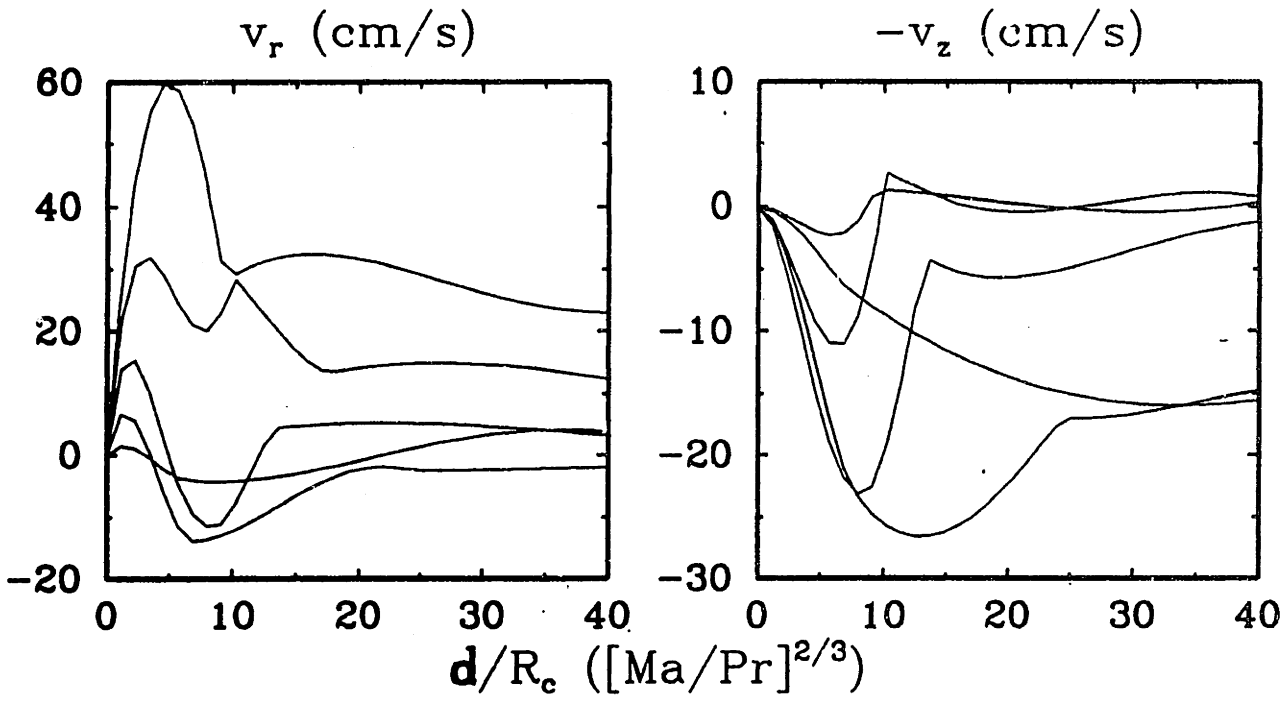

Figure 2-30: Flows near the melt/crucible/gas trijunction due to thermocapillary convection as a function of the distance from the trijunction: (a) radial velocity, and (b) axial velocity components. The simulation results are plotted as five curves starting from the trijunction an emanating with angles of $\theta = 15°, 30°, 45°, 60°$, and $75°$ measured clockwise from the vertical.

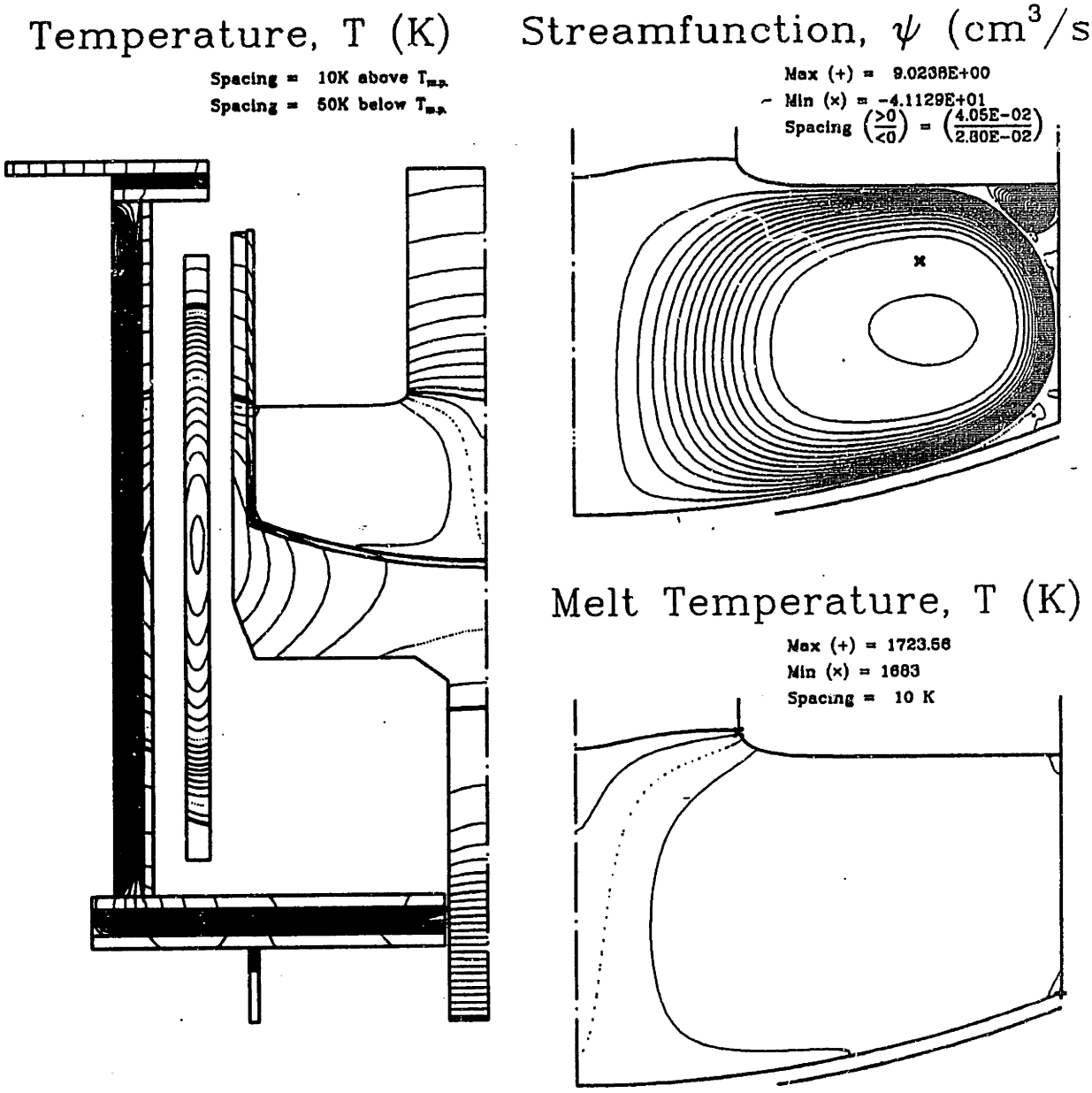

Figure 2-31: Thermal and flow fields with buoyant convection. Isotherms for temperature field are spaced $10K$ apart from $1690K$ and $50K$ apart below $1650K$. The melting-point isotherm appears as the thickest contour. Dotted contours are every $100K$ starting at $1700K$. Positive streamfunction contours are divided evenly between zero and the maximum; negative contours between zero and the minimum. Temperature field in the melt is highlighted to illustrate the effect of natural convection.

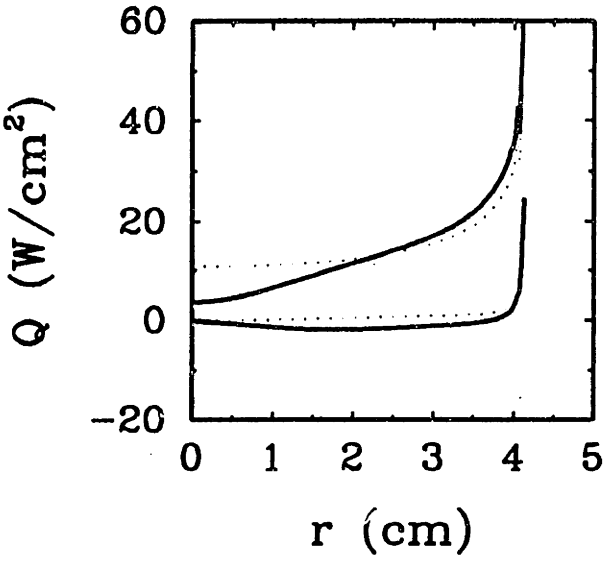

Figure 2-32: Heat flux at the melt/solid interface for the case of buoyancy-driven flow only; results for (——) buoyancy-driven flow, and (···) conduction-dominated simulations are shown. The upper curve is vertical heat flux and the lower curve is the horizontal component.

The melt/solid interface shapes plotted for comparison in Figure 2-35 demonstrate the relative positions with the various flow mechanisms.

The calculations in this section have established the form of the flow field near the melt/solid interface for each of the distinct flow mechanisms. As discussed in Chapter 1, this near-field flow is very important to solute segregation in the system. The actual CZ flow depends on all of the mechanisms however, so it cannot be concluded here that any single flow mechanism dominates the flow near the melt/solid interface. This will be investigated in the next chapter.

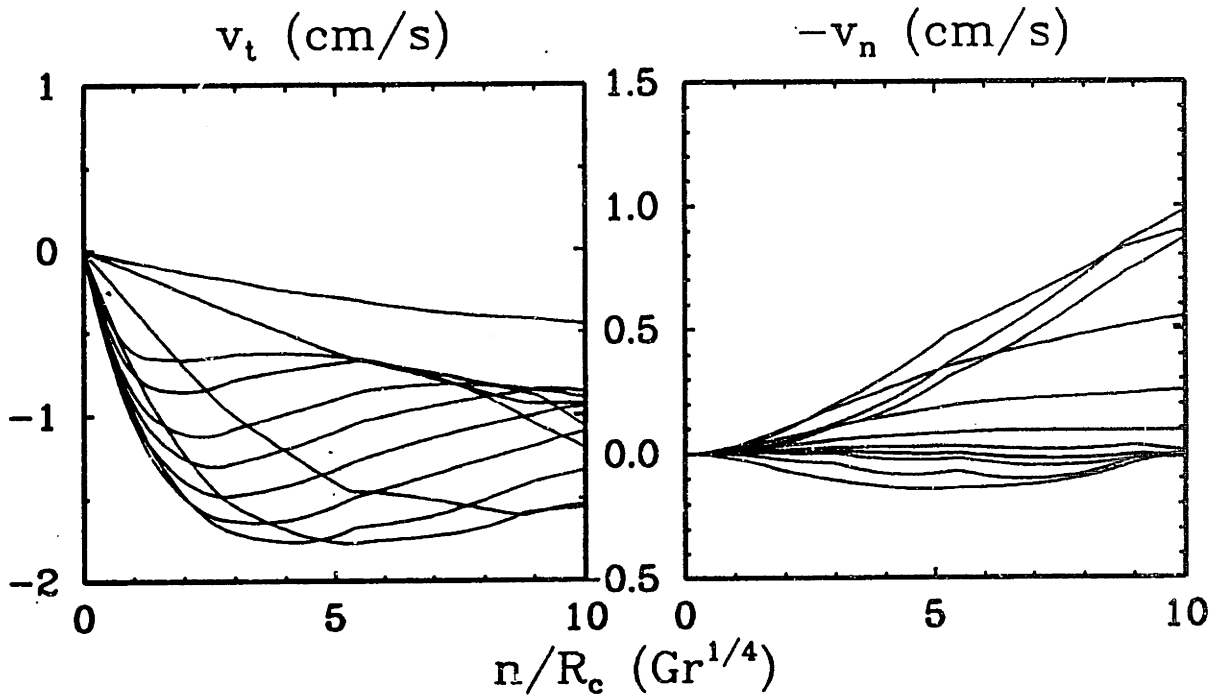

Figure 2-33: Flows near the melt/solid interface due to buoyancy-driven convection as a function of the distance normal to the melt/solid interface: (a) tangential velocity, and (b) normal velocity components. The simulation results are plotted as ten curves starting from the melt/solid interface at $r = 0.0, 0.1, 0.2, 0.3, 0.4, 0.5, 0.6, 0.7, 0.8, 0.9$ and $0.95 \times R_s$.

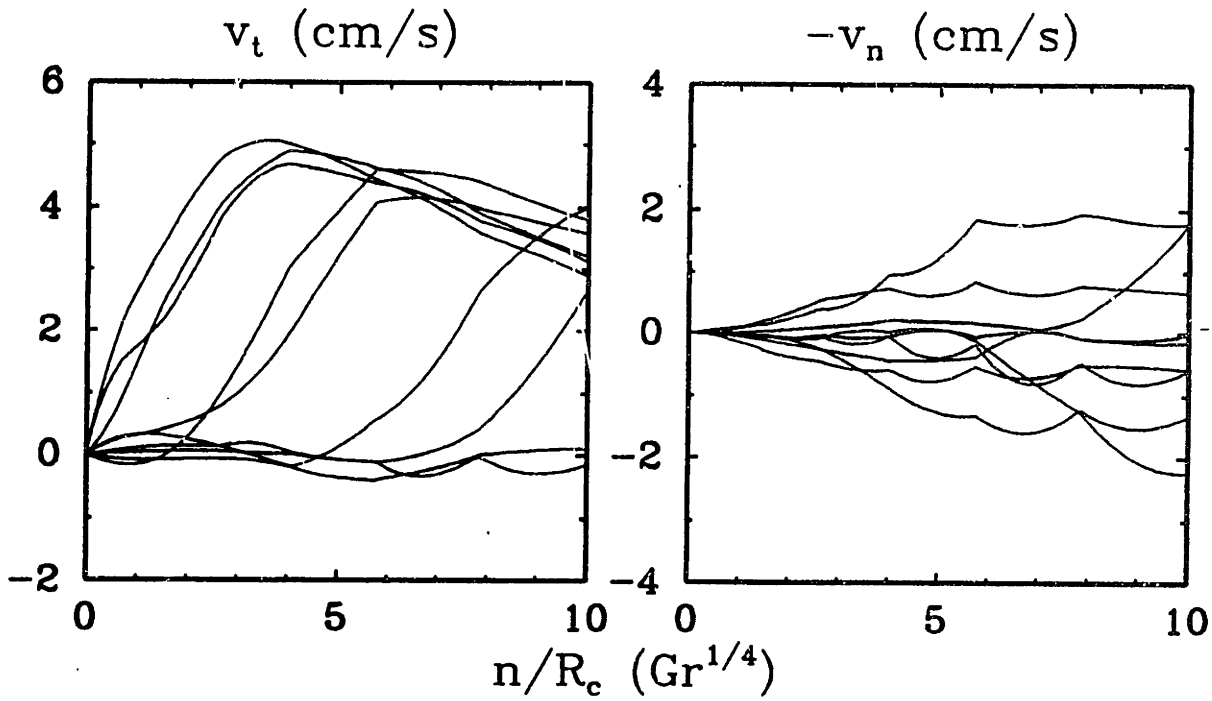

Figure 2-34: Flows near the crucible wall due to buoyancy-driven convection as a function of the distance normal to the crucible wall: (a) tangential velocity, and (b) normal velocity components. The simulation results are plotted as six curves starting from the crucible wall at $z = z_{bottom}(r = R_c) + 0.0, 0.2, 0.4, 0.6, 0.8$, and $0.95 \times [h_{m/g}(r = R_c) - z_{bottom}(r = R_c)]$.

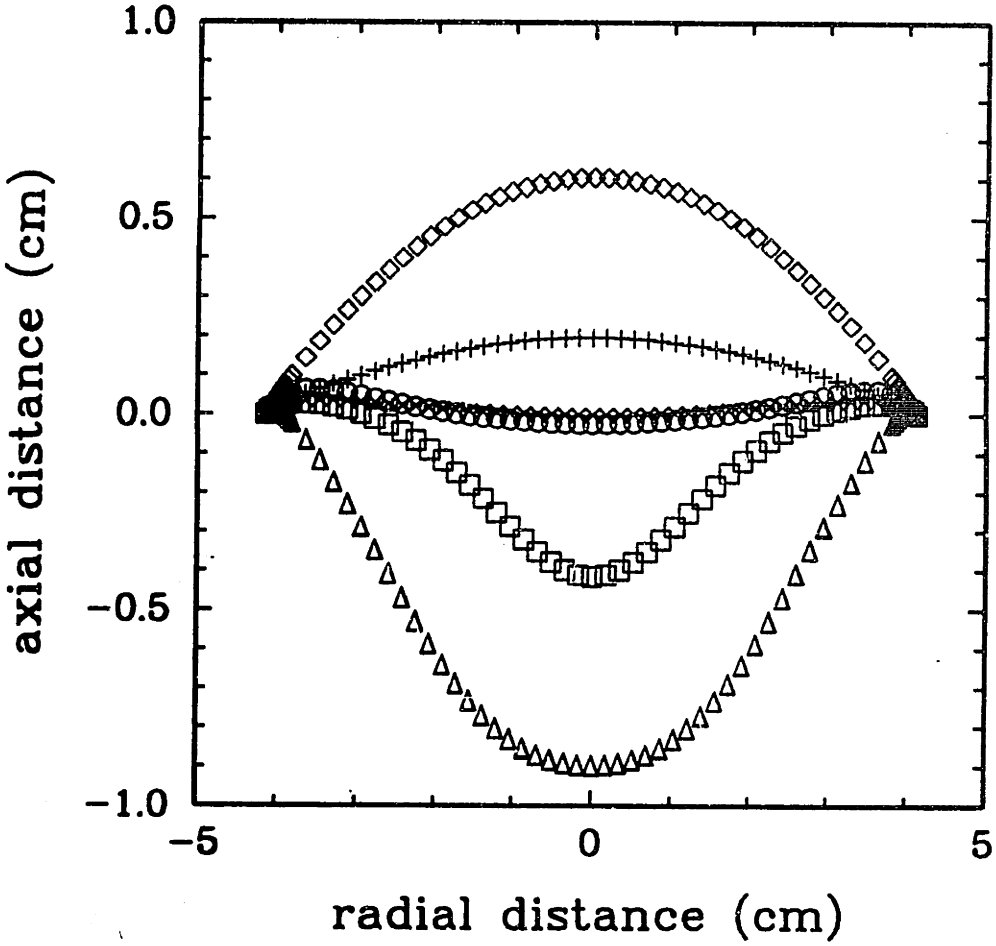

Figure 2-35: Melt/solid interface shapes predicted for calculation with (+++) no convection, and calculations with individual driving forces: (◇◇◇) crystal rotation, (× × ×) crucible rotation, (o o o) combined crystal and crucible rotation, (△ △ △) thermocapillarity and (□ □ □) buoyancy. Horizontal axis is drawn to actual size, vertical axis is drawn with a 5 : 1 scale.

Chapter 3

Comparison of Experimental Measurements with Simulation at Realistic Conditions

Summary

This chapter describes the comparison between the predictions of the IHTCM and the experimental measurements made at IBM. The detail of the measurements is diminutive in comparison to that of the IHTCM. The experimental CZ puller was converted from a production unit and was not designed for extensive online measurements; the time required for the retrofitting of the puller for the measurements reported here was one year. The experimental program was discontinued [1] before any new experiments could be made based on the initial comparison.

Attention is focussed on the detail of the thermal field. A primary objective is to quantify the accuracy of the radiative heat transfer model for predicting the heat flow throughout the CZ apparatus, since most physical phenomena depend on heat transfer. Temperature measurements could only be taken at locations in gaps in the apparatus using a thermocouple protected by a thermowell. Embedded thermocouples were ruled out as impractical, as was direct sensing of melt temperature. These temperature measurements are compared to an extension of the IHTCM which predicts the temperature distribution in a thermowell tube. The IHTCM predicts the thermal measurements reasonably, irrespective of melt convection; this positive comparison lends credibility to the thermoelastic stress prediction, since the thermal field is well-modelled. However, the

[1] All CZ growth activities were discontinued at IBM's East Fishkill facility at that time.

thermoelastic stress exceeds the *CRSS* for all the IHTCM calculations, which means that *any* dislocations present in the crystal would be mobile and propagate and proliferate rapidly throughout the crystal. The crystals grown in the Siltec apparatus in this Thesis are dislocation-free, and therefore stress-enhanced dislocation multiplication did not occur. The lack of dislocations in the grown crystals emphasizes the importance of dislocation *generation* for the growth of dislocation-free material.

Flow modelling with the combined driving forces of crystal rotation, crucible rotation, buoyancy and thermocapillarity is attempted using the melt viscosity as the continuation parameter. Converged solutions of the IHTCM at high values of the viscosity of the melt are first obtained and the viscosity is gradually reduced. A number of limit points are passed as the viscosity comes within an order-of-magnitude of the appropriate value for silicon. However, the literature value is never practically reached; a value of five times the actual value is the minimum simulated viscosity. This tortuous solution trajectory may be indicative of the inappropriateness of the steady, two-dimensional representation of the flow field.

The level of melt convection is compared to experiment by measurements of the melt-solid interface provided by post-growth analysis of the dopant striae in the crystal. This shape is compared to the simulations with all driving forces for flow combined at the lowest viscosity reached, in order to determine whether the thermal convection near the melt/solid interface is well-predicted in spite of the artificially high viscosity. The direction of the deflection is correctly predicted, but the agreement is only qualitative, since the total predicted deflection is twice as large, and the simulated crystal diameter was only $83\,mm$, compared to the $100\,mm$ crystal used for interface determination. The calculations with buoyancy and thermocapillarity also correctly predict the direction of the deflection. Given the uncertainty about the flow field, conclusions regarding the deposition of solute are deferred to the Chapter 4.

3.1 The Experimental System

The CZ system used in the experiments was a SILTEC puller outfitted with a standard $254\,mm$ (crucible inside diameter) hot zone and was used to grow $83\,mm$ diameter silicon crystals at a nominal pull rate of $63.5\,mm \cdot hr^{-1}$. Direct measurement of the temperature field within the growth chamber was accomplished by inserting a thermowell tube into the puller through ports at five radial positions along the top of the growth chamber; the locations of these ports are highlighted in the schematic drawing in Figure 3-1. The

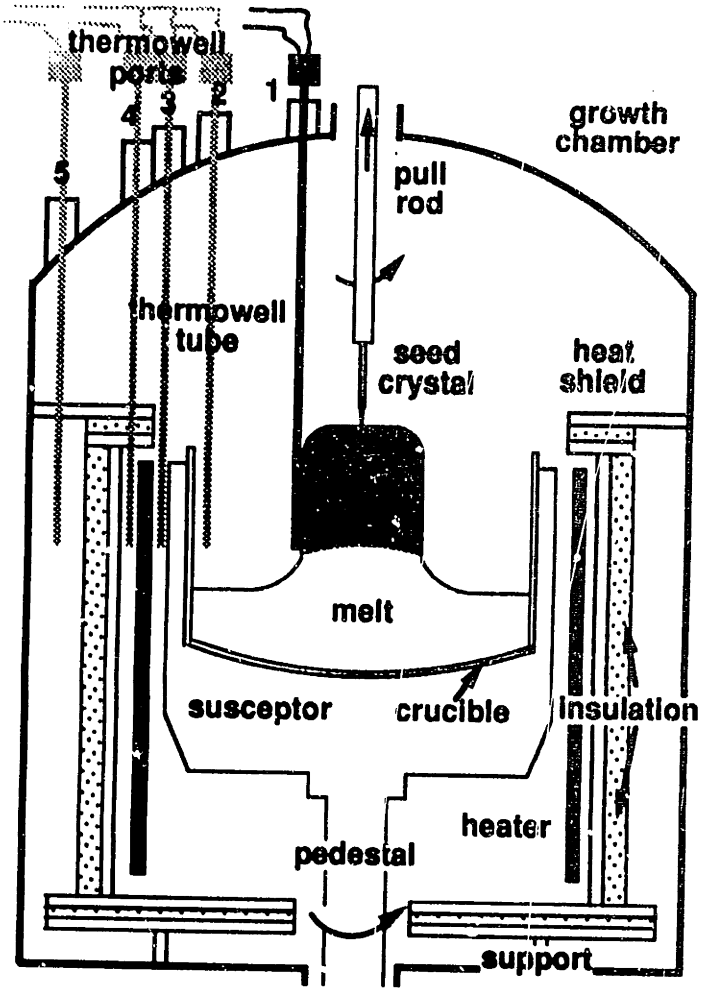

Figure 3-1: Schematic drawing of SILTEC crystal puller showing thermowell ports.

thermowell was constructed to ensure its integrity in the high-temperature environment and to provide electrical insulation for the thermocouple element. The cross-section of the thermowell is shown in Figure 3-2. The thermowell was made of 30 gauge wire, insulated with BeO and sheathed with tantalum tubing of $3.2\,mm$ O.D. The thermowell was alumina tubing of $4.3\,mm$ I.D. and $6.4\,mm$ O.D. Only one such thermowell and thermocouple were used for the measurements reported here. Because of the low operating pressure of $10\,Torr$, the temperature measurements result from radiation between the thermowell and all exposed surfaces in the CZ system, and conduction within the thermowell. The thermocouple was calibrated by touching the tip of the thermowell into the melt to yield a single calibration point at the nominal melting temperature of silicon, which is $1683 \pm 10K$ (Touloukian, 1970).

The temperature at each of the five radial stations was measured in $10\,mm$ increments starting from the lowest position, and allowing one to two minutes for equilibration between measurements. These measurements were made over the course of about two hours during the growth of the main body of a crystal with a diameter of $83\,mm$. The operating

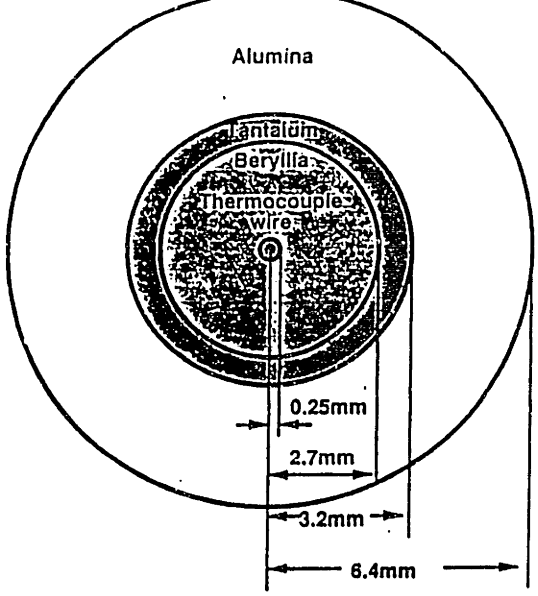

Figure 3-2: Thermowell cross-section.

conditions of the puller for the experiment are listed in Table 2.2. The measured temperature profiles are shown in Figure 3-3 and span a range of 1300 K. The measurements were taken during the crystal growth itself, and the exact time of each measurement point over the two-hour period was not recorded; therefore the exact melt volume and crucible position (the crucible was being raised at a rate of 0.75 $cm \cdot hr^{-1}$) for each measurement is not known. The uncertainty in measured temperatures associated with this is estimated next.

The uncertainty in comparing the measured profiles to the simulation is due to uncertainty in the relative vertical position of the thermowell with respect to the crucible and systematic offset due to calibration of the thermocouple. For the simulation the crucible and melt level positions are fixed with the position estimated by K.M. Kim as corresponding best to the levels during the measurement period. The results using these fixed positions are compared to all temperature measurements, even though the crucible was raised approximately 1.5 cm to compensate melt depletion during the course of the measurements. From the slope of the ambient temperature profiles the 1.5 cm uncertainty in relative position can change the expected temperature measurement up to $\pm 40\,K$. The estimate for calibration offset is based on the simulation results reported in Section 2, which show that the surface of the melt can be greater than 30 K above the melting temperature of silicon, even with natural convection included. An aggregate uncertainty due to these factors of $\pm\,50\,K$ or $\pm\,5$ percent of the maximum temperature range will be used as an acceptable tolerance when comparing predictions to measurements.

A sensitive measurement of the influence of convection in the melt was provided by the shape of the melt/crystal interface during crystal growth as determined by x-ray

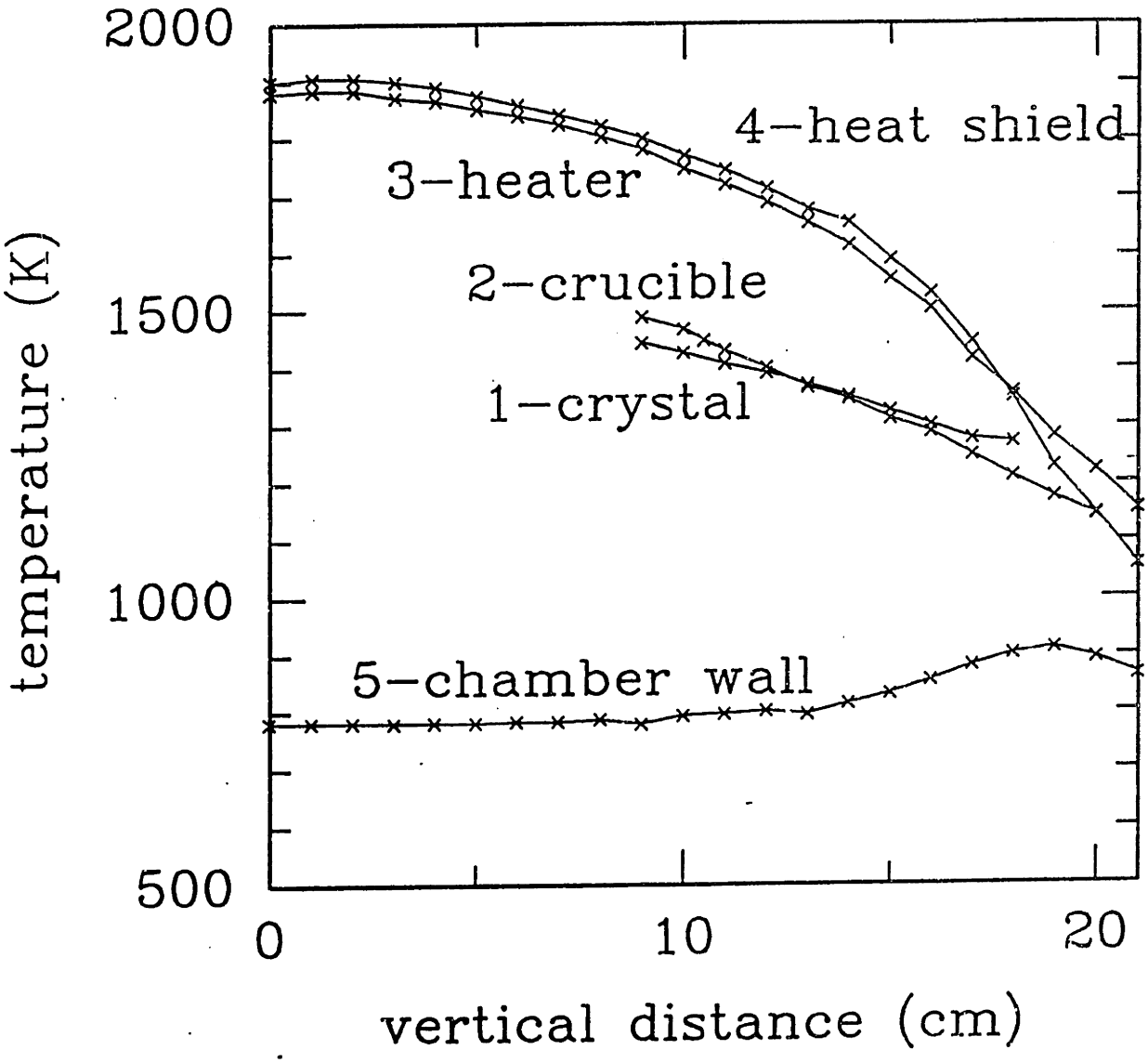

Figure 3-3: Thermal measurements from the SILTEC crystal puller. Horizontal axis marks vertical distance relative to the bottom of the crucible.

topography of the longitudinally sectioned and etched boule. A result for a $100\,mm$ diameter crystal grown in the same apparatus is shown in Figure 3-4a-c. The interface shape during steady growth is deflected toward the melt along the axis of the crystal by $3.6\,mm$. The shape during seeding is seen to be even more convex, while later in the growth it is hard to discern the growth shape. Since the crystal is a larger size it is expected that the deflection for the $83\,mm$ diameter crystal would be somewhat smaller. As a contrast, the melt-solid interface shape for a larger $200\,mm$ crystal grown in a $457\,mm$ crucible with similar heat transfer assembly is shown in Figure 3-5. That shape is deflected by up to $14\,mm$ into the crystal, but the shape is sigmoidal, sometimes referred to as "gull-wing-shaped". Evidently there is a much larger horizontal heat flux due to radiation from the crystal periphery near the trijunction for the $200\,mm$ crystal.

Data on the dislocation density is also garnered from the experiments. The crystals produced in the $254\,mm$ SILTEC hot-zone are regularly grown dislocation-free. This valuable piece of data indicates that the dislocation density predictions are not applicable for this situation. This will be discussed in detail later.

Finally, data can be borrowed to judge the accuracy of the IHTCM by comparing calculations of the oxygen concentration in the crystal to those measured in other systems. Figure 3-6 summarizes data available in the literature from a variety of systems, plotted as the measured oxygen concentration as a function of the ratio of the cross-sectional areas of the crystal and crucible. The crucible diameters and rotation rates of crystal and crucible are also indicated. Figure 3-6 shows that crystals are commonly grown with cross-sectional areas less than 20% of that of the crucible. However, the reported oxygen concentrations vary from $14 - 39\,ppma$, depending on the particular system and combination of rotation rates used. For a particular system it is apparent that higher crucible rotation rates yield a higher oxygen concentration in the crystal, and that higher crystal rotation rates also enhance the oxygen concentration. The enhancement of transport rates via rotation depends on the interaction of the azimuthal flow with natural convective flow and will be discussed in detail in Chapter 4. Radial profiles of the oxygen concentration shown in Figure 3-7 show that higher crucible rotation rates detract from the radial uniformity of the oxgyen profile, while higher crystal rotation rates enhance the radial uniformity of the oxygen profile. These effects on the radial uniformity are attributed to the balance of the stabilizing influence of crystal rotation on the near-field flow opposed to the destabilizing effect of crucible rotation.

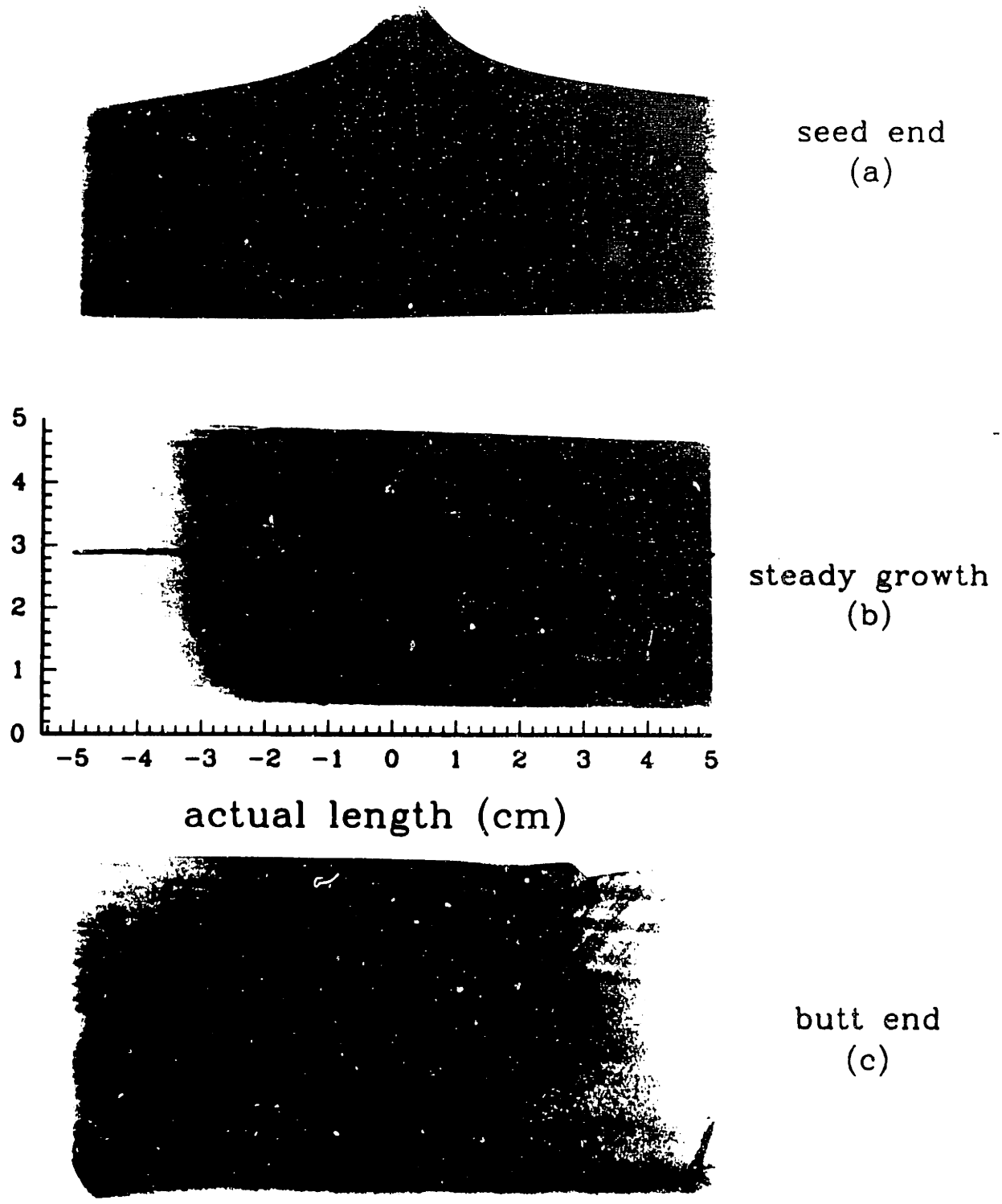

Figure 3-4: Xray topography of melt-solid interface striae for 100 *mm* diameter crystal (a) seed end (b) steady growth at 7.5 *cm* length (c) steady growth at 16.5 *cm* length.

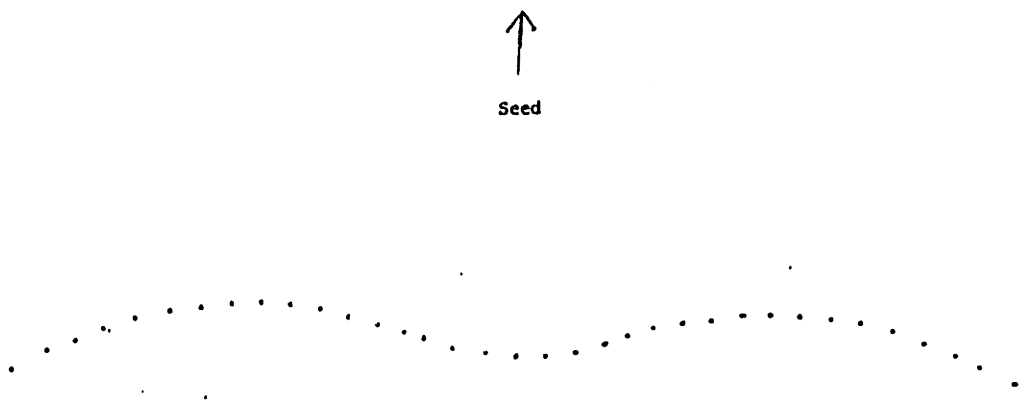

Figure 3-5: Melt-solid interface shape traced from 200 mm diameter crystal.

3.1.1 Thermowell Model

The temperature field predicted by the IHTCM cannot be compared directly to the measurements using the thermowell because the thermocouple does not measure the pointwise temperatures in the domains spanned by the finite-element grid. Instead, the thermowell exchanges radiative energy with all elements of the enclosure and conducts heat through its length to the chamber top. A heat transfer model of the thermowell has been developed which is used to compare the temperature measurements with the predictions of the numerical simulation.

The thermowell is modelled as a cylindrical heat transfer fin in which radial heat transfer meets very little resistance relative to axial heat conduction and radiation to the surrounding enclosure. This assumption is justified because the dimensionless radiation number for the thermowell (scaled with its outer radius) is small, $Rd_{tw} \sim 0.02$. The temperature profile within the thermowell is computed by solution of the one-dimensional energy equation

$$-k_{tw}\frac{d^2T(z)}{dz^2} + \frac{2}{R_{tw}}\sigma_{SB}\epsilon(T(z)^4 - T_{ar}(z)^4) = 0 \qquad (3.1)$$

where k_{tw} is an effective thermal conductivity of the material computed by assuming that the concentric rings of materials in the assembly act as parallel heat transfer resistances; the conductivity of the composite thermowell is calculated as $k_{tw} \simeq 0.47 W \cdot cm^{-1} \cdot K^{-1}$, using the conductivities of pure tantalum and beryllia.

Radiative exchange between the thermowell and the elements of the CZ system is computed from the temperature field from the IHTCM, by assuming that the presence of the thermowell has negligible effect on the temperature field. This assumption is justified

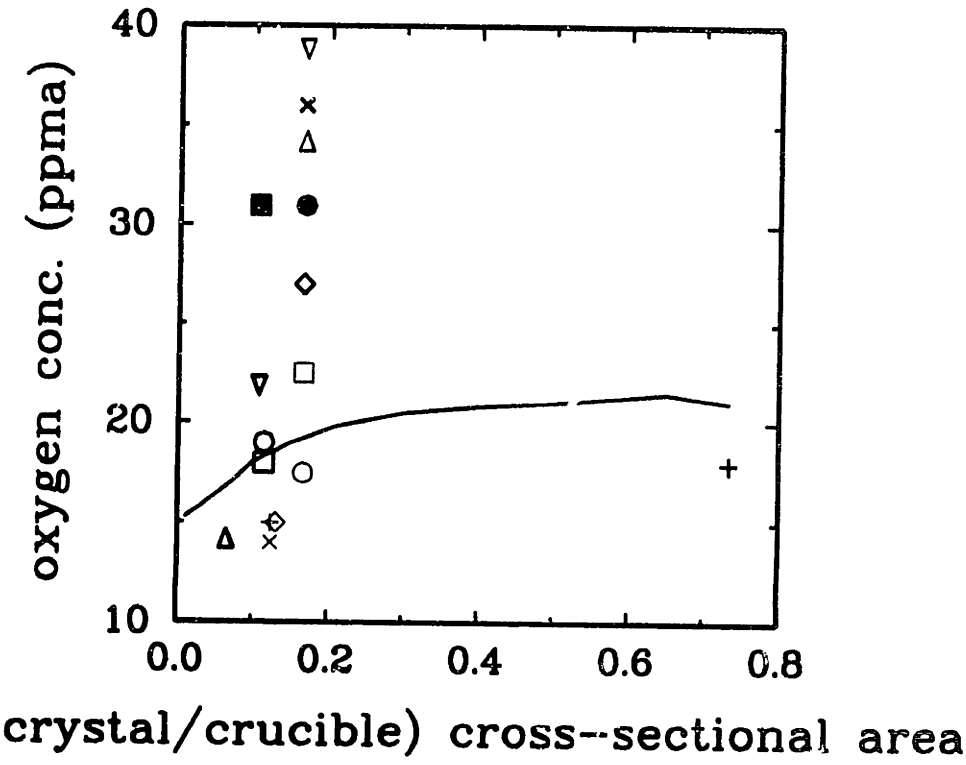

Figure 3-6: Oxygen concentration in crystals grown by several research groups: (——, +) in 300 mm crucible, from Lin and Benson, 1987,
in 108 mm crucible with $\omega_c = -1\,rpm$ and (+) $\omega_s = 25\,rpm$, and (×) $\omega_s = 25\,rpm$, from Yen and Tiller, 1991,
(◇) in 152 mm crucible with $\omega_c = 0\,rpm$ and $\omega_s = 0\,rpm$, from Kim and Smetana, 1986,
in 203 mm crucible with $\omega_s = 22\,rpm$ and (○) $\omega_c = -8\,rpm$, and (□) $\omega_c = -15\,rpm$, from Murgai, 1985,
in 203 mm crucible with $\omega_s = 22\,rpm$ and modulated crucible rotation (△) $0 \leq \omega_c \leq -15\,rpm$, and (▽) $0 \leq \omega_c \leq -25\,rpm$, from Murgai, 1985,
in 305 mm crucible with modulated and ramped crucible rotation (▪) $\omega_c = (-9 \pm 2.5)/(0.5t)\,rpm$, and (●) $\omega_c = (-25 \pm 2.5)/(0.5t)\,rpm$, t in hours, from Murgai, 1985,
in 305 mm crucible with (×) modulated and ramped crucible rotation $0 \leq \omega_c \leq -25/(0.5t)\,rpm$, and (◇) $\omega_c = -25/(0.5t)\,rpm$, t in hours, from Murgai, 1985,
in 300 mm crucible with (○) $\omega_s = 5\,rpm$ and $\omega_c = -5\,rpm$, and (□) $\omega_s = 15\,rpm$ and $\omega_c = -1\,rpm$, from Thomas et al., 1990,
in 300 mm crucible with (△) $\omega_s = 30\,rpm$ and $\omega_c = -0.3\,rpm$, from Hoshi et al., 1985, and ,
in 305 mm crucible with (▽) $\omega_s = 15\,rpm$ and $\omega_c = -8\,rpm$, from Braggins and Thomas, 1986.

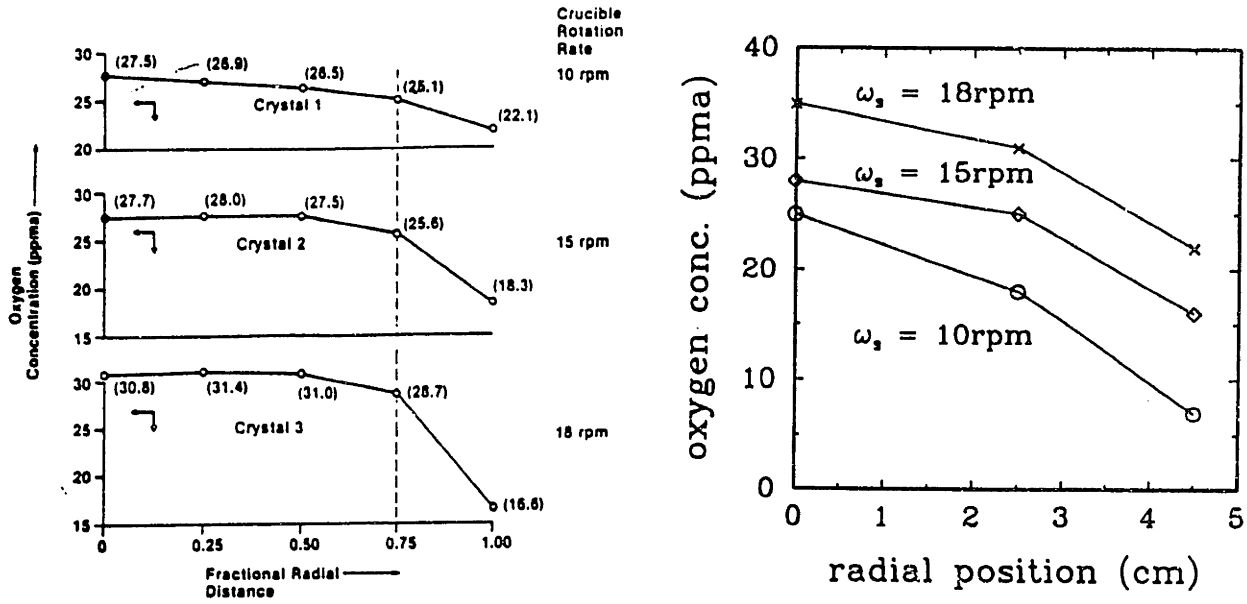

Figure 3-7: Radial oxygen profiles with (a) varying crucible rotation rate (from Murgai, 1985), and (b) varying crystal rotation rate (from Braggins and Thomas 1986).

for three reasons. First, the maximum heat flux carried by the thermowell assembly is estimated to be at most $5W$, compared to over $30\,kW$ of heat moving in the entire CZ system. A result discussed below shows that the temperature of the thermowell tube is almost exactly the same as the radiative ambient temperature, which is also evidence that its presence perturbs the thermal field little. Also, the projected area of the thermowell tube is only two percent of the area of the crystal, which makes it much smaller than any other component in the system. Finally rotation of the crystal and crucible are expected to smooth the azimuthal asymmetry caused by the placement of the thermowell.

Radiative heat flux to the thermowell is computed by Gebhart's method, Equations (2.4) and (2.9), generalized to include the three-dimensional view factors from the system components to the thermowell. An effective ambient temperature at each axial location along the length of the thermowell tube is computed by azimuthally averaging around the tube's periphery.

Equation (3.1) is integrated using one-dimensional, quadratic finite elements with the essential boundary condition that the temperature of the thermowell at the chamber wall is equal to the specified wall temperature. As an example, the temperature field computed in the thermowell, $T(z)$ is compared in Figure 3-8 to $T_{ar}(z)$ for the thermowell for the case with the thermowell next to the crystal (position 1 in Figure 3-1), and close to the

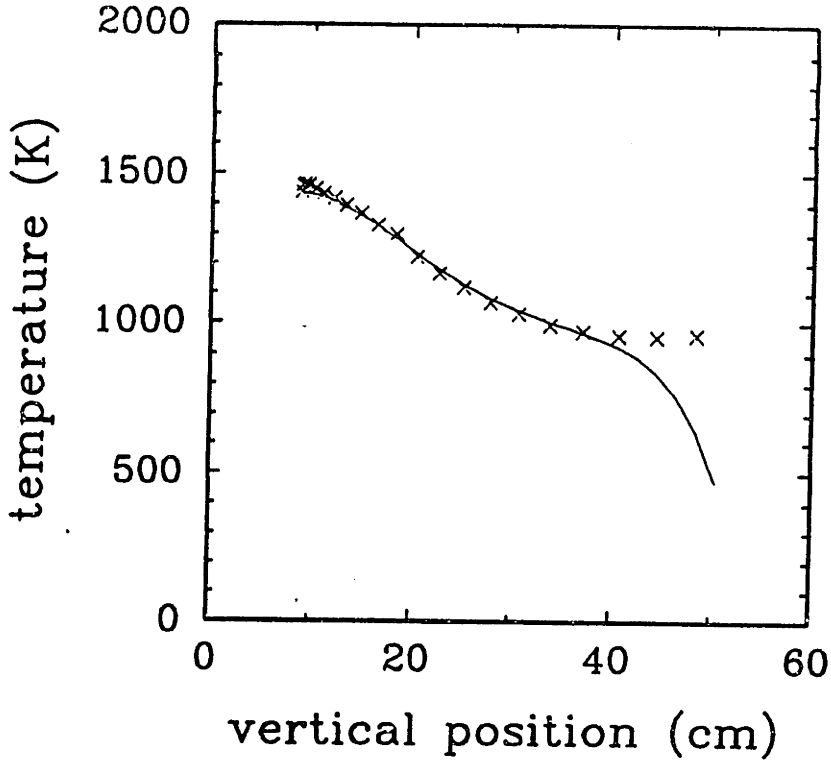

Figure 3-8: The effective ambient temperature computed by the thermowell model compared to the computed thermowell temperature, as a function of the axial distance along the thermowell tube. Thermowell location is adjacent to the crystal radial surface.

melt surface. The temperature predicted at the point of the thermocouple bead ($6.4\,mm$ from the end of the tube) is about $30\,K$ lower than the effective ambient temperature for radiation. Therefore conduction in the tube affects the comparison with the temperature measurements. This situation arises since the tip faces straight downward onto the highly reflective ($\epsilon_m = 0.05$) melt surface and hence views an effective ambient about $50\,K$ less than the sides of the tube.

3.2 Simulations with combined convective forces

From the simulations in Chapter 2 it is clear that no single flow mechanism dominates the convective heat transfer in a two-dimensional steady-state model of a silicon CZ system. Crystal rotation produces a meridional motion that opposes the direction of flow driven by buoyancy and thermocapillarity. Even though the meridional motion caused by crucible rotation is weak, the rotational motion throughout the melt impedes any meridional circulation. It converts meridional momentum into azimuthal momentum through the Coriolis force which presses buoyancy-driven flow into thin, vertically-stretched cells that collect near the crucible wall; this mechanism has been explored in

detail by (Ball and Farouk, 1988).

Asymptotic scalings (Jones, 1988) were reviewed in Chapter 1 for the four flow mechanisms described in Chapter 2 and the relative influence of each effect on convective heat transfer in the limit of strong convection was predicted by the simulations. This analysis concluded that buoyancy-driven flow dominates convection in the interior of the melt, but that rotation is the most important influence near the melt/crystal interface. These estimates are useful and agree qualitatively with the prediction of both considerable buoyant convection in the bulk of the melt and a separation layer between the crystal and the meridional flow; see Figures 3-9–3-12. However, a scaling analysis cannot be used to give an *a priori* indication of the temperature difference across the melt, the shape of the melt/crystal interface and the near-field flow in front of the melt/solid interface. These predictions depend on the details of the flow, especially near the interface, and the precise balance of the different convective mechanisms.

Steady-state flows corresponding to the proper combination of the four driving forces have been computed using continuation methods to increase the intensity of the flow. The magnitude of the melt viscosity is used as the continuation parameter because convection is weaker when the viscosity is artificially high. Calculations proceeding toward the viscosity of silicon from a high value give a sequence of states that should approach the desired one, if the state exists and it is unique. This method was used successfully to calculate the combined rotation case in Chapter 2. An attempt to calculate this same scenario by increasing first crucible rotation and then crystal rotation was unable to reach the final state. It is felt that continuation in viscosity has the advantage of forming boundary-layers only with all the flow mechanisms combined; alternatively, continuation would proceed in several parameters either individually or simultaneously and boundary-layers which are sensitive to parameter changes are formed before the final state is reached. Convergent calculation using the finest finite-element mesh (2,656 elements) used in the computations were not possible for the correct viscosity for silicon. Results are shown in Figures 3-9–3-13 at five different melt viscosities. The important parameters characterizing these results are also summarized in Table 3.1.

Calculations are presented from a parameter range of 20 to 5 times the actual viscosity of silicon. The solution stepping procedure passes many limit points in this interval (see Figure 3-15); multiple solutions exist for the discretized equations below about $9cP$. These limit points are associated with the evolution of the flow field. The thermal fields in Figures 3-9-3-13 are seen to differ very slightly, with the maximum ΔT varying by $\pm 2.3K$ over the parameter range. However, the flow structure changes substantially. In

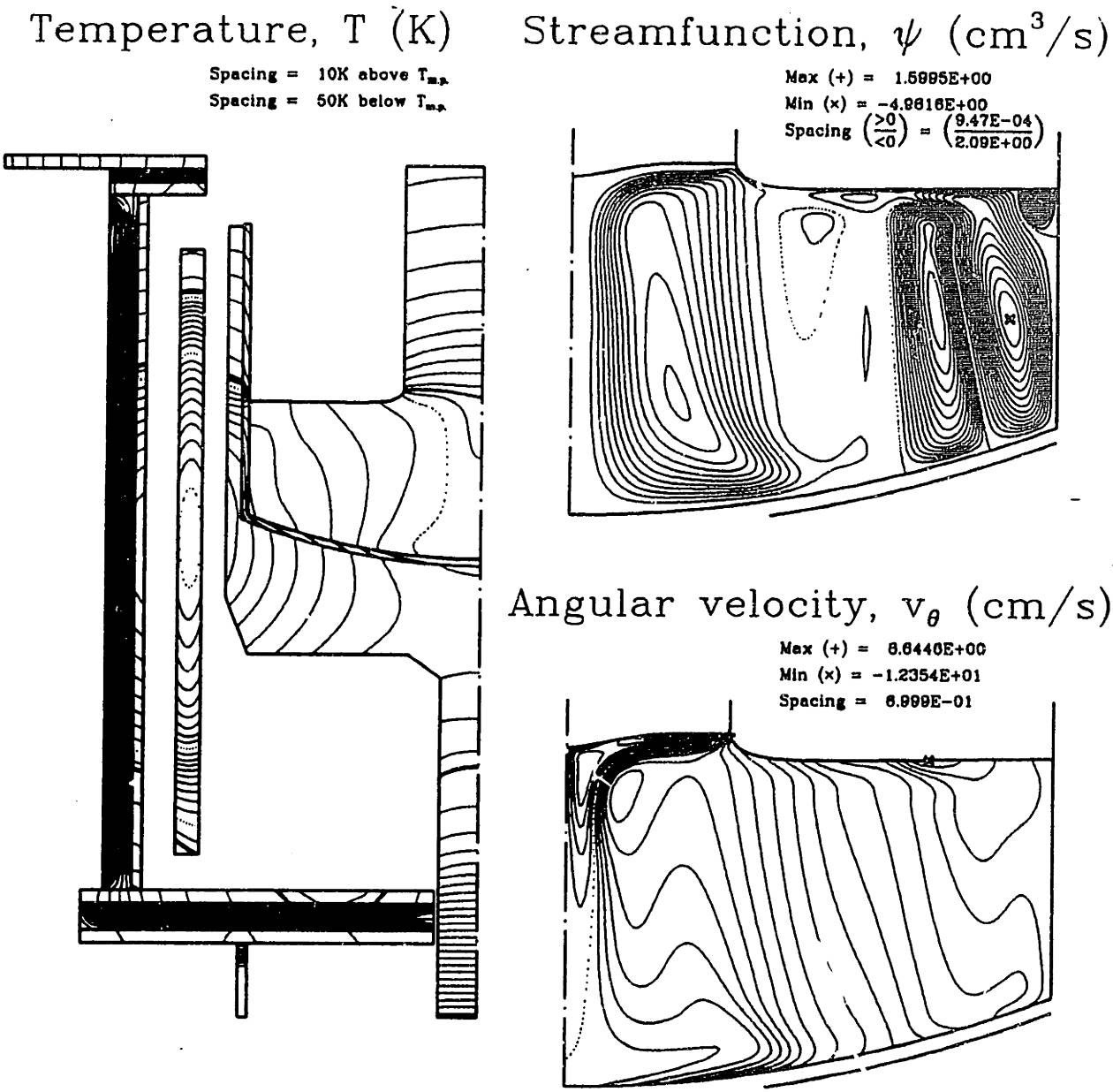

Figure 3-9: Effect of varying the viscosity with all the flow mechanisms in the simulation at the growth parameters listed in Table 2.2 and physical properties listed in Table 1.4. The viscosity for this calculation is $14.0cP$, 20 times the appropriate value for silicon listed in Table 1.4. Isotherm spacing is $10K$ above melting point and $50K$ below the melting point. Streamfunction and azimuthal velocity contours are uniformly spaced between the maximum value and zero for positive contours and between the minimum value and zero for negative contours.

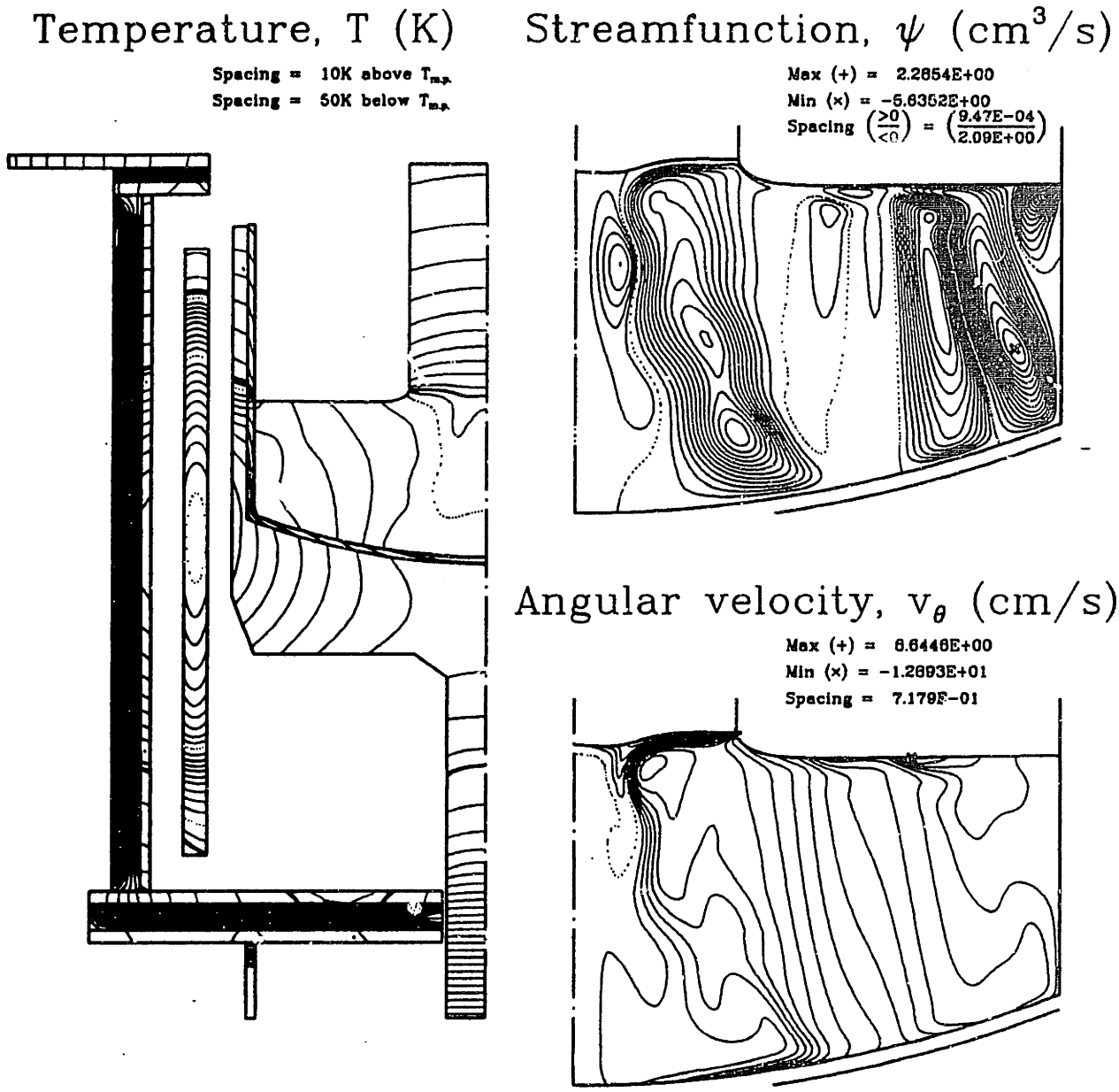

Figure 3-10: Effect of varying the viscosity with all the flow mechanisms in the simulation; the viscosity for this calculation is $8.08cP$, 11.54 times the appropriate value for silicon. Isotherm spacing is $10K$ above melting point and $50K$ below the melting point. Streamfunction and azimuthal velocity contours are uniformly spaced between the maximum value and zero for positive contours and between the minimum value and zero for negative contours.

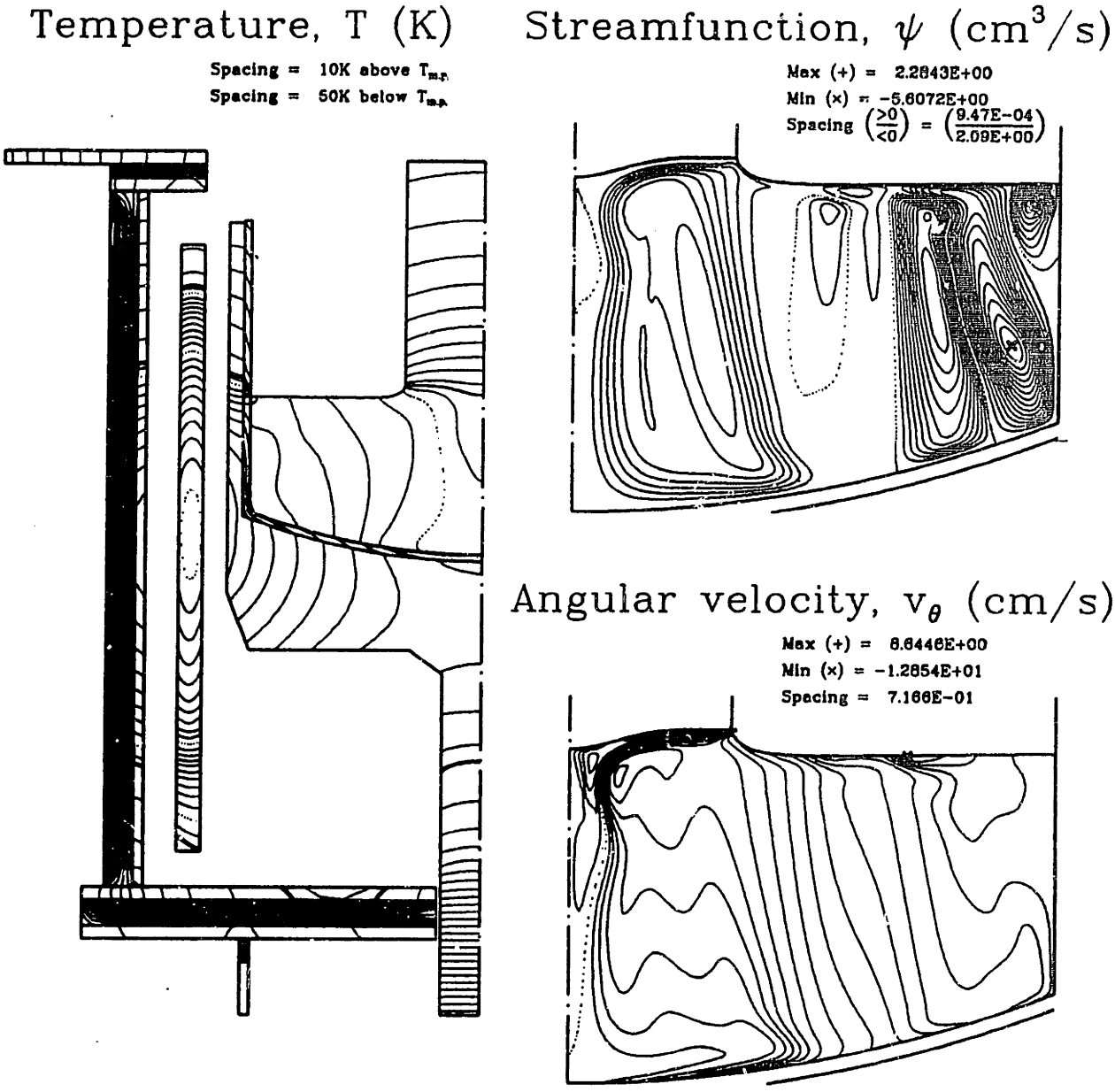

Figure 3-11: Effect of varying the viscosity with all the flow mechanisms in the simulation; the viscosity for this calculation is $8.17cP$, 11.67 times the appropriate value for silicon. Isotherm spacing is $10K$ above melting point and $50K$ below the melting point. Streamfunction and azimuthal velocity contours are uniformly spaced between the maximum value and zero for positive contours and between the minimum value and zero for negative contours.

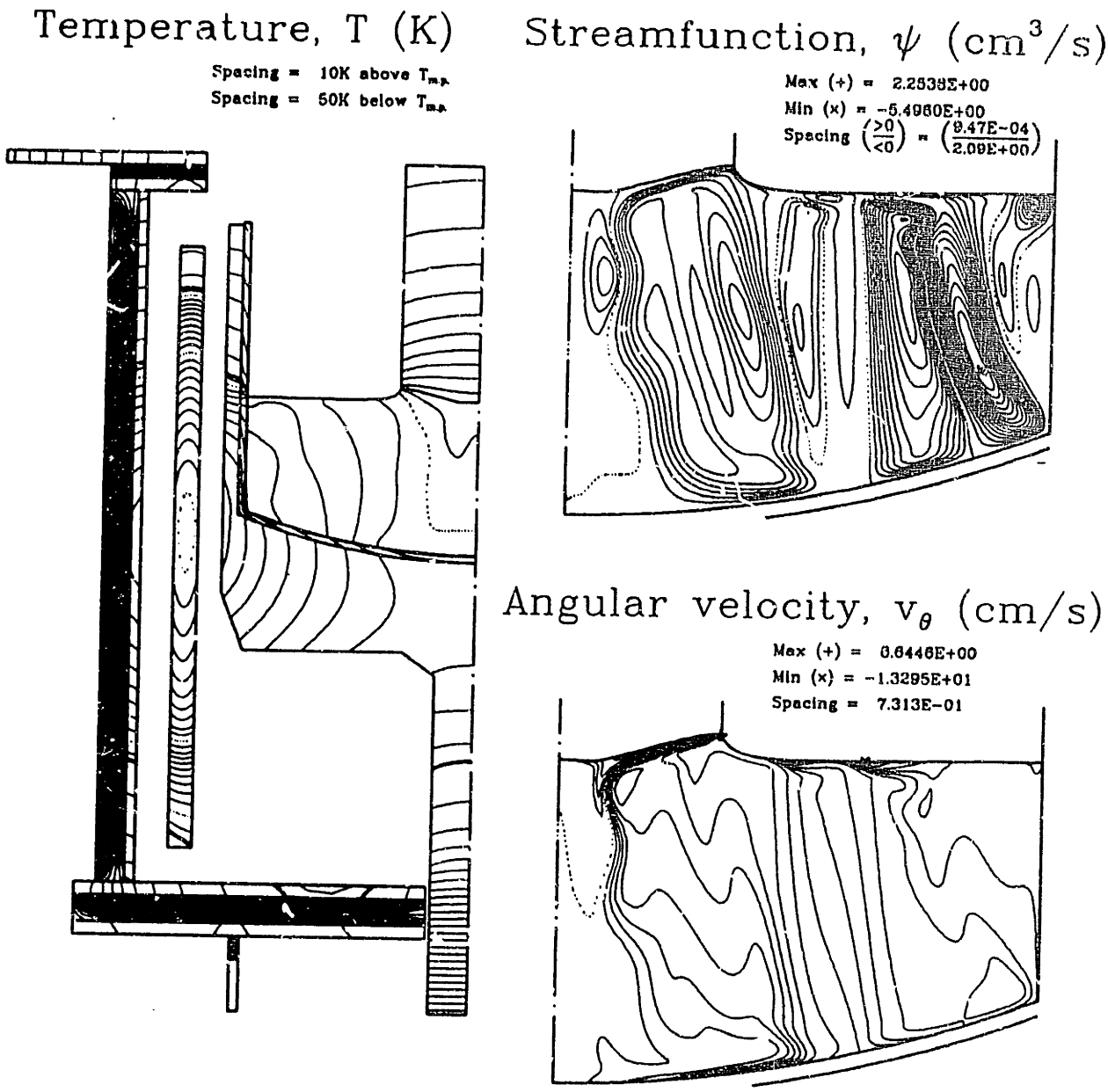

Figure 3-12: Effect of varying the viscosity with all the flow mechanisms in the simulation; the viscosity for this calculation is $5.09cP$, 7.27 times the appropriate value for silicon. Isotherm spacing is $10K$ above melting point and $50K$ below the melting point. Streamfunction and azimuthal velocity contours are uniformly spaced between the maximum value and zero for positive contours and between the minimum value and zero for negative contours.

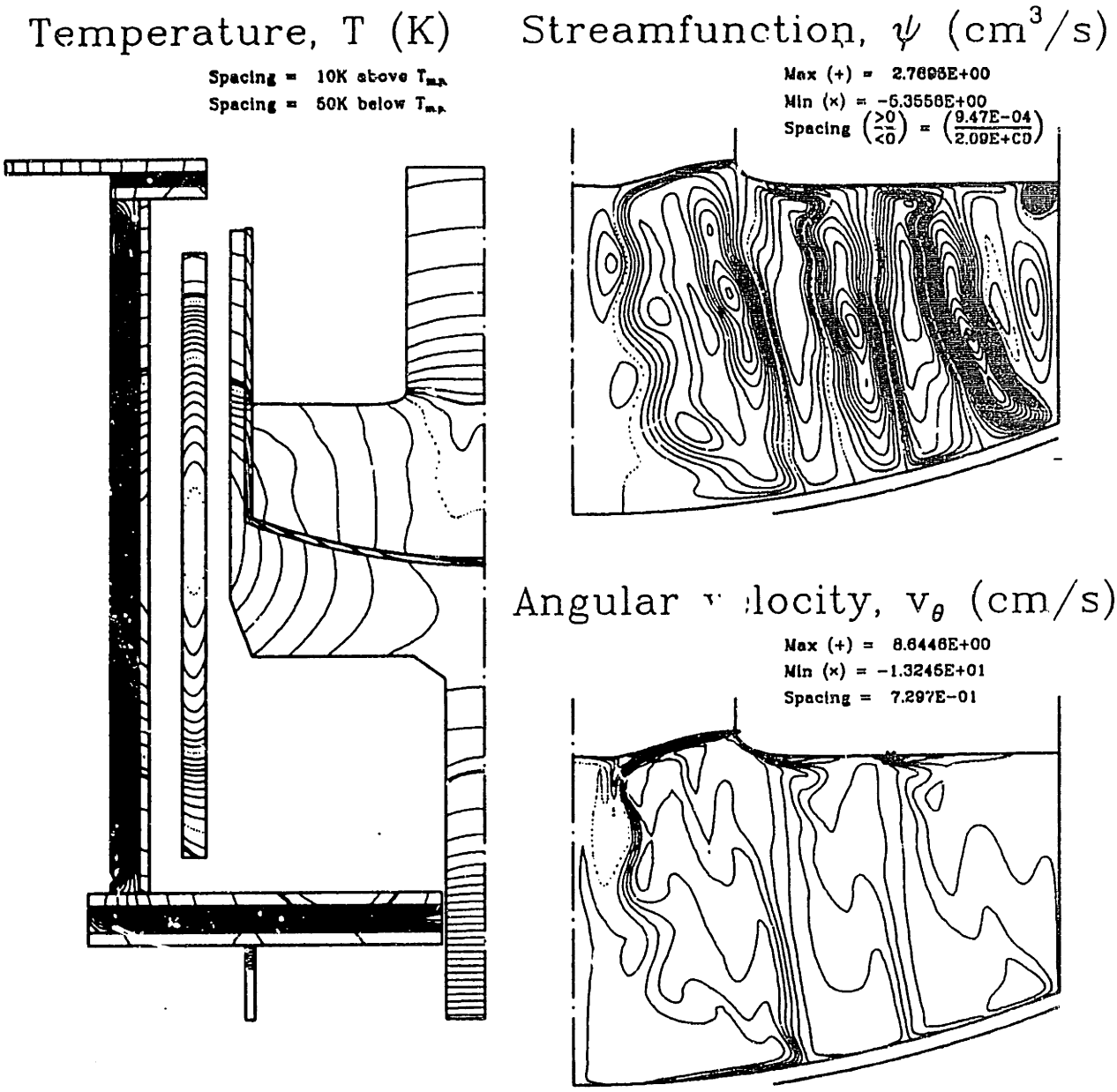

Figure 3-13: Effect of varying the viscosity with all the flow mechanisms in the simulation; the viscosity for this calculation is $3.54cP$, 5.06 times the appropriate value for silicon. Isotherm spacing is $10K$ above melting point and $50K$ below the melting point. Streamfunction and azimuthal velocity contours are uniformly spaced between the maximum value and zero for positive contours and between the minimum value and zero for negative contours.

Table 3.1: Summary of simulation results with viscosity as continuation parameter.

μ (cP)	T_{max} (K)	$\mathcal{P}$ (kW)	ΔT_m (K)	Δh (mm)	ψ_{max}	ψ_{min}	$(v_\theta)_{max}$	$(v_\theta)_{min}$	$(\tau_{m/s})^{max}$ $(CRSS)$
					$(cm^3 \cdot s^{-1})$		$(cm \cdot s^{-1})$		
14.0	1906.4	42.44	70.90	3.360	1.600	-4.962	8.645	-12.35	2.87
8.08	1905.3	42.37	69.35	3.187	2.285	-5.635	8.645	-12.89	2.95
8.17	1905.4	42.37	69.55	4.842	2.284	-5.607	8.645	-12.85	2.91
5.09	1904.0	42.25	69.19	7.042	2.254	-5.496	8.645	-13.30	3.78
3.54	1907.8	42.47	73.83	6.168	2.770	-5.356	8.645	-13.25	3.52

Figure 3-9 the individual driving forces for flow clearly manifest themselves and the expected dominant forces are seen to apply. A cell similar in shape to the Taylor-Proudman circulation persists under the crystal due to crucible rotation, although its shape has been distorted, and its circulation rate greatly increased from $-0.16\,cm^3 \cdot s^{-1}$ with crucible rotation alone to $-3.0\,cm^3 \cdot s^{-1}$ with the mechanisms combined. Crystal rotation manifests itself by establishing a separation layer between the Taylor-Proudman-shaped cell and the crystal surface. Buoyancy drives the flow cell along the vertical wall of the crucible. Thermocapillarity distorts both of the aforementioned flow cells along the free surface: the Taylor-Proudman cell is bolstered substantially by Marangoni flow and stretches to meet the curved meniscus where Marangoni forces dominate, and the buoyant cell is stretched inward along the meniscus by the Marangoni flow.

The primary flow in the melt interior is driven by crucible rotation in the azimuthal direction and buoyancy in the meridional direction. It is seen in Figures 3-10–3-13 that as viscosity is decreased, more complex buoyancy-driven structure appears, but over smaller length scales due to Coriolis force impeding meridional motion. The flow ultimately becomes as convoluted as the flows predicted by time-dependent finite-difference calculations (Kim and Langlois, 1986). It is interesting to see what becomes of the boundary-layers compared with the original calculations with isolated flow mechanisms, especially the near-field flow in front of the melt-solid interface. Figure 3-14 shows that the meridional transport is governed by the flow normally associated with crystal rotation only for small radii $r < 0.2R_s$, and for the most part the near-field meridional flow along the melt/solid interface deviates substantially from that of pure rotation. This indicates the considerable effect of natural convection on the near field flows and questions the wisdom of the traditional BPS model for solute segregation, where crystal rotation is assumed to dominate the flow near the melt/crystal interface and the motion is equated with the

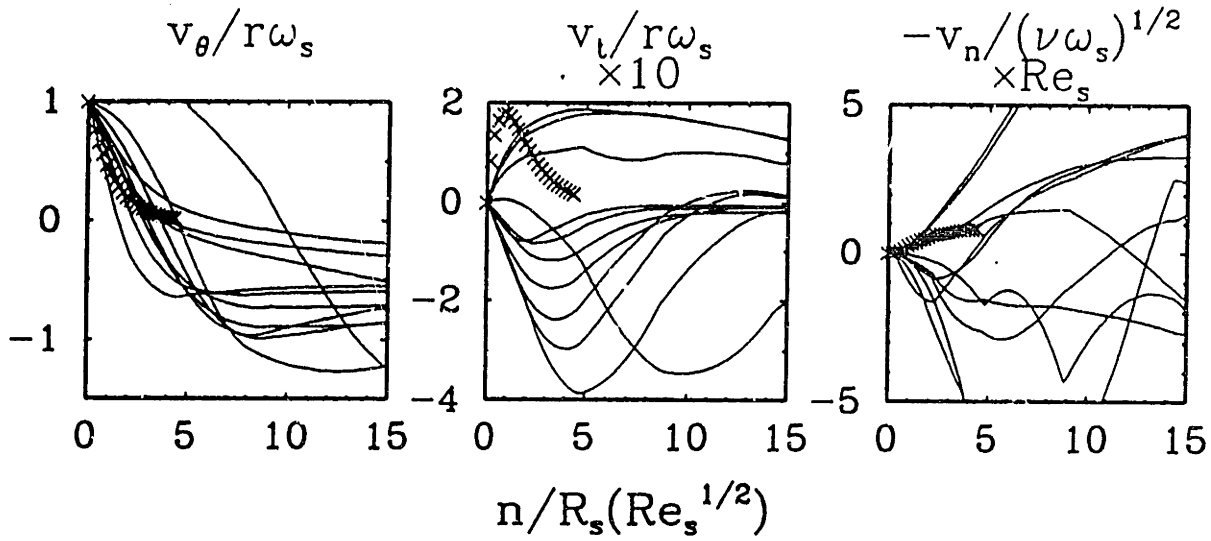

Figure 3-14: Boundary-layer structure of velocity components near the melt/solid interface for IHTCM solution with all driving forces for flow combined at $\mu = 3.54cP$. Calculation is plotted in terms of (a) azimuthal velocity, (b) tangential velocity, and (c) normal velocity components as a function of distance normal to the melt/solid interface. ($\times$ $\times$ $\times$) indicates the von Kármán similarity solution, while (——) indicates the simulation results, plotted starting from the melt/solid interface at r = (1) 0.05, (2) 0.1, (3) 0.2, (4) 0.3, (5) 0.4, (6) 0.5, (7) 0.6, (8) 0.7, (9) 0.8, (10) 0.9 and (11) 0.95 $\times$ R_s.

von Kármán flow.

The trajectory of the model solution with decreasing viscosity is depicted in Figure 3-15, which shows the three velocity components and temperature varying with viscosity at four different points in the melt domain. As viscosity is reduced and the trajectories move generally from right to left in Figure 3-15 a limit point is encountered first at $\mu \simeq 6.2\,cP$, and can be most clearly seen in the plots of v_θ and v_r of Figure 3-15b. The trajectory proceeds along increasing viscosity until $\mu \simeq 9.0\,cP$, where a second limit point occurs and can be seen clearly in all the variables 3-15a. Several less noticeable limit point are passed: near $\mu \simeq 4.8\,cP$ (see plots of v_z and v_r in Figure 3-15d) and near $\mu \simeq 4.0\,cP$ (see plots of v_z and v_r in Figure 3-15c). Finally, the solution trajectory becomes mired, passing through many limit points and being unable to proceed significantly in either increasing or decreasing viscosity around $\mu \simeq 3.5\,cP$.

Attempts to improve the resolution of this mesh and further reduce the viscosity

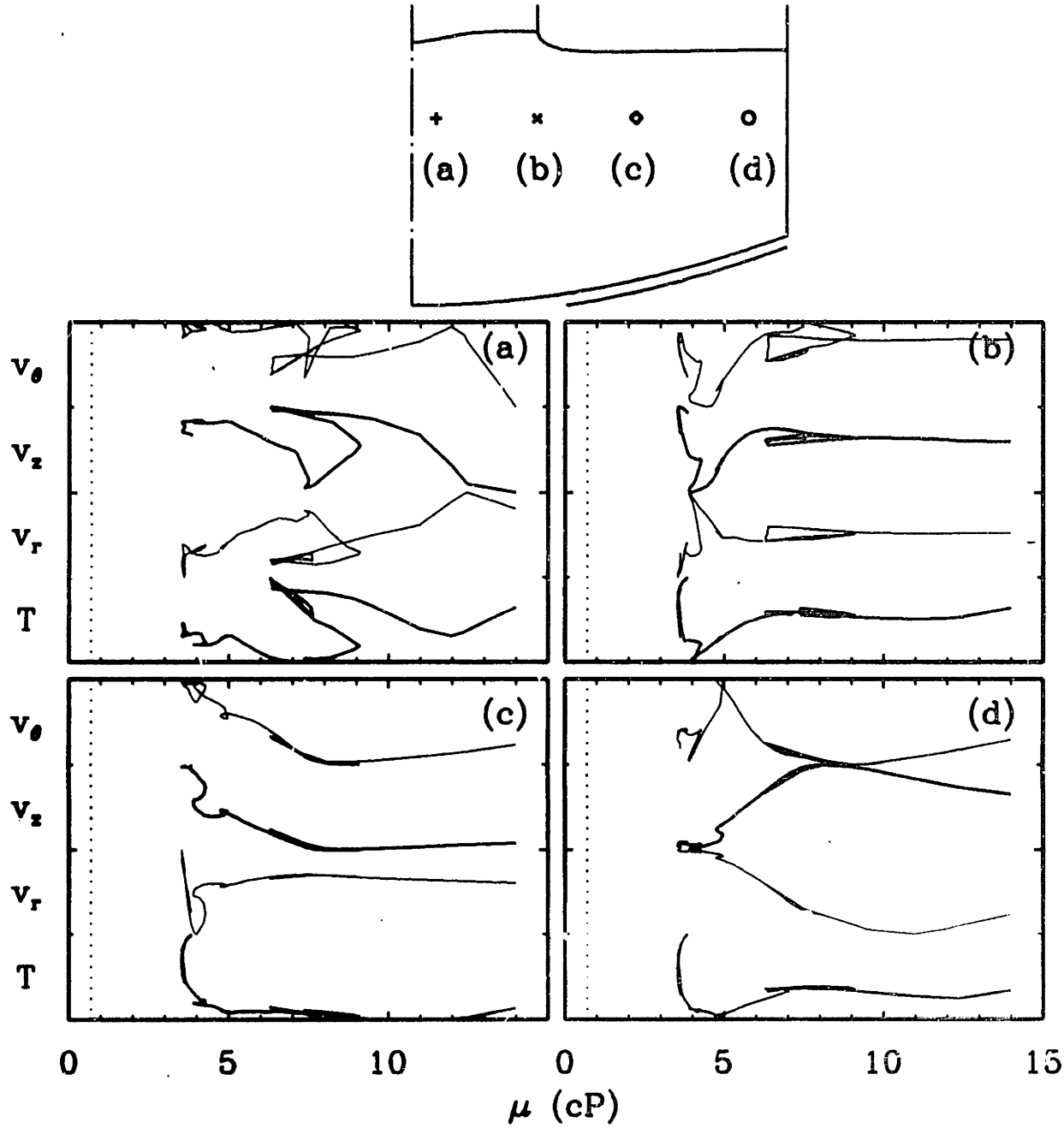

Figure 3-15: Plot of the trajectory of IHTCM solutions with all flow mechanisms combined with viscosity decreasing as the continuation parameter. Plot of solution variables T, v_r, v_z and v_θ at four points in the melt, (a) (+) under the crystal near the centerline, (b) (×) under the crystal/melt/ambient trijunction, (c) (◇) in the bulk of the melt under the free surface, and (d) (○) near the crucible wall, are shown. The vertical line (⋮) denotes the molecular viscosity of silicon, $\mu_{Si} = 0.7\,cP$.

with the current model are of dubious utility. Besides being computationally taxing and of uncertain success, the flow at these conditions is most likely three-dimensional and time-dependent. Simulations of two-dimensional axisymmetric flow in this geometry have shown time-dependence in the melt flows (Kim and Langlois, 1986). Furthermore, semiconductor flows in cylindrical geometries have been shown to first undergo bifurcations to a three-dimensional flow before becoming three-dimensional and time-dependent (Neumann, 1990). Therefore, the burdensome task of resolving the calculation to correct viscosity was not pursued further. In light of these results, the simulations in Chapter 2 with natural convection only will be used in this Chapter as an upper bound on convective heat transport in the system.

3.3 Comparison With Temperature Measurements

The thermowell temperatures predicted using the temperature fields computed with IHTCM can be compared directly with the measurements reported in Figure 3-3 by using the thermowell model. The uncertainty in the measured values is as great as the maximum difference between the simulation results with different convection mechanisms. Consequently the temperature measurements cannot be used to differentiate between simulation results with and without convection. This is reinforced by comparing the temperature along the crystal periphery for the calculations with no convection at all, and the maximum computed convection given by thermocapillarity; see Figure 3-16. This temperature profile, indicative of the thermal field in the crystal, is seen to vary by less than $10K$, well within the characteristic uncertainty of the comparison. In spite of this deficiency, the comparison with the measured temperatures still determines the accuracy of the thermal profile since the uncertainty is only $\pm 5\%$ of the entire span of the temperature measurements. Agreement on the slope and curvature of the thermal profile, although the temperature profiles may be shifted, is a further positive indication of the predictive abilities of the model. In order to distinguish between the different flow mechanisms, a more precise and pointwise-accurate measure is required: comparison with the observed melt-solid interface shape will be used for this purpose.

The comparison is shown in Figure 3-17 for all five radial positions of the thermowell. Results are shown for the measurements, including the uncertainty bounds estimated in Section 3.1, and predictions of the IHTCM for the case with no flow at all, the most intense convection (thermocapillary) that was computed, and the case with flow mechanisms combined at the minimum attained viscosity. These represent the bounds of

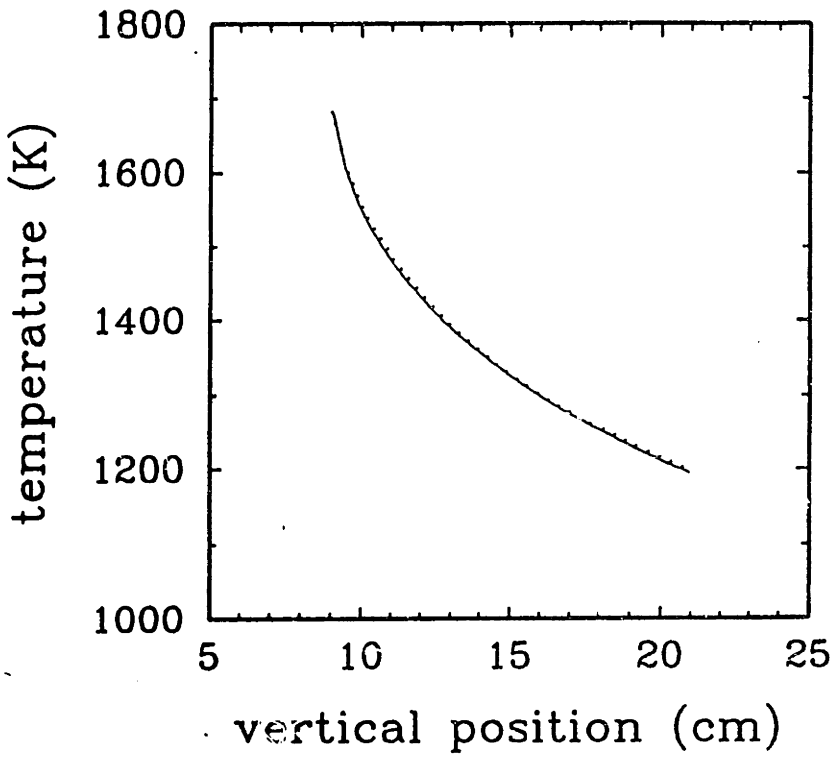

Figure 3-16: Comparison of temperature profiles along the crystal surface for the simulations with maximum and minimum convection. The curves represent the calculation without convection (···) and the calculation with thermocapillary motion (———).

minimum melt convection, maximum convection and the closest estimate of realistic convection. The accuracy of the temperature near the crystal surface is most important, and both the values and the gradients of the temperature field there are well-predicted by the simulations. The results from positioning the thermowell between the susceptor and the heater, and along the outer surface of the heater show similar accuracy, with the calculations reproducing the measurements to within the uncertainity of the data. It is interesting that the calculations and the data for the position near the outer surface of the heater almost can be overlaid if the curves are shifted slightly, possibly indicating inaccuracy in the position of the probe. The temperature near the chamber wall is predicted extremely well, considering the model has less detail there than closer to the crystal. Even the rise in temperature with approach to the unshielded graphite plate at the top of the heaters is reproduced.

The sensitivity of these predictions to details of the melt convection is demonstrated in Figure 3-18 where the comparison with the experimental data is expanded to include the calculations reported in Chapter 2 for buoyancy and combined crystal and crucible rotation. Essentially all the simulation results lie within the uncertainity bounds for the experimental data; hence, drastic changes in the melt motion have only small effects on the temperature field within the entire CZ system, because the melt represents only small fraction of the thermal mass in the chamber. Therefore the IHTCM performs reasonably well at predicting the temperature field, irrespective of the accuracy of the simulation for melt convection. Unfortunately further measurements could not be made to meticulously document the melt level and crucible position at each measurement point; this could minimize the inherent uncertainty in the comparison. It appears that conduction-dominated models are preferable for analyses limited to the thermal field throughout the CZ chamber (for example Bornside et al., 1991), since the considerable costs and difficulties associated with resolving the melt flow are avoided. As well, the sensitivity of the thermal field to convection is most profound close to the melt/solid interface; thermal studies of the crystal removed from the interface region would also be well-served by a conduction/radiation model.

In spite of the similarities between the temperature fields predicted on the length scale of the apparatus, changing the mode and intensity of convection has a profound effect on the heat flux near the melt/crystal interface and hence on the interface shape. This variation is shown in Figure 3-19 for the interface shapes computed with various convection sources. The measured melt/solid interface shape for a 100 mm crystal grown in a 305 mm-diameter Siltec crucible also is shown and is convex at the crystal axis with

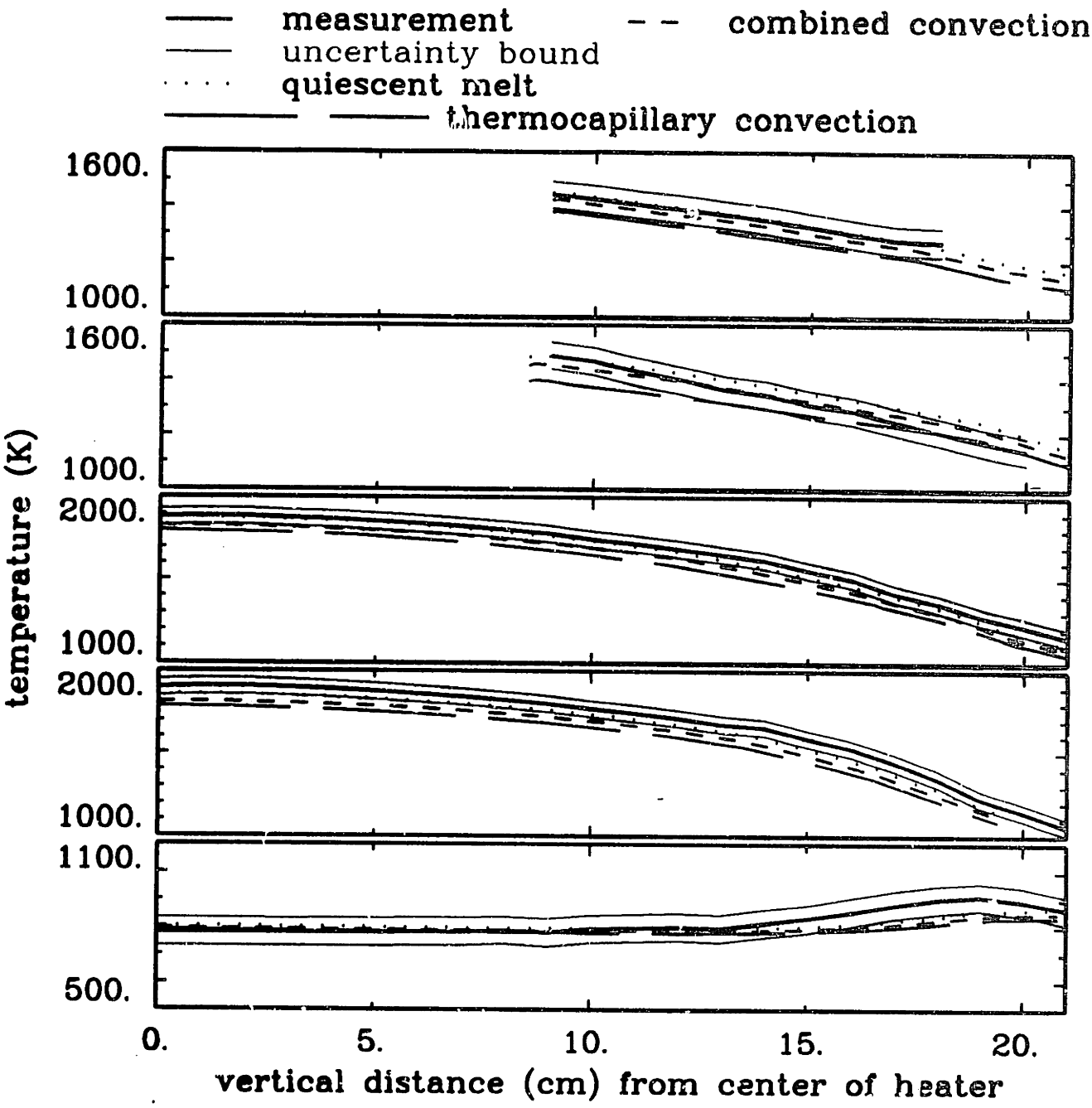

Figure 3-17: Comparison of temperature profiles measured with the thermowell to predictions of the thermowell model for the simulations featuring no convection, maximum predicted convection and combined convection. The curves represent the measurements (—), the uncertainty bounds on the data (—), calculations without convection (···), calculations with thermocapillary motion (—— —— ——) and calculations with the combined flow mechanisms (- - - -).

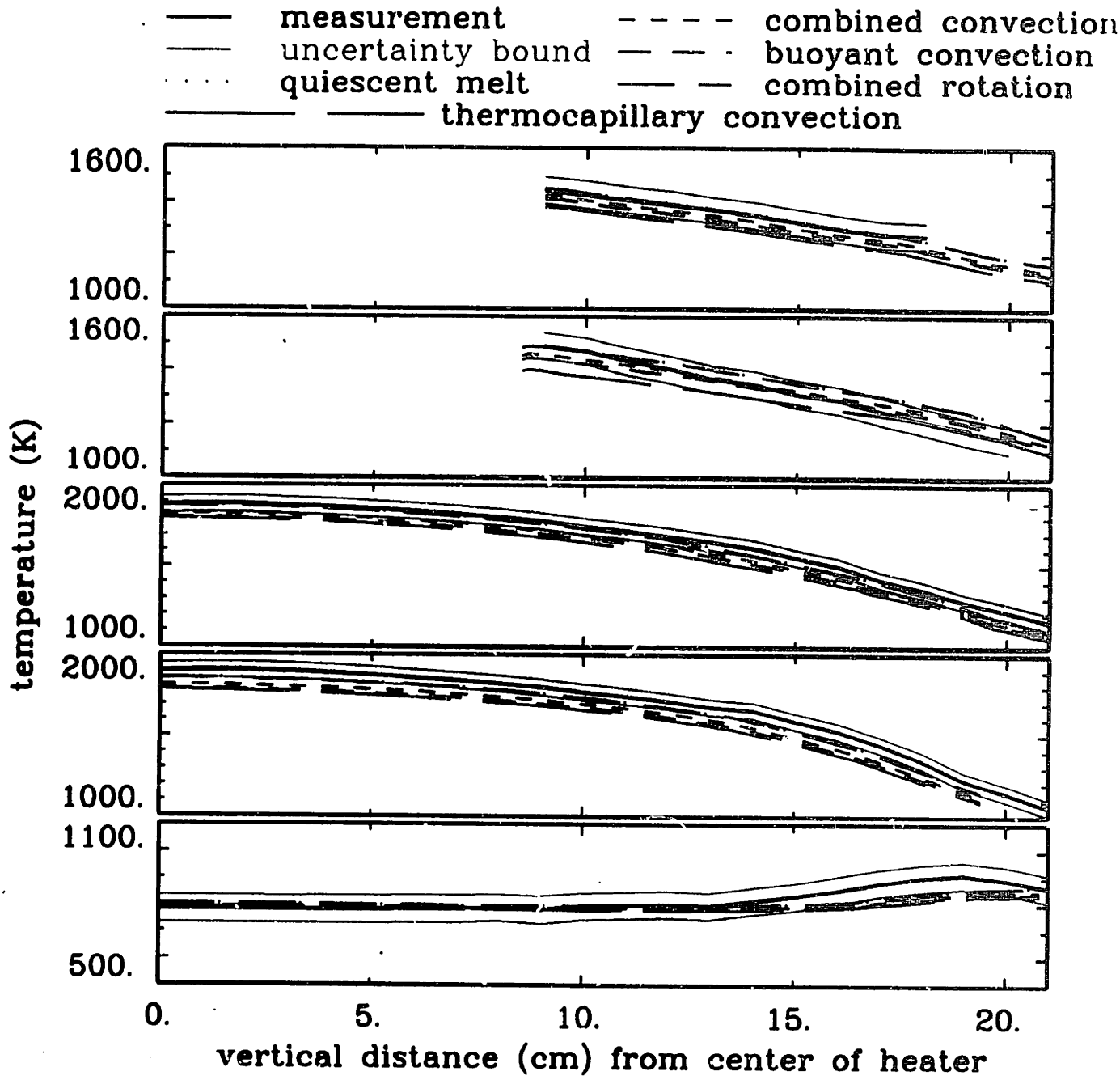

Figure 3-18: Comparison of temperature profiles measured with the thermowell to predictions of the thermowell model for the simulations using different convective driving forces. The curves represent the measurements (▬), the uncertainty bounds on the data (—), calculations without convection (···), calculations with combined convective forces (- - - -), calculations with buoyancy (– – –), calculations with combined rotations (— — —) and calculations with thermocapillary motion (—— —— ——).

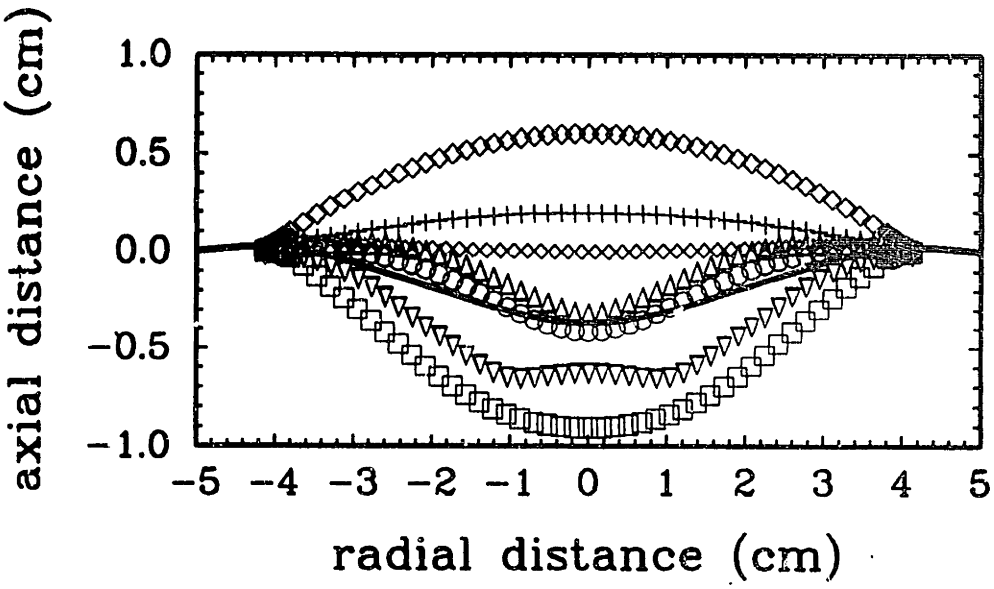

Figure 3-19: Melt/crystal interface shapes from the simulations with individual and combined convection mechanisms. (▬) measurement; (+++) no convection; (× × ×) crucible rotation; (◇◇◇) crystal rotation; (○○○) buoyancy; (□□□) thermocapillarity; (△△△) combined forces with $\mu = 14.0cP$; (▽▽▽) combined forces with $\mu = 3.54cP$.

an interface deflection that is much less than is predicted for buoyancy-driven and surface tension-driven convection. This shape is interpreted as evidence of both the prevalence of natural convection on the near-field flow there, and the damping effect of rotation on natural convection, since the measured deflection is best matched with combined convection or simple buoyancy. The measured shape also features little curvature near the centerline; this is qualitatively predicted only by the simulation with combined driving forces at $\mu = 3.54cP$, although the interface in the calculation deflects slightly upward at the center.

3.4 Thermoelastic Stress Analysis

The sensitivity of the predictions of crystal quality to the details of the melt/crystal interface shape and the temperature field near the interface were explored by computing the thermoelastic stress field for each of the simulations described earlier. The results

are plotted as contours of the von Mises stress invariant scaled with the critical resolved shear stress of silicon estimated at the melting point. Contour plots of the dimensionless von Mises stress are shown in Figure 3-20 for the four different convection conditions shown in Figures 3-9, 3-11, 3-12 and 3-13. Foremost in these results is the qualitative observation that large stresses occur near the melt/crystal interface, irrespective of the form of the convection; the maximum stress at the melt/solid interface is also a local maximum, which is critical in determining the boundary-layer structure of the dislocation field (Maroudas and Brown, 1991a) for dislocated material.

It also is interesting that including convection in the analysis, and thereby lowering the temperature gradients in the melt, only marginally lowers the thermoelastic stress in the crystal. The flattest interface was computed with crucible rotation only; it does not give the lowest stress due to the fact that the temperature field is two-dimensional. In fact, the minimum stress of all the computations in Chapters 2 and 3 is computed for the case of isolated buoyant convection.

3.5 Outlook

The major shortcoming of the IHTCM is its inability to compute the combined flow state given the mesh used. The flow in the actual system is likely three-dimensional and time-dependent, and in order to depict the experimental parameters, this must be taken into consideration. The major shortcoming of the experimental measurements was the sketchy report of precise melt level and crucible height during the temperature measurements. Since the experimental program was cancelled, work has proceeded on further model development in order to predict the combined flow state.

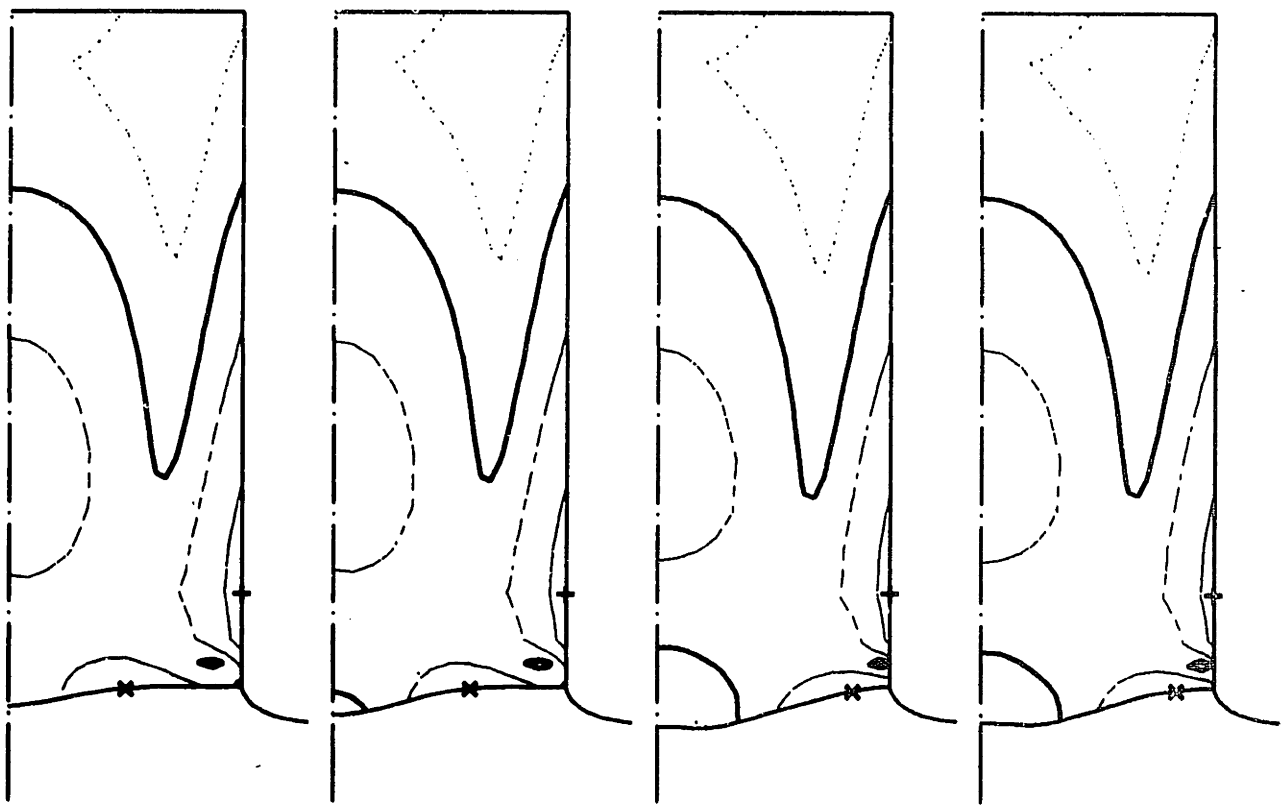

Figure 3-20: Computations of the von Mises stress in the crystals and temperature fields predicted by simulations with combined convection forces and decreasing viscosity. Stress contours are at 0.5, 1, 2, 4 and 8 times the value of the CRSS; CRSS=$1.8 \times 10^7 dyn \cdot cm^{-2}$. Viscosity of simulations are: (a) $14.0cP$, (b) $8.17cP$, (c) $5.09cP$, and (d) $3.54cP$

Chapter 4

Modelling Turbulence in the Melt

Summary

The simulations discussed in Chapter 3 show that IHTCM model does not give unique steady-state solutions as the correct viscosity of a silicon melt is approached with natural convection and rotation combined. This motivates the consideration of a more general description than two-dimensional and /steady flow. In this Chapter the notion of unsteady flow is revisited in more quantitative terms than in Chapter 1. Results of observations and calculations from the literature for silicon and other low-Prandtl-number fluids in CZ and other geometries are used to infer three-dimensionality and time-dependence of the flow in CZ. A time-averaged two-dimensional model is then developed and the $K-\epsilon$ model for turbulent viscosity is employed to predict the average transport rates in the limit of turbulent flow. This model is implemented in a low-Reynolds-number form (Jones and Launder, 1972), and results are presented that illustrate a practical implementation of the $K-\epsilon$ model and its potential for improving the predictive capabilities of the IHTCM. Predictions of turbulent flow with combined mechanisms are compared quantitatively with the measurements described in Chapter 2, and qualitatively with results from the literature.

4.1 Time-Dependence and Turbulence in CZ silicon Growth

Short time-scale fluctuations have been clearly observed in the flow of industrial CZ silicon systems (Kobayashi et al., 1991). The spectrum of oscillating frequencies has not been clearly distinguished and therefore the precise nature of this time-dependence remains

uncertain. While increasing the system dimensions and hence the driving forces for convection will definitely yield turbulent flow after some point, it has yet to be proven that turbulence is present in systems comparable to the 254 mm hot zone SILTEC. To judge turbulence requires insight into its generation and sustenance. This section describes in simple terms the characteristics of a turbulent flow.

4.1.1 Characteristics of turbulence

Turbulence is the most complicated of fluid motions. It differs from laminar flow in that streamlines fluctuate randomly over small distances with high temporal frequencies. It is inherently three-dimensional and characterized by a self-reinforcing cascade of energy from larger to smaller flow structures through a continuous spectrum. The transition to turbulence in confined flows is discernable as oscillatory behavior with some combination of discrete modes, which are deduced experimentally by reduction of a measured quantity into component frequencies.

The turbulent energy cascade can be explained by considering the behavior of a *vortex line*, a column of rotating fluid. The vorticity equation takes the form

$$\frac{\partial \boldsymbol{\omega}}{\partial t} + \mathbf{v} \cdot \boldsymbol{\nabla}\boldsymbol{\omega} = \boldsymbol{\omega} \cdot \boldsymbol{\nabla}\mathbf{v} + \boldsymbol{\nabla} \cdot (\mu \boldsymbol{\nabla}\boldsymbol{\omega}), \tag{4.1}$$

where $\boldsymbol{\omega}$ is the vorticity defined by $\boldsymbol{\omega} = \boldsymbol{\nabla} \times \mathbf{v}$. The nonlinear term $\boldsymbol{\omega} \cdot \boldsymbol{\nabla}\mathbf{v}$, representing the interaction between the vorticity and the velocity-gradient, has two important effects when the velocity field is three-dimensional. The components of the velocity gradient orthogonal to the vortex's axis transfer vorticity into other directions, while the collinear component exerts a tensile stress. These are referred to as *tilting* and *stretching* effects, respectively. Given a large three-dimensional perturbation, the tilting of a vortex line transfers enough energy into other directions that the *induced* three-dimensional flow creates yet more distortion in the original vortex, propagating rapidly to a hodgepodge of randomly-oriented vortex lines. Meanwhile the stretching of a vortex, by conservation of momentum, causes its diameter to shrink and its rotational speed and kinetic energy to increase. Thus ensues highly chaotic motion with a transfer of energy to smaller length scales. Viscosity limits the smallest eddies at wavelengths on the order of Re^{-1}. A power spectrum from a flow in the latter stages of transition to turbulence is shown in Figure 4-1.

The *Shannon sampling theorem* (Reid, 1983) dictates that unbiased frequencies can be deduced when the sampling interval is less than one-half the period of the highest

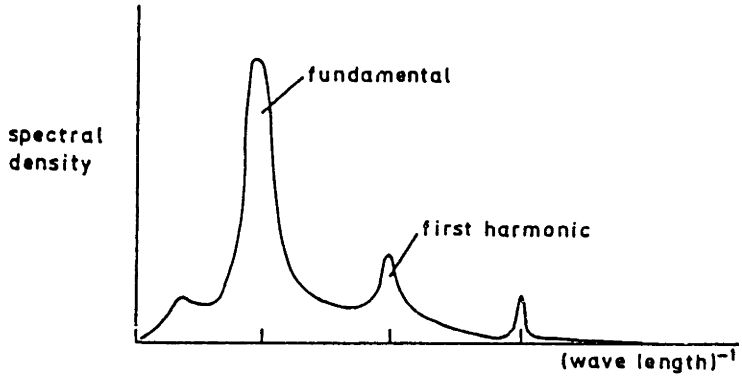

Figure 4-1: Power spectrum of a flow in the latter stages of transition to turbulence, showing the decay of energy at higher frequency (equivalent to inverse wavelength). Taken from Bradshaw, 1978.

frequency oscillation. For CZ flows, oscillations due to the rotation of crystal at $20\,rpm$ have a period of $3\,s$ or some integer fraction of $3\,s$. To establish the turbulent cascade to higher frequencies requires discriminating between frequencies of less than one second. The time-scale of *thermal* fluctuations observed in the literature does not approach this precision[1], and so unqualified proof of turbulence in CZ flows is lacking. The next subsection revisits the literature to determine the nature of the time-dependence in CZ and analogous situations. Conclusions also are inferred from the flow of other low Pr fluids and geometries.

4.1.2 Observations Regarding Three-Dimensional and Time-Dependent Flow

Rotation is a source of instability in CZ since any azimuthal variation is temporally unstable due to the angular flow. Transients due to crystal rotation (period $\sim 3\,s$) and crucible rotation (period $\sim 7.5\,s$) appear as primary modes of oscillation in the temperature-time

[1]The low Prandtl number of molten silicon means that eddies must be $\sim$ 100 or more times larger than the smallest eddies to impact a thermal measurement, and so the highest frequencies cannot be detected.

traces produced in experiments, suggesting that most apparatuses possess a single hottest spot. The gear-shaped patterns observed in clear, high Prandtl number fluid experiments on the other hand (Jones, 1983a) would result in the observed frequency being the rotational frequency multiplied by the number of lobes in the gear-shape.

Natural convection is the primary origin of instability. Several early studies of low Pr melts clearly showed that periodic and aperiodic thermal fluctuations were present in horizontal boats, that they caused growth striae and they could be suppressed by magnetic fields (Cole and Winegard, 1962, Cole and Winegard, 1965, Chedzey and Hurle, 1966; Hurle, 1966, Utech and Flemings, 1966). Later experiments on the vertical Bridgman growth of Ge with $Gr \sim 10^7$ (Kim et al., 1978) showed a transition between periodic and more complex behavior, speculatively called a "turbulent" regime. Recent experiments using flow visualization in actual CZ configuration with silicon (Kakimoto et al., 1988) concluded that natural convective flow in a (relatively small) $75\,mm$ diameter crucible was steady and axisymmetric, but that adding crystal and crucible rotation yielded asymmetric and time-dependent flows with oscillation periods that can be attributed to rotation.

Data from a $39\,cm$ diameter CZ silicon melt with no crystal present, but with varying rotation (Kobayashi et al., 1991) are shown in Figure 4-2a. The temperature-time trace from the experimental log shows a dominant oscillation with exactly the same period as the crucible rotation. The same paper reports the *enhancement* of heat transfer with crucible rotation rate; see Figure 4-2b. Evidently this observation is due to three-dimensional interactions, since increasing rotation rate would *impede* meridional transport through the Coriolis force otherwise. There is a lack of detailed data on flows in CZ to substantiate the hypothesis of three-dimensional interactions enhancing heat transfer, and so experiments with other low Pr fluids in simpler geometries are reviewed next.

Useful information about how such complicated flows may arise in CZ can be inferred from experiments with mercury flows in rectangular channels, e.g. Pratte and Hart, 1990 or with semiconductor melts in cylinders. Fixing the Grashof[2] number from $0 \rightarrow 2.5 \times 10^5$, steady, time-periodic, quasiperiodic and aperiodic regimes were observed in the mercury melts (Pratte and Hart, 1990) as shown Figure 4-3. Most importantly, the initial instabily was *perpendicular* to the principal temperature gradient, in spite of the two-dimensional heating. Restricting the channel width accordingly increased the critical Gr

[2]This Grashof number is defined using the channel depth as the characteristic dimension, although the temperature gradient is in the horisontal direction. Rescaling this group by the channel length, which is more commensurate with the scaling in this thesis, would produce $Gr \sim 10^8$.

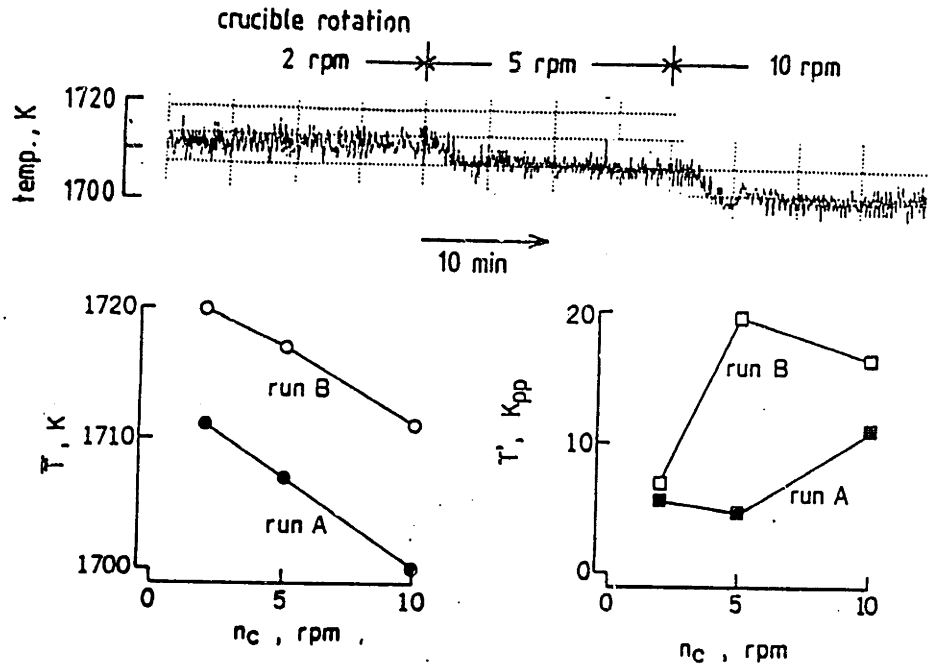

Figure 4-2: (a)Temperature-variation with time in a heated 39 cm crucible containing silicon, (b) the influence of changing the crucible rotation rate on average temperature on the melt surface at the centerline, and (c) the influence of changing the crucible rotation rate on the amplitude of temperature fluctuations on the melt surface at the centerline, taken from Kobayashi et al., 1991

for the onset of time-dependent phenomena.

The analogous experiment, the flow of mercury in a differentially-heated annulus, has been attempted (after Skafel (1972) Pratte and Hart, 1990) and observed three-dimensional azimuthal waves analogous to the transverse waves in the rectangular channel. More extensive measurements have been obtained for the Rayleigh-Bénard experiment with flow in a closed cylinder differentially heated from below. Results for low aspect-ratio melts of gallium (Müller et al., 1984), show that the onset of convection with increasing Rayleigh number is axisymmetric and steady, but bifurcates to a non-axisymmetric flow before becoming oscillatory, and eventually aperiodic. Experiments also have been performed with heating from the side and cooling from both bottom and top (Baumgartl et al., 1990). The result was that flows were exclusively nonaxisymmetric for any Rayleigh number, and also were unsteady at realistic conditions (Baumgartl et al., 1989).

It is expected that the actual CZ flow deviates from two-dimensional and steady-state behavior since the IHTCM simulation computes a very tortuous trajectory while attempting to reach the correct viscosity of silicon. Observations mentioned above witnessed enhancement of convection with increased rotation rate, in clear violation of two-dimensional analysis and experiments with other low Pr fluids in parallelepipeds and cylinders all showed that the onset of time-dependence is three-dimensional. These observations suggest that the unsteady behavior in CZ is also inherently three-dimensional , and that therefore the transport involves the interaction between both natural convection and rotation.

4.1.3 Calculations of three-dimensional and Time-Dependent Flow

Many unsteady-flow simulations have been performed for two-dimensional and axisymmetric flows in CZ. Such simulations do not come to a steady state, but rather oscillate "slowly" (Kim and Langlois, 1990) about an intricate five-to-six-celled structure (see Figure 4-4) for relevant crucible sizes. It is claimed that "the multiple eddy pattern $\cdots$ reflects the attempt of the axisymmetric model to approximate a more general flow" (Kim and Langlois, 1989), but those authors do not provide insight as to the potential effect of three-dimensional -behavior. three-dimensional flow-fields in CZ have been predicted (Mihelčić and Wingerath, 1987); however, those simulations imposed an asymmetric thermal boundary, did not include crucible rotation, had too low a thermal

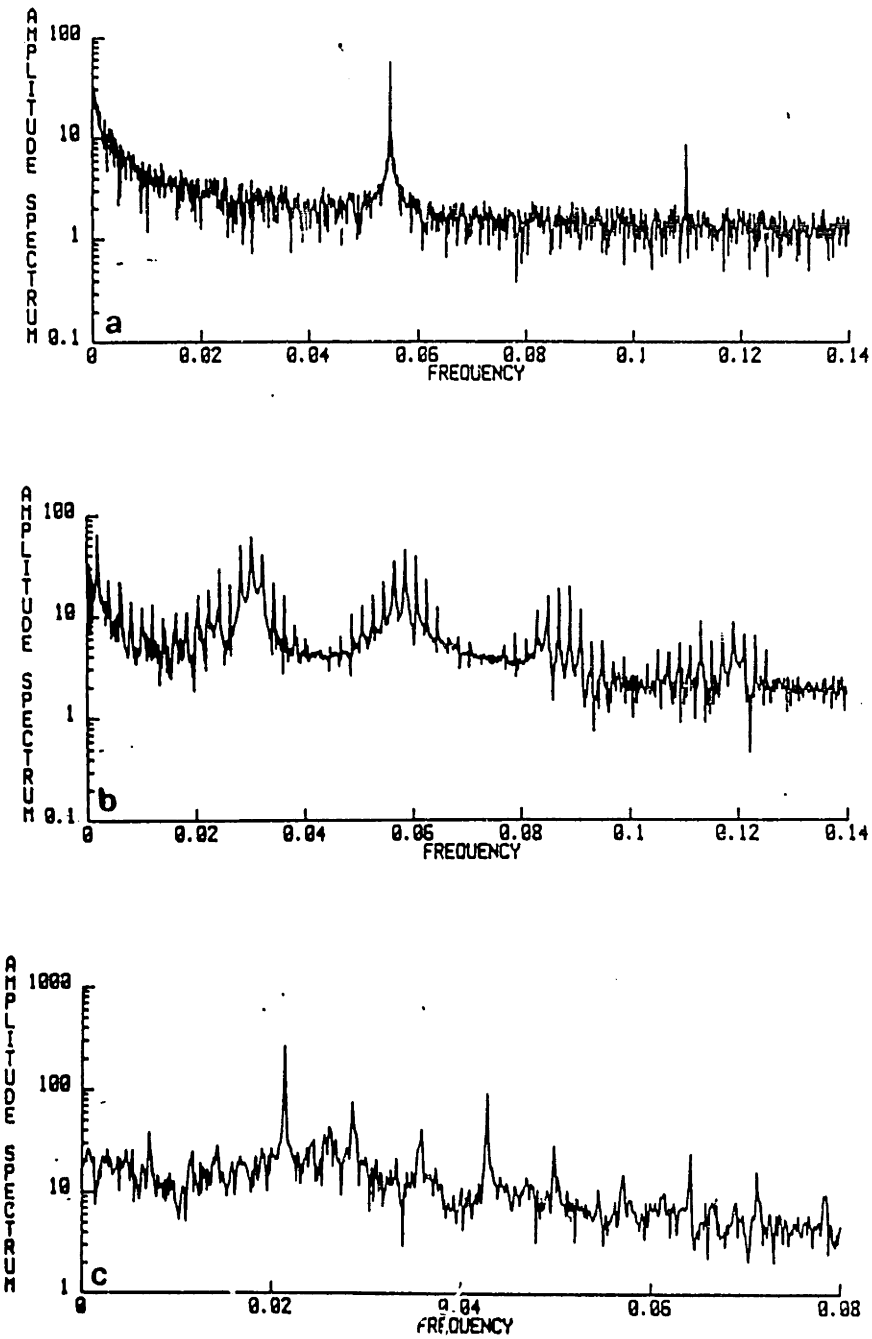

Figure 4-3: Power spectra of the temperature-variation with time from natural convection experiments using mercury. Shown are (a) a monochromatic oscillation, (b) quasi-periodic oscillations, and (c) chaotic oscillations. Taken from Pratte and Hart, 1990.

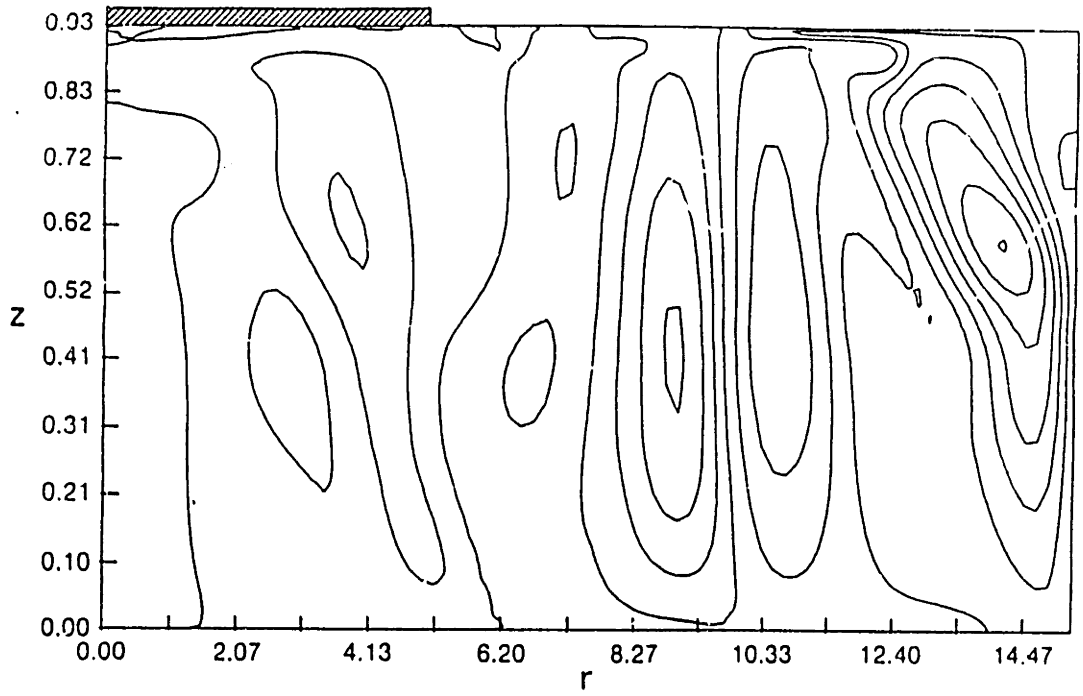

Figure 4-4: Streamlines of two-dimensional and axisymmetric flow about which solution oscillates "slowly", as computed by Kim and Langlois, 1990.

expansion coefficient ($\beta = 10^{-5}K^{-1}$), small crucible diameter ($6.3\,cm$) and thus very weak time-dependence was predicted. Similar fluids have been more completely studied in simpler geometries, such as rectangular channels and cylinders.

Calculations with natural convection as the driving force (Roux, 1990) have been compared to the experiments of mercury flow mentioned in the previous subsection. The calculations confirmed the experimental finding that the onset of time-dependence is strongly correlated with the aspect ratio and hence the degree of three-dimensionality of the flow. The three-dimensional flow in cylinders heated from below has also been calculated (Neumann, 1990). Transition to three-dimensional flow was found to occur in advance of the transition to time-dependent flow, and the three-dimensional flow had a substantially higher ability to transfer heat (see Figure 4-5). Time-dependent flow was shown to occur at lower Gr for the nonaxisymmetric flow. Calculations for a cylinder with heated sidewalls and cooled top and bottom (Baumgartl et al., 1990) show transition from two-dimensional and steady to two-dimensional and unsteady flow with increasing Gr for purely buoyant convection. As $Gr \rightarrow 10^7$ which is realistic for the conditions of crystal growth the flow becomes three-dimensional and steady, and eventually three-dimensional and unsteady.

Therefore, all computations in similar situations support the notion that the flow

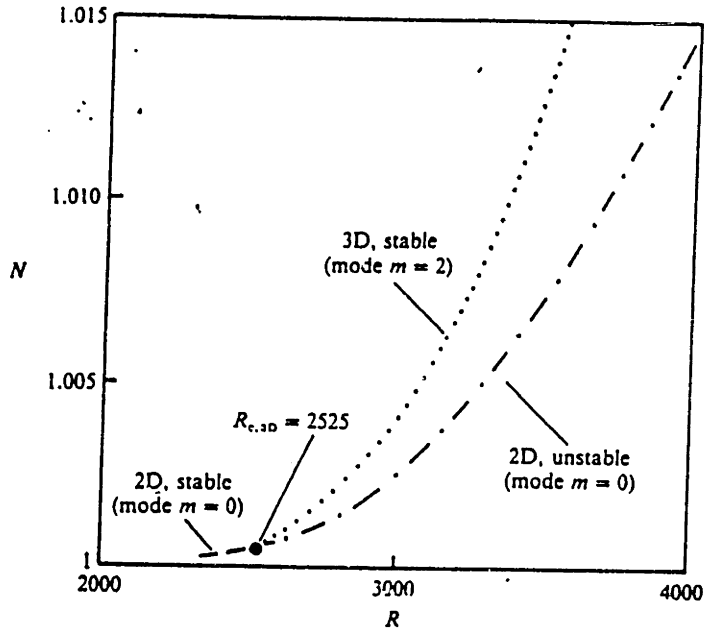

Figure 4-5: Enhancement of heat transfer by transition to steady, three-dimensional flow; from Neumann, 1990.

in CZ is three-dimensional and time-dependent. The three-dimensionality of the flow enhances transport in the melt and coaxes the onset of time-dependence to lower Gr than for a two-dimensional flow. Whether the flow becomes fully turbulent in the SILTEC system cannot been answered; however, the effects of turbulence can be predicted. The limit of fully-developed turbulence provides an upper bound on the average transport rates for complex three-dimensional and unsteady flow and the remainder of this Chapter describes the attempt to calculate this upper bound by solving directly for *averaged* quantities. The development of the IHTCM to predict the average transport rates (Tennekes and Lumley, 1972) in the limit of turbulent flow is described in Sections 4.2, 4.3. and 4.4.

4.2 The $K - \epsilon$ turbulence model

Turbulence stymies practical time-dependent analysis of CZ melt flow. The spatial resolution required throughout the bulk for the turbulent eddies scales with Re^{-1}, and the temporal resolution needed to capture the fluctuations is similarly very small. To calculate the evolution predicted by the three-dimensional , time-dependent Navier-Stokes equations for this situation would devour computer time in order to generate a reliable

average depiction of the physical state of the system. This is a deficient approach since the quantities of interest for the crystal grower are the quantities which vary over a time-scale of minutes and a length scale on the order of the crucible dimensions, which can be practically observed and controlled. A more prudent model for design and control purposes is therefore one that can directly predict the time-averaged quantities of transport.

4.2.1 Time-averaged equations of change

The transport equations are reconsidered in a framework in which energy and momentum vary with time in such a way that the time-derivatives of instantaneous temperature and velocity are nonzero. The melt-solid interface condition is linear and therefore remains unchanged by time-averaging, and the meniscus is coupled weakly to fluctuations in the melt level and it is considered fixed in time. Axisymmetry is assumed, since any gear-shaped modes associated with rotation (Jones, 1983a) are assumed to become swamped by smaller eddies in a turbulent flow. The development of averaged equations is otherwise independent of turbulence and the time-varying equations are stated thus:

$$\rho C_p \frac{\partial T}{\partial t} + \rho C_p \mathbf{v} \cdot \boldsymbol{\nabla} T = \boldsymbol{\nabla} \cdot (k \boldsymbol{\nabla} T) \tag{4.2}$$

$$\rho \frac{\partial \mathbf{v}}{\partial t} + \rho \mathbf{v} \cdot \boldsymbol{\nabla} \mathbf{v} = -\boldsymbol{\nabla} P + \boldsymbol{\nabla} \cdot \left[\mu \left(\boldsymbol{\nabla} \mathbf{v} + \boldsymbol{\nabla} \mathbf{v}^{\dagger} \right) \right] + \rho \beta \mathbf{g} (T - T_{m.p.}) \tag{4.3}$$

$$\boldsymbol{\nabla} \cdot \mathbf{v} = 0. \tag{4.4}$$

The time derivatives $\partial T/\partial t$ and $\partial \mathbf{v}/\partial t$ are not zero for unsteady melt flow. Fluctuations are deemed sufficiently random that ensemble-averages are approximated with time-averages, and ephemeral enough that the melt level can be considered fixed. The wavelengths of the eddies are assumed to be much smaller than the system dimensions, so that the flow comprises a continuum of eddies. All variables in the equations of change are stated in terms of time-varying plus time-averaged quantities, for example:

$$\mathbf{v}(t) = \overline{\mathbf{v}} + \mathbf{v}'(t), \overline{\mathbf{v}(t)} = \overline{\mathbf{v}} + \overline{\mathbf{v}'(t)} \equiv \overline{\mathbf{v}}, \Longrightarrow \overline{\mathbf{v}'(t)} = 0. \tag{4.5}$$

The nonlinear terms make the time-averaged equations different from the steady-state equations, viz.:

$$\mathbf{v}(t)\mathbf{v}(t) = \overline{\mathbf{v}}\,\overline{\mathbf{v}} + \overline{\mathbf{v}}\mathbf{v}'(t) + \mathbf{v}'(t)\overline{\mathbf{v}} + \mathbf{v}'(t)\mathbf{v}'(t),$$

$$\begin{aligned}\overline{\mathbf{v}(t)\mathbf{v}(t)} &= \overline{\mathbf{v}}\,\overline{\mathbf{v}} + \overline{\mathbf{v}}\,\overline{\mathbf{v}'(t)} + \overline{\mathbf{v}'(t)}\,\overline{\mathbf{v}} + \overline{\mathbf{v}'(t)\mathbf{v}'(t)} \\ \Longrightarrow \overline{\mathbf{v}(t)\mathbf{v}(t)} &= \overline{\mathbf{v}}\,\overline{\mathbf{v}} + \overline{\mathbf{v}'(t)\mathbf{v}'(t)}. \qquad (4.6)\end{aligned}$$

Time-averaging the instantaneous equations of change produces the corresponding relations for the time-averaged variables:

$$\rho C_p \frac{\partial \overline{T}}{\partial t} + \rho C_p \overline{\mathbf{v}} \cdot \nabla \overline{T} = \nabla \cdot (-\rho C_p \overline{\mathbf{v}'T'} + k \nabla \overline{T}) \qquad (4.7)$$

$$\rho \frac{\partial \overline{\mathbf{v}}}{\partial t} + \rho \overline{\mathbf{v}} \cdot \nabla \overline{\mathbf{v}} = -\nabla \overline{P} + \nabla \cdot \left[-\rho \overline{\mathbf{v}'\mathbf{v}'} + \mu \left(\nabla \overline{\mathbf{v}} + \nabla \overline{\mathbf{v}}^{\dagger} \right) \right] + \rho g \beta (\overline{T} - T_{m.p.}) \qquad (4.8)$$

$$\nabla \cdot \overline{\mathbf{v}} = 0. \qquad (4.9)$$

The only difference other than substituting time-averaged quantities in place of the variables in Equations (4.2)-(4.4) is the appearance of variables corresponding to the additional transport of heat and momentum, due to the nonlinear convective terms

$$\overline{\mathbf{v} \cdot \nabla T} = \overline{\mathbf{v}} \cdot \nabla \overline{T} + \nabla \cdot \overline{\mathbf{v}'T'} \qquad (4.10)$$

$$\overline{\mathbf{v} \cdot \nabla \mathbf{v}} = \overline{\mathbf{v}} \cdot \nabla \overline{\mathbf{v}} + \nabla \cdot \overline{\mathbf{v}'\mathbf{v}'} \qquad (4.11)$$

where $\rho C_p \overline{\mathbf{v}'T'}$ is the eddy heat flux and $\rho \overline{\mathbf{v}'\mathbf{v}'}$ is the Reynolds stress tensor, so-named because these give heat flux and stress contributions to the time-averaged energy and momentum equations.

4.2.2 The notion of eddy viscosity

The Reynolds stress can be calculated via transport equations or approximated by an expansion in the velocity gradients, where spatial and temporal scales of the eddies relative to the mean flow are the arguments of the expansion. In the case of complete separation of the scales characterizing eddy and average motion, i.e. $\tau_0/T_0 \ll 1$ and $\lambda_0/L_0 \ll 1$, the first term of a Taylor series is an adequate approximation, where τ_0 is taken to be an eddy time-scale, T_0 is a mean-flow time-scale, λ_0 is an eddy length-scale and L_0 is a mean-flow length-scale (Speziale, 1991). These conditions enable convenient formulation, but prevent directional information to pass between length scales so that the turbulent eddies have no structural dependence to the mean flow; the importance of this simplification will be stressed later. Under the conditions of frame-invariance (that rotation of coordinates does not change the form), the Reynolds stresses are approximated

to leading order as (Speziale, 1991)

$$\overline{\mathbf{v}'\mathbf{v}'} \simeq \frac{2}{3}K\delta - \frac{\lambda_0^2}{\tau_0}(\nabla\overline{\mathbf{v}}^\dagger + \nabla\overline{\mathbf{v}}) \quad [+O(\lambda_0)^2...], \tag{4.12}$$

where $K = \frac{1}{2}\overline{\mathbf{v}'\mathbf{v}'}_{ii}$ is the kinetic energy in the fluctuating velocity. The quotient λ_0^2/τ_0 is interpreted as a kinematic viscosity relating the time-averaged velocity gradients to the Reynolds stresses. The *eddy viscosity* is defined as

$$\mu_T \equiv \rho\frac{\lambda_0^2}{\tau_0}, \tag{4.13}$$

and is strictly a property of eddy motion relating the Reynolds stresses to the shear in the mean flow and has no dependence on molecular properties.

Methods for prescribing the eddy heat-flux assume a balance between the convective and the diffusive terms in its transport equation, (Launder, 1978). By an argument similar to the expansion of Reynolds stress in velocity gradients, the eddy heat flux is expressed in terms of the temperature gradient as

$$\rho C_p\overline{\mathbf{v}'T'} = -k_T, \nabla\overline{T} \tag{4.14}$$

where k_T, the scalar eddy conductivity, is related to the eddy viscosity μ_T by an eddy Prandtl number Pr_T

$$Pr_T = \frac{\mu_T}{k_T/C_p} \equiv \frac{\nu_T}{\alpha_T}. \tag{4.15}$$

The eddy heat flux and Reynolds stress tensor are expressed in terms of gradients of the average velocity, average temperature, a scalar eddy viscosity and eddy Prandtl number. The discussion next focusses on the prescription for the eddy viscosity. Henceforth the model becomes a turbulence model, since the eddy viscosity conforms to observations of turbulent flow. *Turbulent viscosity* replaces eddy viscosity. Similarly, the turbulent heat flux replaces eddy heat flux; a value of $Pr_T = 0.9$ for the turbulent Prandtl number, is widely accepted to correlate the turbulent heat flux with the turbulent viscosity (Launder, 1978).

The simplest eddy viscosity relation, Prandtl's mixing length expression arises from an analogy between eddy motion and the random motion of ideal monatomic gas molecules. In one dimension it is expressed as $\mu_T = \rho l_m^2\left|\frac{dv_x}{dy}\right|$, where l_m is a mixing length for the eddies. Since this hypothesis bases eddy transport strictly on local properties of the mean flow, it erroneously excludes leading order turbulent physics, since turbulent energy

cannot be transported. This model can give gross inaccuracies, such as the prediction of zero turbulent transport when $\nabla\overline{\mathbf{v}}$ is zero: in flow over a backward-facing step the observed turbulent transport can be a maximum at the mean flow reattachment point (Launder and Spalding, 1972). This deficiency is rectified by considering the turbulent viscosity to be related to the turbulent kinetic energy K (Speziale, 1991), which requires that an extra transport equation be introduced. This approach still requires the specification of an arbitrary length or time scale ($\mu_T \sim \rho K^{\frac{1}{2}}\lambda_0$, or $\mu_T \sim \rho K\tau_0$), in order to achieve consistent dimensionality. The physical significance of this flaw is an absence of history effects on the turbulent kinetic energy, and so the predictions are not greatly improved. *One-equation* models are not commonly used for this reason (Speziale, 1991).

4.2.3 The $K-\epsilon$ prescription for turbulent viscosity

A self-consistent turbulent viscosity is predicted if the scalar turbulent dissipation rate $\epsilon \equiv \frac{\mu}{\rho}\overline{\nabla\mathbf{v}'^{\dagger}} : \overline{\nabla\mathbf{v}'}$, which appears explicitly as a linear variable in the kinetic energy equation, is also calculated. Thus the turbulent viscosity is defined as

$$\mu_T = \rho C_\mu \frac{K^2}{\epsilon}, \tag{4.16}$$

where C_μ is a dimensionless constant.

The basic set of field equations comprising the $K-\epsilon$ model of turbulence is

$$\rho C_p \overline{\mathbf{v}}\cdot\nabla\overline{T} = \nabla\cdot\left[(k+k_T)\nabla\overline{T}\right] \tag{4.17}$$

$$\rho\overline{\mathbf{v}}\cdot\nabla\overline{\mathbf{v}} = -\nabla\overline{P} + \nabla\cdot\left[(\mu+\mu_T)\left(\nabla\overline{\mathbf{v}}+\nabla\overline{\mathbf{v}}^{\dagger}\right)\right] + \rho g\beta(\overline{T}-T_{m.p.})\mathbf{e}_z \tag{4.18}$$

$$\nabla\cdot\overline{\mathbf{v}} = 0 \tag{4.19}$$

$$\begin{aligned}\rho\overline{\mathbf{v}}\cdot\nabla K = {} & \mu_T\left[\left(\nabla\overline{\mathbf{v}}+\nabla\overline{\mathbf{v}}^{\dagger}\right):\nabla\overline{\mathbf{v}}\right] + g\beta\mathbf{e}_z\cdot\frac{k_T}{C_p}\nabla\overline{T} \\ & -\rho\epsilon \\ & +\nabla\cdot\left[\left(\mu+\frac{\mu_T}{Pr_K}\right)\nabla K\right]\end{aligned} \tag{4.20}$$

$$\begin{aligned}\rho\overline{\mathbf{v}}\cdot\nabla\epsilon = {} & C_{\epsilon 1}\frac{\epsilon}{K}\mu_T\left[\left(\nabla\overline{\mathbf{v}}+\nabla\overline{\mathbf{v}}^{\dagger}\right):\nabla\overline{\mathbf{v}}\right] + C_{\epsilon 1}\frac{\epsilon}{K}g\beta\mathbf{e}_z\cdot\frac{k_T}{C_p}\nabla\overline{T} \\ & -C_{\epsilon 2}\rho\frac{\epsilon^2}{K} \\ & +\nabla\cdot\left[\left(\mu+\frac{\mu_T}{Pr_\epsilon}\right)\nabla\epsilon\right]\end{aligned} \tag{4.21}$$

$$\mu_T = C_\mu \rho \frac{K^2}{\epsilon} \qquad k_T = \frac{\mu_T C_p}{Pr_T}. \tag{4.22}$$

This approach yields five dimensionless constants $C_\mu, Pr_K, Pr_\epsilon, C_{\epsilon 1}$, and $C_{\epsilon 2}$. These are fitted to data in order that the $K-\epsilon$ model accurately describe practical flow situations.

4.2.4 Application of the $K-\epsilon$ turbulence model

The $K-\epsilon$ model or any linear eddy-viscosity model of turbulence simplifies the expansion of Reynolds stress by assuming independence of the directional properties of turbulent eddies from the mean flow. One obvious example of this is that the components τ_{ii} of the Reynolds stress normal to a streamline are equal according to the $K-\epsilon$ model. Accordingly it cannot predict any cross-sectional mean flow components in unidirectional flow, in contradiction to observations (Speziale, 1991); see Figure 4-6a. In general, characterizing the turbulent energy cascade uniquely by a single dissipation rate ϵ, as is done in the $K-\epsilon$ model, is a statement of *universal equilibrium* (Batchelor, 1953). Turbulent flows in universal equilibrium are assumed to transfer energy into the cascade from the largest wavelengths at the rate governed by the viscous dissipation of the smallest wavelengths. The rate of this energy transfer is determined by a single parameter, the viscous dissipation rate, and the statistical structure of intermediate eddies is then independent of the structure of the larger wavelengths. *Isotropic turbulence* is a state of flow wherein correlations of velocity and its derivatives at different points are constant under rotation or reflection of coordinate axes. These symmetries automatically fulfill the universal-equilibrium condition and thus isotropic turbulence can be predicted accurately by the $K-\epsilon$ model. Isotropic turbulence is approached in flows at high Reynolds-number (Bradshaw, 1978), and hence high-Reynolds-number and isotropic turbulent flows are used to determine the constants in the $K-\epsilon$ equations. The constant $C_{\epsilon 2}$ is fitted to data on isotropic ***homogeneous*** turbulence, which leaves only the term $C_{\epsilon 2}\epsilon^2/K$ in the ϵ-equation. The remaining constants satisfy the relation

$$C_{\epsilon 1} = C_{\epsilon 2} - \frac{\kappa^2}{Pr_\epsilon C_\mu}, \tag{4.23}$$

to which the ϵ equation reduces in a locally isotropic flow with logarithmic velocity profile, such as that observed in the fully-turbulent regime near walls. The values of the constants $(C_{\epsilon 1}, Pr_\epsilon, C_\mu, Pr_K)$ are determined by matching experimental data for turbulent shear flows and confined flows (Patel et al., 1985); in these regressions special *wall-functions* are added which fix the solution field near walls which cannot be predicted with the $K-\epsilon$

model. Their accepted values are (Speziale, 1991):

$$C_\mu = 0.09\ , Pr_K = 1.0\ , Pr_\epsilon = 1.3\ , C_{\epsilon 1} = 1.44\ , C_{\epsilon 2} = 1.92. \tag{4.24}$$

Therefore, the $K - \epsilon$ model equations are valid in regions where the turbulence is nearly isotropic and require additional functions to bridge the behavior near walls. For high-Reynolds-number flows the $K - \epsilon$ equations are typically integrated only in the bulk where the turbulence approaches isotropy; these solutions are matched to the boundaries by the use of algebraic expressions known as wall-functions which enforce the observed decay of the turbulence quantities near stationary plates. CZ flow is both confined by walls and swirling.

The presence of walls will have to be accommodated in this work; wall-functions do not correctly account for turbulent boundary layers at low and transitional Reynolds-numbers, separated flows, and the flow over rotating surfaces or surfaces with heat transfer, all of which are present in CZ (Patel et al., 1985). However, *low-Reynolds-number* $K - \epsilon$ prescriptions have been developed to realize more general behavior and will be used in this research. The anisotropic influences of streamline curvature and swirl may still render the $K - \epsilon$ model deficient for modelling CZ. Some accuracy improvement has been achieved by augmenting the $K - \epsilon$ model with algebraic stress prescriptions (Benim, 1990) and nonlinear terms in the Reynolds stress expansion (Speziale, 1987); see Figure 4-6b. These added complications offer no overwhelming advantage at this point in the present development since the standard $K - \epsilon$ form still qualitatively predicts the correct two-dimensional mean flows.

4.2.5 Boundary conditions and near-wall behavior

The boundary conditions for the equations for K and ϵ near a solid wall pose little difficulty when ϵ is taken to be the *isotropic* dissipation rate, which is consistent with the underlying assumptions and empirical constants of the $K - \epsilon$ model of turbulence. Given no-slip boundary conditions on solid surfaces,

$$K = 0 \tag{4.25}$$

is a straightforward boundary condition for the turbulent kinetic energy. However, on the free surface, a condition expressing the lack of turbulent energy flux across the boundary

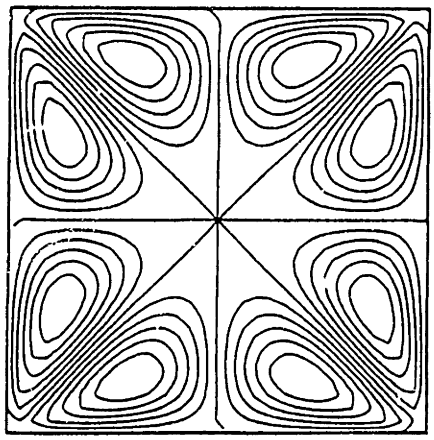

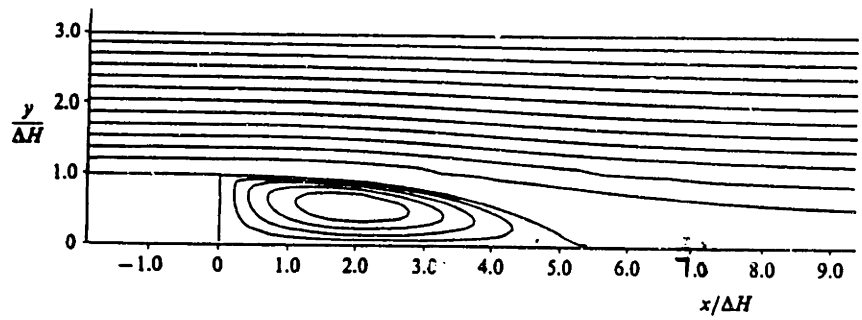

(b)

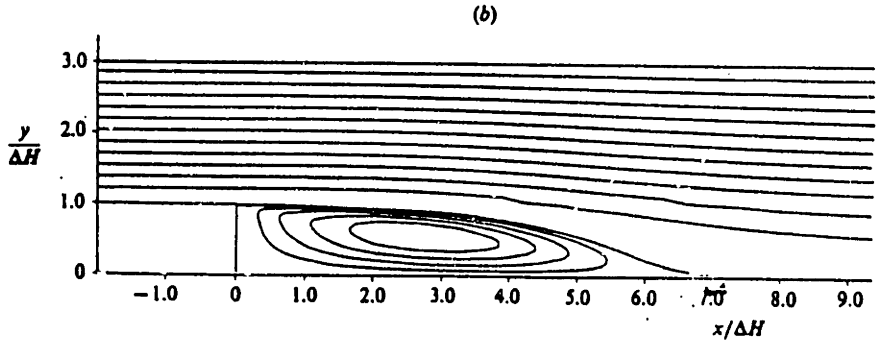

Figure 4-6: Predictions using a nonlinear $K-\epsilon$ model from Speziale, 1987: (a) secondary turbulent flows in duct with noncircular cross section, and (b) improved prediction of reattachment point over linear $K-\epsilon$ model.

is appropriate:

$$\mathbf{n} \cdot \nabla K = 0 \tag{4.26}$$

The appropriate boundary condition on a solid wall for the *isotropic* ϵ variable is

$$\epsilon = 0 \tag{4.27}$$

since there exists no isotropic turbulence there (Jones and Launder, 1972); at a solid boundary the *total* dissipation rate is *not* zero because the wall enforces a strong directional preference on the turbulent eddies, and this must be accounted for. The separate contributions to the total dissipation rate are seen when total dissipation is defined in terms of two-point velocity correlation tensor as:

$$R_{ij} \equiv \sum_{i=1}^{3}\sum_{j=1}^{3} \frac{\mu}{\rho}\left[\frac{\partial^2 R_{ii}}{\partial \xi_j \partial x_j} - \frac{\partial^2 R_{ii}}{\partial \xi_j \partial x_j}\right]_{\xi_j=0}; \tag{4.28}$$

the first term is the dissipation of the isotropic portion of R_{ij} and is identically zero at a solid wall. For the free surface the condition

$$\mathbf{n} \cdot \nabla \epsilon = 0 \tag{4.29}$$

is appropriate and is commonly used for free-surface flows (Kobayashi et al., 1991). These four conditions comprise a consistent set of boundary conditions for the $K - \epsilon$ model.

The *near-wall* total dissipation is not isotropic, as mentioned above. The total dissipation near the wall is underestimated by the isotropic value calculated in the ϵ equation; it is given by $\frac{\mu}{\rho}\overline{\nabla \mathbf{v}'^{\dagger} : \nabla \mathbf{v}'}$, where ∇ can also be taken as simply the normal derivative at the wall, $\nabla_n = (\mathbf{n} \cdot \nabla)\,\mathbf{n}$, since tangential derivatives are zero at the wall. An expansion of the turbulent velocity normal to the solid boundary provides the variation of total dissipation there. Near a solid boundary located at $y = 0$ in Cartesian coordinates the velocities can be expressed as a series using the normal distance y as the argument of the expansion

$$\begin{aligned} v_t &= b_t y + c_t y^2 + \ldots \\ v_n &= \qquad c_n y^2 + \ldots \quad . \end{aligned}$$

Using these expansions and the definition of total dissipation, its variation at the wall is

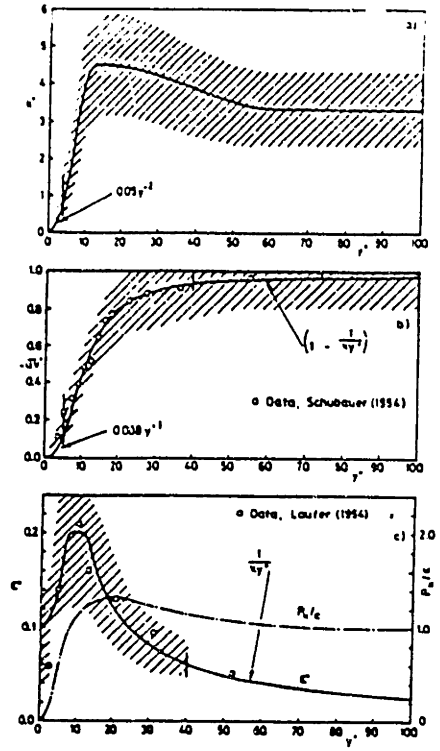

Figure 4-7: Variation of turbulence quantities near a solid wall, from Patel et al., 1985: (a) kinetic energy, (b) Reynolds stress, and (c) total dissipation rate

given to leading order by

$$\epsilon_{total} = 2\frac{\mu}{\rho}\left(\nabla K^{\frac{1}{2}}\right)^{\dagger} \cdot \left(\nabla K^{\frac{1}{2}}\right). \tag{4.30}$$

Profiles are shown in Figure 4-7 for kinetic energy, Reynolds stress, dissipation rate and ratio of kinetic energy production to dissipation rate near a solid boundary. Peaks in both the total dissipation rate and kinetic energy occur near the wall and a finite value of the total dissipation rate persists at the wall. Observations of near wall flows are characterized by three distinct regions: the viscous sublayer where molecular viscosity and wall effects dominate, the fully-turbulent region, where turbulence is largely isotropic and the buffer layer between these two extremes where the behavior is mixed. The dimensionless variable y^+ is used to measure the distance from the wall, where $y^+ = yv_*\rho/\mu$ provides a natural scaling for the influence of turbulent effects, $v_* \equiv \sqrt{\tau_{yx}/\rho}$ is the friction velocity and τ_{yx} is the shear stress at the wall. In the viscous sublayer for $y^+ < 6$ the tangential velocity profile determined by viscous friction as

$$v_x = \frac{y\tau_{yx}}{\mu} = y\frac{v_*^2\rho}{\mu}. \tag{4.31}$$

The linear behavior matches a logarithmic profile at y_0 as

$$v_x = (v_*/\kappa)(\log yv_*\rho/0.13\mu), \tag{4.32}$$

where κ is the von Kármán constant, which is obtained from measurements. The constant 0.13 is also obtained from measurements (Landau and Lifschitz, 1987). The *buffer layer* ranges from $6 < y^+ < 30$ and the logarithmic law is valid from $30 < y^+ < 160$; fully-turbulent flow is considered to occur for $y^+ > 60$ (Patel et al., 1985).

Total dissipation can be accommodated by the $K-\epsilon$ model (Jones and Launder, 1972) by modifying all scaling terms containing the dissipation variable, and including functions for the total dissipation rates in the K and ϵ equations. The constants $(C_\mu, C_{\epsilon 1}, C_{\epsilon 2})$ are made functions of the turbulent viscosity to adjust the scaling terms and extra terms D and E are included to explicitly represent total dissipation in the K and ϵ equations (Jones and Launder, 1972). The extra dependences only affect the equations at low turbulent viscosity, thereby matching the original $K-\epsilon$ equations in the bulk (Patel et al., 1985).

4.3 Experience with the $K-\epsilon$ model

For flows of industrial interest the $K-\epsilon$ model has been applied exclusively using *ad hoc* measures to guarantee convergence (Smith, 1984). Artificial diffusion is employed widely. This smooths variations in field variables, making the computation feasible on a coarser mesh, but changes the physics of the model; see Brooks and Hughes, 1982 for further discussion. Artificial diffusion is usually implemented by smoothing the generation terms in the K and ϵ equations (Brittain, 1986; Smith, 1984) and is an unsatisfactory improvisation for solving the highly nonlinear $K-\epsilon$ equations. It effectively changes the length and time scales which constitute the turbulent viscosity and therefore it obscures the physical meaning of the solution. The discussion in this Section first focusses on literature accounts of prior experience with the wall-function implementation of the $K-\epsilon$ equations, which is more commonly used. The potential benefits of the low-Reynolds-number form are then discussed, and experiences of dealing with the additional terms are reviewed.

4.3.1 Convergence difficulties with the $K-\epsilon$ equations

The $K-\epsilon$ model with wall-function boundary conditions

Two wall function boundary conditions are applied on each solid boundary, one corresponding to the tangential velocity in the meridional plane and one for the azimuthal velocity. The wall function boundary condition is accommodated in the finite element framework as a natural boundary condition on stress similar to the thermocapillary condition in Chapter 2. The wall-function boundary relates the unknown shear stress to the local velocity components. It is important to note that the wall shear stress may fall to zero and then scalings based on the wall shear stress are invalid. An alternative scaling is used, based on adopting the Neumann boundary condition on K. In locally isotropic flows this scaling results in a scaling identical to the $\sqrt{\tau_{xy}}$ used to develop Equation (4.32). The new scaling for the friction velocity v_* is given as

$$v_* = C_\mu^{1/4} K_h^{1/2}, \tag{4.33}$$

where K_h is the kinetic energy at a small distance h from the solid boundary. The wall-functions are applied not at solid boundaries, but are displaced a small distance h from them. Linear velocity profiles are imposed between the actual boundary and the artificial boundary for the wall-functions, located at a distance h from the solid walls. The Neumann boundary condition on K is applied

$$\mathbf{n} \cdot \nabla K = 0, \tag{4.34}$$

and the boundary condition on ϵ is

$$\epsilon_h = C_\mu^{3/4} K_h^{3/2} / \kappa h, \tag{4.35}$$

which then yields the following form for the universal wall law

$$\frac{v_x^+ v_*}{\tau_w} = \frac{1}{\kappa} \log(h v_* \rho / 0.13\mu), \tag{4.36}$$

where τ_w is the tangential shear stress at the wall. This enables the expression of τ_w in terms of the solution, which is employed as the expression of a natural boundary

condition for tangential stress:

$$\tau_w = v_x^+ v_* \frac{\kappa}{\log(hv_*\rho/0.13\mu)}. \tag{4.37}$$

For low values of $y^+ < 11.6$, then the viscous asymptote can be used:

$$\tau_w = \frac{v_x^+ v_*}{Reh}. \tag{4.38}$$

Depending on the calculated value of y^+, then, which depends on K, the expression for τ_w can be used to supply a natural condition for one meridional component and the azimuthal component of the momentum equation. The other meridional component is then given by the kinematic boundary condition for preventing penetration of the solid surface.

The motivation for employing wall-functions is to completely avoid calculating the transport in near-wall regions where the kinetic energy changes from its fully-turbulent value to zero and the turbulence-quantities are influenced by the molecular viscosity and the presence of walls. In very high-Reynolds-number flows the behavior near the walls is of little consequence, and the molecular viscosity is usually neglected in Equations (4.17)–(4.22) because the turbulent viscosity dominates up to the artificial boundary where the wall-functions are applied (Smith, 1984).

4.3.2 Experiences with the wall-function $K - \epsilon$ formulation

The $K - \epsilon$ equations are highly nonlinear and their form does not explicitly guarantee uniqueness or ellipticity. Ellipticity of the solution set is essential for robust solution methods and is lost when the dissipation variable becomes negative, since the turbulent viscosity is given by $\mu_T = C_\mu \frac{K^2}{\epsilon}$. Convergence difficulties due to the appearance of negative values of ϵ are common (Smith, 1984). Underrelaxed or quasi-Newton iteration schemes in combination with artificial diffusion reportedly prevent divergence of the iterative procedure encountered when using the Newton-Raphson method (Hutton, et al., 1987). Even for a fairly simple geometry such as the backward-facing step, it was found that the turbulent generation terms had to be smoothed, a quasi-Newton iteration method had to be used, and a previous solution from an upwind-finite-difference model had to be used (Smith, 1984).

It is well-known that an elliptic solution field with steep gradients can be better-approximated by increasing the discretization of the domain, and that the motivation for

artificial diffusion is to avoid the cost for the increased discretization by penalizing the accuracy of the numerical solution (Finlayson, 1980). The difficulties encountered with the wall-function formulation of the $K-\epsilon$ equations seem to originate in an unwillingness to provide adequate discretization of the computational domain and in the inability to produce a fully-converged initial guess, from which small increments in parameter-space can be taken. Certainly laminar flow does not provide a good initial guess, because the wall function formulation becomes singular as the turbulence-quantities approach zero. Analytical solutions are only applicable for the simplest flow situations.

4.3.3 Experiences with the low-Reynolds-number $K-\epsilon$ formulation

The ability to bridge low-Reynolds-number behavior is precisely the strength of the low-Reynolds-number $K-\epsilon$ model which makes it attractive for this work. It will be shown in Section 4.4 that the laminar solution at viscosities close to that of silicon does not provide an adequate initial guess for the $K-\epsilon$ model. However, since the low-Reynolds-number $K-\epsilon$ model can simulate low-Reynolds-number behavior, an initial guess can be generated by using a very high artificial viscosity which satisfies the model equations. Then continuation in viscosity can be used to approach the realistic conditions. The intimidating cost of the increased discretization required to resolve the areas of rapid change near the walls which are completely avoided by using wall-functions probably accounts for the lack of effort in this area. In addition, the extra terms featured in the low-Reynolds-number $K-\epsilon$ formulation require special attention since they involve limits that approach division by zero and are therefore difficult to compute.

Few of the authors simulating complex geometries (such as a backward-facing step) report using low-Reynolds-number forms of the equations to obtain results, and none have reported exploiting the laminar limit as a means to guarantee that the solution procedure stays within the radius of convergence. One study that employed both low-Reynolds-number and wall-function forms (Polansky et al., 1984) suggested that the low-Reynolds-number form converges where the wall-function formulation fails, although it required much greater discretization near the walls and artificial diffusion was still applied liberally. Since the $K-\epsilon$ model has not been implemented in a finite-element/Newton solver without considerable *ad hoc* adjustments, an original scheme has been devised to guarantee convergence of the $K-\epsilon$ equations in the IHTCM without changing the prediction. This effort also represents a unique application of the low-Reynolds-number form to

a materials processing problem; it has been used mainly for pipe flows (Brittain, 1986), low Prandtl-number pipe flows (Cotton and Jackson, 1990; Jackson et al., 1989) and the backward-facing step (Polansky et al., 1984).

4.4 Implementation of the $K-\epsilon$ /IHTCM

4.4.1 Choice of low-Reynolds-number form

A low-Reynolds-number form of the $K-\epsilon$ equations is employed, where the functional dependence of the constants on turbulent Reynolds number, and total dissipation terms are explicitly included in the equation formulation, with consistent boundary conditions on K and ϵ . A review of such methods is given by Patel et al., 1985 and concluded that the approach used by Launder and Sharma (LS) yielded better results than many other models for near-wall flows, and most of the additional terms are taken from that work. Besides the explicit prediction of near-wall flow, low-Reynolds-number forms are algorithmically more straightforward to implement than wall-functions and potentially can predict more general flows.

The LS formulation includes an extra dissipation term D in Equation (4.42) in order to account for total dissipation near the wall. The choice for the term $D \equiv 2\frac{\mu}{\rho}\left(\nabla K^{\frac{1}{2}}\right)^{\dagger}\cdot\left(\nabla K^{\frac{1}{2}}\right) = \frac{\mu}{2\rho K}(\nabla K)^2$ yields the correct wall value for total dissipation and the correct linear variation for it at the wall. D becomes negligible in the fully turbulent regime for flow over a flat plate as required (Patel et al., 1985). It is expressed in linear powers of K for convenience in the numerical formulations.

An extra term E similarly increases dissipation in Equation (4.43) near the wall. Its form is similar to the extra term in the Equation (4.42) (Patel et al., 1985), $E \equiv 2\frac{\mu}{\rho}\left(\nabla\epsilon^{\frac{1}{2}}\right)^2 = \frac{\mu}{2\rho\epsilon}(\nabla\epsilon)^2$. The sensitivity of the model to different forms of this term is reflected in the near-wall peak in the kinetic energy profile and the form used here predicts the near-wall variation in K very well; see Figure 4-8.

The $K-\epsilon$ equations were added to the original finite-element code described in Chapter 2. To avoid the complexity of providing analytical derivatives for all the terms in the turbulence equations, a numerical approximation to the Jacobian matrix was implemented. The form of the K and ϵ equations in the IHTCM is given as

$$\rho C_p \overline{\mathbf{v}}\cdot\nabla\overline{T} = \nabla\cdot\left[(k+k_T)\nabla\overline{T}\right] \tag{4.39}$$

$$\rho\overline{\mathbf{v}}\cdot\nabla\overline{\mathbf{v}} = -\nabla\overline{P}+\nabla\cdot\left[(\mu+\mu_T)\left(\nabla\overline{\mathbf{v}}+\nabla\overline{\mathbf{v}}^{\dagger}\right)\right]+\rho g\beta(\overline{T}-T_{m.p.})\mathbf{e}_z \tag{4.40}$$

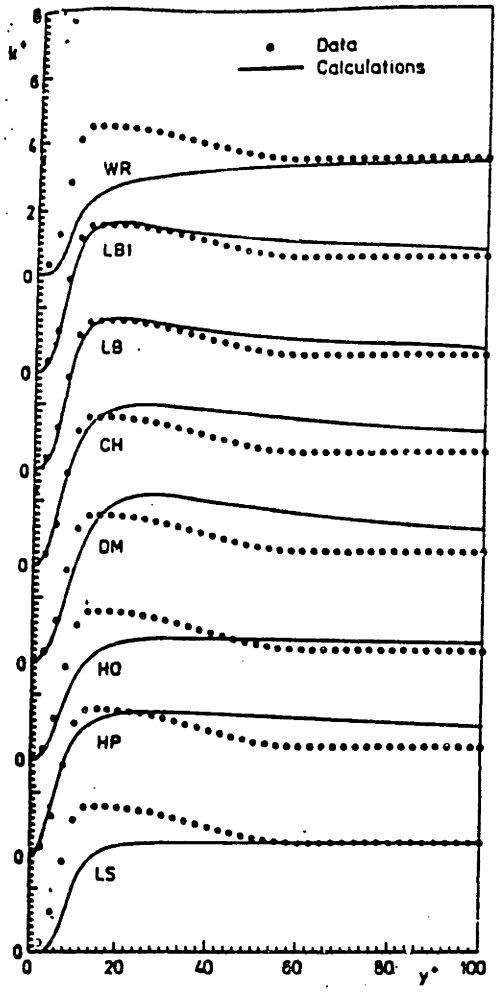

Figure 4-8: Variation of turbulence kinetic energy near a solid wall, from Patel et al., 1985. Comparison of measured profile (——) with predictions (• • •). Effect of E term is seen in the peak of K at $y^+ \sim 12$. The form used in the $K - \epsilon$ /IHTCM is denoted by HP, while the form used by Launder and Sharma is denoted by LS.

$$\nabla \cdot \overline{\mathbf{v}} = 0 \tag{4.41}$$

$$\begin{aligned}\rho\overline{\mathbf{v}} \cdot \nabla K = {} & \mu_T \left[\left(\nabla\overline{\mathbf{v}} + \nabla\overline{\mathbf{v}}^\dagger \right) : \nabla\overline{\mathbf{v}} \right] + g\beta \mathbf{e}_z \cdot \frac{k_T}{C_p} \nabla \overline{T} \\ & - \rho\epsilon - \frac{\mu}{2\rho K} (\nabla K)^2 \\ & - \nabla \cdot \left[\left(\mu + \frac{\mu_T}{Pr_K} \right) \nabla K \right]\end{aligned} \tag{4.42}$$

$$\begin{aligned}\rho\overline{\mathbf{v}} \cdot \nabla \epsilon = {} & C_{\epsilon 1} \frac{\epsilon}{K} \mu_T \left[\left(\nabla\overline{\mathbf{v}} + \nabla\overline{\mathbf{v}}^\dagger \right) : \nabla\overline{\mathbf{v}} \right] + C_{\epsilon 1} \frac{\epsilon}{K} g\beta \mathbf{e}_z \cdot \frac{k_T}{C_p} \nabla \overline{T} \\ & - C_{\epsilon 2} \rho \frac{\epsilon^2}{K} - \frac{\mu}{2\rho\epsilon} (\nabla \epsilon)^2 \\ & + \nabla \cdot \left[\left(\mu + \frac{\mu_T}{Pr_\epsilon} \right) \nabla \epsilon \right]\end{aligned} \tag{4.43}$$

$$\mu_T = C_\mu \rho \frac{K^2}{\epsilon} \qquad k_T = \frac{\mu_T C_p}{Pr_T}$$

$$Re_T = \frac{K^2}{\nu\epsilon} \qquad C_\mu = 0.09 \exp\left[\frac{-3.4}{\left(1 + \frac{Re_T}{50}\right)^2} \right]$$

$$C_{\epsilon 1} = 1.44 \qquad C_{\epsilon 2} = 1.92 \left(1.0 - 0.3 \exp\left[-Re_T^2 \right] \right),$$

where the turbulence-Reynolds-number, Re_T, is a dimensionless turbulent viscosity used to gauge the degree of fully-developed turbulence.

4.4.2 New approaches to computing the $K - \epsilon$ equations

The Galerkin Finite-Element Method employed by the present IHTCM solver is ideal for elliptic equations. However, the form of the $K - \epsilon$ equations does not exclude negative values of the diffusive coefficients, which destroy the ellipticity. Also, the appearance of both K and ϵ in denominators means that limits involving division by near-zero quantities occur, and are difficult to compute. Negative values of K and ϵ are aphysical, and so a method is devised to avoid them in order to retain ellipticity is justifiable. Several methods described in this Section were attempted in a trial-and-error fashion, without resorting to global upwinding that affects the prediction. By maintaining a model free of artificial diffusion, the solutions presented here should be more accurate representations of the $K - \epsilon$ description of turbulence than those discussed in the literature for flows more complex than simple straight circular pipe flows.

The problem of a denominator becoming zero or negative may be prevented by the addition of a 'regularization parameter' (Beris et al., 1985) to the denominators in ques-

tion. Regularization changes the result of the computation, but gradual reduction of the parameter can recover the proper solution. For example the D term in the kinetic energy equation can be rewritten using π_r as the regularization parameter in order to avoid division by near-zero quantities:

$$\lim_{\pi_r \to 0} \frac{\mu}{2\rho(\pi_r + K)} (\nabla K)^2 \to D. \tag{4.44}$$

Regularization of the turbulent viscosity is needed only to initialize the calculations reported here when K and ϵ are very small; it is to the D and E terms that this regularization is most important, since they become contumeliously large near solid boundaries. When all denominators are regularized in this way with any nonzero parameter, the trivial solution $K = \epsilon = 0$ everywhere in the melt domain is computed for the laminar solution of the other variables. This strongly suggests that multiple solutions exist for the low-Reynolds-number $K - \epsilon$ model, and that laminar flow is a computable limit which can be approached with regularization.

Uniqueness of a single transport equation can only be guaranteed if its source terms are monotonically decreasing functions of the equation variable, which is violated in the $K - \epsilon$ model, because the K and ϵ production terms involve $+K^2$ as a premultiplier. The systematic identification of all solution branches of the $K - \epsilon$ model even for a simple flow, using the tools of bifurcation analysis, has yet to be performed to the knowledge of this author.

Ellipticity can be guaranteed by introducing a parameter π_g which appears in the numerator of the generation term in the kinetic energy equation, Equation (4.42):

$$\lim_{\pi_r \to 0} \rho C_\mu \frac{(\pi_g + K)^2}{\epsilon} \to \mu_T. \tag{4.45}$$

Given an initial guess of all $K > 0$ and $\epsilon > 0$, this term generates positive values of K and ϵ even at low Reynolds-numbers, and thereby avoids the need to regularize the turbulent viscosity. For small values of K and ϵ, this production will be exactly balanced by molecular diffusion. For a solution to the $K - \epsilon$ formulation at low Reynolds-number, continuation methods can be used to increase the driving forces for flow and attain a turbulent state.

4.4.3 Initializing the continuation procedure

The term $\left[\left(\nabla\bar{v}+\nabla\bar{v}^{\dagger}\right):\nabla\bar{v}\right]$ is the driving force for turbulence-quantities in the $K-\epsilon$ model and it is a measure of the shear and extension in the mean flow; the magnitude of this term for the laminar solutions involving crucible rotation (Figure 2-17), buoyancy (Figure 2-31) and all flow mechanisms combined (Figure 3-13) is plotted in Figure 4-9. In the finite-element representation, the velocity field continuous, but its gradient are not, and so the generation term is not continuous across elements so contours cannot be drawn between them; however, it is seen that the driving force for turbulence-quantities is strong for crucible rotation only in the thin shear layers adjacent to the crystal and crucible and so turbulent generation is not expected to have a major effect for crucible rotation. The driving force for turbulence from buoyancy is stronger throughout the melt; turbulent generation is expected to occur to a higher degree, with the maximum generation being near the crucible bottom toward the centerline. For the combined flow the driving force is strongest, having substantial presence throughout the melt and adding the $K-\epsilon$ model is expected to have the largest differential effect on its profile. Solving the augmented equation set starting from these laminar solutions was attempted; the sizeable driving forces for turbulence in the model resulted in rapid divergence, even when negative updates to K and ϵ were discarded in order to preserve ellipticity.

A solution of the $K-\epsilon$ /IHTCM model was sought at high viscosity so that a converged laminar result could be used as an initial guess and subsequently continuation could be used to approach the correct viscosity. Both regularization and generation parameters π_r and π_g were added to the turbulent viscosity with values of $10^{-7}\,cm^2\cdot s^{-3}$ and $5\times10^{-4}\,cm^2\cdot s^{-2}$, respectively. A converged result was obtained by first fixing the turbulent viscosity at $C_\mu\frac{\pi_g^2}{\pi_r}$ and calculating K and ϵ with only generation present; using this as an initial guess the dissipation terms were added; the nonlinear low-Reynolds-number terms were added next; the turbulent viscosity next was made a function of K and ϵ; and finally the regularization parameters were dropped from all denominators. A solution for the case of crucible rotation as the lone driving force is shown in Figure 4-10 and features π_g as the only additional term. The artificial generation of K and ϵ is shown to be balanced entirely by viscous transport; the molecular viscosity is extremely high, $\mu=10^6 cP$. Decreasing the value of π_g toward zero accordingly lowers the values of K and ϵ . Thus, the laminar flow state at low Reynolds-numbers can be computed in the limit of $\pi_g\rightarrow 0$ as long as there is a small amount of artificial turbulent generation present. The trivial solution is computable when all the denominators are regularized and $\pi_g=0$, but that limit does not initialize the continuation scheme, since it simply

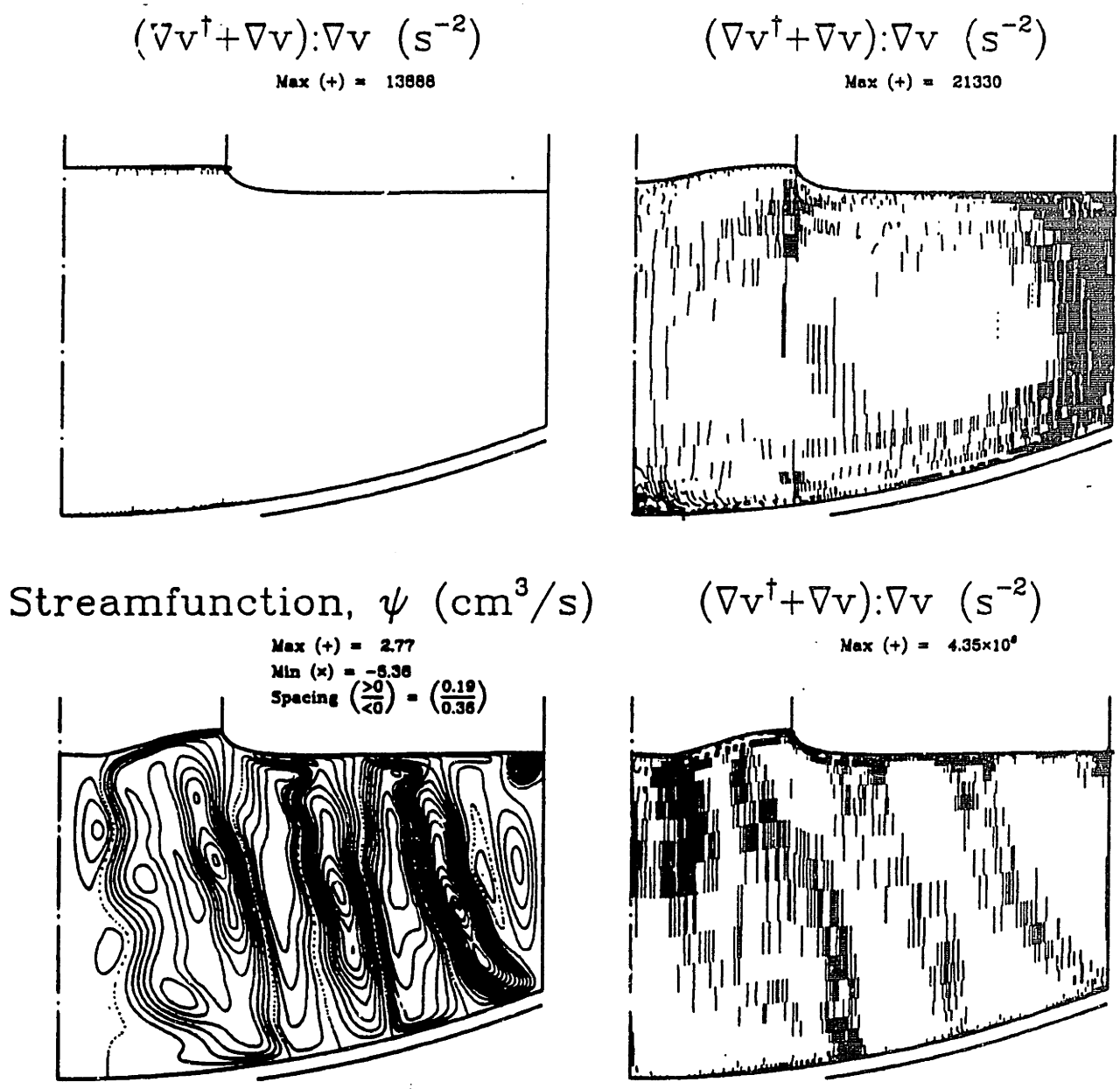

Figure 4-9: Plots of the driving force for turbulence, computed from laminar solutions for (a) crucible rotation, and (b) buoyancy flow; (c) the streamfunction for combined flow mechanisms, and (d) the turbulent driving force for combined flow mechanisms. The quantity $\left[\left(\nabla\overline{\mathbf{v}}+\nabla\overline{\mathbf{v}}^{\dagger}\right):\nabla\overline{\mathbf{v}}\right]$, plotted in figures (a),(b) and (d) is not continuous across elements and so the density of the contours reflects its magnitude.

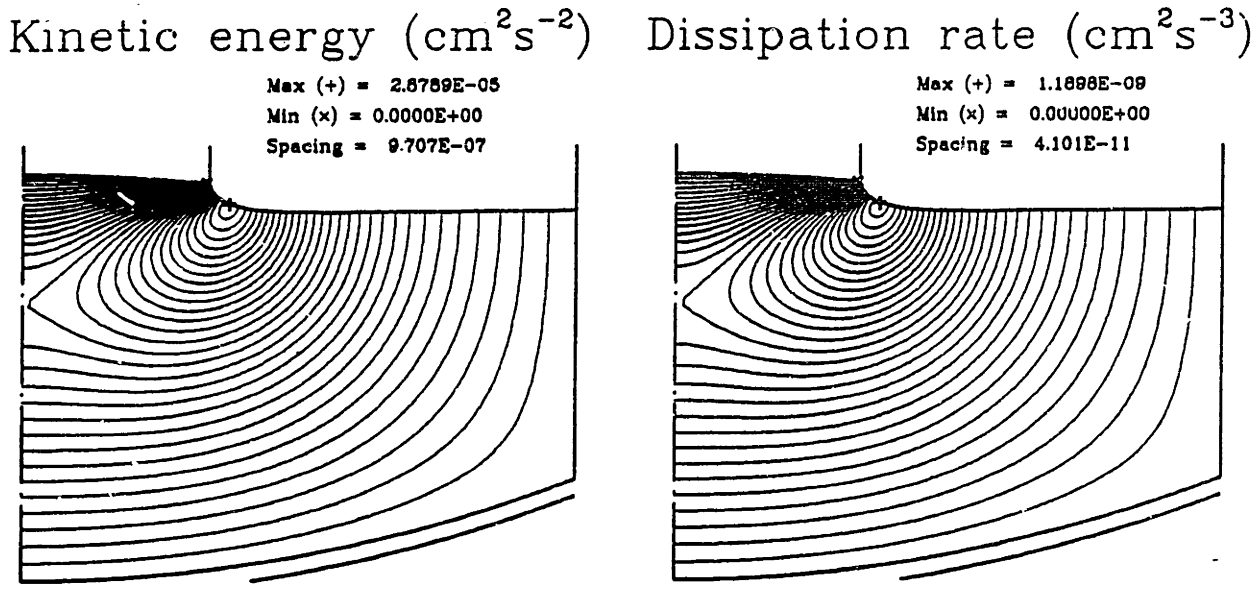

Figure 4-10: Kinetic energy and dissipation rate for high-viscosity simulation with crucible rotation only: (a) kinetic energy, and (b) dissipation rate.

continues to yield zero K and ϵ and the laminar solution for the remaining variables.

4.4.4 $K-\epsilon$ /IHTCM predictions of the laminar-flow limit

Calculations with decreasing viscosity successfully retained positive K and ϵ , but produced negligible change to the mean flow variables, since very little turbulent viscosity was generated. This continuation procedure was discontinued when only very small steps in molecular viscosity could be made, and arclength continuation was likewise ineffective, in spite of regularizing all denominators and increasing the artificial generation parameter. Solutions for driving forces of crucible rotation, buoyancy and all driving forces combined are presented in Figures 4-11–4-13 at the minimum molecular viscosities reached in this way. The mean-flow profiles are governed by molecular viscosity, and the turbulence-quantities simply reflect the magnitude of the driving force term $\left[\left(\nabla\bar{\mathbf{v}}+\nabla\bar{\mathbf{v}}^{\dagger}\right):\nabla\bar{\mathbf{v}}\right]$, the contours resembling Figure 4-9. The turbulent viscosity reaches a maximum in boundary-layers near the perimeter of the melt but decays in the bulk and never contests the value of the molecular viscosity. The constants in the low-Reynolds-number formulation were varied to discover the reason for the lack of turbulent

generation in the bulk. The constants in the function f_μ multiplying the generation term were found to give extreme variations in the solution; f_μ maintained its minimum value of almost exactly 3.34×10^{-2} throughout the melt for the simulations in Figures 4-11-4-13, due to the low turbulence-Reynolds-number. The function f_μ should approach the value 1.0 in the bulk when there is sufficient driving force, as is expected for the cases with buoyancy and all driving forces combined.

4.4.5 Computing turbulence with the $K-\epsilon$ /IHTCM: a hybrid model

Evidently the low-Reynolds-number model can predict the laminar flow limit. However, this ability is not an enhancement over the IHTCM and it was felt that turbulent results with large amounts of turbulent viscosity could be generated with the model by an alternative means of continuation. Continuation to lower molecular viscosity using Newton's method could not track the transition between these two regimes. A similar difficulty in establishing a change in regimes had been overcome previously for laminar simulations. A similar barrier to increasing crystal rotation at fixed crucible rotation at the correct viscosity of silicon motivated continuation in viscosity as described in Chapter 2. In light of the sensitivity to the value of f_μ, a hybrid model was devised which forces the solution field to match high Reynolds-number behavior in the bulk artificially, by solving the low-Reynolds-number equations only near the solid boundaries, and the standard $K-\epsilon$ equations, Eqs. (4.17)-(4.22), elsewhere, which is equivalent to forcing f_μ to be 1.0. A four-element layer was chosen arbitrarily for the low-Reynolds-number equations. Continuation in viscosity had not succeeded in spanning the transition between the two regimes because of the drastically different solution structures. With the hybrid model, the complex transition between regimes is avoided, because the laminar state is never computed. After reaching the turbulent regime the transition from low to high turbulent viscosity should occur within the four-element layer of the hybrid model. The domain of the low-Reynolds-number calculations can then be increased to encompass the entire domain.

Solutions to this hybrid model were computed with decreasing viscosity. Using[3] $\pi_g = 5 \times 10^{-4}\, cm^2 \cdots^{-2}$, simulations with buoyancy as the only driving force, and all driving forces combined exhibited considerably enhanced turbulent viscosity throughout the bulk

[3]This generation term was applied only to the appearance of μ_T multiplying the generation term in the kinetic energy equation.

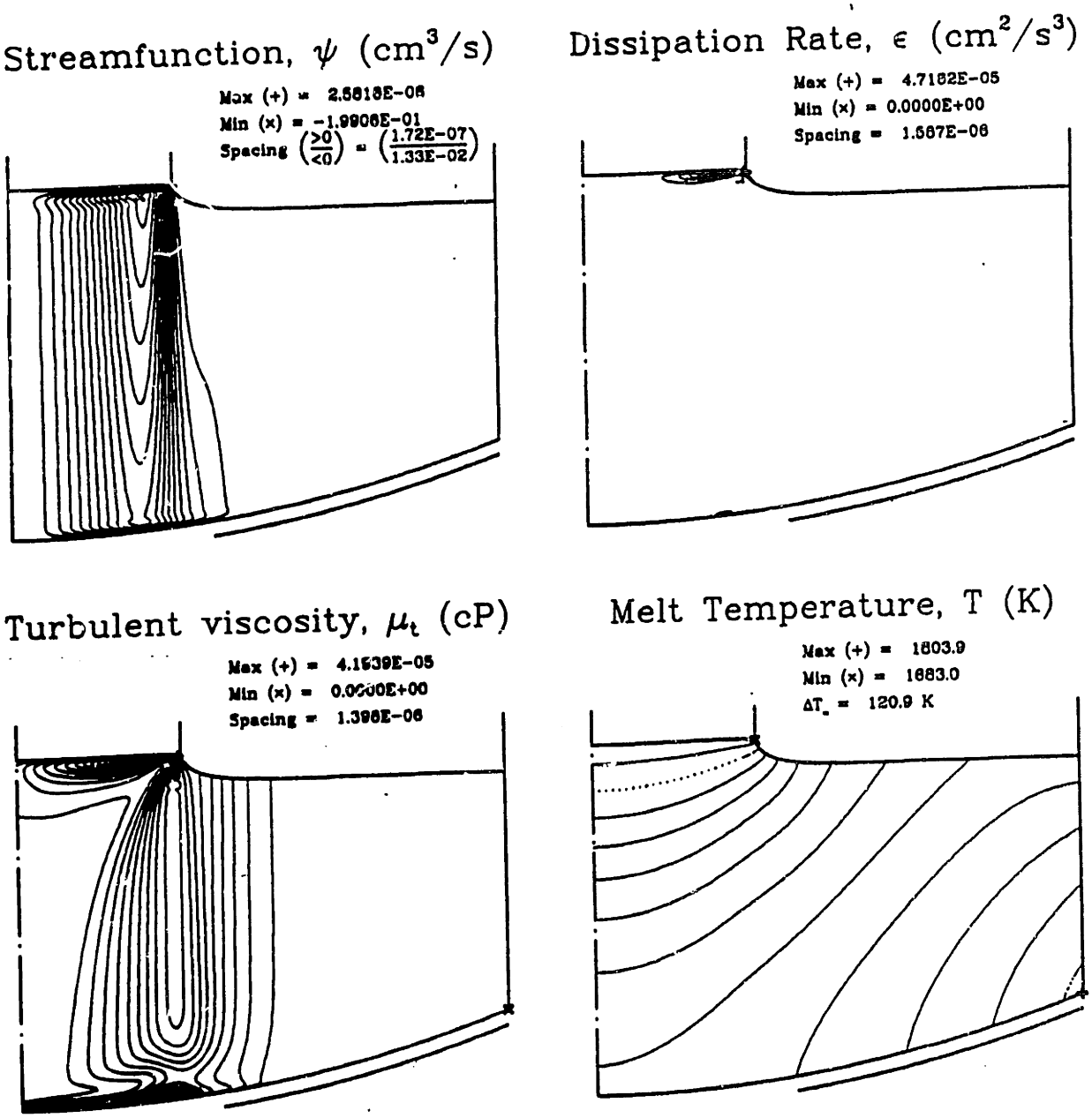

Figure 4-11: Laminar solutions computed using low-Reynolds-number $K-\epsilon$ model with crucible rotation alone at minimum attained molecular viscosity ($0.86cP$): (a) streamfunction, (b) dissipation rate, (c) turbulent viscosity, and (d) melt temperature.

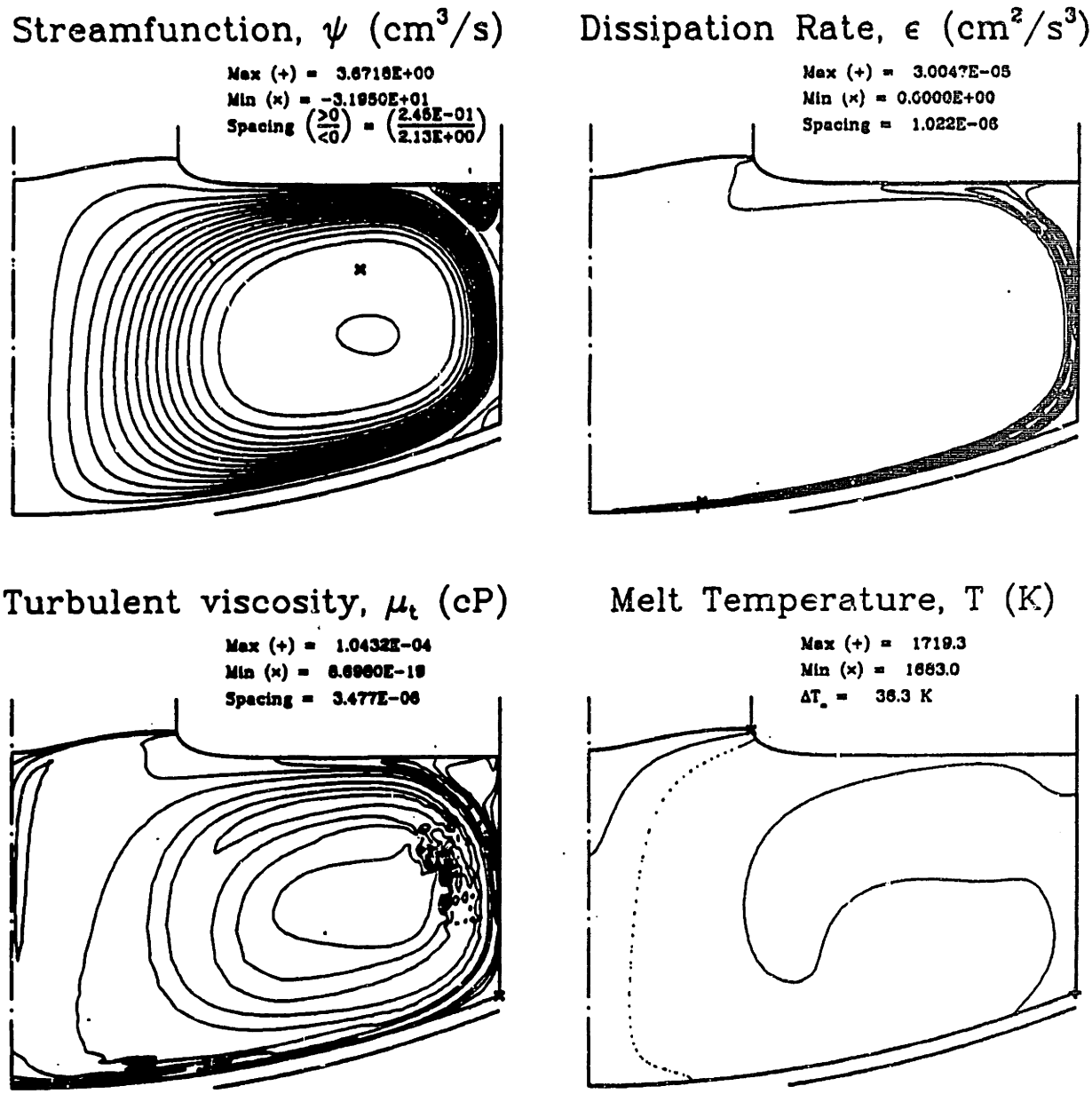

Figure 4-12: Laminar solutions computed using low-Reynolds-number $K-\epsilon$ model with buoyancy alone at minimum attained molecular viscosity ($2.0cP$): (a) streamfunction, (b) dissipation rate, (c) turbulent viscosity, and (d) melt temperature. The low ΔT_m was due to the generation parameter π_g appearing in the expression for k_T, which was eliminated in subsequent runs.

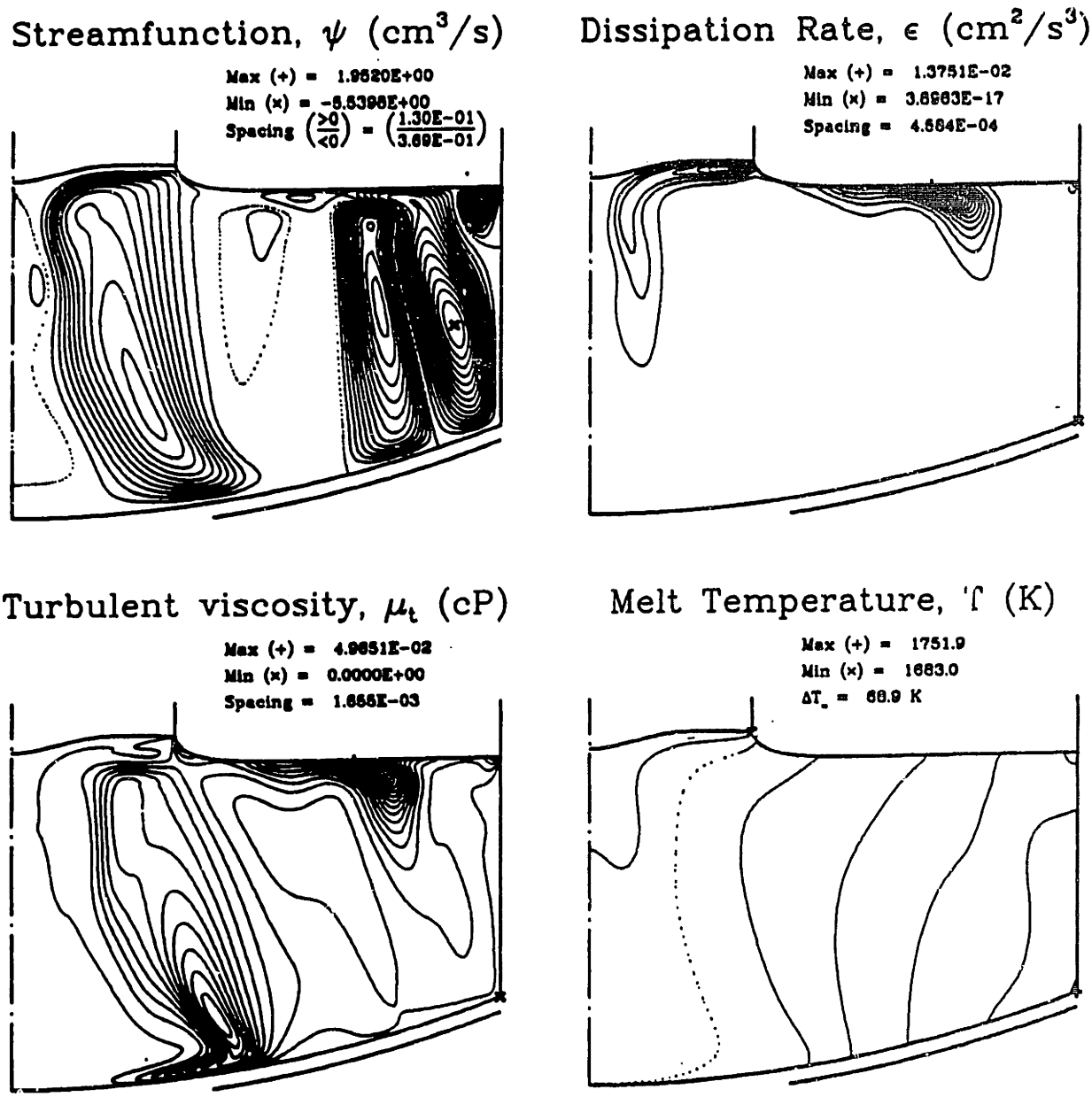

Figure 4-13: Laminar solutions computed using low-Reynolds-number $K-\epsilon$ model with all driving forces combined at minimum attained molecular viscosity ($11.75cP$): (a) streamfunction, (b) dissipation rate, (c) turbulent viscosity, and (d) melt temperature.

compared to the laminar-like results; see Figures 4-15 and 4-16. The simulation featuring crucible rotation showed enhanced viscosity only if π_g was increased to $1.0\,cm^2 \cdot s^{-2}$, which was greater than the computed value of K throughout most of the melt; see Figure 4-14. The enhancement in this case was entirely due to the artificial parameter π_g. The shape of the turbulent viscosity field in Figure 4-14c bears little resemblance to the distribution of shear forces; the lack of genuine driving force for turbulent production was confirmed by reductions in π_g which showed steady decline in the transport with decreasing π_g. Therefore, crucible rotation alone does not yield turbulent enhancement in the $K - \epsilon$ model and the sequence of calculations was terminated.

The solution to the hybrid model with buoyancy as the lone driving force is shown in Figure 4-15 and develops a higher turbulent viscosity than the laminar-like calculations, especially in the region of highest shear. The transition between the hybrid regions in Figure 4-15b and 4-15c appear as dark bands four elements thick at the crucible bottom near the centerline. At the molecular viscosity of $42.0cP$ the mean flow is very similar to laminar flow. However, the solution to the hybrid model with all forces in Figure 4-16c has a turbulent viscosity that exceeds the molecular viscosity by a factor of about 10, and the streamfunction is correspondingly simplified from the multicellular pattern in Figure 3-13 to the two-cell pattern shown in Figure 4-16a. The complex multicellular patterns which made the continuation path so tortuous in the laminar flow calculations do not appear. The turbulent viscosity is highest along the free surface, which is expected because of the high shear rates that generate turbulence there. the enhancement of turbulent viscosity is clearly seen in Figure 4-16 and is due to the high-Reynolds-number form of the $K - \epsilon$ equations in the bulk: this can be seen by the thick black four element-wide layers where most of the total dissipation occurs.

4.4.6 Regularization of total dissipation terms D and E

Simulations using the $K - \epsilon$ /IHTCM with buoyancy as the lone driving force were computed to a viscosity of $42.0cP$ (60 times the viscosity of silicon), with the hybrid scheme described above. Below $42.0cP$ solutions could not be computed on the mesh used without taking extremely small steps in μ. This restriction to the domain of convergence seemed to be due to large values of the D and E terms appearing near the wall in extremely steep boundary-layers, as shown in see Figure 4-17a and 4-17b. As an alternative to using a mesh fine enough to resolve the near-wall variations, the D and E terms only were smoothed near the walls by adding the regularization parameters

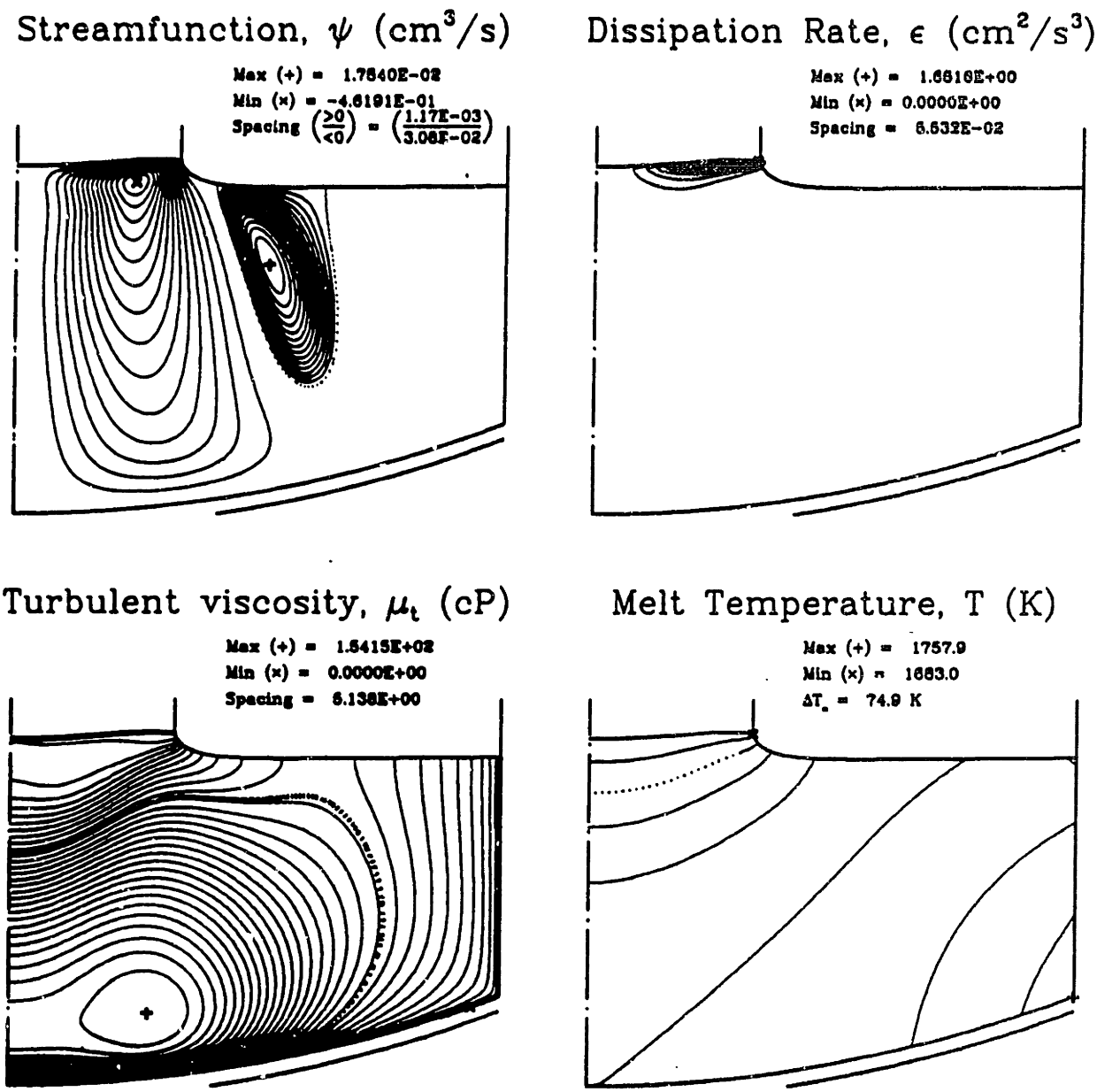

Figure 4-14: Simulation computed using hybrid $K-\epsilon$ model with crucible rotation alone at molecular viscosity of $0.90cP$: (a) streamfunction, (b) dissipation rate, (c) turbulent viscosity, and (d) melt temperature. In figure (c) the solid curve indicates where turbulent viscosity exceeds the molecular viscosity and the dotted curve shows where the turbulent conductivity exceeds the molecular conductivity.

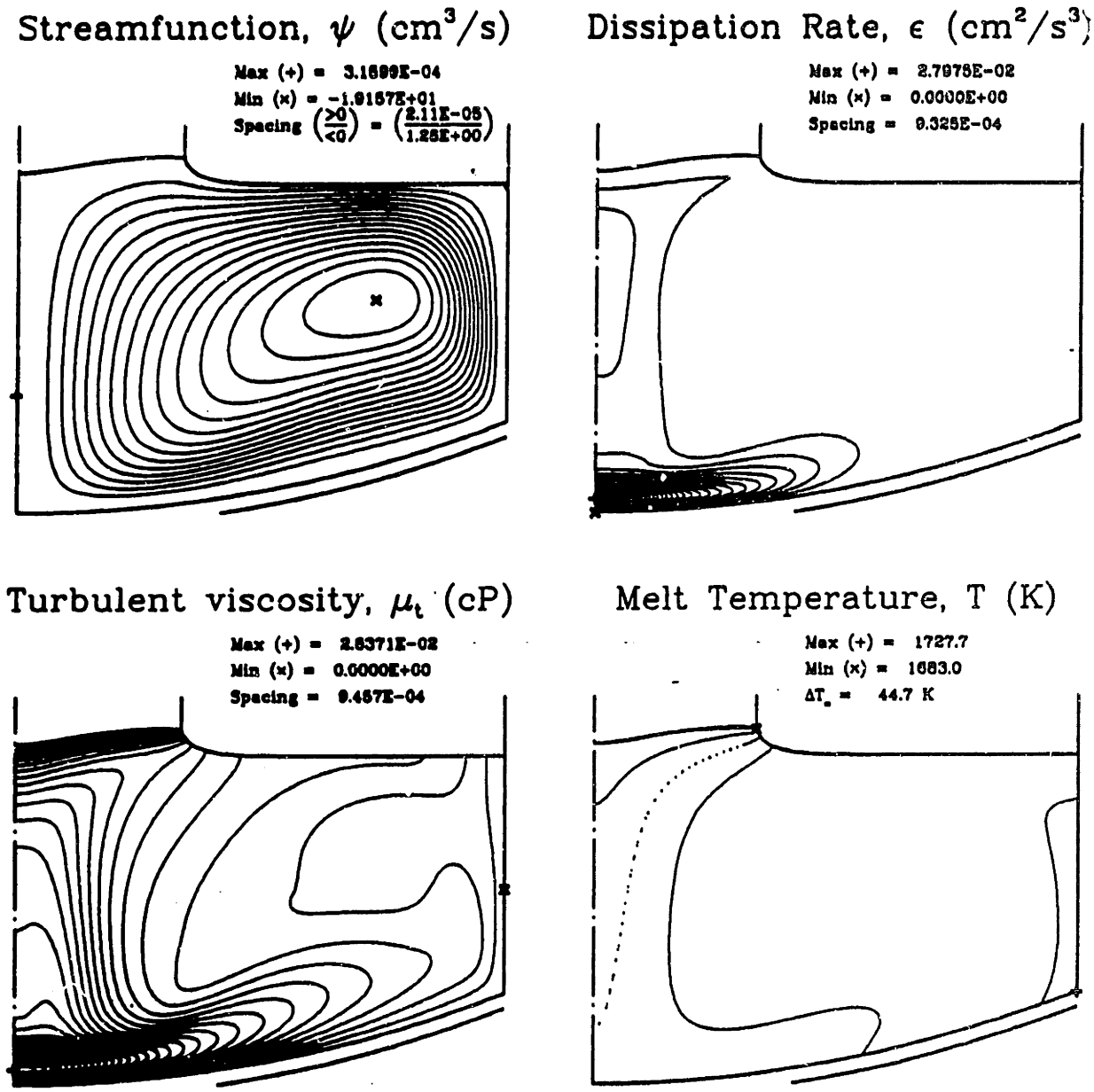

Figure 4-15: Simulation computed using hybrid $K - \epsilon$ model with buoyancy only at molecular viscosity of 42.0cP: (a) streamfunction, (b) dissipation rate, (c) turbulent viscosity, and (d) melt temperature.

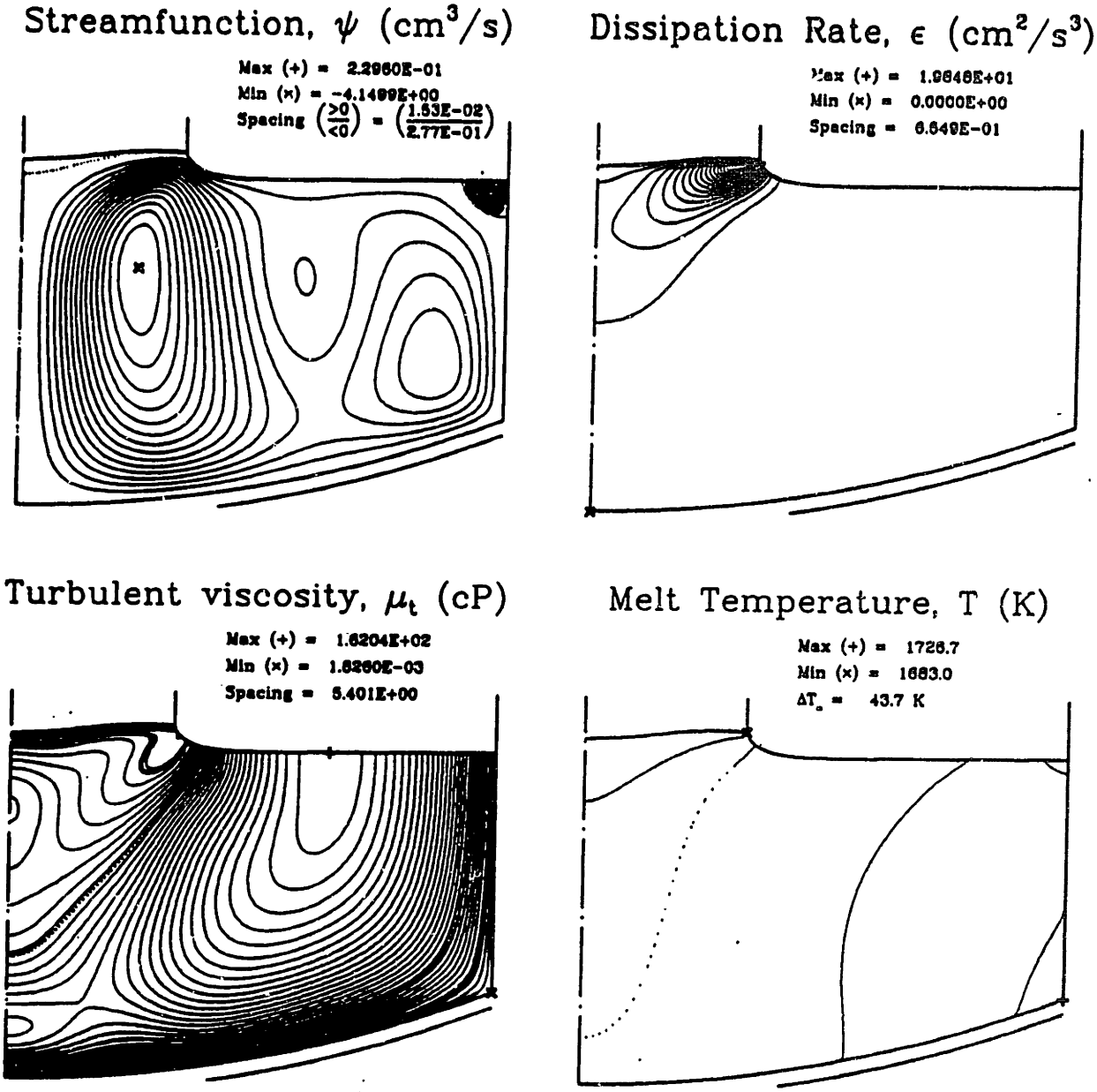

Figure 4-16: Simulation computed using hybrid $K-\epsilon$ model with all driving forces combined at $\mu = 17.5cP$: (a) streamfunction, (b) dissipation rate, (c) turbulent viscosity, and (d) melt temperature. In (c) the solid curve indicates where turbulent viscosity exceeds the molecular viscosity and the dotted curve shows where the turbulent conductivity exceeds the molecular conductivity.

$\pi_D = 10^{-6}\, cm^2 \cdot s^{-2}$ and $\pi_E = 10^{-4}\, cm^2 \cdot s^{-3}$ to the D and E terms, respectively. The solution for this case is shown in Figure 4-18, and is barely different from the result shown in Figure 4-15, but the peak values in the terms D and E change considerably. The choice of the magnitude of the regularizers was made to make the ratios between the regularization parameters and the variables K and ϵ both approximately 10^{-5}

$$\frac{\pi_D}{K^{max}} \simeq \frac{\pi_E}{\epsilon^{max}} \simeq 10^{-5}. \tag{4.46}$$

Simulations using the $K-\epsilon$ /IHTCM with all driving forces combined were computed to a viscosity of $17.5cP$ (25 times the viscosity of silicon), before resorting to the regularization scheme described above. The large values of the D and E terms again appear in a very steep boundary-layer, as shown in Figures 4-19a and 4-19b. The peak values in D and E change drastically without any effect on the solution variables when regularization is implemented, as shown in Figure 4-20.

4.5 $K-\epsilon$ /IHTCM predictions at realistic conditions

4.5.1 Buoyancy-driven flow

Regularizing the source and sink terms D and E in Equations (4.42) and (4.43), enabled continuation for buoyancy-driven flow to the molecular viscosity of silicon using the hybrid $K-\epsilon$ model, yielding the solution shown in Figure 4-21. The dark bands in Figure 4-15b are not present as the solution becomes fully turbulent within the four-element low-Reynolds-number zone. Next the artificial parameter π_g was reduced to zero, resulting in very little change to the solution; see Figure 4-22. Thus the enhanced transport observed in these calculations is due to the turbulent generation from the velocity gradients in the mean flow and not the artificial generation parameter π_g. Therefore, *artificial generation of turbulence was necessary only to leap the transition between laminar and turbulent regimes in the low-Reynolds-number $K-\epsilon$ model calculations.*

The most important result from this sequence of calculations was obtained by gradually increasing the domain where the low Reynolds-number equations are applied until it encompasses the entire melt (this calculation is shown in Figure 4-23), thereby eliminating the need for the hybrid model. Although this manoeuvre was implemented in several

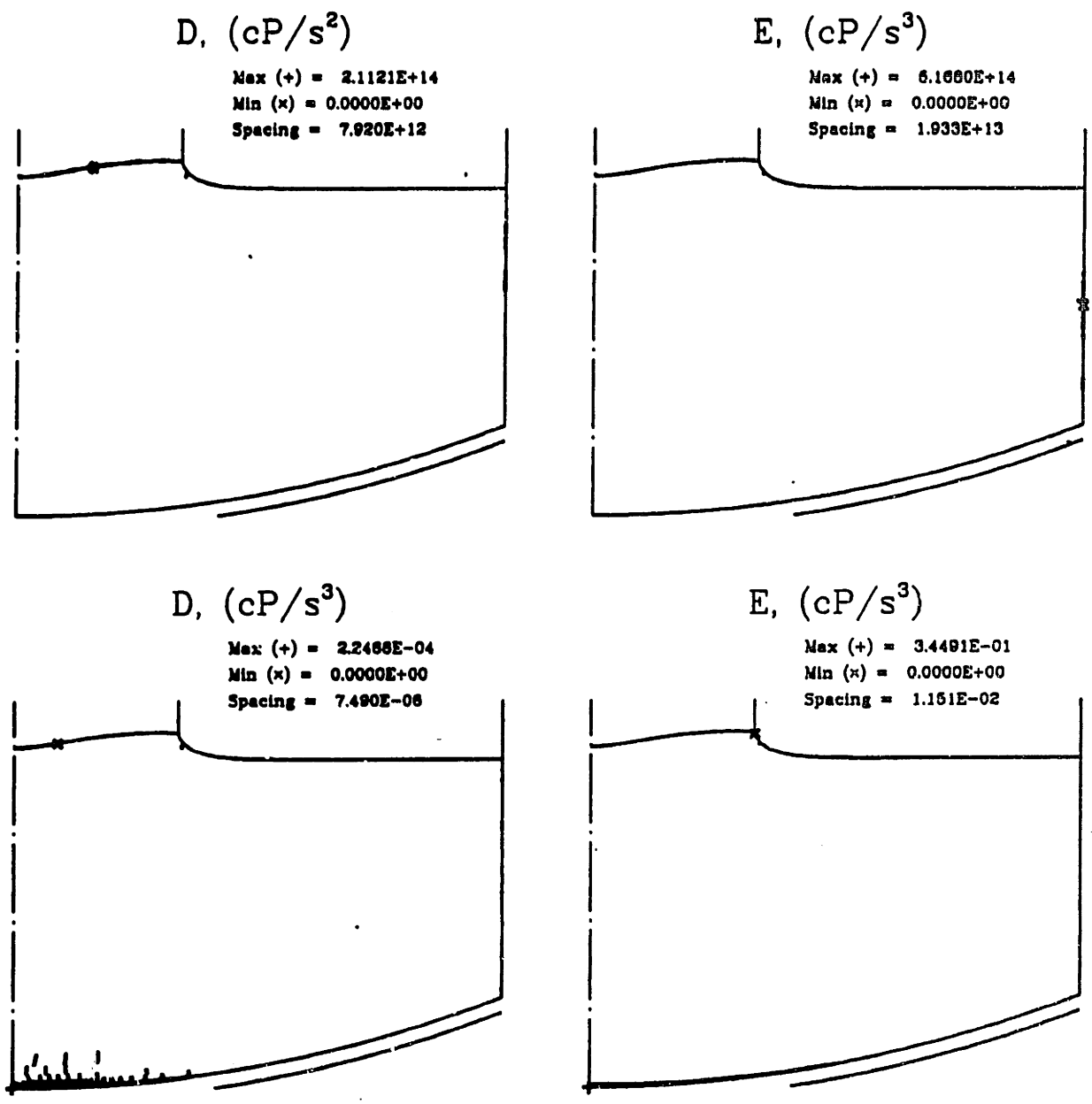

Figure 4-17: Comparison of magnitude of terms D and E in Equations 4.33 and 4.34 using hybrid $K - \epsilon$ model without regularization [(a) and (b)], and with regularization [(c) and (d)]. Simulation is for buoyancy-driven flow at $\mu = 42.0cP$.

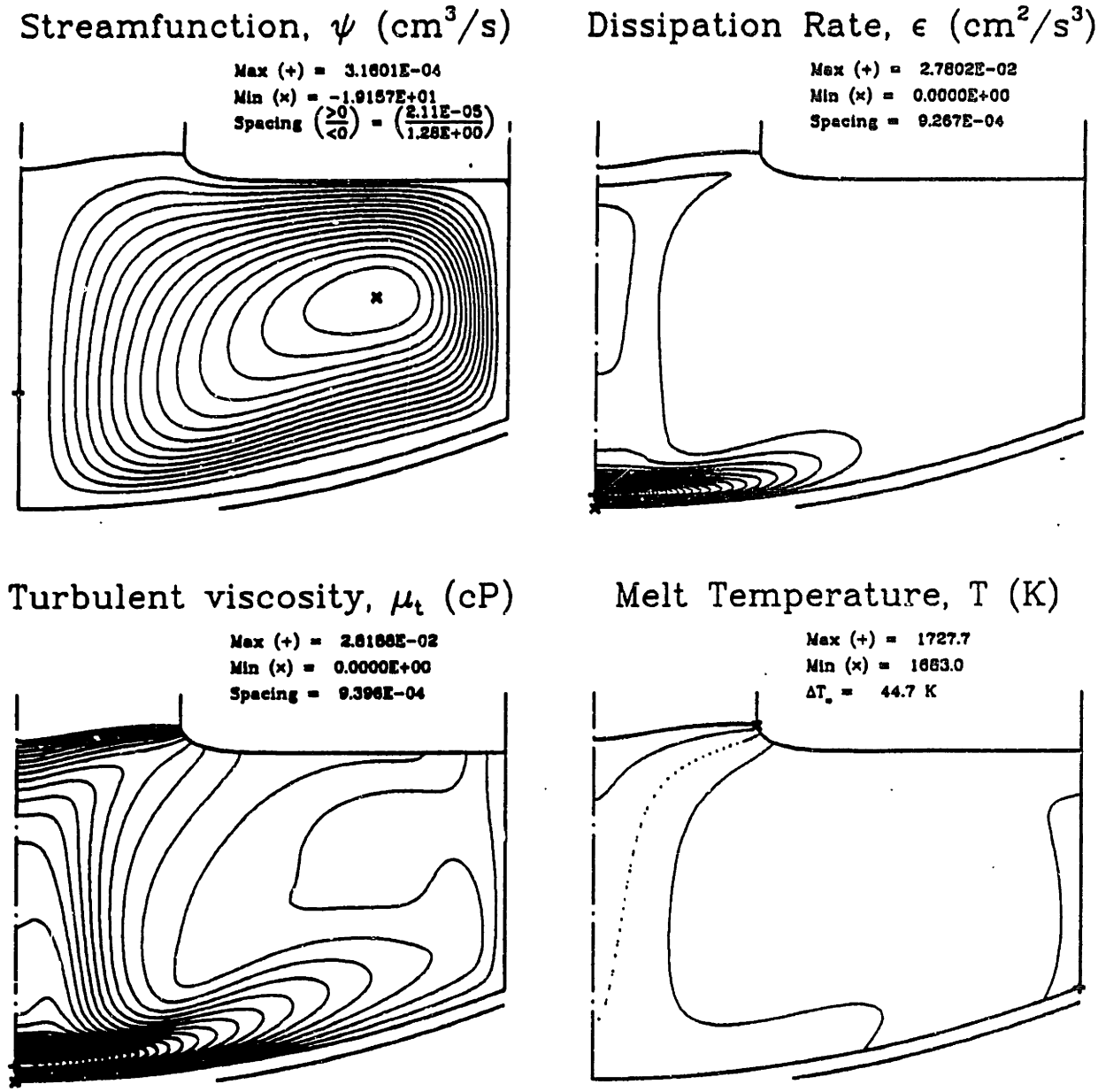

Figure 4-18: Simulation computed using hybrid $K - \epsilon$ model having regularization to terms D and E of Equations 4.33 and 4.34 with buoyancy only at $\mu = 42.0cP$: (a) streamfunction, (b) dissipation rate, (c) turbulent viscosity, and (d) melt temperature. Compare to solution in Figure 4-15.

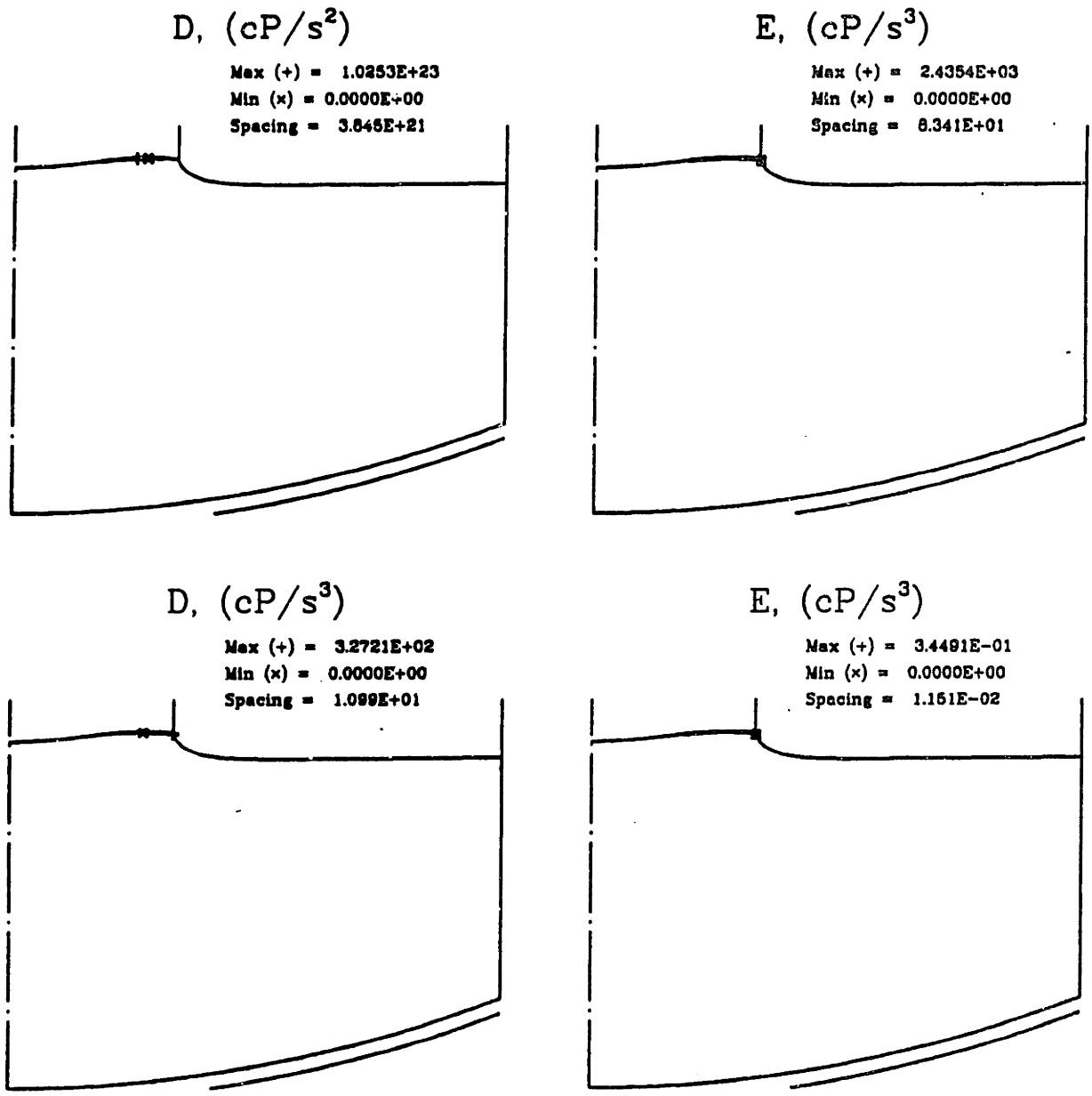

Figure 4-19: Comparison of magnitude of terms D and E in Equations 4.33 and 4.34 using hybrid $K-\epsilon$ model without regularization [(a) and (b)], and with regularization [(c) and (d)]. Simulation is for all flow mechanisms combined at $\mu = 17.5cP$.

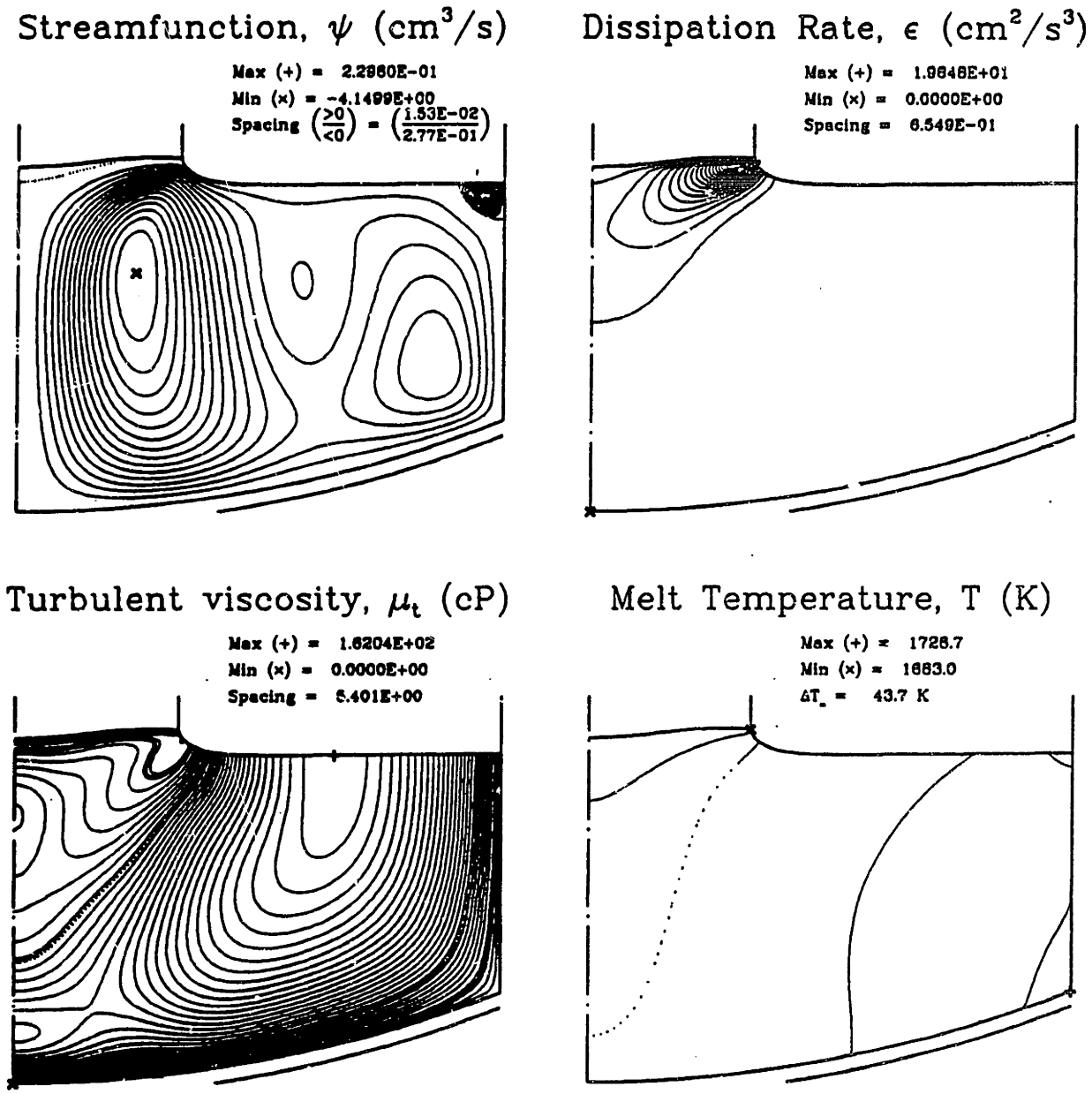

Figure 4-20: Simulation computed using hybrid $K-\epsilon$ model having regularization to terms D and E with all flow mechanisms combined at $\mu = 17.5cP$: (a) streamfunction, (b) dissipation rate, (c) turbulent viscosity, and (d) melt temperature. In figure (c) the solid curve indicates where the turbulent viscosity exceeds molecular viscosity and the dotted curve shows where the turbulent conductivity exceeds the molecular conductivity. Compare to solution in Figure 4-16.

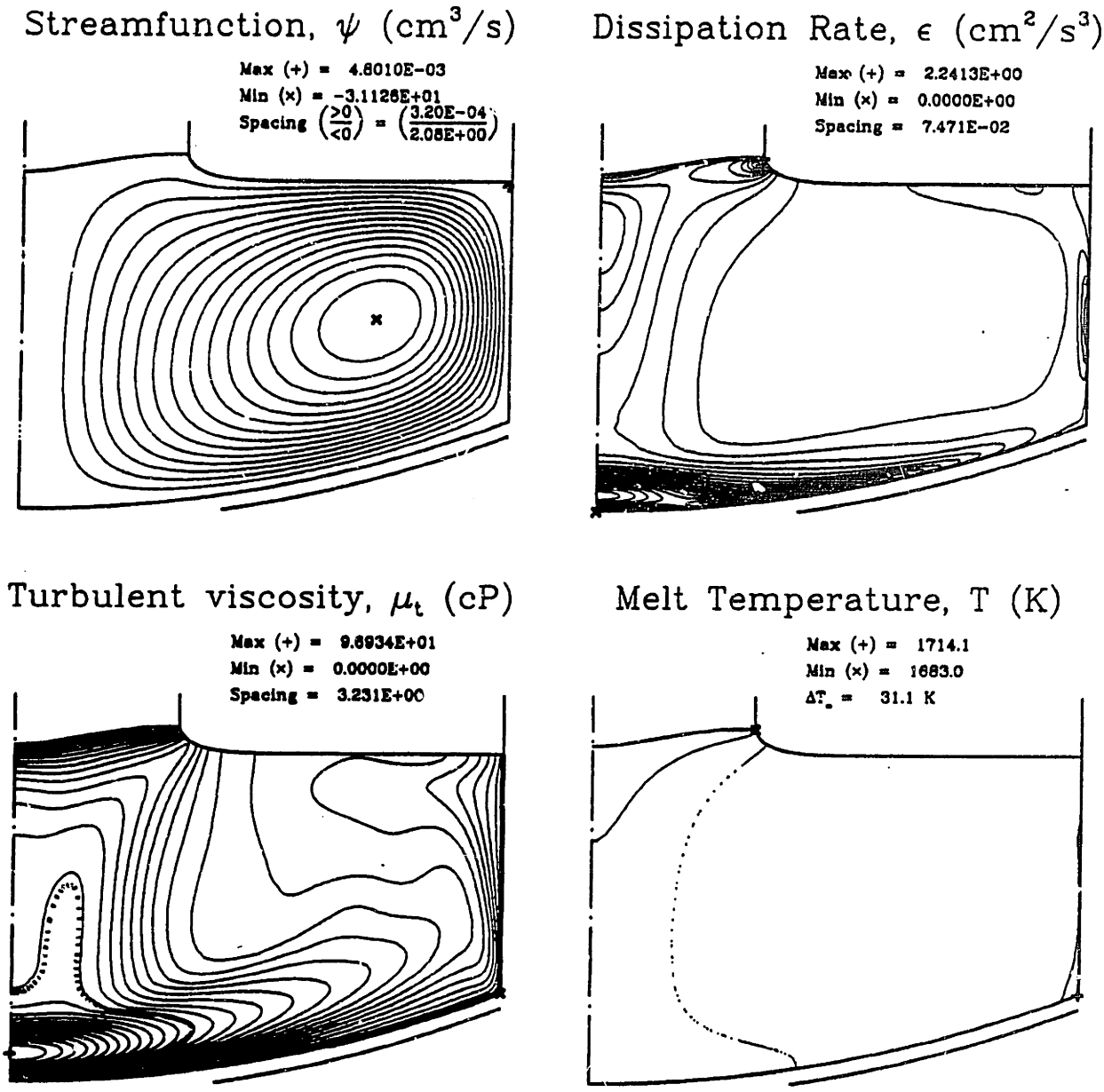

Figure 4-21: Simulation computed using hybrid $K-\epsilon$ model having regularization to terms D and E with buoyancy-driven flow at $\mu = 0.7cP$: (a) streamfunction, (b) dissipation rate, (c) turbulent viscosity, and (d) melt temperature. In figure (c) the solid curve indicates where the turbulent viscosity exceeds molecular viscosity and the dotted curve shows where the turbulent conductivity exceeds the molecular conductivity.

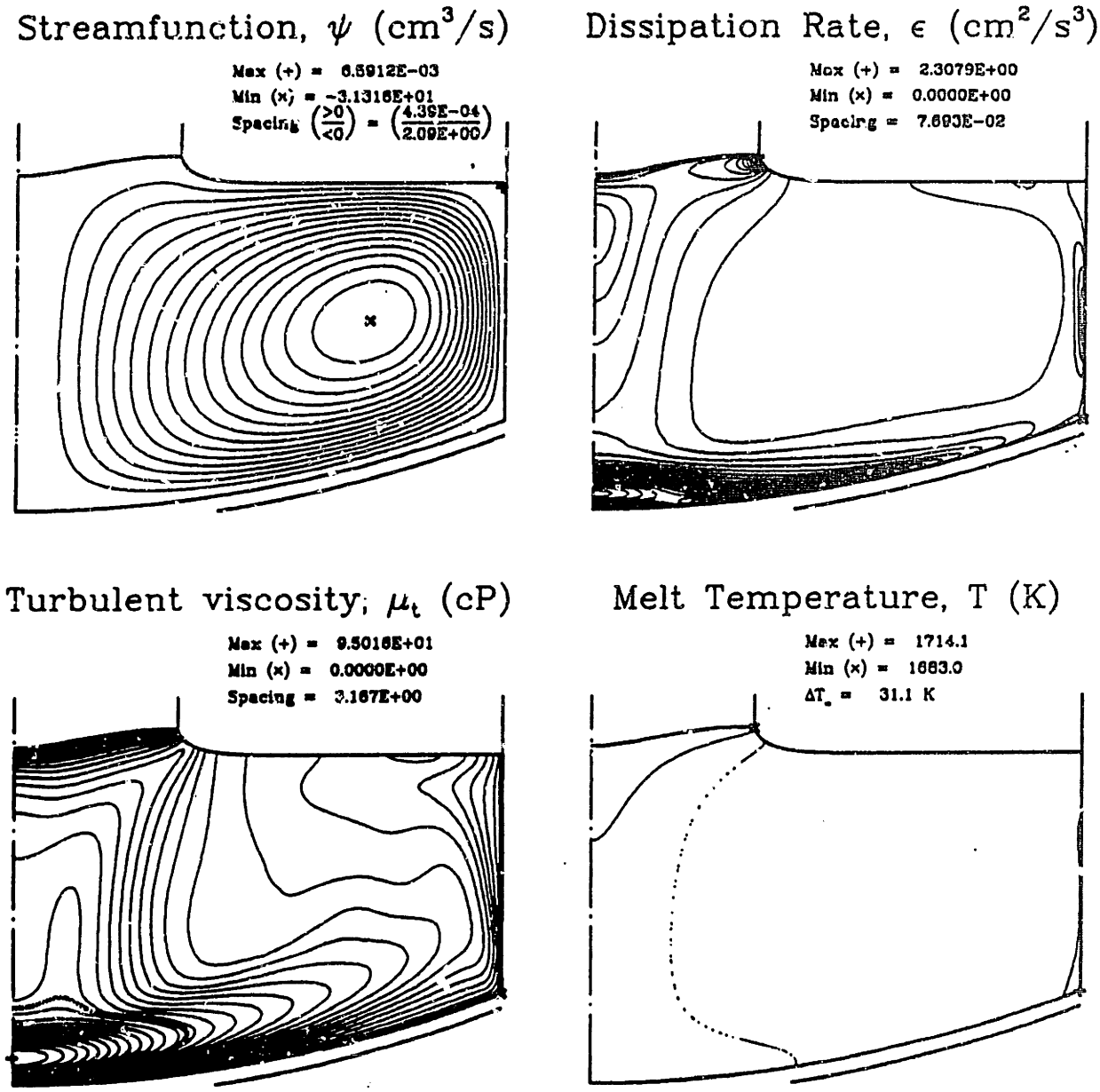

Figure 4-22: Simulation computed using hybrid $K-\epsilon$ model having regularization to terms D and E but no artificial generation parameter with buoyancy-driven flow at $\mu = 0.7cP$: (a) streamfunction, (b) dissipation rate, (c) turbulent viscosity, and (d) melt temperature. In figure (c) the solid curve indicates where the turbulent viscosity exceeds the molecular viscosity and the dotted curve shows where turbulent conductivity exceeds the molecular conductivity. Compare to Figure 4-21.

steps, the solution changed little, because the flow field was already fully-turbulent within the low-Reynolds-number region of the former hybrid model. The heat transfer in the melt in Figure 4-23 is enhanced over the laminar calculation for buoyant flow shown in Figure 2-31. Convection from the mean flow is the primary mode of heat transfer in the region between the crucible wall and the crystal for both cases, since the circulation rate of the primary flow cell is comparable in both simulations, and the core of the melt is nearly isothermal as well. The enhancement of heat transfer is due to the isotropic turbulent convection in the region under the crystal. In the laminar case, radial conduction governs heat transfer there, since the flow is aligned perpendicular to the temperature gradient; in the $K-\epsilon$ /IHTCM simulation, radial heat transfer by turbulent convection exceeds conduction for most of the melt under the crystal and greatly increases heat transfer there.

Behavior of buoyant turbulent flow was further investigated by increasing the molecular viscosity by continuation from $0.7\,cP$. The highest viscosity reached in this way was was $9.625\,cP$ and the solution is shown in Figure 4-24. It appears that the flow evolves somewhat toward the laminar state, losing some of its ability to transfer heat. The solution procedure was not able to proceed further on the mesh used, however, and so the transition between a turbulent and laminar flow was not to be computed without use of the hybrid $K-\epsilon$ model. Several of the important solution variables, $\Delta\overline{T}_m$, $|\overline{\psi}^{min}|$, $\Delta\overline{h}$, ϵ^{max} and μ_T^{max}, are shown with increasing molecular viscosity in Figure 4-25. Increasing the molecular viscosity steadily impedes the heat transfer and mean circulation rate, but $\Delta\overline{h}$, and μ_T pass through extrema in this range. Therefore the decreased heat transfer is due to poorer convective mixing from the mean convection term $\overline{\mathbf{v}}\cdot\nabla\overline{T}$ in the range of molecular viscosity $0.7\,cP < \mu < 5\,cP$ which outweighs the increased turbulent transport, and the decrease in heat transfer between $5\,cP < \mu < 9.5\,cP$ is due to the combination of poorer convective mixing from the mean flow and the decreased turbulence. The changes in the interface deflection can be directly correlated to the effect of the turbulent viscosity on flow near the melt/solid interface. It is interesting that μ_T does not reach a constant value as $\mu \rightarrow 0.7\,cP$; evidently the increasing mean velocity and consequently the increasing dissipation rate for $\mu < 5\,cP$ is the cause. The dissipation rate increases most noticeably at the melt/crystal/ambient trijunction, which can be explained by the large temperature gradient just below the melt/crystal interface which drives buoyant flow. At that point the velocity gradient increases dramatically at low viscosity, preferentially increasing the near-wall dissipation since the behavior is locally governed by the low-Reynolds-number functions. Calculations have verified that

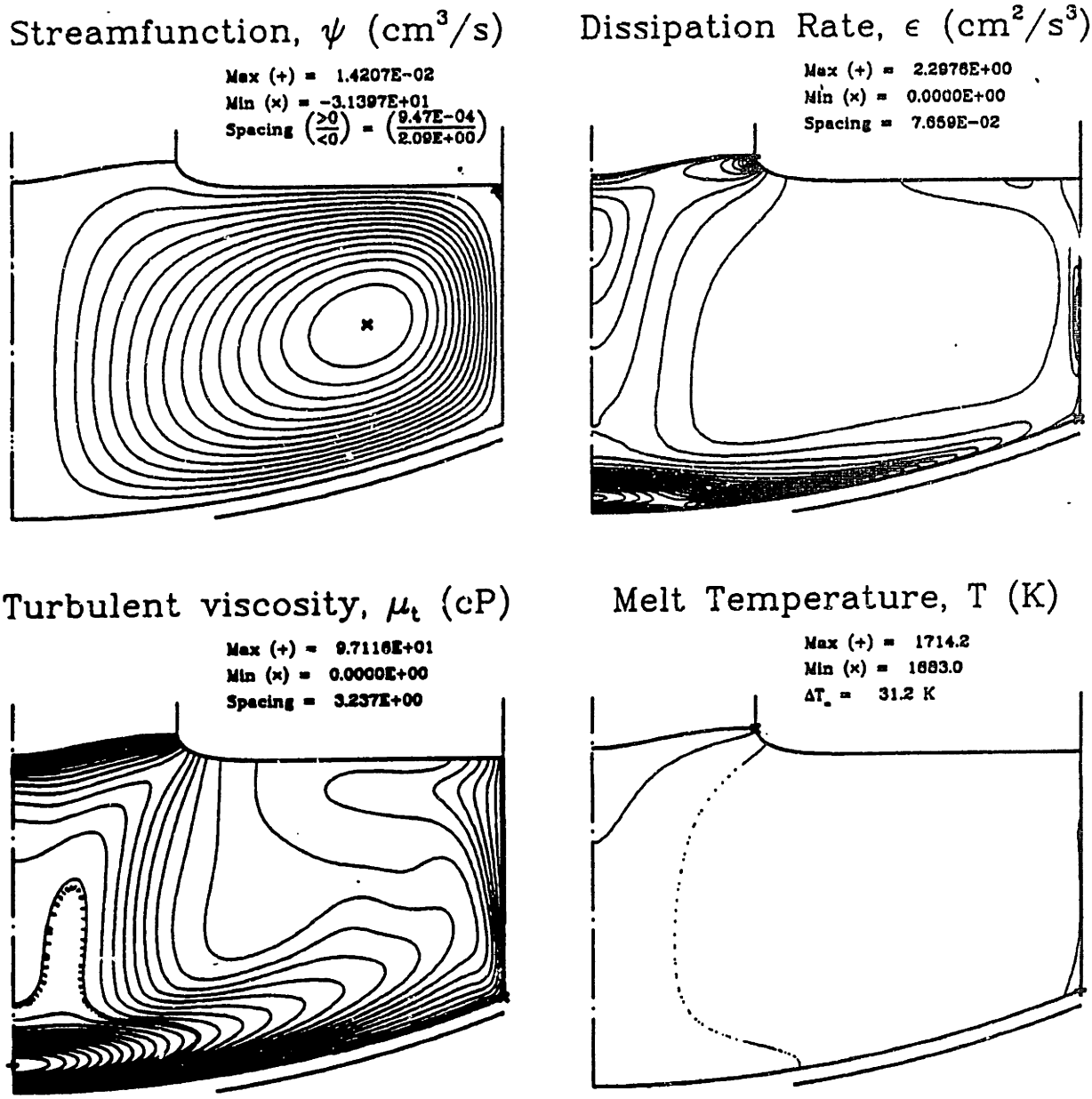

Figure 4-23: Simulation computed using low-Reynolds-number $K-\epsilon$ model having regularization to terms D and E but no artificial generation parameter with buoyancy-driven flow at $\mu = 0.7cP$: (a) streamfunction, (b) dissipation rate, (c) turbulent viscosity, and (d) melt temperature. In figure (c) the solid curve indicates where the turbulent viscosity exceeds the molecular viscosity and the dotted curve shows where the turbulent conductivity exceeds the molecular conductivity. Compare to Figure 4-22.

this behavior is not affected by changing the magnitude of the regularization parameters used in the D and E terms. Behavior whereby the flow reverts from being more turbulent to more laminar with *increasing* velocity has been observed before in experiments on strongly-accelerated boundary-layer flows (Launder, 1964; Morretti and Kays, 1965) and cannot be predicted by turbulence-formulations with wall-functions. It has been calculated before using low-Reynolds-number turbulence models (Jones and Launder, 1972) for near-wall boundary-layers.

4.5.2 Combined flow mechanisms

Continuation in viscosity achieved a molecular viscosity of $1.7\,cP$, which is 2.26 times that of silicon, for a sequence of calculations with all flow mechanisms combined, yielding the solution shown in Figure 4-26. Attempts to decrease the viscosity further resulted in divergence of the iterations, where the largest updates from the Newton iteration were applied to the variables K and ϵ at the node on the free surface immediately adjacent to the melt/crucible/ambient trijunction. The abrupt peak in the dissipation field in Figure 4-26c reflects the presence of a singularity there, as discussed in Section 2.4.2 in association with the thermocapillary force, and results in a logarithmic dependence of the maximum dissipation rate on molecular viscosity. As mentioned in Section 2.4.2 this behavior is still integrable with the finite-element formulation and can be better approximated by greatly increasing the local discretization or by introducing a singular basis function. The difficulty could be avoided in an *ad hoc* fashion by reducing the value of the thermocapillary coefficient as a function of proximity to the wall. However, it is shown below in Figure 4-30 that the variables $\overline{T}, \overline{\mathbf{v}}$ and $\overline{h}$ are insensitive to the exact value of molecular viscosity in this range, so that decreasing the molecular viscosity to $0.7cP$ would yield little change the solution field.

The artificial parameter π_g is reduced to zero along with extending the low-Reynolds-number equations throughout the melt, introducing only a slight change to the solution; see Figure 4-27. Thus the enhanced transport observed with combined flow is due to generation of turbulence in the $K-\epsilon$ model from gradients in the mean-flow velocity and not the artificial generation parameter, although the parameter was necessary to initialize this sequence of calculations as well. The solution structure remained almost constant with the removal of the hybrid model, reflecting that the transition to high turbulence-Reynolds-number was achieved in the low-Reynolds-number layer, as demonstrated in Figure 4-27 The heat transfer in Figure 4-27 is governed by turbulent convection

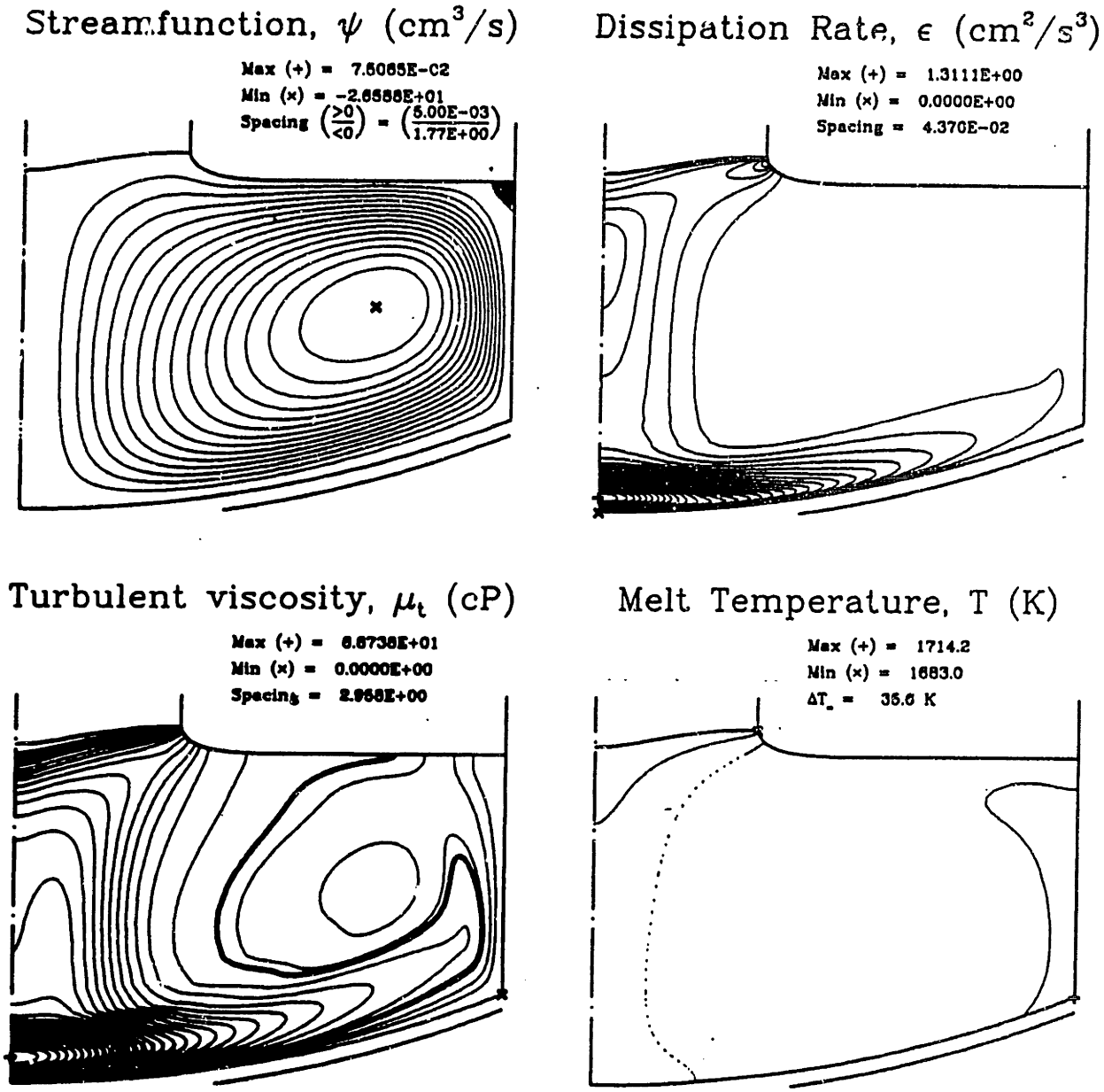

Figure 4-24: Simulation computed using low-Reynolds-number $K-\epsilon$ model having regularization to terms D and E but no artificial generation parameter with buoyancy-driven flow at molecular viscosity of $9.625cP$: (a) streamfunction, (b) dissipation rate, (c) turbulent viscosity, and (d) melt temperature. In figure (c) the solid curve indicates where the turbulent viscosity exceeds the molecular viscosity and the dotted curve shows where the turbulent conductivity exceeds the molecular conductivity.

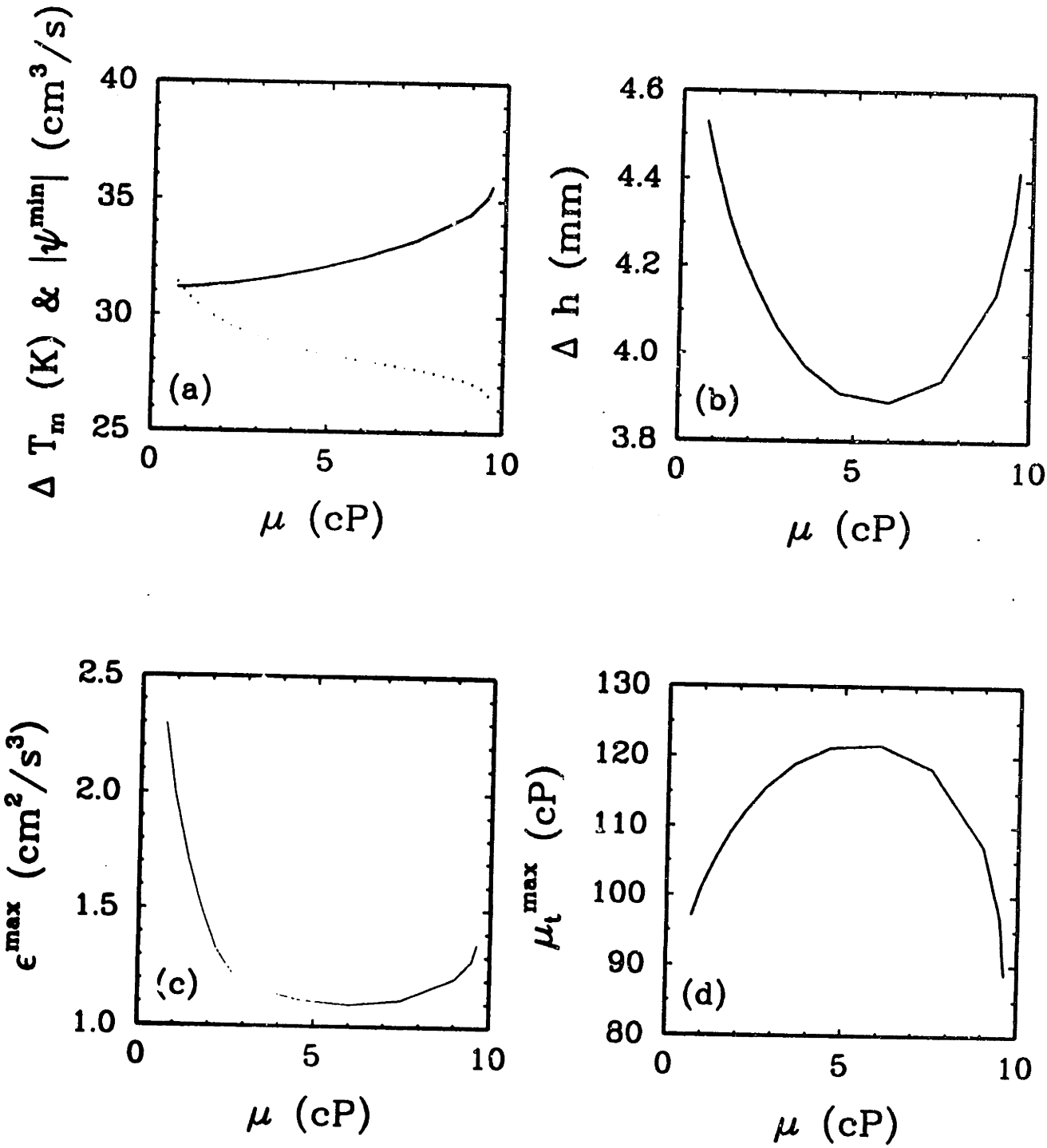

Figure 4-25: Effect of increasing μ on (a) the temperature difference across the melt $\Delta\overline{T}_m$ (—) and the maximum circulation rate of the the primary cell $|\overline{\psi}^{min}|$ (.....); (b) the maximum interface deflection $\Delta\overline{h}$; (c) the maximum dissipation rate ϵ^{max}; and (d) the maximum turbulent viscosity μ_t^{max} for buoyancy-driven flow computed with the low-Reynolds-number $K-\epsilon$ model: $0.7 \leq \mu \leq 9.625cP$.

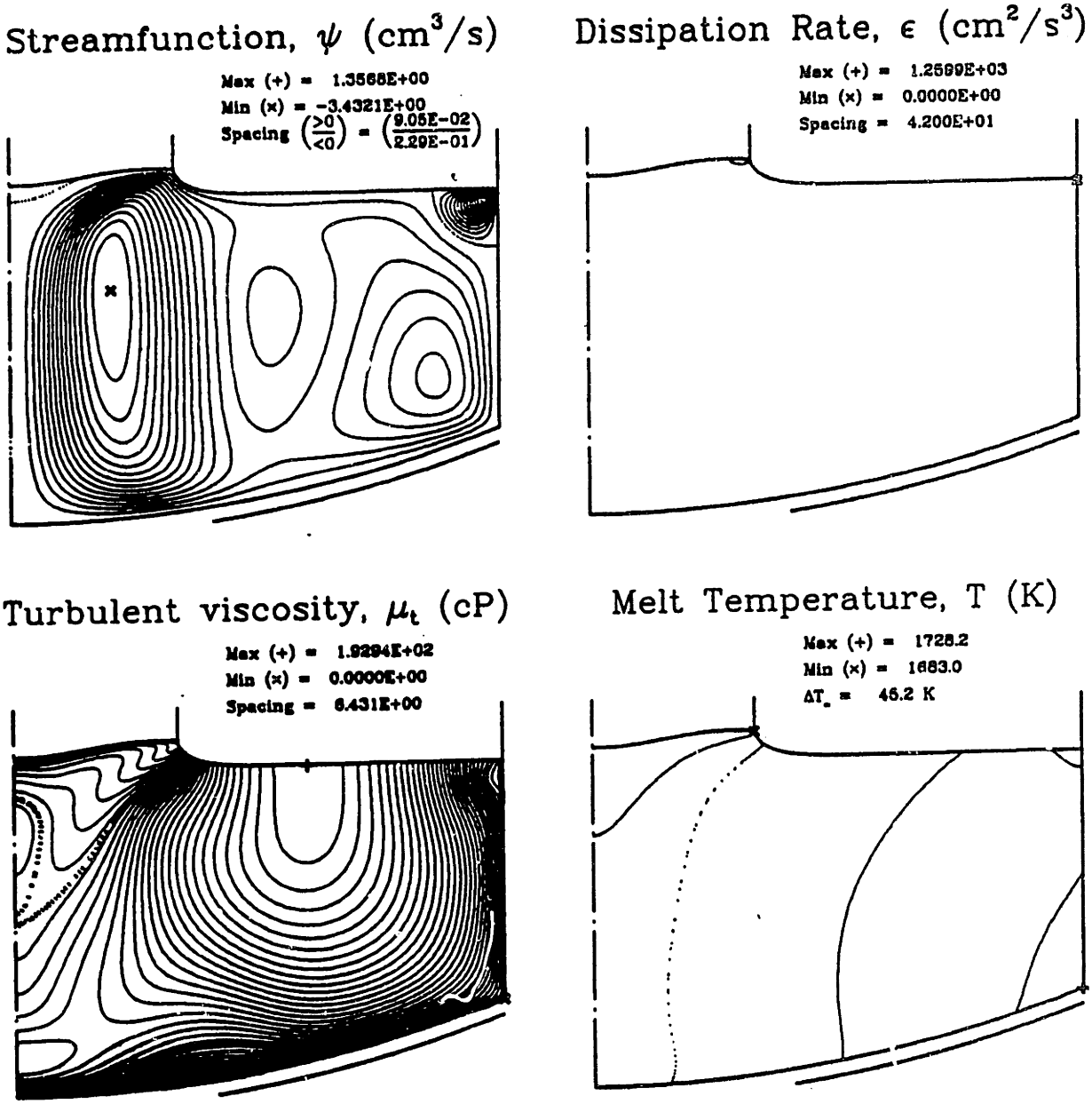

Figure 4-26: Simulation computed using hybrid $K - \epsilon$ model having regularization to terms D and E with all flow mechanisms combined at $\mu = 1.7cP$: (a) streamfunction, (b) dissipation rate, (c) turbulent viscosity, and (d) melt temperature. In figure (c) the solid curve indicates where the turbulent viscosity exceeds the molecular viscosity and the dotted curve shows where the turbulent conductivity exceeds the molecular conductivity.

throughout the bulk of the melt, and by the mean convection term close to the melt-solid interface where the turbulent transport becomes zero. This fact is verified by changes in rotation rate discussed later which greatly diminish the *average* circulation rate and affect the interface deflection, yet have little effect on the overall temperature gradient because turbulent convection dominates. This contrasts sharply with the result for buoyant flow only in Figure 4-23, where thermal convection by the mean velocity distribution dominated heat transfer between the crucible wall and the crystal, and turbulent convection was dominant only in the melt underneath the crystal.

The simulations results of laminar flow with all driving forces combined could not be extrapolated to the correct viscosity for silicon because of the variability in the solution as the viscosity of silicon was approached. Very small changes in the molecular viscosity at a value of about $3.5\,cP$ had a large effect on the laminar fields, and hence no confident extrapolation could be made to the correct value of $0.7\,cP$. However in the $K-\epsilon$ model the sensitivity to change in molecular viscosity is reflected largely in the values of the K and ϵ variables approaching the singularity at the melt/crucible/ambient trijunction. Increasing the viscosity by $+1.0\,cP$ from $1.7\,cP$ to $2.7\,cP$ negligibly affects the mean transport and interface shape, but reduces the maximum dissipation rate substantially, as shown in Figure 4-28. A decrease by $-1.0\,cP$ from $1.7\,cP$ to $0.7\,cP$, which is the correct viscosity of silicon, is expected to increase the maximum dissipation rate with little effect on the temperature, velocity and interface shapes, and therefore the heat transfer, flow and free-boundary shapes depicted in Figure 4-27 are expected to be correct for the molecular viscosity of $0.7\,cP$ also.

Continuing to increase the molecular viscosity in this way yields a mild decrease in transport rates. The solution at the highest computed value of $5.5\,cP$ is shown in Figure 4-29, and the values of several important solution parameters are plotted in Figure 4-30. These results show the decreasing importance of molecular viscosity on the mean flow as the value appropriate for silicon is approached. The resistance to heat transfer increases slightly with increasing molecular viscosity, reflecting the added resistance to convective transfer in the viscous sublayers and buffer layers adjacent to the walls. The increasing molecular viscosity causes a small increase in turbulent viscosity, which also occurred in the calculations with buoyancy alone and is due to an decrease in the dissipation rate near walls.

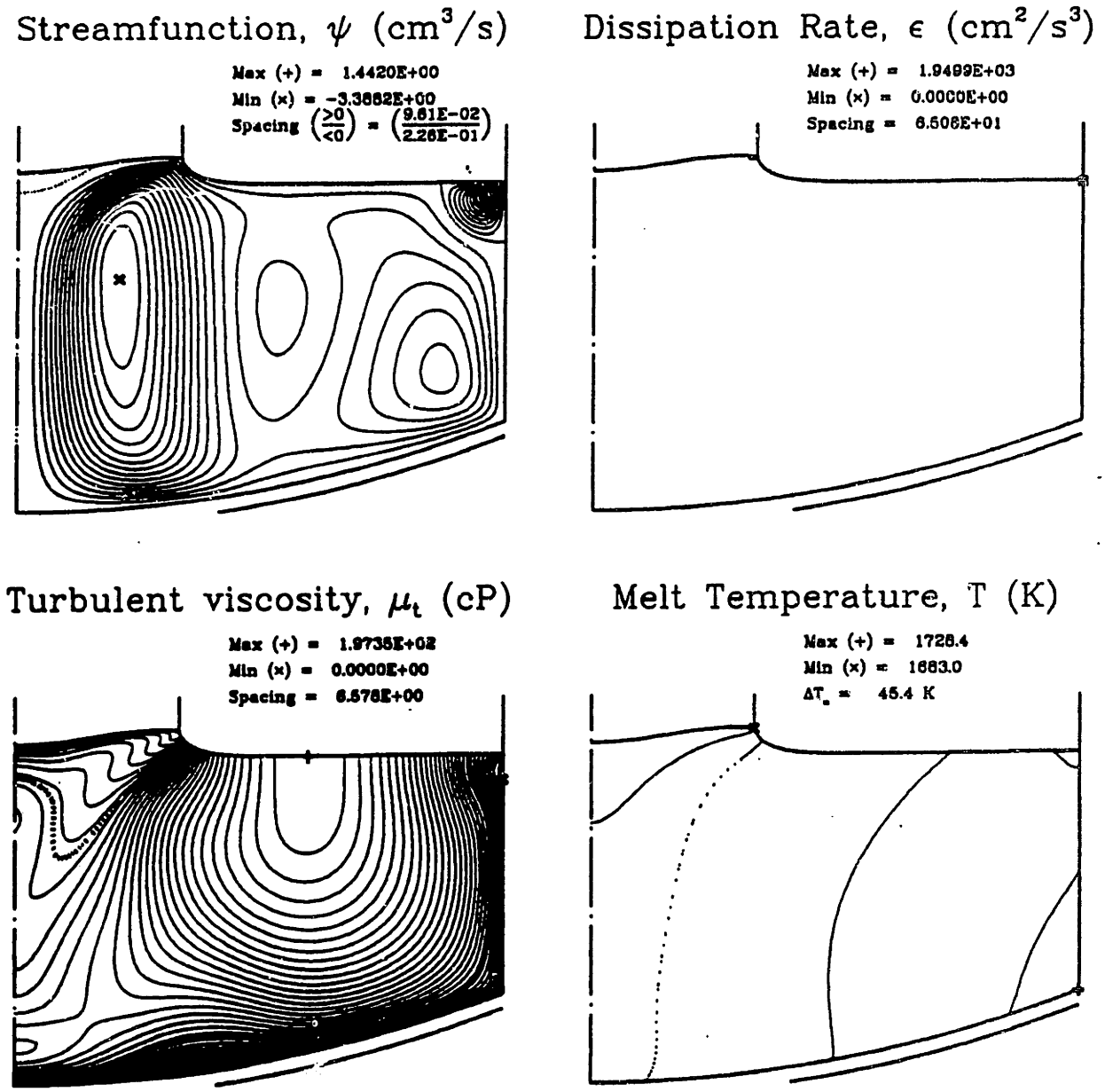

Figure 4-27: Simulation computed using low-Reynolds-number $K-\epsilon$ model having regularization to terms D and E but no artificial generation parameter with all flow mechanisms combined at $\mu = 1.7cP$: (a) streamfunction, (b) dissipation rate, (c) turbulent viscosity, and (d) melt temperature. In figure (c) the solid curve indicates where the turbulent viscosity exceeds the molecular viscosity and the dotted curve shows where the turbulent conductivity exceeds the molecular conductivity.

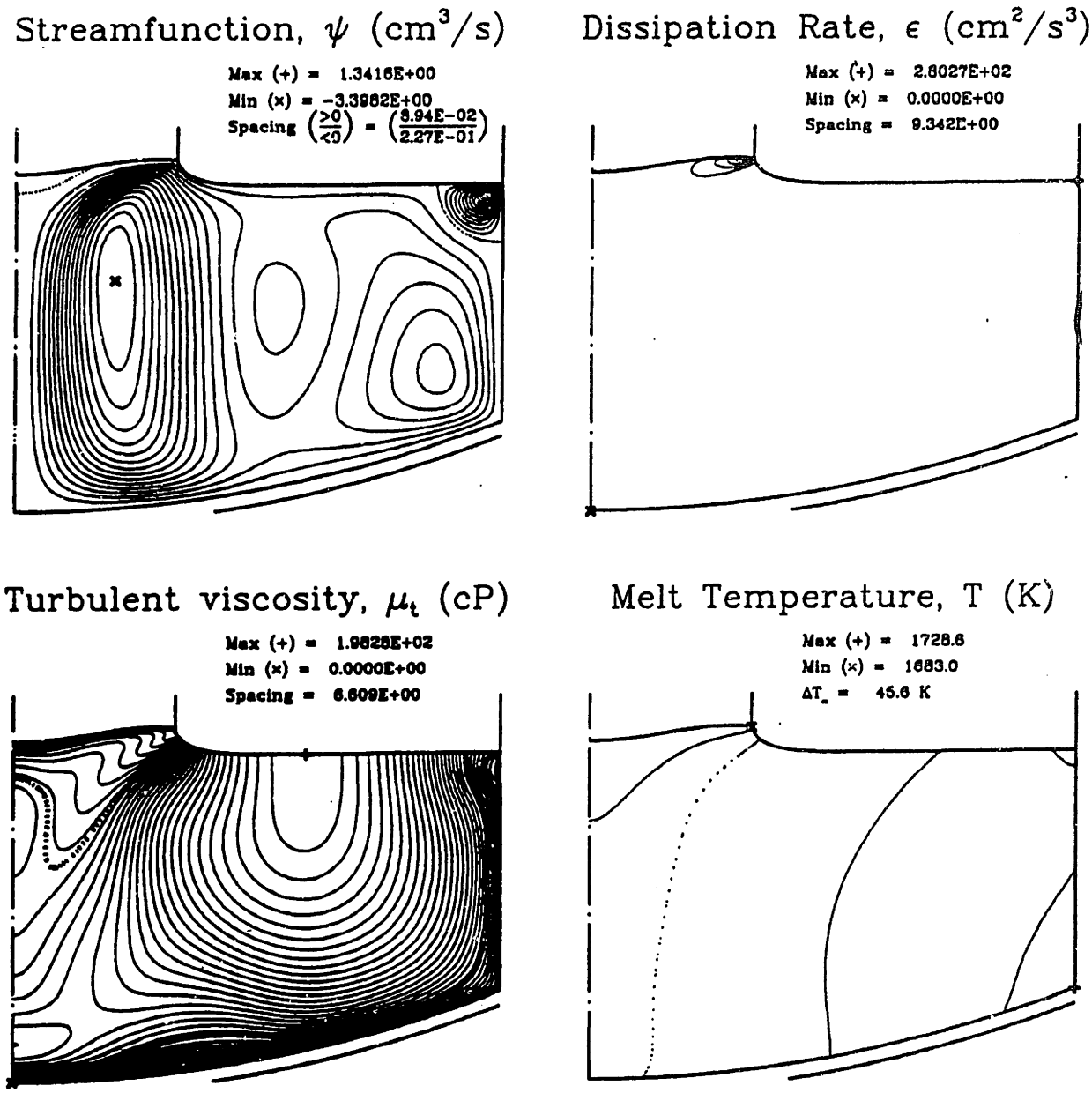

Figure 4-28: Simulation computed using low-Reynolds-number $K-\epsilon$ model having regularization to terms D and E but no artificial generation parameter with all flow mechanisms combined at $\mu = 2.7cP$: (a) streamfunction, (b) dissipation rate, (c) turbulent viscosity, and (d) melt temperature. In figure (c) the solid curve indicates where the turbulent viscosity exceeds the molecular viscosity and the dotted curve shows where the turbulent conductivity exceeds the molecular conductivity. Compare with Figure 4-27.

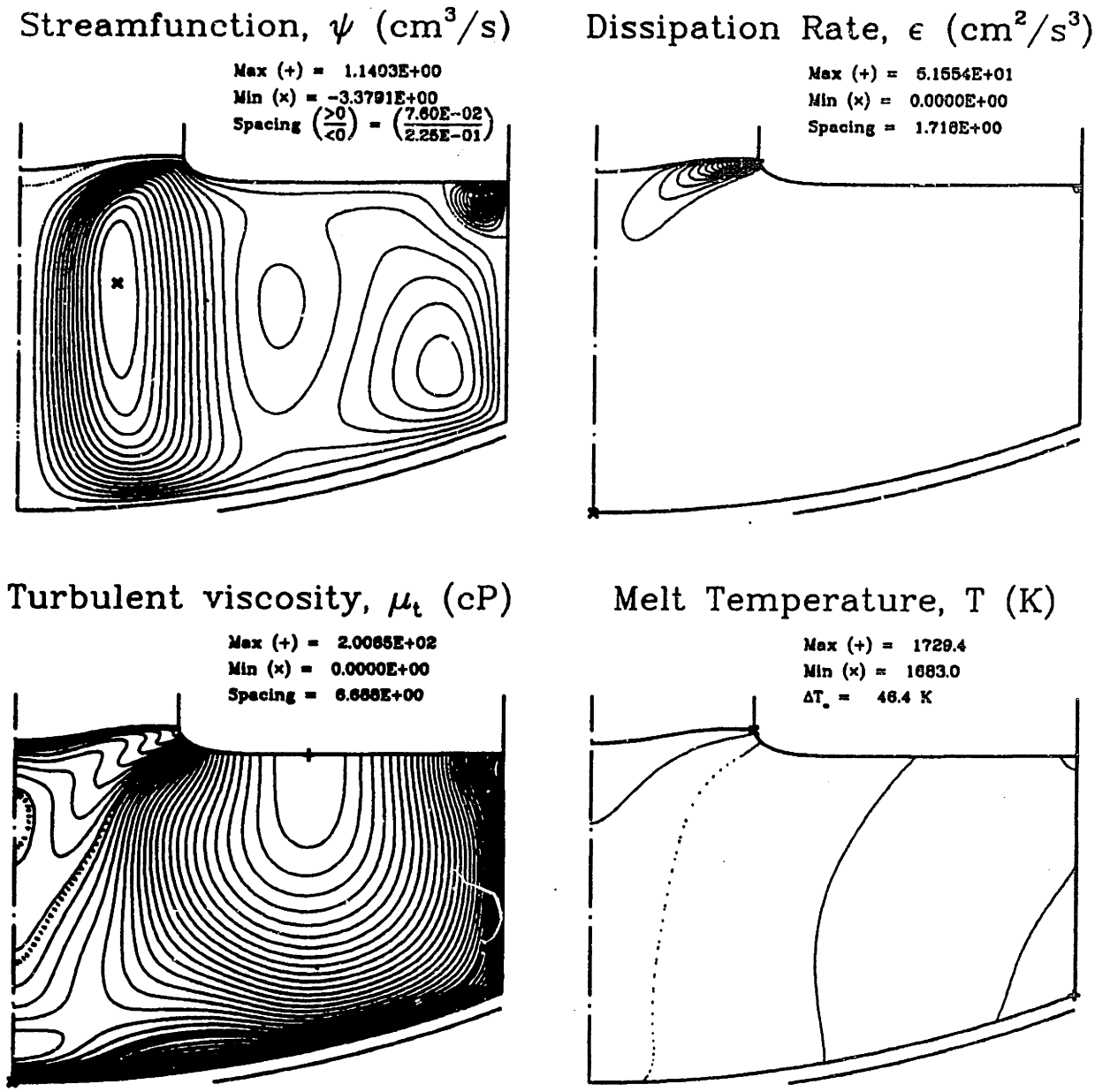

Figure 4-29: Simulation computed using low-Reynolds-number $K-\epsilon$ model having regularization to terms D and E but no artificial generation parameter with all flow mechanisms combined at $\mu = 3.95cP$: (a) streamfunction, (b) dissipation rate, (c) turbulent viscosity, and (d) melt temperature. In figure (c) the solid curve indicates where the turbulent viscosity exceeds the molecular viscosity and the dotted curve shows where the turbulent conductivity exceeds the molecular conductivity.

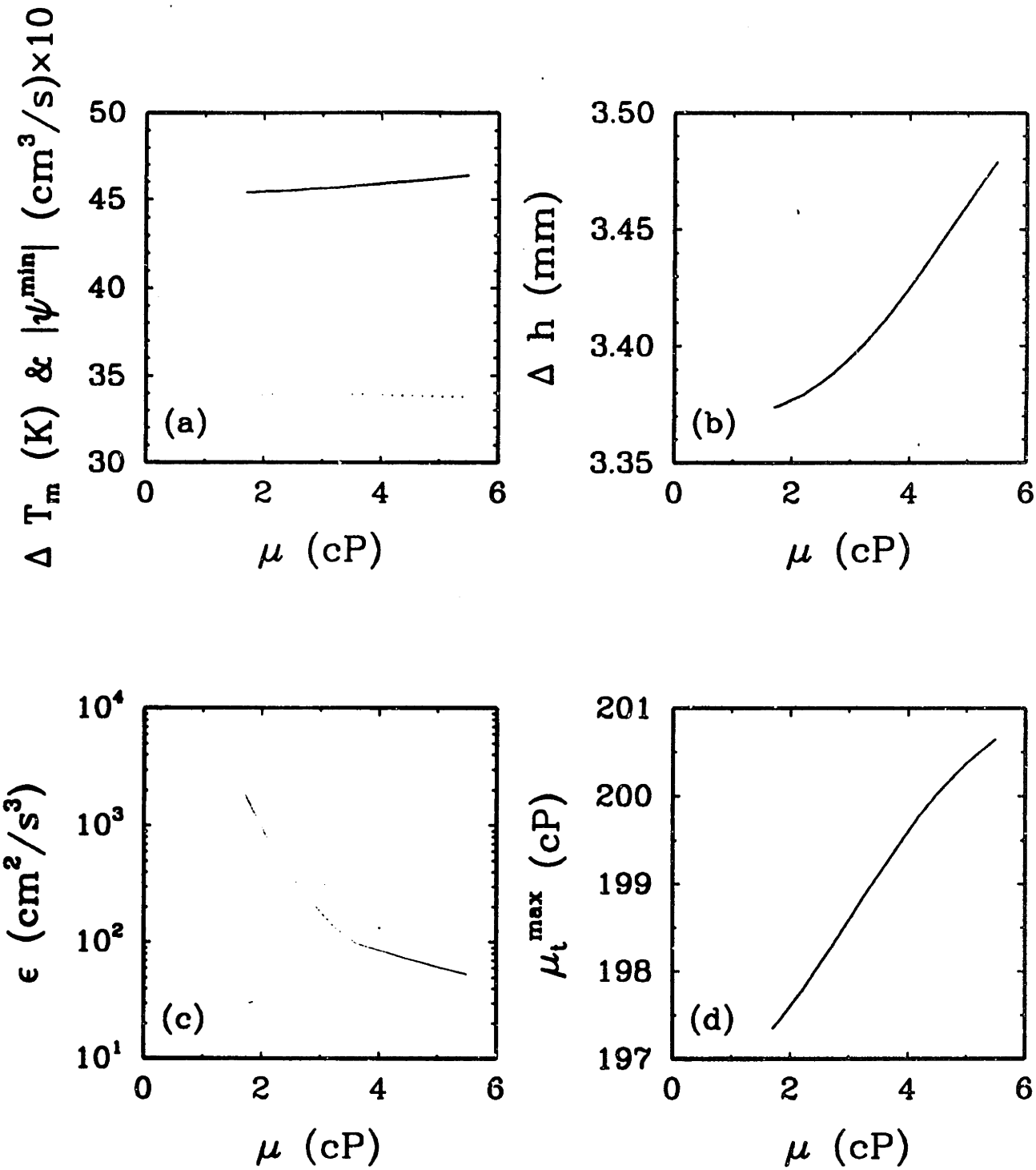

Figure 4-30: Effect of increasing μ on (a) the temperature difference across the melt $\Delta\overline{T}_m$ (—) and the maximum circulation rate of the the primary cell $|\overline{\psi}^{min}|$ (.....); (b) the maximum interface deflection $\Delta\overline{h}$; (c) the maximum dissipation rate ϵ^{max}; and (d) the maximum turbulent viscosity μ_t^{max} for all flow mechanisms combined with low-Reynolds-number $K-\epsilon$ model: $0.7 \leq \mu \leq 5.5cP$.

4.6 Comparison of $K-\epsilon$ /IHTCM results to measurements

4.6.1 Measurements on the Siltec system

In this Section the turbulent results from the $K-\epsilon$ /IHTCM are compared with the measurements described in Chapter 3 and to observations from the literature with the purpose of determining the accuracy of the physical depiction by the $K-\epsilon$ /IHTCM. The initial comparison with experiments in Section 3.3 showed that the temperature measurements were reasonably well-predicted, but that the IHTCM could not predict the nature of the melt flow at realistic conditions. The $K-\epsilon$ /IHTCM has achieved a reliable prediction of the melt flow, and so the measurements of the Siltec system are revisited here to reaffirm the accuracy of the temperature field and the magnitude of the thermoelastic stress in the crystal, and to compare precisely the measured interface shape with prediction from the $K-\epsilon$ /IHTCM. Since the $K-\epsilon$ /IHTCM converges more readily than the previous IHTCM, the effect of varying crucible rotation rate is explored and compared qualitatively with data from Kobayashi et al., 1991; predictions are also made at varying crystal and crucible rotation rates to compare qualitatively with measurements of the oxygen concentration in CZ-grown crystals (Yen and Tiller, 1991; Lin and Benson, 1987; Kim and Langlois, 1990).

The average flow streamlines in Figure 4-27 are much different than the steady-state flow structure in Figure 3-13. The temperature measurements are compared with these calculations and those from the laminar model in Figure 4-31. Both predictions fall within the bounds of uncertainty in the comparison, since the melt represents only a small amount of the thermal resistance which is reflected in the measured temperatures. The thermoelastic stress computations shown in Figure 4-32 are also of similar magnitude, irrespective of whether laminar or turbulent flow model is used, since the temperature gradients which drive them are determined mostly by the radiative environment of the crystal. The interface shape differs substantially however, which is significant since this is the most sensitive measure of the strength of melt convection that is available from experiment. The $K-\epsilon$ /IHTCM simulation converges much more readily with changes in flow parameters due to the large turbulent viscosity, and it permits changing the operating parameters from $(R_s, \omega_s) = (41\,mm, 20\,rpm)$ to $(50\,mm, 15\,rpm)$ to match the different experimental conditions for the measurement of interface shape. The solution for these conditions is shown in Figure 4-33. The $K-\epsilon$ /IHTCM predicts the observed

deflection more accurately than the laminar flow model as well, which indicates that heat transfer prediction in the critical melt/solid interface region is improved by turbulence modelling.

4.6.2 The effect of crucible rotation

The flexibility of the $K-\epsilon$ /IHTCM to handle substantial changes in operating parameters enabled varying the simulated crucible rotation rate between $1.5\,rpm$ and $17.5\,rpm$. The motivation for this was the report of enhanced transport with increasing crucible rotation by Kobayashi et al., 1991, which was depicted in Figure 4-2. Several of the important solution variables are plotted with crucible rotation rate in Figure 4-37 and the solutions at $5\,rpm$ and $15\,rpm$ are shown in Figures 4-35 and 4-36, respectively. Heat transfer is enhanced by increasing the rotation rate over $7\,rpm$ in qualitative agreement with the experimental findings. The reason for this enhancement is that the kinetic energy is generated by the velocity gradients in the azimuthal flow created by the interaction of the azimuthal flow with circulation in the meridional plane. This gradient can be seen by the deviation of the azimuthal flow contours in Figures 4-35 and 4-36 from the vertical alignment expected for solid-body motion. Rotation only impedes meridional transport for two-dimensional flow. Rotational energy enhances transport *isotropically* using the $K-\epsilon$ model of turbulence.

4.6.3 Comparison to published data on oxygen uptake

The mass flux of oxygen was predicted with the $K-\epsilon$ /IHTCM and compared with data measured on various CZ systems. In a $108\,mm$ hot-zone Siltec furnace with $\omega_c = -1\,rpm$, the effect of increasing crystal rotation from $25\,rpm$ to $4\,rpm$ was to increase the average oxygen uptake by about 10% (Yen and Tiller, 1991). In a $350\,mm$-diameter unnamed crucible (Lin and Benson, 1987) the effect of increasing crucible rotation from $9\,rpm$ to $12\,rpm$ or from $12\,rpm$ to $15\,rpm$ was to increase the average oxygen uptake by successive increments of about 10%. The direction of these changes is in qualitative agreement with the results of the $K-\epsilon$ /IHTCM plotted in Figure 5-2, which show that oxygen uptake increases with the magnitudes of both crystal and crucible rotation. The oxygen radial profile from a $305\,mm$ hot-zone Siltec furnace at Westinghouse Corporation operating at $(\omega_c, \omega_s) = (-8\,rpm, +15\,rpm)$ (Kim and Langlois, 1990) also is compared to the radial profile from the $K-\epsilon$ /IHTCM at the same rotation conditions and crystal radius. The profiles agree qualitatively. One difference is that the concentration profile predicted in

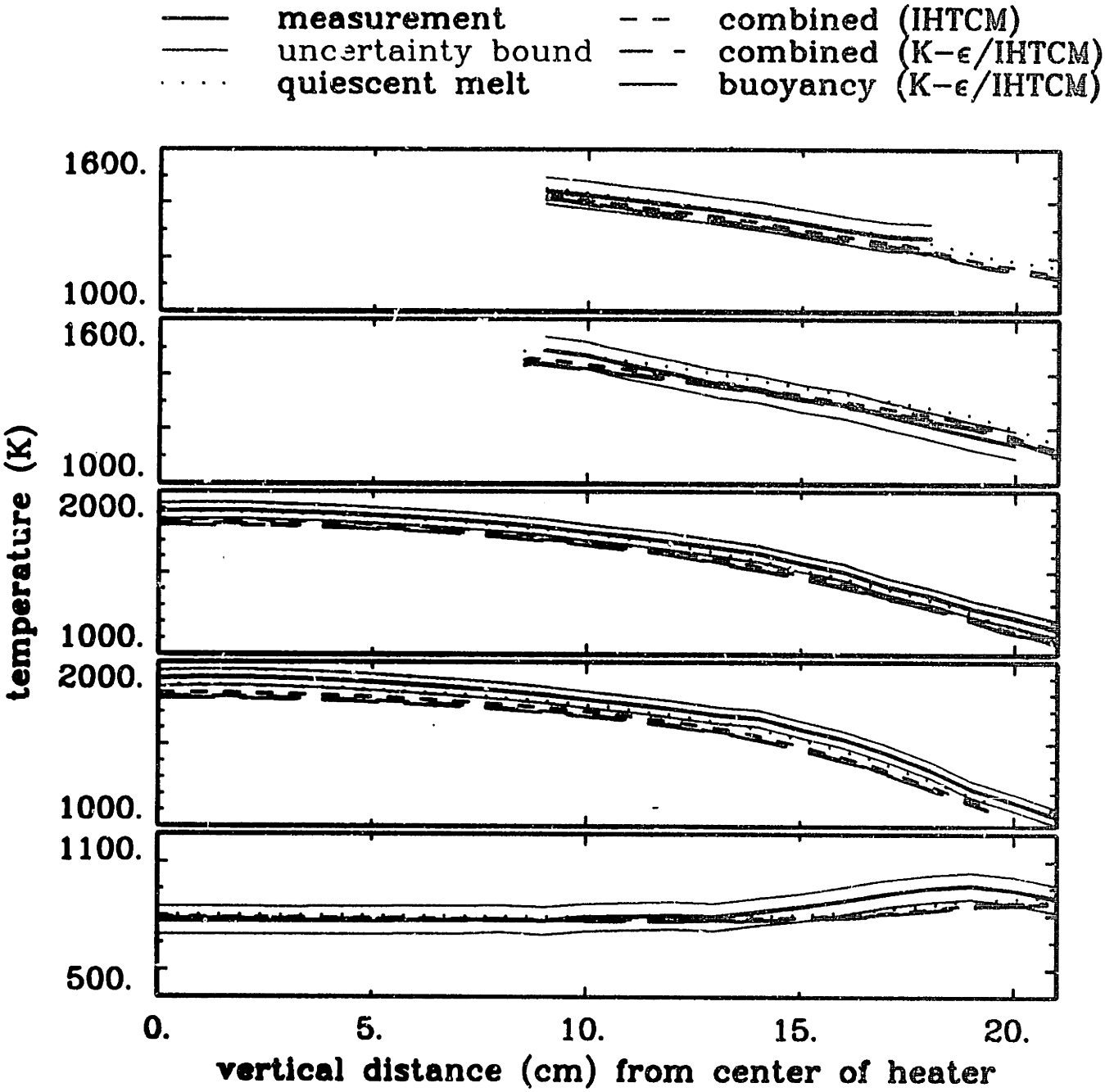

Figure 4-31: Comparison of temperature profiles measured with the thermowell to predictions of the thermowell model for the simulations using the laminar IHTCM and the $K-\epsilon$ /IHTCM. The curves represent the measurements (—), the uncertainty bounds on the data (—), calculations without convection (···), calculations with combined convective forces using the IHTCM (- - - -), calculations with buoyancy using the $K-\epsilon$ /IHTCM(– – –), calculations with all convective forces combined using the $K-\epsilon$ /IHTCM (— — —).

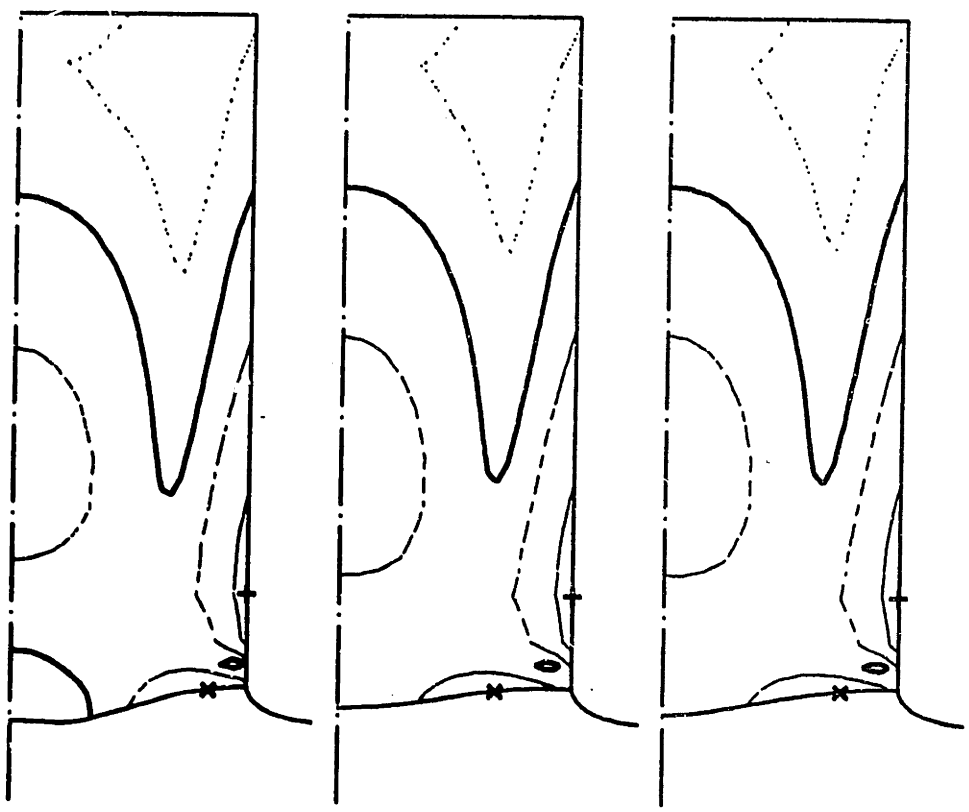

Figure 4-32: Prediction of the von Mises stress in the crystals Stress contours are 0.5, 1, 2, 4 and 8 times the value of the CRSS; CRSS=$1.8 \times 10^7 dyn \cdot cm^{-2}$. The models used for the simulations are (a) IHTCM with all flow mechanisms combined at $\mu = 3.54cP$ (b) $K - \epsilon$ /IHTCM with buoyancy only at $\mu = 0.7cP$ (c) $K - \epsilon$ /IHTCM with combined flow mechanisms at $\mu = 1.7cP$.

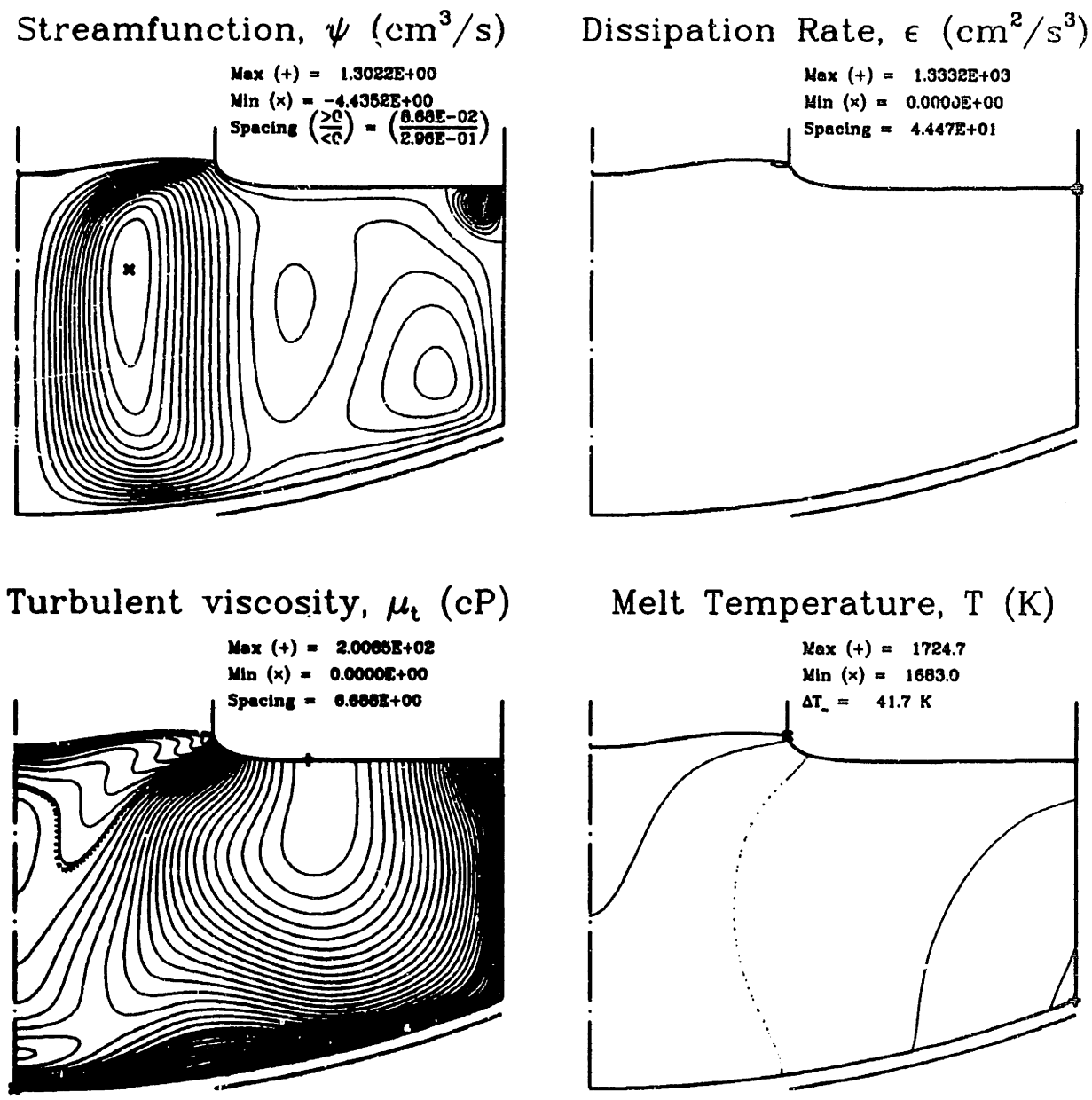

Figure 4-33: Simulation computed using $K-\epsilon$ /IHTCM with all flow mechanisms combined at molecular viscosity of $1.7\,cP$ with crucible rotation rate $= 15\,rpm$ and crystal diameter $= 100\,mm$. (a) Streamfunction, (b) azimuthal velocity, (c) turbulent viscosity and (d) melt temperature. In (c) the solid black line indicates where Reynolds stress exceeds molecular viscosity and the dotted line shows where turbulent heat flux exceeds heat conduction.

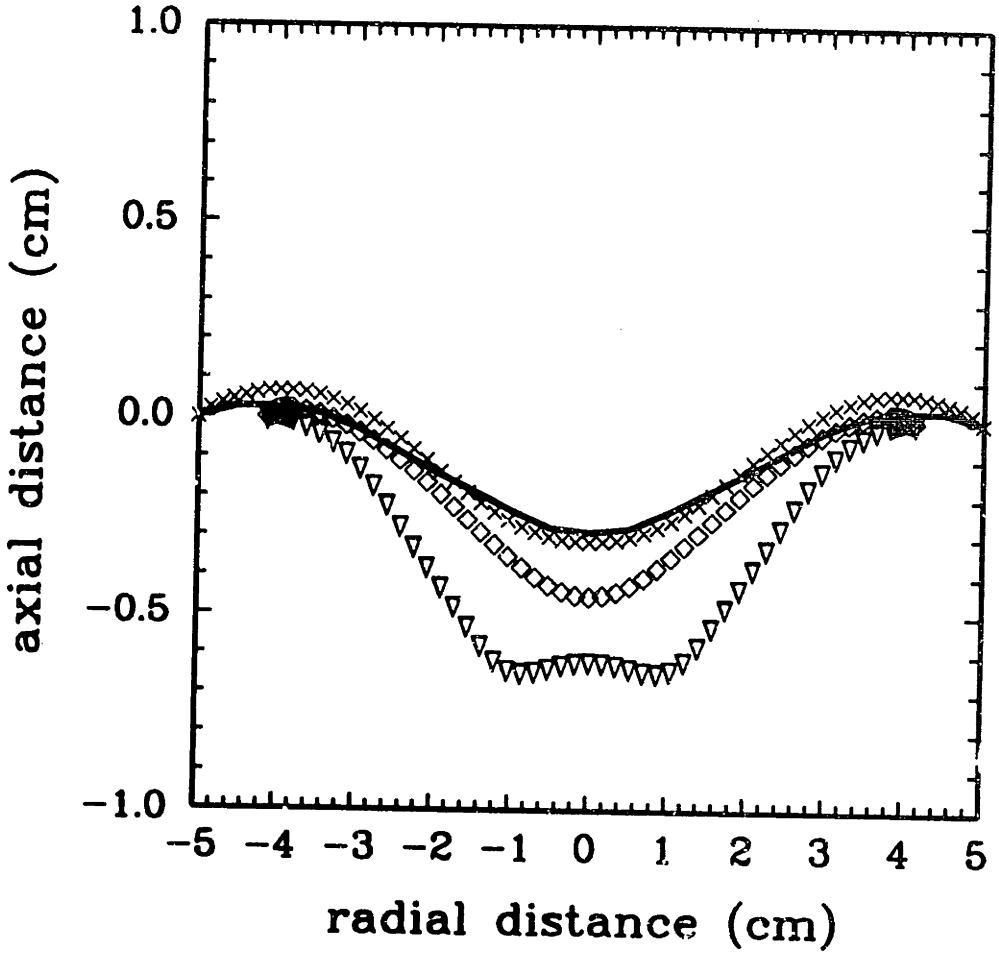

Figure 4-34: Melt/crystal interface shapes from the simulations with individual and combined convection mechanisms: (—) measurement for crystal of $100\,mm$ diameter; (+++) simulation with no convection; $(\times\times\times)$ $K-\epsilon$ /IHTCM prediction with combined flow mechanisms and $\mu = 1.7\,cP$ for crystal of $100\,mm$ diameter; $(\triangledown\ \triangledown\ \triangledown)$ IHTCM simulation with combined flow mechanisms and $\mu = 3.54\,cP$. Horizontal axis is drawn to actual size, vertical axis is drawn with a 5 : 1 scale.

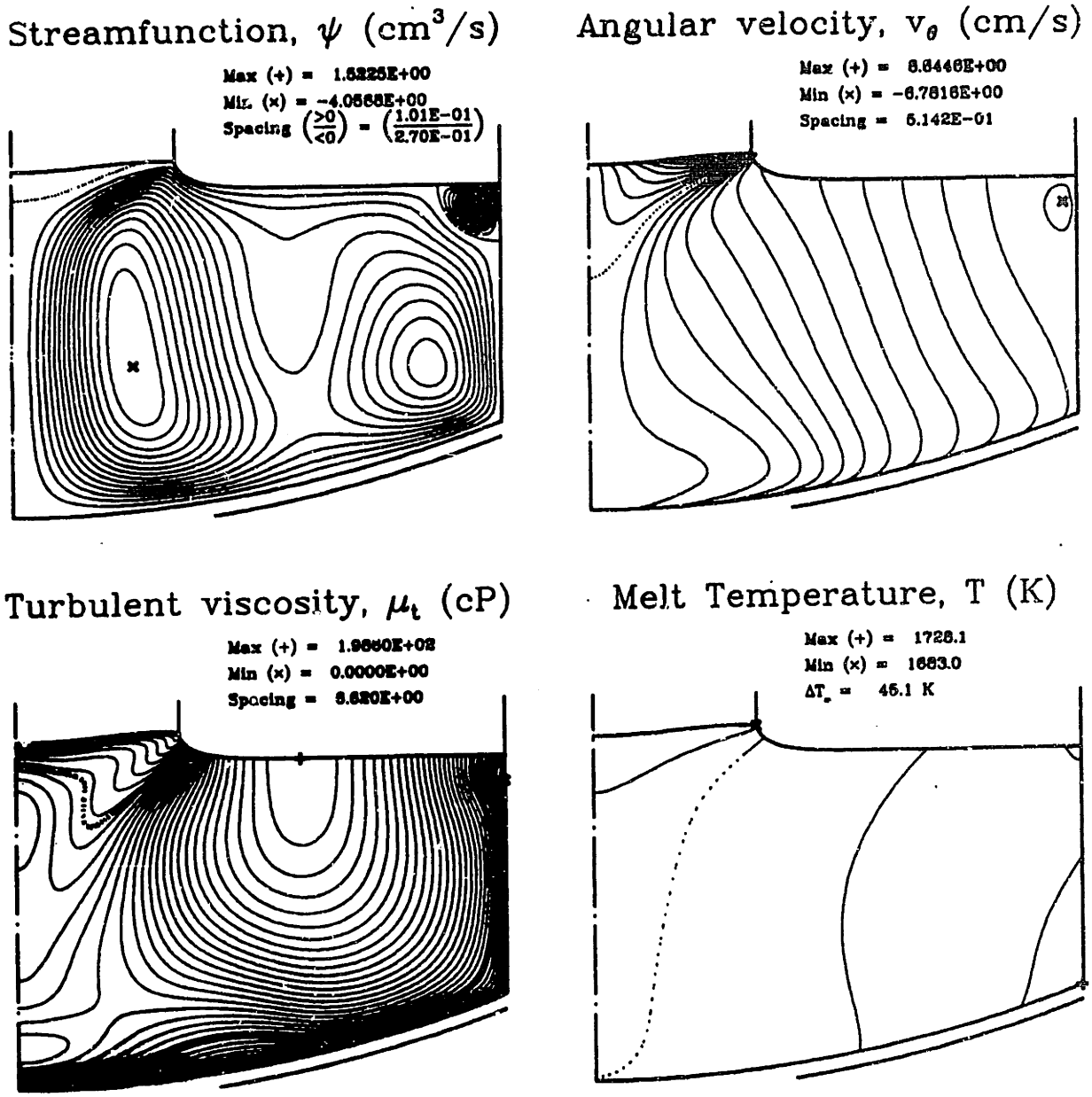

Figure 4-35: Simulation computed using low-Reynolds-number $K-\epsilon$ model having regularization to terms D and E but no artificial generation parameter with all flow mechanisms combined at $\mu = 1.7cP$ with crucible rotation rate $= 5\,rpm$. (a) Streamfunction, (b) azimuthal velocity, (c) turbulent viscosity, and (d) melt temperature. In figure (c) the solid curve indicates where the turbulent viscosity exceeds the molecular viscosity and the dotted curve shows where the turbulent conductivity exceeds the molecular conductivity.

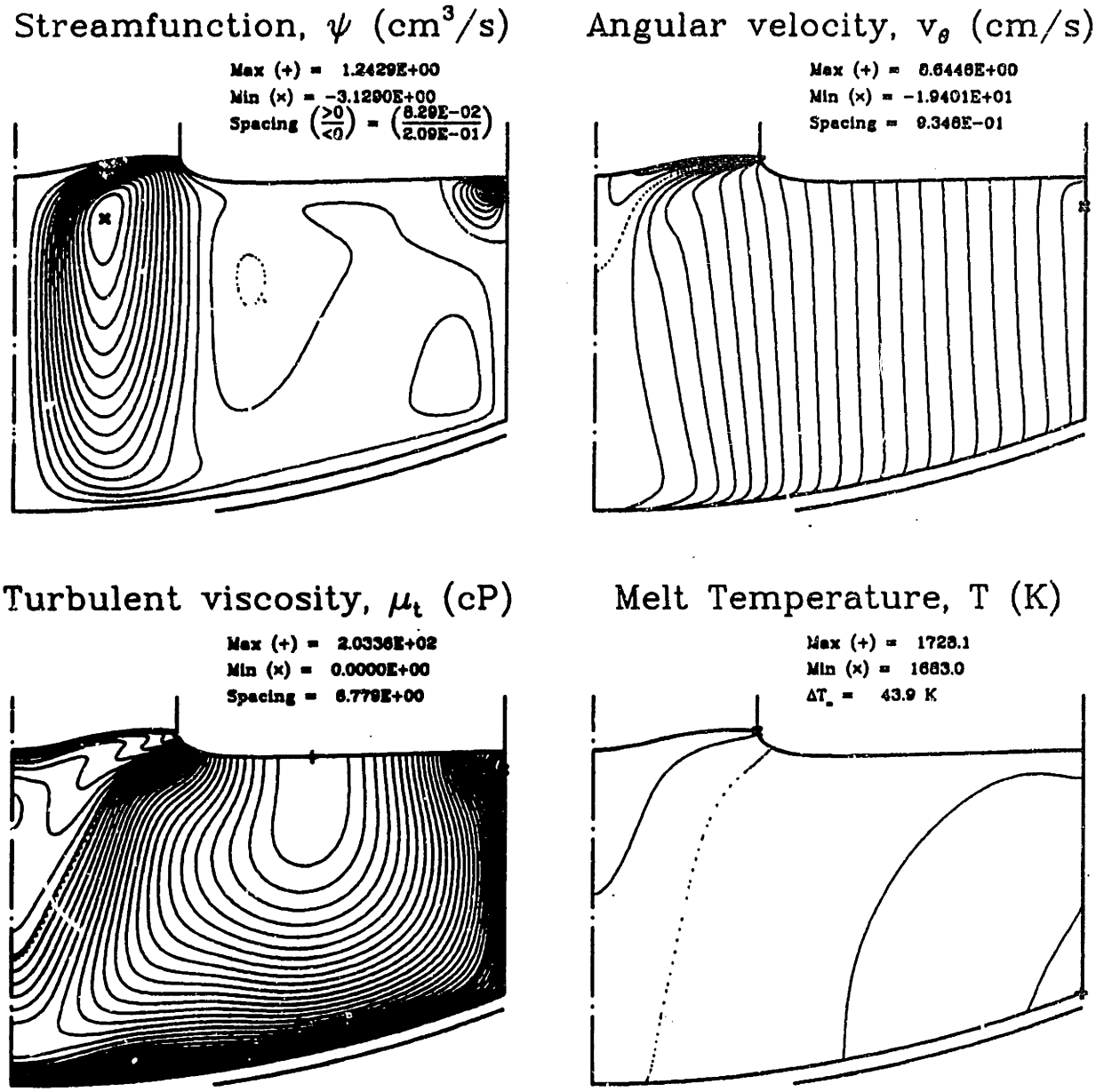

Figure 4-36: Simulation computed using low-Reynolds-number $K-\epsilon$ model having regularization to terms D and E but no artificial generation parameter with all flow mechanisms combined at $\mu = 1.7cP$ with crucible rotation rate = $15\,rpm$. (a) Streamfunction, (b) azimuthal velocity, (c) turbulent viscosity, and (d) melt temperature. In figure (c) the solid curve indicates where the turbulent viscosity exceeds the molecular viscosity and the dotted curve shows where the turbulent conductivity exceeds the molecular conductivity.

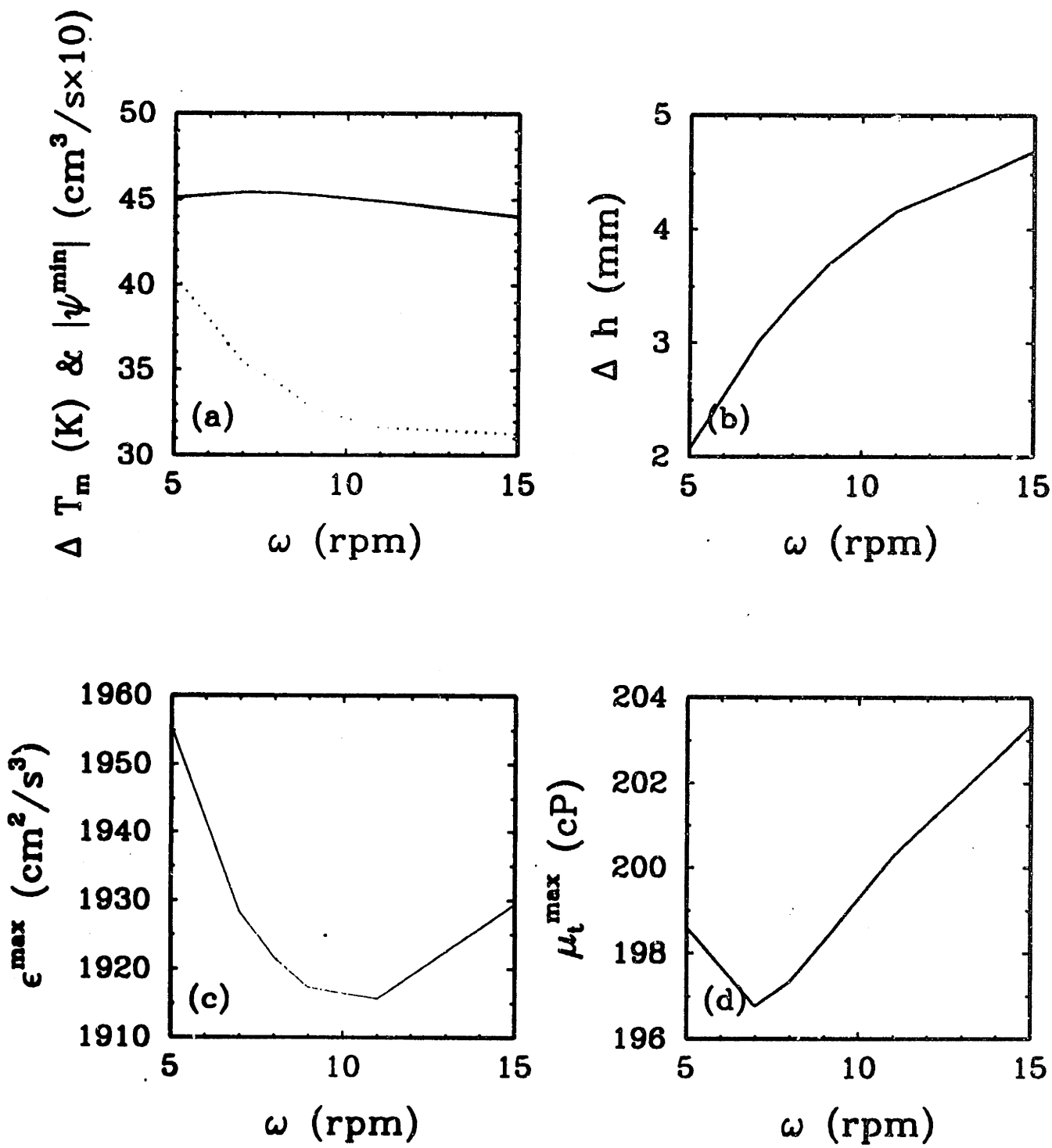

Figure 4-37: Effect of increasing crucible rotation rate on (a) $\Delta\overline{T}_m$ (—) and $|\overline{\psi}^{min}| \times 10$ (...), (b) $\Delta\overline{h}$, (c) ϵ^{max}, and (d) μ_T^{max} for all flow mechanisms combined with low-Reynolds-number $K-\epsilon$ model with molecular viscosity $= 1.7cP$ and crucible rotation rate $5 \leq \omega_c \leq 15\,rpm$.

the simulation rises to only 50% of its peak value 0.5 cm from the crystal radius while the concentration there is 85% of its peak in the experimental profiles. Oxygen can be expected to diffuse only on the order of 10^{-2} cm in the crystal during 10 h of growth at the high temperatures in the CZ chamber, and so solid-phase diffusion should not smooth the measured profiles enough to account for the difference in uniformity. The lack of radial uniformity predicted by the $K-\epsilon$ /IHTCM with all convective mechanisms present in Figure 4-38b is due to the transport by scalar turbulent diffusion and the free surface's acting as an infinite sink for oxygen. The mass flux toward the free surface estimated by the turbulent diffusivity is large, resulting in the gentle profile near the crystal's edge.

The isopleths depicted in Figure 4-38 differ substantially from what is assumed by conventional models of solute segregation, which assume a diffusion boundary-layer in front of the crystal and a constant solute concentration in the bulk phase. The $K-\epsilon$ /IHTCM therefore predicts that the flux of oxygen through the bulk is not determined by steady vigorous mixing, but rather by transient fluctuations throughout the bulk during crystal growth with crucible rotation, since the turbulent transport dominates the mean transport terms when all convective mechanisms are present. This contrast is depicted schematically in Figure 4-39, which compares the isopleths from Figure 4-38 to an idealized view of the concentration field where there is complete mixing in the bulk flow.

4.7 Outlook

This Chapter has described the justification, development and implementation of the $K-\epsilon$ /IHTCM which estimates the transport through the CZ melt in the limit of turbulent flow. Results have been presented that show that the $K-\epsilon$ /IHTCM reliably predicts a unique average flow state at viscosities approaching that of the molecular viscosity of silicon, with *ad hoc* modifications that limit excessively large terms in the low-Reynolds-number $K-\epsilon$ equations without affecting the solution fields globally. In addition, the most sensitive measure of heat transfer in the melt, the melt/solid interface shape is more closely predicted by the $K-\epsilon$ modifications to the IHTCM. The $K-\epsilon$ /IHTCM also qualitatively predicts the increase of heat transfer with crucible rotation (Kobayashi et al., 1991), which evidently occurs because of the interaction between rotation and natural convection. The enhancement of oxygen transfer with increasing crucible rotation rotation rate via isotropic turbulent convection is clearly shown, and agrees qualitatively with all the published results on oxygen uptake in industrial-scale

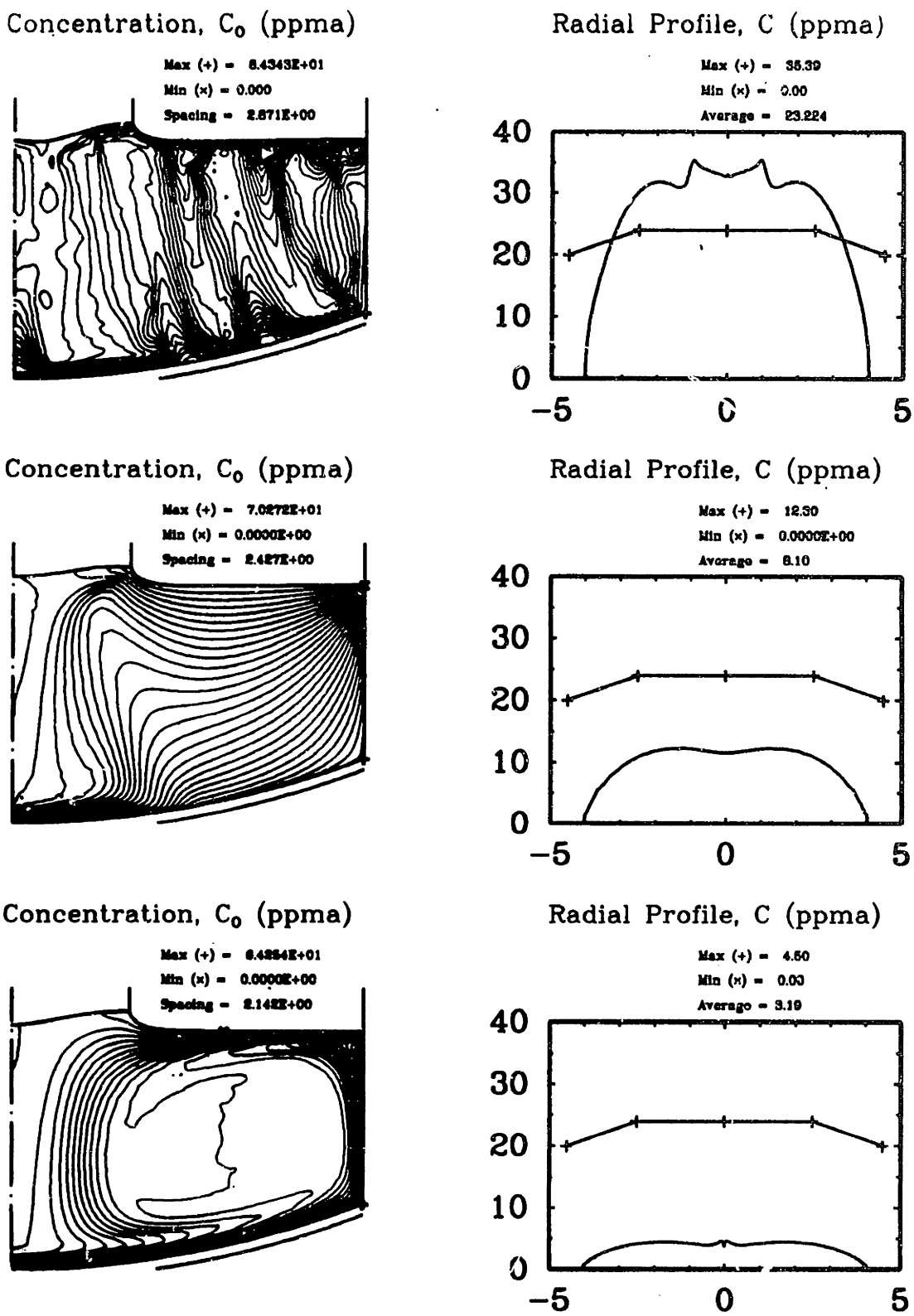

Figure 4-38: Oxygen isopleths in the melt and radial profiles of oxygen uptake in the crystal for simulations of: (a) all flow mechanisms combined with the IHTCM at $\mu = 3.54cP$, (b) all flow mechanisms combined with the $K-\epsilon$ /IHTCM at $\mu = 1.7cP$, and (c) buoyant flow only with the $K-\epsilon$ /IHTCM at $\mu = 0.7cP$.

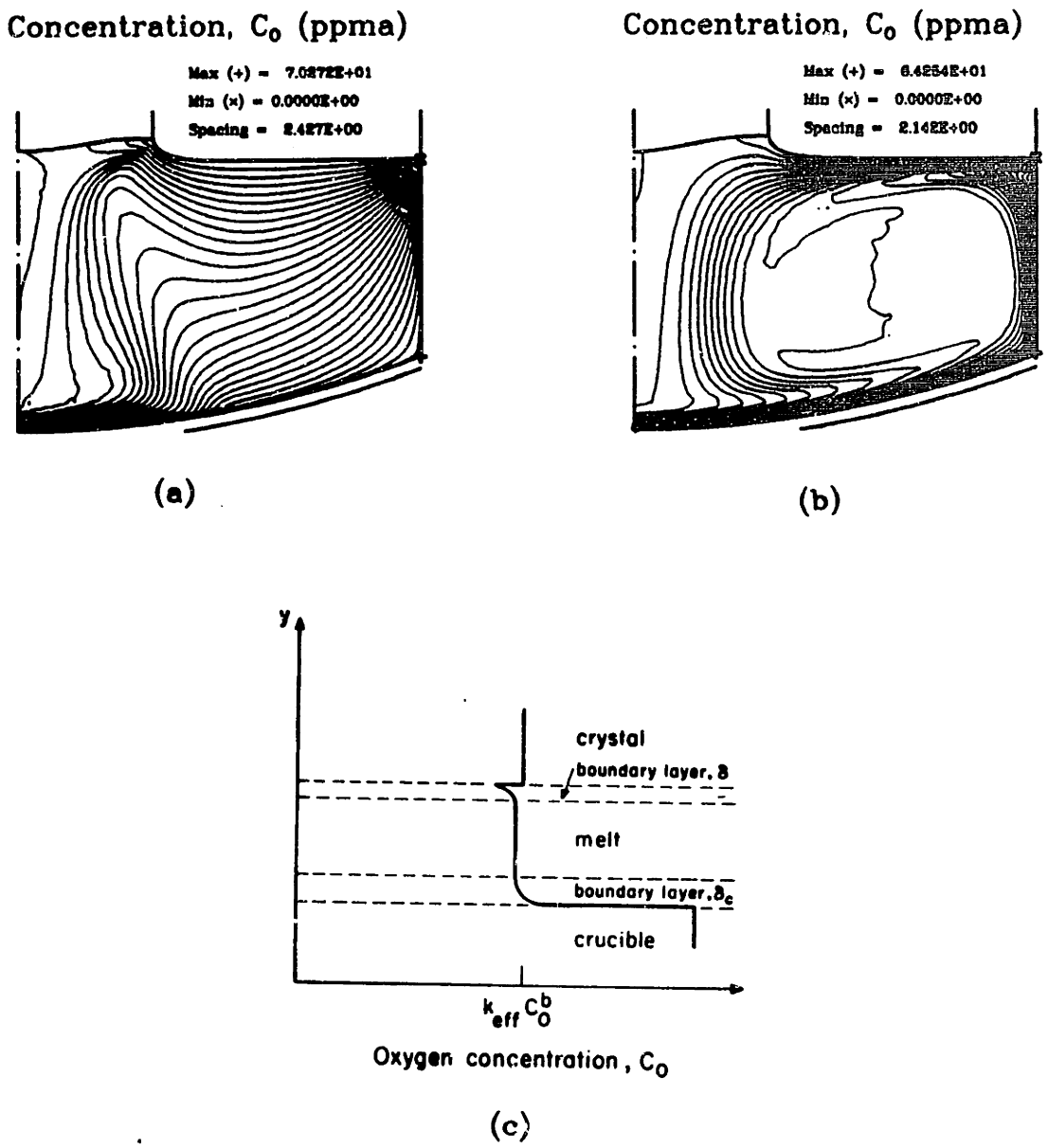

Figure 4-39: Oxygen concentration in the melt (a) as predicted by the $K-\epsilon$ /IHTCM with all flow mechanisms combined (b) as predicted by the $K-\epsilon$ /IHTCM with buoyancy only (c) as envisioned by models that assume steady, vigorous mixing in the bulk flow; after Carlberg et al., 1932.

crucibles.

The final chapter will draw practical conclusions regarding the optimization of control and design strategies in CZ silicon growth, by potential applications oi the IHTCM and $K-\epsilon$ /IHTCM models and the experiences discussed in Chapters 2 to 4.

Chapter 5

Toward optimization of CZ silicon growth

Summary

Although application of results on the SILTEC apparatus was preempted, several conclusions important to the model-based optimization necessary for improving silicon growth have been reached through the calculations described in Chapters 2 through 4. The accurate thermal predictions of the IHTCM, made possible by radiative heat-transfer modelling, strongly dismiss thermal stress minimization for the prevention of dislocations in large-diameter silicon growth. Rather, the solution to this problem lies in suppressing the nucleation of dislocations. Models of axisymmetric and steady melt flow have produced a multiplicity of solutions close to the realistic viscosity, and therefore cannot predict the transport in large-diameter melts with rotation and undamped natural convection. The $K-\epsilon$ /IHTCM for turbulent flow uniquely predicts realistic conditions and accurately predicts the heat-transfer near the melt/solid interface. As well, the achievement of a robust $K-\epsilon$ -model formulation in the IHTCM has shown that augmented axisymmetric and steady-state finite-element/Newton models can account for the effects of turbulent heat transfer in large CZ systems. This chapter interprets the results of Chapters 2–4, drawing the conclusions stated above. Also, in a purely illustrative context, operating parameters are varied to explore the potential of the $K-\epsilon$ /IHTCM for optimizing a large-scale CZ crystal-puller.

5.1 On achieving dislocation-free crystals and controlled oxygen deposition in large-diameter silicon boules

In calculation with either laminar or turbulent fluid mechanics, the temperature field near the crystal is modelled accurately, and with the $K-\epsilon$ /IHTCM the heat flux at the melt/crystal interface also is modelled accurately. With this confidence in the thermal modelling, calculations of the thermal stress at the melt/solid interface consistently exceed the CRSS at the melting point. Accordingly, if *even a single* dislocation were present in the growing crystal, it would be expected to propagate and proliferate rapidly.

However, no dislocations are formed in the experimental crystals and these two facts constitute the strongest possible proof that the control of thermoelastic stress in the crystal is not the sole remedy for preventing dislocations for larger-diameter boules. Preventing the generation of dislocations by inhibiting the clustering of point defects which nucleate dislocations should be the objective of further research on dislocations in large-diameter silicon boules.

Models like the $K-\epsilon$ /IHTCM may ultimately be the tool used to predict the likelihood of dislocation generation in large-diameter silicon boules, when the missing model component is provided in the form of a relation between macroscopic quantities such as crystal temperature or oxygen concentration, and the likelihood of *any* dislocation generation occurring. For a given piece of equipment strictly empirical correlations could be made, but by far the more insightful tool would be one that directly addresses the mechanism for dislocation formation. As described in Chapter 1, the nucleation of dislocations from clusters of self-interstitials or oxygen precipitates is a likely mechanism, and is presently being studied (Maroudas, 1992). If a relation between the probability of dislocation generation and macroscopic quantities is established, then models like the $K-\epsilon$ /IHTCM will be the key tools to relate the likelihood of dislocation formation to controllable processing parameters and system design. For materials which are routinely grown with dislocations, such as *GaAs* and *InP*, the $K-\epsilon$ /IHTCM can be immediately implemented as a control and design tool, using thermoelastic stress minimization to optimize the dislocation density.

The effects of changing operating parameters on the oxygen concentration in CZ-grown silicon have been qualitatively predicted with the $K-\epsilon$ /IHTCM. The enhancement of oxygen transport with increasing crucible rotation could not be predicted with two-

dimensional and laminar flow models, and this points to the potential of the $K-\epsilon$ /IHTCM as a useful design tool for optimizing the oxygen concentration in CZ-grown silicon. The wide range of oxygen concentrations reported in the literature indicates that the oxygen concentration in CZ-grown silicon depends greatly on the specific growth conditions; therefore, the *quantitative* comparison of oxygen segregation with the $K-\epsilon$ /IHTCM is an outstanding area for further research.

For other dopants added to the polysilicon charge, the $K-\epsilon$ /IHTCM is not applicable in its present form. The total dopant loading in the melt is not a quasi-steady-state quantity, since there is only a sink, which is the growing crystal, and there is no continuous source of dopant to balance the dopant removal. In the case of oxygen, the dissolution of the crucible wall provides the source of oxygen which mostly evaporates from the melt surface and also is incorporated into the growing crystal.

5.2 On the model-based optimization of CZ silicon growth

5.2.1 An optimization example with the $K-\epsilon$ /IHTCM.

A previous case-study of optimization with a thermal-capillary model addressed the minimization of the thermoelastic stress in the crystal using a mixed approach of design options and control parameters by computational experiment (Bornside et al., 1991). Newton-based search methods for multivariable optimization are a logical extension of Newton-based thermal-capillary models (Kinney, 1989) but the emphasis on physical modelling has precluded their development in this work. Because the $K-\epsilon$ /IHTCM can be used to simulate results across wide ranges of parameter-space at realistic growth conditions, it can be used for a computational experiment to isolate an optimum control strategy. An illustrative example seeks the combination of crucible and crystal rotation rates that optimizes the output of the crystal puller as measured by a weighted combination of the deviation from average oxygen concentration and the oxygen radial uniformity between $0 \leq r \leq 0.92R_s$, and maximum thermoelastic stress at the melt/solid interface. The parameter-space of (ω_c, ω_s) probed by the computational experiment is shown in Figure 5-1. The results from varying crucible rotation as described in Section 4.6.2 are used to initialize calculations with varying crystal rotation which span the depicted range of operating conditions. The response surface for the average oxygen concentration in the parameter range $4\,rpm < -\omega_c < 15\,rpm$ and $10\,rpm < \omega_s < 26\,rpm$ is shown in

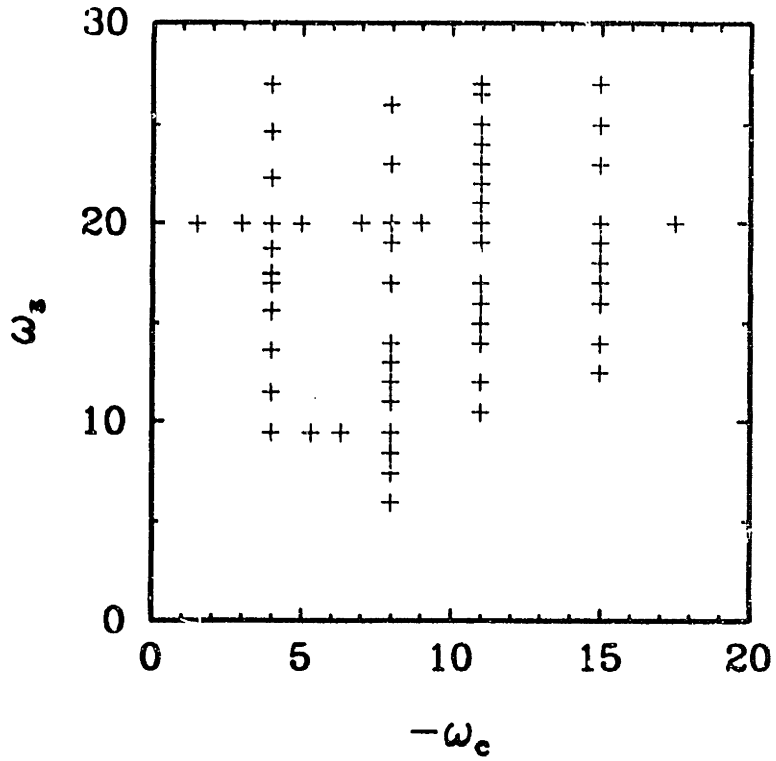

Figure 5-1: Points in ω_c/ω_s-space spanned by computational experiment with varying crystal and crucible rotation rates.

Figure 5-2; a minimum of 5.9 *ppma* is achieved for $(\omega_c, \omega_s) = (-4, 10)$ and a maximum of 11.6 *ppma* for $(\omega_c, \omega_s) = (-11, 26)$. It is seen that the surface is nearly constant with varying crucible rotation between the coordinates $(\omega_c, \omega_s) = (-15, 26)$ and $(-10, 26)$; the surface twists in the plotted range and also is nearly constant for varying crystal rotation between the points $(-4, 10)$ and $(-4, 20)$. The reasons for the maximum occurring at high crystal and crucible rotations are that increased crucible rotation tends to increase turbulent transport throughout the bulk, and crystal rotation tends to increase the mean flux to the crystal surface.

The response surface for oxygen uniformity is shown in Figure 5-3 and naturally is very similar in shape to the plot of average oxygen concentration, since the deviation is produced mostly by the decay to zero concentration near the crystal periphery. At the highest crystal rotation rates the uniformity is enhanced by increasing crystal rotation rate. This can best be seen by contrasting the shape of Figure 5-3b with Figure 5-2 along a path of increasing crystal rotation at constant crucible rotation of $-4\,rpm$. A minimum deviation of 1.7 *ppma* is achieved for $(\omega_c, \omega_s) = (-4, 10)$ and a maximum of 3.1 *ppma* is achieved for $(\omega_c, \omega_s) = (-15, 26)$.

The final response surface for optimized variables is the predicted maximum thermoelastic stress at the melt/solid interface, shown in Figure 5-4. The shape of this plot